UNIVERSITY OF SOUTHAMPTON

FACULTY OF ENGINEERING AND THE ENVIRONMENT

AIRBUS NOISE TECHNOLOGY CENTRE

Broadband Noise Generation of a Contra-Rotating Open Rotor Blade

by

James Raymond Gill

Thesis for the degree of Doctor of Engineering

January 15, 2015

UNIVERSITY OF SOUTHAMPTON

ABSTRACT

FACULTY OF ENGINEERING AND THE ENVIRONMENT

AIRBUS NOISE TECHNOLOGY CENTRE

Doctor of Engineering

Noise Generation of a Contra-Rotating Open Rotor Blade

by James Gill

Requirements to improve the propulsive efficiency of aircraft engines have revived interest in contra-rotating open rotor (CROR) engines. However, CRORs exhibit tonal and broadband noise emissions which are a barrier of entry into commercial service. Until recently, studies have concentrated on tonal noise emissions because they are considered to be louder than broadband emissions. However, recent work has shown that CROR broadband noise can also be significant.

This project uses computational aeroacoustic methods to study the mechanisms underlying broadband rotor-wake interaction (BRWI) noise, which is a dominant CROR broadband noise source. Predictions of BRWI noise have thus far assumed the rotor blades to be flat plates, and have not accounted for the effects of the blade geometry on the noise. In this project, the effects of blade geometry on turbulence interaction noise are comprehensively studied, including the effects on the noise due to airfoil thickness, leading edge radius, angle-of-attack and camber. Airfoil thickness and leading edge radius are shown to reduce the noise at high reduced frequencies, with the noise being more sensitive to thickness than to leading edge radius. The effects of angle-of-attack and camber are found to be small for interactions between an airfoil and isotropic turbulence. The mechanisms which cause the changes to the noise are also investigated. The project concludes with a study of the turbulence interaction noise for realistic CROR blades and conditions to evaluate the error incurred when rotor blades are assumed to be flat plates. It is found that while CROR blade geometry does affect BRWI noise, the effect is sufficiently small that flat plate theory can be confidently used in most circumstances.

In addition to examining the effects of airfoil geometry on the noise, this project investigates efficient methods to computationally simulate turbulence interaction noise. It is shown that the noise is sensitive to transverse turbulent disturbances, but is not sensitive to spanwise or streamwise ones. Therefore, accurate noise predictions are obtained by representing the turbulence as only transverse disturbances, which leads to significant savings in computational cost.

Contents

List of Figures

List of Tables

DECLARATION OF AUTHORSHIP

I, JAMES GILL, declare that the thesis entitled “Noise Generation of a Contra-Rotating Open Rotor Blade”, and the work presented in the thesis are both my own, and have been generated by me as the result of my own original research. I confirm that:

- This work was done wholly or mainly while in candidature for a research degree at this University;
- Where any part of this thesis has previously been submitted for a degree or any other qualification at this University or any other institution, this has been clearly stated;
- Where I have consulted the published work of others, this is always clearly attributed;
- Where I have quoted the work of others, the source is always given. With the exception of such quotations, this thesis is entirely my own work;
- I have acknowledged all main sources of help;
- Where the thesis is based on work done by myself jointly with others, I have made clear what was done by others and what I have contributed myself;
- Parts of this work have been published by the author, as listed in Section 1.2.

Signed: ....

Date: ....

Acknowledgements

I would like to thank my supervisors Professor Xin Zhang, and Professor Phil Joseph for providing support and guidance throughout the four years of my EngD. Thanks must also go to Thomas Nodé-Langlois for invaluable discussions, and for organising and supporting my placement in Toulouse.

I would also like to acknowledge the Engineering and Physical Science Research Council (UK), and Airbus, who provided and supported this project via the Airbus Noise Technology Centre.

Thanks must also go to my colleagues, Ryu, Chris, Mike, Fernando, and Xiaoxian for providing many hours of interesting conversation and debate, and for making the last four years fun as well as productive.

Finally, I would like to thank my wife Laura, for everything else.

Nomenclature

Roman

A	$= \sqrt{1 - M_X^2 \sin^2 \theta}$	
c	Airfoil chord length	[m]
c_0	Speed of sound	[m.s^{-1}]
d	Airfoil semi-span	[m]
E^*	Conjugate of the fresnel integral	
f	Frequency	[Hz]
$G(x, y, X, \omega)$	Two-dimensional time harmonic Green's function	
g^{LE}	Non-dimensional transfer function between upwash velocity and pressure jump across a flat plate	
$H_0^{(2)}$	Hankel function of order 0 and of the second kind	
J	Bessel function of the first kind	
K	Chord-based reduced frequency $K = \frac{c}{\lambda}$	
k	Wavenumber	[m^{-1}]
k^{lim}	Maximum wavenumber limit	[m^{-1}]
K_t	Thickness-based reduced frequency $K_t = \frac{t}{\lambda}$	
L^{LE}	Unsteady loading term in flat plate response model	
L_1	Leading edge scattering of sound	
L_2	Trailing edge back-scattering of sound	
L_b	Buffer zone width	[m]
M	Mach number	

N_r	Number of independent realisations of the turbulent field	
p	Pressure	[Pa]
p_{rms}	Root-mean square pressure	[Pa]
r_0	Observer radius	[m]
R_{le}	Leading edge radius	[m]
Re	Reynolds number	
S_{pp}	Power spectral density of the far-field radiated pressure	[Pa^2.s]
T	Time	[s]
t	Maximum airfoil thickness	[m]
T_{ij}	Lighthill stress tensor	
U	Flow velocity	[m.s^{-1}]
U^{n+1}	Solution vector after each time step	
U_{target}	Target value in buffer region	
v	Upwash turbulent velocity	[m.s^{-1}]
v_0	Upwash gust amplitude	[m.s^{-1}]
$W(\boldsymbol{k})$	Turbulence velocity spectrum	[m$^{3/2}$.s^{-1}]
X	Chordwise position	[m]
x	Observer x co-ordinate	
x_b	Distance from the domain boundary	[m]
y	Observer y co-ordinate	
Y^+	Non-dimensional wall distance	

Greek

α	Angle-of-attack	[deg]
β	Coefficient to set shape of a damping function in the buffer zones	
β_X	$= \sqrt{1 - M_X^2}$	
Λ	Turbulence integral length-scale	[m]

λ	Vortical gust wavelength	[m]
μ_a	Acoustic reduced frequency	
μ_h	Hydrodynamic reduced frequency	
ω	Angular frequency of gust	[rad.s^{-1}]
Φ_{vv}	1D turbulence upwash velocity spectrum	[m^3.s^{-2}]
ρ	Density	[kg.m^{-3}]
σ	$= \sqrt{x^2 + \beta_X^2 y^2}$	
$\sigma_{l,m,n}$	Random phase term	
σ_{max}	Coefficient to set shape of a damping function in the buffer zones	
θ	Observer angle	[rad/deg]

Subscripts

$_0$	Referenced to freestream conditions
$_X$	In the direction of the blade chord
$_x$	In the x-axis direction

Superscripts

$\hat{}$	Quantity expressed in the frequency domain

Vectors and Matrices

(r_0, θ)	Cylindrical co-ordinate system used in analytical method	
(x, y, z)	Cartesian co-ordinate system used in CAA method	
$\boldsymbol{\zeta} = (\zeta_x, \zeta_y, \zeta_z)$	Unit-vector of the gust direction	
$\boldsymbol{k} = (k_x, k_y, k_z)$	Turbulent wavenumber vector	
$\boldsymbol{u}_{2C} = (u, v, w = 0)$	Two-component gust perturbations	[m.s^{-1}]
$\boldsymbol{u}_{3C} = (u, v, w)$	Three-component gust perturbations	[m.s^{-1}]

Acronyms

2D	**T**wo-**D**imensional
3D	**T**hree-**D**imensional

ANTC	**A**irbus **N**oise **T**echnology **C**entre	
AoA	**A**ngle-**o**f-**A**ttack	
BoB	**B**roadband noise of **o**pen rotor **B**lades	
BRTE	**B**roadband **R**otor **T**railing **E**dge	
BRWI	**B**roadband **R**otor-**W**ake **I**nteraction	
CAA	**C**omputational **A**ero**A**coustics	
CFD	**C**omputational **F**luid **D**ynamics	
CFL	**C**ourant-**F**riedrichs-**L**ewy	
CROR	**C**ontra-**R**otating **O**pen **R**otor	
DNS	**D**irect **N**umerical **S**imulation	
FW-H	**F**fowcs **W**illiams and **H**awkings	
LDDRK	**L**ow-**D**issipation and low-**D**ispersion **R**unge-**K**utta	
LEE	**L**inearised **E**uler **E**quations	
LES	**L**arge-**E**ddy **S**imulation	
OASPL	**O**ver**A**ll **S**ound **P**ressure **L**evel	[dB]
PSD	**P**ower **S**pectral **D**ensity	
PWL	sound **P**o**W**er **L**evel	[dB]
RANS	**R**eynolds **A**veraged **N**avier **S**tokes	
RPM	**R**andom **P**article **M**esh	
SEM	**S**ynthetic **E**ddy **M**ethod	
SNGR	**S**tochastic **N**oise **G**eneration and **R**adiation	
SPL	**S**ound **P**ressure **L**evel	
URANS	**U**nsteady **R**eynolds **A**veraged **N**avier **S**tokes	

Chapter 1

Introduction

There is an ever-growing requirement to reduce the impact of aircraft operations on the environment. The trend of worldwide aviation growth, which has shown considerable resilience to external shocks such as oil and financial crises, is compounding the need for efficient and non-polluting aircraft [1]. The European Commission has outlined a vision of future aircraft emissions requirements, which are known as the Flightpath 2050 targets. These targets call for 75%, 90%, and 65% reductions in CO_2, NO_x, and noise emissions respectively, against 2000 baselines [2]. Responses to the Flightpath 2050 requirements can be seen in various efforts by industry and academia to reduce the fuel consumption, emissions, and noise generation of current and future aircraft.

The use of contra-rotating open rotor propulsion systems (or CRORs) is one of the most promising technological strategies to meet requirements such as the Flightpath 2050 targets. It has been recognised for many years that propeller-based engines can provide more efficient propulsion than future turbofans, because they exert a relatively small force on a large mass of air. CRORs can provide further efficiency gains in similar aircraft performance ranges (such as M = 0.7-0.8) to traditional propeller designs [3]. This additional efficiency has been found as approximately 8% and is caused by two mechanisms:

- Recovery of swirl energy which is imparted on the flow by the rotor [4]. The generation of swirl uses energy but does not contribute to thrust, and thus reduces propulsive efficiency. In the case of a CROR engine, the imparted swirl due to the front rotor is recovered by the rear rotor as it moves in the opposing direction.

- The absence of an outer nacelle on the engine gives a very large effective bypass ratio.

CRORs are not a new innovation. Work was conducted on CROR designs between 1970 and 1990 by companies such as NASA and General Electric [5], and CRORs were used on aircraft such as the Antonov An-22 [6]. However, the CROR concept was eventually dropped for a variety of reasons. The most significant issue was a high level of tonal and broadband noise emissions. Additional factors included cost, a drop in oil prices, and reliability concerns over complex gearbox components [4].

Recently, CROR designs are receiving renewed interest because oil prices have increased once again, and because recent environmental targets require a doubling of historic improvement rates. Such a large change to the rate of improvement requires step changes in technology, such as a move towards new engine technologies like CROR designs. However, the road to service entry is not straightforward. CROR designs still cause high levels of both tonal and broadband noise pollution. This noise must be mitigated before service entry can be considered.

1.1 Aims of the Current Work

This project aims to improve the current understanding of CROR broadband noise, and to provide enhanced modelling techniques such that noise mitigation can be more easily considered in the future. The current work focuses on broadband rotor-wake interaction (BRWI) noise, which is a dominant broadband noise source from CROR engines.

Full scale simulations of CROR broadband noise are not yet practical due to excessive computational costs. The most successful studies to date that have modelled

BRWI noise have used analytical approaches that assume that the CROR blades are unloaded flat plates. The work described in this thesis uses computational aeroacoustic (CAA) methods to test the accuracy of noise predictions when the blades are assumed to be flat plates. This is done by making a comprehensive and fundamental parameter study of the effects of airfoil geometry on turbulence interaction noise, which is the noise generation mechanism underlying BRWI noise. A direct test of the ability of analytical methods to model BRWI noise is also made, where the noise from realistic CROR blade profiles is predicted and compared with predictions from analytical theory.

In addition to testing the effects of real airfoil geometry, investigations are made into improved methods to computationally model turbulence interaction noise. The aim is to reduce the computational expense of the CAA simulations without loss of noise prediction accuracy.

1.2 Original Contributions

The original contributions of this thesis are listed in this section.

- The effects of thickness and leading edge radius on the noise due to symmetric airfoils at zero angle-of-attack are studied computationally, at varying Mach number, for single frequency harmonic vortical gusts convecting with a steady meanflow. The noise is studied more thoroughly and at higher reduced frequencies than has been previously presented in literature.
- The effects on CAA noise predictions are studied when simplifying assumptions are made concerning the non-uniform flow-field surrounding an airfoil. The validity of assuming an inviscid or a uniform meanflow is assessed.
- The underlying mechanism that causes changes to turbulence interaction noise for real airfoil geometries is investigated and described.
- A 2D synthesised homogeneous and isotropic frozen turbulence field is used for the first time to computationally investigate airfoil geometry effects on turbulence interaction noise.

- The relative importance of transverse, streamwise, and spanwise disturbances to turbulence interaction noise are compared.
- The ability of a single velocity-component modelling approach (which forces turbulent disturbances only in the transverse direction) to predict the noise from real airfoils with camber, and at non-zero angle-of-attack, is investigated.
- Noise predictions from a realistic CROR blade profile encountering upstream turbulence are made with both a CAA and an analytical approach. The predictions are compared to directly show the error incurred when assuming a flat plate geometry to model CROR BRWI noise.

Some of the work included in this thesis has been presented in the 19th and 20th AIAA/CEAS Aeroacoustics Conferences [7–9], has been published in the Journal of the Acoustical Society of America [10], and is being considered for publication [11].

1.3 Thesis Outline

The remainder of this chapter provides a literature review of the current ability to predict CROR noise. The general characteristics of CROR noise are discussed in Section 1.4, including the relative importance of tonal and broadband noise contributions. In Section 1.5 an overview is given of both analytical and numerical modelling methods, and how they can be used to predict CROR noise. Previous work on the effects of airfoil geometry on turbulence interaction noise is also discussed in detail in Section 1.6. The discussion of previous literature is used in Section 1.7 to explain and to justify the assumptions and the choice of CAA methods that are used in this thesis.

Chapter 2 presents a computational study into the effects on gust interaction noise due to real airfoil geometries. Symmetric airfoils at zero angle-of-attack are investigated at multiple flow speeds. The CAA method is discussed and validated against analytical theory for a thin airfoil case, before other airfoil geometries are considered. Insight is provided into the underlying mechanism which causes changes to the noise for real airfoil geometries. The accuracy of flat plate analytical model predictions of the noise from real airfoils is also assessed.

Chapter 3 extends the noise analysis of symmetric real airfoils at zero angle-of-attack to consider incoming turbulent disturbances. The CAA method is extended to model the interactions between an airfoil and homogeneous isotropic frozen turbulence, as opposed to the single frequency harmonic disturbances that were used in Chapter 2. A suitable method with which to synthesise a turbulent inflow is chosen, following a review of turbulence synthesis methods. Part of the airfoil geometry study from Chapter 2 are repeated using the new CAA method with synthesised turbulence, but using airfoil geometries and flow conditions which more closely resemble the conditions of a CROR rotor blade. The impact of turbulence characteristics (such as integral length-scale) on the noise is also assessed.

Chapter 4 extends the CAA method once again to consider the noise from an airfoil interacting with fully 3D isotropic and homogeneous turbulence, comprising of disturbances in all three component directions. Simulations are made to compare the noise from an airfoil interacting with three-component (streamwise, transverse, and spanwise disturbances), two-component (transverse and streamwise disturbances) and one-component (transverse disturbances) turbulence. Using these simulations, the relative importance of each disturbance component on the noise is assessed. Chapter 4 introduces the single velocity-component modelling approach, in which the turbulence is represented by only transverse disturbances, and assesses its accuracy in predicting the noise from real symmetric airfoils at zero angle-of-attack.

Chapter 5 uses the described CAA methods to consider airfoils with non-zero values of camber and angle-of-attack. The effects of camber and of angle-of-attack on the turbulence interaction noise are assessed, and the ability of the single velocity-component modelling approach to model these affects is also investigated.

Chapter 6 builds upon the knowledge gained in previous chapters in order to computationally model the noise from a realistic CROR blade profile. This chapter aims to directly evaluate the error incurred when BRWI noise is modelled using methods which assume the blades to be flat plates. Example broadband noise predictions are also given by using the CROR prediction code developed by Node-Langlois *et al.* [9]

in order to give a proper context to the conclusions which are made.

Chapter 7 discusses key conclusions, and suggests future areas of research.

1.4 CROR Noise

Considerable effort has been dedicated to the reduction of CROR noise. However, the majority of noise reduction techniques discussed in literature relate to the tonal noise contributions (see Ref. [12] for example) because these are generally considered to the dominant noise type in comparison to broadband noise. Tonal noise contributions are typically caused by periodic interactions between the front and rear rotor blades as they pass each other, or by the periodic rotation of the blades. Therefore, by altering the periodic nature of these interactions, the tonal noise contributions can be reduced.

One method to reduce the tonal noise is to use an unequal number of blades on the front and rear rotors. This technique has been shown by a number of authors to reduce tonal CROR noise (see Ref. [13] for example). Mismatched blade numbers alter the directivity pattern of the rotor configuration and reduce the emitted noise, particularly on the rotor axis.

Other methods have been suggested to reduce noise pollution, such as using smaller blade diameters on the rear rotor in order to avoid tip vortex interactions, using swept blades to reduce effective blade velocities, and altering the spacing between rotors to reduce aerodynamic interactions [14, 15]. Perhaps the most widely understood method is a result of acoustic analogies, such as the one made by Lighthill [16] for quadrupole noise, which shows that aerodynamic noise is proportional to the flow velocity, usually following a power law. Therefore, any reduction in blade flow velocity can have a significant impact on noise. The rotor speed can be reduced by using larger blade diameters, such that an equivalent thrust is achieved at lower velocity.

Broadband noise contributions to CROR noise have often been assumed to be small in comparison to tonal noise predictions. However, recent analysis of work conducted by Rolls-Royce [17] has suggested that the effects of broadband noise on the third octave sound pressure levels of an open rotor configuration can be significant, particularly above frequencies of 400 Hz. Work by Parry *et al.* [18] has also shown that broadband noise can be an important noise contributor for various CROR designs and operating conditions. Therefore, there is a need to understand the mechanisms which underlie the process of broadband noise generation in CRORs.

Until recently, little analytical, computational, or experimental work had been conducted to study CROR broadband noise. However, work by Blandeau and Joseph began to address this issue through the development of semi-analytical and semi-empirical models for the prediction of broadband noise from CROR designs [14, 19–21]. These models concentrate on two primary noise generation mechanisms, which have been identified through comparison with ducted fan noise:

- ***Broadband Rotor-Wake Interaction (BRWI) noise*** [19]. This is the broadband noise generated due to the interaction of the unsteady turbulent wake of the front rotor with the leading edge of the rear rotor. This results in an unsteady loading on the rear rotor which radiates as broadband noise.
- ***Broadband Rotor Trailing-Edge (BRTE) noise*** [21]. This is the process by which a turbulent eddy will radiate noise more strongly in the vicinity of the sharp edge of a solid surface. Unlike BRWI noise, this mechanism is present for all rotors and is not exclusively a feature of CROR designs.

Other potential sources of CROR broadband noise that are not studied by Blandeau and Joseph are:

- Interaction of the tip vortices from the front rotor with the leading edge of the rear rotor. This can be mitigated by using a smaller rear rotor diameter compared with the front rotor.
- Ingestion of atmospheric turbulence by the front rotor.
- Interaction from the turbulent wake of an upstream pylon on the leading edge of the front rotor (installation effects). This effect is now receiving attention from authors such as Kingan [22] and Node-Langlois *et al.* [9], who recently presented analytical formulation models to predict the broadband noise due

to the interaction of an open rotor with an upstream or downstream pylon. This involves an extension of the method derived by Blandeau [14] to consider non axi-symmetric noise sources.

1.5 Modelling CROR Noise

This section discusses methods which can be used to model CROR noise. Two general methods are considered here, which consist of analytical and numerical approaches. Analytical approaches usually simplify a situation such that it can be modelled via the derivation of mathematical equations. Numerical approaches often apply a generic set of equations to a variety of situations, and obtain results via iterative methods.

1.5.1 Analytical Modelling

Analytical models are popular in aeroacoustic studies because they can provide fast and reasonably accurate predictions of noise from sources which are well understood. The fast and repeatable nature of analytical noise predictions makes analytical modelling ideal for use in parameter design studies. Considerable work has been conducted in order to obtain analytical predictions of the unsteady flow mechanisms that are relevant to CRORs.

The two noise mechanisms that are most significant to CROR broadband noise are Broadband Rotor-Wake Interaction (BRWI) noise and Broadband Rotor Trailing-Edge Interaction (BRTE) noise. Because BRTE noise from rotating blades is not exclusively a feature of CROR designs, it has been studied more extensively in single rotor applications. However, BRTE noise is not the focus of this project, so it is not discussed in detail here. Discussions can be found in Refs. [14, 23–25], for example.

One issue which must be addressed when analytically modelling the noise of turbomachinery is how to account for the rotational motion of the blades. Typically, one of two possible approaches is used. The first of these methods uses the Ffowcs

Williams and Hawkings (FW-H) equation [26] which is discussed in more depth in Section 1.5.2. In this instance, approximations for the pressure field surrounding the airfoil trailing edge are used as an input to the FW-H equation in order to compute the radiated far-field sound. The second method was suggested by Amiet in 1977 [27] to reduce computational expense by approximating the noise from a rotating airfoil by the average angular position of the noise due to a translating airfoil. This approach was shown to be accurate by Blandeau and Joseph over most frequencies of interest [21].

BRWI noise has not been studied as extensively as BRTE noise because it is a less common noise source. However, a similar noise source occurs in turbofan engines, where the wake from fan blades interacts with the leading edge of an outlet guide vane (OGV) which produces noise. The underlying mechanism in both of these cases is the generation of noise due to turbulence impinging on the leading edge of an airfoil.

Early work by Sears [28] derived a model to predict the unsteady lift and moment from a flat plate encountering a sinusoidal gust in incompressible flow. This theory was extended to consider compressible flow problems by Graham [29] and Amiet [30]. Amiet used this theory to predict turbulence interaction noise emissions from an isolated flat plate interacting with oncoming turbulence. Models that are used to predict the turbulence interaction noise in CROR engines, and to predict rotor-stator interaction noise in turbofans, are often still based on Amiet's flat plate theory.

By adopting a similar approach to Amiet, Blandeau and Joseph developed a model for CROR BRWI noise [19] and combined this with a model for BRTE noise to allow predictions of the total uninstalled CROR broadband emission [20]. These models assumed the rotor blades to be unloaded, acoustically isolated, flat plates in uniform flow. Spanwise effects were computed by splitting the blades into 'strips' as suggested by Amiet [27]. Further assumptions such as isotropic, homogeneous and frozen turbulence were also used to provide a statistical representation of the turbulent flow characteristics.

Blandeau and Joseph used their model to perform a parameter study to investigate how various CROR configurations can affect the broadband noise [20]. It was found that BRTE noise dominates at cruise and approach conditions, but that both BRTE and BRWI noise are significant during take-off. It was also found that increasing the speed of the front rotor can reduce the BRWI noise at take-off. In this case, increasing the speed of the front rotor reduces the blade loading, and thus the size of the turbulent wake, so that the rear rotor interacts with a reduced turbulent disturbance and generates less noise.

The BRWI model presented by Blandeau and Joseph [19], and later by Blandeau *et al.* [31], was developed further by collaborative efforts between the Airbus Noise Technology Centre (ANTC) at the University of Southampton, and Airbus [9]. Node-Langlois *et al.* [9] fed the BRWI noise predictions with input data obtained from steady and unsteady CFD RANS simulations to improve prediction accuracy. This was done because it was recognised that noise predictions are sensitive to some input parameters. Values of the wake size and strength, and the turbulence integral lengthscale, were extracted from CFD as opposed to the empirical models that were used by Blandeau and Joseph. Using this method, Node-Langlois *et al.* showed that the effects of varying thrust were modelled well, although a constant under-prediction of the noise by approximately 5 dB was present. Some example predictions from this model are discussed in Chapter 6.

Carazo *et al.* [32, 33] also described an analytical model for the prediction of CROR noise. This model was an extension of Amiet's theory [30] that accounted for blade sweep and chord variation with blade span. However, this extension has been used only for tonal noise predictions thus far, and does not consider broadband noise.

Table 1.1 gives a summary of the most relevant analytical contributions for CROR BRWI broadband noise predictions.

Blandeau and Joseph [20] comment that the most questionable simplification made in their prediction of CROR BRWI noise is that the blades are considered to be flat plates at zero AoA. This project focuses on improving understanding and predictions of BRWI noise by testing the error incurred when blades are assumed to be flat plates.

The effects on BRWI noise due to assuming a flat plate are addressed in the current

Author	**Year**	**Contribution**
Sears [28]	1941	Derived the unsteady lift response of a flat plate encountering sinusoidal gusts
Ffowcs-Williams *et al.* [34]	1968	Applied the exact FW-H equation to point dipoles in circular motion
Graham [29]	1970	Extended gust response solutions to 3D through similarity rules
Amiet [35]	1974	Provided a low frequency response function for flat plate gust interactions
Amiet [36]	1975	Provided high frequency response solutions for flat plate gust interactions
Amiet [30]	1975	Derived far-field acoustic power spectral density expressions produced by a flat plate airfoil in a turbulent stream
Amiet [23]	1976	Extended gust interaction solutions to predict noise due to turbulent flow past a trailing edge
Amiet [27]	1977	Suggested a simplified approach for rotating blades to avoid expensive FW-H computations
Blandeau & Joseph [17]	2009	Presented a semi-analytical model for broadband noise predictions in CRORs, due to BRWI interactions
Blandeau & Joseph [19]	2010	Compared the relative importance of BRWI and BRTE noise at differing flight conditions for an uninstalled open rotor
Carazo *et al.* [32]	2011	Extended Amiet's theory to account for blade sweep and chord variation with span.
Blandeau *et al.* [31]	2013	Described some mathematical corrections to the original BRWI model
Node-Langlois *et al.* [9]	2014	Used CFD input data to improve the accuracy of BRTE and BRWI noise predictions.

Table 1.1: Contributions towards analytical predictions of BRWI noise.

project by extensively investigating the effects of real airfoil geometries on turbulence interaction noise, which is the underlying source of BRWI noise. The effects on noise caused by airfoil thickness, angle-of-attack, and camber are addressed for generic airfoil profiles in Chapters 2 to 5. Additionally, the geometry effects of blades at realistic conditions in a CROR engine are tested in Chapter 6. A review of previous work on the effects of airfoil geometry is given in Section 1.6.

1.5.2 Numerical Modelling

Due to the complexities of aeroacoustics and aircraft noise generation, it is often not possible to study the noise with an analytical method. Analytical methods can require the use of several assumptions to permit noise predictions, and if the underlying physics of the sound generation are not well understood it may not be clear whether these assumptions are valid. At present this is particularly true for the case of broadband noise generation by CROR engines because this noise type has not been studied in detail until recently. Numerical methods, usually termed computational aeroacoustic (CAA) methods, can provide alternative modelling techniques.

Computational Aeroacoustics

A natural starting point from which to discuss CAA methods is the field of computational fluid dynamics (CFD). However there are several differences between CAA and CFD which require changes to be made to CFD methods before they can be used in CAA studies [37]:

- The human hearing frequency range covers approximately 20 Hz - 20 kHz, which represents the scales of interest in a CAA problem. The lower limit of 20 Hz usually corresponds to large wavelengths which require a large simulation domain to be used. The upper limit of 20 kHz requires a high grid density to resolve the smallest wavelengths. The combination of a large domain and a globally high grid density can significantly increase the computational expense of CAA in comparison to CFD simulations. This additional expense can be mitigated with the use of high-order spatial discretisation schemes such as those by Hixon [38], Ashcroft and Zhang [39], and Kim [40,41]. These schemes provide an improved frequency resolution for a specified grid density. However, compromises must still be made between computational cost and the highest frequency that can be resolved in a CAA simulation.

- In CAA, the primary interest is usually in the noise radiated to the far-field. Therefore, the computational grid must resolve acoustic waves up to a large distance away from a body. This contrasts with CFD grids, which generally remain fine only in the vicinity of solid bodies because the interest lies in determining the forces acting upon the body itself. However, hybrid methods can be used to lower the computational expense, and are discussed below.

- Even loud noises will radiate only a small amount of energy. Therefore, there is a large difference in magnitude between the mean values of a flow, and the values of any acoustic fluctuations. Care must be taken in CAA to keep the computational error of the simulation below the magnitude of the acoustic fluctuations.

- CFD schemes are often quite dissipative in their treatment of acoustic fluctuations in order to provide numerical stability. This would cause unacceptable levels of signal attenuation when studying noise. Therefore, CAA codes typically apply weak numerical filtering so that any acoustic perturbations are not artificially damped. However, as a result of the low filtering levels and low-dissipation properties of the numerical schemes, CAA codes are often sensitive and can be difficult to use for stable simulations.

Hybrid Methods

Hybrid methods provide a compromise between accuracy and computational expense in CAA simulations. Hybrid methods do not directly compute the radiated noise in a simulation. Instead, the flow-field is initially simulated and then used as an input into a second calculation that obtains the noise prediction. As a result of this, such methods disregard any effects on the flow due to the sound created. This process removes several restrictions that are usually caused by the acoustic analysis, such as the need for high spatial resolution away from the body of interest.

The first calculation stage of a hybrid method is required to accurately model the sources of noise in a simulation. Ideally, this would use Direct Numerical Simulation (DNS) to obtain a prediction of the flow. However, for most practical engineering applications, DNS is still too computationally expensive. Instead, a common approach is to use Large Eddy Simulations (LES), Reynolds-Averaged Navier-Stokes (RANS) simulations, or Hybrid-LES simulations for source modelling. LES and Hybrid-LES both exactly compute the macroscopic flow properties which are resolved by the grid, and then model small scale turbulence effects with either a sub-grid scales model or a RANS model. RANS simulations model the turbulence at all scales.

The second calculation stage of a hybrid method is typically based on an acoustic analogy. This is a re-arrangement of the equations of conservation of mass and momentum, such that the right hand side represents the equivalent sound sources and the left hand side represents the sound propagation in an idealised medium [42]. The most widely known acoustic analogy is by Lighthill [16], and can be written as

$$\frac{\partial^2 \rho}{\partial t^2} - c_0^2 \nabla^2 \rho = \frac{\partial^2 T_{ij}}{\partial x_i \partial x_j} \qquad \text{where} \qquad T_{ij} = \rho U_i U_j + p_{ij} - c_0^2 \rho \delta_{ij} \tag{1.1}$$

where T_{ij} is the Lighthill stress tensor. T_{ij} represents the equivalent sound sources that are found in the first calculation stage of the hybrid method. However, Lighthill's analogy assumes that the sound problem takes place in an idealised atmosphere at rest, and is therefore not suitable for many engineering problems. Both Curle and Ffowcs Williams and Hawkings provided extensions to this analogy to include the effect of solid surfaces [26,43]. The latter is used more widely because it permits the modelling of moving surfaces. Farassat developed a numerically favourable solution to the Ffowcs Williams-Hawkings equation, which is known as Formulation 1A [44]. This formulation discards the quadrupole source terms which are computationally expensive because they require a volume integration. Because of this assumption, Formulation 1A should only be used in linear flow regions where quadrupole terms can be assumed to be small. While hybrid methods simplify CAA simulations and have proven successful in circumventing many problems associated with CAA, their use is limited due to their inherent assumptions of stationary or uniform mean flow with respect to an observer.

For situations when a hybrid method is not applicable, other methods exist to allow the far-field noise to be estimated without excessive computational cost. These can include the use of linearised Euler equations (LEE) to model the acoustic perturbations away from bodies of interest, which require less computational effort to solve than the Navier-Stokes equations. However, care must be taken to ensure that the flow can be approximated as linear in the LEE region, and that the transfer of information between the two sets of governing equations is handled appropriately [42].

Near-field Propagation Methods

An alternative approach to hybrid methods is to focus on studying the acoustic propagation as a standalone process, as opposed to part of a hybrid method.

The process consists of synthesising a series of pressure of vortical disturbances, and allowing these to either propagate to the far-field, or at least to a region of linear flow where an acoustic analogy can then be used. The propagation can be studied by using governing equations such as the Euler equations, LEE, or linearised Navier-Stokes equations. LEE tend to be the least expensive, which makes them popular. Example studies of propagation methods are by Angland and Zhang [45] who investigated landing gear installation effects, and Richards *et al.* [46] who modelled the noise radiation from a realistic engine exhaust geometry. Additional governing equations have been developed for propagation simulations in order to overcome issues such as computational stability. A review of these methods is given by Zhang [47].

Propagation simulations can reduce the cost when modelling the noise from complex geometries. However, they require a good knowledge of the pressure or vortical source region so that it can be synthesised in the propagation simulation.

CROR CAA Applications

This section discusses previous computational efforts to predict the noise from CROR engines. Initial noise investigations of CRORs only allowed for simplified numerical modelling due to computational constraints. These studies concentrated on macroscopic flow elements to study the noise generation (through use of methods such as the Baldwin-Lomax Turbulence model [48]), and neglected any small scale effects which arise as a result of viscous flow at high Reynolds numbers.

The vastly increased computational power available today has allowed computationally expensive simulations to predict CROR noise. Results from these simulations can be compared with both experimental measurements and analytical predictions. These simulations are ideal to investigate the effects on noise of viscous 3D flow mechanisms such as tip vortex interaction and rotor wake interaction. They also allow visualisation and investigation of flows in ways that are not possible experimentally or analytically.

One example of a computational study to predict CROR noise is by Spalart *et al.* [13]. This study performed an Unsteady Reynolds-Averaged Navier-Stokes (URANS) simulation (combined with FW-H far-field predictions) of a generic CROR configuration to obtain noise predictions. Body-fitted grids with sliding blocks were used. The study investigated the effects on noise when using mismatched blade numbers on the front and rear rotors.

The use of CAA methods for studying CROR designs is non-trivial due to the complications introduced by their moving geometry. Sliding grids are often required, as was done in the study by Spalart *et al.* [13] and by Busch *et al.* [49], for example. Detailed discussion on the application of CAA methods to CROR noise is also given by Stuermer and Yin [50], who used hybrid grid techniques to create an accurate and easily modified grid, for which the flow-field was computed using the DLR TAU code [51]. This study highlighted strong aerodynamic interactions between the rear rotor and the blade wakes, and also between the rear rotor and the tip vortices from the front rotor. Both interaction mechanisms were identified as strong noise sources. Additionally, the potential effects of the rear rotor on the front rotor were found to be non-negligible, and quadrupole terms in far-field noise predictions were shown to be relevant even at low flight speed conditions.

Other recent studies are now using CAA applications to directly investigate ways to minimise CROR noise. Schnell *et al.* [52] coupled a URANS CFD model with an optimisation routine in order to reduce CROR tonal noise whilst retaining the engine thrust. Parameters such as the blade geometry, rotor speed, and loading balance between the front and rear rotors were varied in the optimisation process. Although the acoustic modelling was simplified for reduced computational expense (the primary objective was to reduce the size of the front rotor wake) this study successfully reduced tonal noise at almost all tested frequencies and directivities by ~ 3 dB, while retaining the same thrust. Therefore Schnell *et al.* [52] have shown that there is potential for numerical simulations in noise optimisation studies, despite their relative computational expense. (Schnell *et al.* [52] do not detail the overall computational expense of their optimisation).

Akkermans *et al.* [53] have also investigated the reduction of CROR noise with a CAA method. Trailing edge blowing was applied to the front rotor blades to reduce the wake deficit and to therefore reduce interactions between the wake and the rear rotor. Akkermans *et al.* [53] applied this technique to the Airbus AI-PX7 CROR configuration and showed that the front rotor wakes could be reduced without impacting the aerodynamic performance. However, the full effects on CROR noise were not clear due to geometry issues associated with tip vortex interactions in the simulation.

Computational predictions of the noise from complete CROR engines have thus far been restricted to studying tonal noise due to the computational cost of broadband noise simulations. However, Spalart *et al.* [54] note that a DES broadband study is planned in future [13]. Neglecting broadband sources is usually justified because the broadband noise is assumed to be small in comparison to tonal noise. However, as previously discussed, it has been shown by Parry *et al.* [18], for example, that broadband contributions can be significant to the overall CROR noise. Table 1.2 gives a summary of recent numerical studies which have focused on predicting CROR tonal noise. Table 1.3 gives additional details of the CAA codes mentioned in Table 1.2.

Author	**Year**	**Geometry**	**Code and mesh**	**No. Cells**	**Study Description**
Stuermer *et al.* [50]	2009	Generic CROR with 8x8 and 10x8 blades	TAU with Chimera mesh approach	45.8 m	Studied mismatched blade effects and quadrupole source importance
Spalart *et al.* [54]	2010	Generic CROR with 8x8 and 8x7 blades	NTS with Body-fitted sliding blocks	10 m	Studied mismatched blade effects
Deconinck *et al.* [55]	2010	Generic 8x8 CROR (45^0 section)	FINE	3.3 m	Demonstrated a computationally efficient method of studying CROR tonal noise
Deconinck *et al.* [56]	2011	Generic 8x8 CROR (45^0 section)	FINE	9.1 m	Verified CAA technique with grid convergence and FW-H surface studies
Guerin *et al.* [57]	2012	Airbus AI-PX7 CROR blade	TRACE with mixing plane method	17 m	Used a RANS-informed analytical model for noise predictions. Flat plate assumption was made in acoustic predictions
Falissard *et al.* [58]	2012	DREAM CROR geometry	*elsA* with chimera method	200 m	CFD study of DREAM experimental setups to gain insight into CROR installation effects on tonal noise
Colin *et al.* [59]	2012	Unknown	*elsA*	100 m	Investigated effects of different FW-H surface placement on CROR noise. Investigated hub-vortex interaction noise significance
Sharma & Chen [60]	2012	F31A31 NASA geometry	TACOMA	N/A	Used linearised RANS analysis for CROR noise prediction, and validated against experimental results
Schnell *et al.* [52]	2012	Variable geometry	TRACE with mixing plane method	N/A	Coupled URANS computations in an optimisation procedure to reduce tonal noise while retaining engine thrust
Akkermans *et al.* [53]	2013	AI-PX7	TAU	62 m	Used trailing edge blowing to reduce front rotor wakes

Table 1.2: Recent CAA contributions to predicting CROR tonal noise.

Name	**Governing equations**	**Accuracy**	**Grid type**	**Turbulence model**
NTS [54]	URANS (with DES option)	3rd & 5th order upwind	Structured finite volume	Spalart-Allmaras
TAU [51]	URANS	2nd order central differencing	Unstructured finite volume	Spalart-Allmaras
FINE [55]	URANS	Unknown	Structured	Spalart-Allmaras
TRACE [57]	Steady RANS or URANS	2nd order central differencing	Unstructured finite volume	Spalart-Allmaras
elsA [58]	URANS	2nd order central differencing	Structured finite difference	$k-\omega$ SST

Table 1.3: Details of the capabilities of CAA solution codes used in recent computational CROR studies.

1.6 Effects of Real Airfoil Geometry on Turbulence Interaction Noise

As previously discussed, analytical models which predict CROR BRWI noise use simplifying assumptions. For example, in their model to predict BRWI noise, Blandeau and Joseph [20] assume that the rotor blades can be approximated as flat plates with zero camber at zero angle-of-attack. The effects on turbulence interaction noise (or leading edge noise) predictions due to neglecting the real airfoil geometry of the rotor blades has been tested by previous authors, but a consensus has not been reached on all aspects. The previous work is discussed in this section.

Previous experimental, CAA and analytical studies have investigated the effects of a real airfoil shape on the noise due to unsteady vortical disturbances interacting with an airfoil leading edge. These have typically concentrated on the effects due to airfoil thickness, angle-of-attack, and camber. Previous work has not considered the effects on noise due to the leading edge radius, which is an additional length-scale considered in the current project.

1.6.1 Effects of Angle-of-Attack and Camber

Analytical flat plate theory is restricted to studying the interactions between gusts and flat plates at zero AoA. The effect of the AoA limitation on the accuracy of noise predictions has been measured and predicted by authors such as Staubs [61], Devenport *et al.* [62] and Paterson and Amiet [63], among others [64–69]. Most predictions of of AoA effects to date have been made with analytical approaches that are based on rapid distortion theory.

The effect of AoA on the noise due to interactions with isotropic turbulence has been generally concluded as small (reported by Devenport *et al.* as approximately a 1 dB change when varying the AoA of a NACA 0012 airfoil between 0° and 12°). In addition to considering angle-of-attack, Devenport *et al.* also considered the effect of camber (which is not modelled by flat plate theory) on a S831 airfoil at 30 ms^{-1} and found it to have a small effect on the noise, similar in magnitude to the effect of AoA. Moreau *et al.* [67] also applied a semi-empirical camber correction to Amiet's analytical theory [30] and found the effects of camber to be small. The effects consisted of a slight increase in the noise on the pressure side of the airfoil, and a slight deacrease on the suction side. Moriarty *et al.* [68] modelled the effects of camber analytically by combining Guidati's boundary element theory [70] with Amiet's theory [30], and also report the effects on the noise to be small.

In addition to measuring the noise, Devenport *et al.* [62] used the panel method of Glegg and Devenport [71] to study the behaviour of the airfoil gust response function with varying AoA. They showed that the gust response function is affected, and is shifted in the k_y spectrum when AoA is introduced. This was attributed to the movement of the stagnation streamline towards the pressure-side of the airfoil. Devenport *et al.* concluded that the insensitivity of turbulence interaction noise to AoA is caused by an averaging of the gust response function with the shape of the isotropic turbulence spectrum.

1.6.2 Effects of Thickness

The effect of airfoil thickness on leading edge noise has received considerable attention from previous authors, because thickness has a more significant effect on noise than camber or AoA.

Experimental studies

Paterson and Amiet [63] measured the noise due to an isolated NACA 0012 airfoil interacting with nearly isotropic grid-generated turbulence at speeds of up to 165 ms^{-1}. The noise spectrum and directivity were measured in addition to the surface pressure distribution on the airfoil surface. They found that the unsteady pressure on the airfoil surface was strongest near the leading edge, but a significant response was seen at all chord positions. The study was the first to note that airfoil thickness reduces the noise compared to flat plate predictions, with the effect being more pronounced at high frequencies. A 5 dB reduction in noise was measured at $\theta = 90^\circ$ from the NACA 0012 airfoil compared with analytical flat plate solutions. However the study did not explore trends between the noise reduction and increasing airfoil thickness. The 5 dB reduction in noise due to the thickness of the NACA 0012 airfoil was measured at a thickness-based reduced frequency $K_t = t/\lambda = 1$ (where t is airfoil thickness and λ is the vortical gust wavelength). This reduced frequency was suggested by Paterson and Amiet as a measure of when flat plate theory breaks down and can no longer be considered accurate.

Another study into the effects of thickness on leading edge noise was performed by Olsen and Wagner [72]. They investigated the noise from a range of airfoils interacting with grid-generated turbulence at 94 ms^{-1}. Airfoils with thicknesses varying from $t = 0.03c$ (i.e. 3% thickness) to $t = 0.37c$ were used, as opposed to the single NACA 0012 airfoil considered by Amiet and Paterson. Olsen and Wagner reported that the noise reduction "increases linearly with both frequency and t ", with thicker airfoils radiating less noise than thin ones. The apparent linear increase in the noise reduction effects with both thickness and frequency was also reported by Roger and Moreau [24]. They compared measurements from several studies and found that the noise reduction effects collapsed to a single curve when thickness, flow speed, and the turbulence length-scale were taken into account.

Devenport *et al.* [62] and Hall *et al.* [73] have both found that thicker airfoils generate less noise at high frequencies. Devenport *et al.* investigated the effect on noise of three different airfoil shapes placed in homogeneous turbulence. The three chosen airfoils had various values of thickness, chord, leading edge radius, and camber. Therefore the measured effects on noise for each airfoil contained influences from several length-scale changes, making it difficult to systematically study the various geometry effects on the noise. Oerlemans and Migliore [74, 75] also measured the noise from a variety of airfoil shapes placed in grid-generated turbulence. They observed a trend where airfoils with more rounded leading edges generated less noise. Hall *et al.* made changes to the front 20% of the airfoil chord by varying the leading edge thickness of an airfoil. It was found that the maximum noise reduction compared to a baseline airfoil with small leading edge thickness, occurs at reduced frequencies (based on leading edge thickness) of order one.

Computational Aeroacoustic Studies

Compared to experimental and analytical studies, there are fewer CAA studies which investigate the effects of airfoil geometry on leading edge noise. Furthermore, these studies have often been restricted to modelling a small number of discrete frequencies using single frequency harmonic gusts. The use of single frequency harmonic gusts as a simplified turbulent inflow may affect the sensitivity of leading edge noise to airfoil geometry because this approach is limited to modelling gusts with parallel wavefronts. Therefore, the effects of airfoil geometry on the noise due to the variety of swept gusts that are contained in turbulent flow is not accounted for. Evers and Peake [76] have shown with an analytical model to predict cascade noise that the leading edge noise due to turbulence exhibits a weaker sensitivity to airfoil geometry than to flow containing harmonic disturbances. However, the use of harmonic disturbances is still regarded as useful in revealing general trends between the leading edge noise and changes in airfoil geometry.

Atassi *et al.* [77] used a CAA approach to investigate the effects of thickness on the noise due to a harmonic gust. They investigated Joukowski airfoils with thicknesses ranging from 3% to 12% of the airfoil chord. A Kirchoff method was used to predict the far-field noise based on a numerical solution of the unsteady flow-field about an isolated airfoil interacting with a periodic vortical gust [78]. This solution used a 9-point central differencing implementation of the 2D LEE in the frequency domain, where the mean potential flow was computed analytically. This study found that in $M = 0.5$ flow at reduced frequencies of $K = c/\lambda \sim 1$ or higher, the effect of thickness was to reduce the noise at downstream observer locations, and increase it at upstream locations. Therefore, the basic shape of the directivity was unaltered, but the resulting pattern was skewed towards the upstream direction when compared with flat plate predictions. Atassi *et al.* attributed this phenomenon to the oncoming flow "seeing a finite rounded edge at larger thicknesses (as opposed to an infinitesimally thin flat plate) from which acoustic pressure can radiate". It was also observed that the thickness effect on noise is more pronounced at higher freestream Mach numbers.

Lockard and Morris [79] performed a CAA study in the time domain of the noise radiated by NACA 4-series airfoils encountering harmonic vortical gusts. They used both inviscid Euler and viscous Navier-Stokes calculations to model vortical gust interactions up to $K \sim 1.2$ in $M = 0.5$ flow. Directivities were obtained directly from pressure data along grid lines in the simulation. Lockard and Morris made similar conclusions to Atassi *et al.*, where airfoil thickness caused an upstream skewing of the directivity pattern such that the noise was reduced at downstream observer locations by a greater amount than at upstream locations. Lockard and Morris gave the realistic airfoil curvature and changes to the meanflow as the dominant causes for the change in the noise.

Guidati and Wagner [70] used a boundary-element method to study the interaction of harmonic sinusoidal gusts with NACA 4-digit airfoils. Airfoil thicknesses of 5%, 10% and 15% were investigated in flows with Mach numbers ranging from $M = 0.4$ to $M = 0.6$. Guidati and Wagner found again that thicker airfoils radiate less noise than thin ones, and noted that the source terms in their model are strongly dependent on the flow surrounding the airfoil.

Lau *et al.* [80,81] used harmonic gust interactions to study the effects on the noise of real airfoils with wavy leading edges. In an extension to this work, Haeri *et al.* [82] used a CAA method with a synthetic turbulence generator to study the noise. A synthetic eddy method was used to generate a three-dimensional inflow disturbance which followed the Von-Kármán spectrum.

Christophe *et al.* [83] modelled the noise of a NACA 0012 airfoil placed in an anisotropic turbulent jet, using a large-eddy simulation (LES). The noise was from the simulation was predicted at low frequencies by applying Curle's analogy to the surface pressure data, and at high frequencies using Amiet's theory [30], fed by turbulence paramters obtained in the simulation. However, the simplified theory used constant turbulence properties along the airfoil span, noting that future work would split the airfoil in spanwise strips to overcome this limitation.

Deniau *et al.* [84] also performed a compressible LES simulation of turbulence interaction noise. This work simulated an airfoil in a full wind tunnel, allowing the installation effects of a small turbulent jet to be accounted for. The installation effects can cause issues when experimentally measuring the noise of airfoils at angle-of-attack, because the circulation can deflect the turbulent jet and thus alter the effective airfoil angle-of-attack. A RANS method was coupled to an LES method to reduce computational costs, and transverse turbulent disturbances were injected using a Fourier summation approach.

The effects of airfoil thickness were not addressed by Haeri *et al.*., Christophe *et al.*, or Deniau *et al.* However, the studies are mentioned here for their inclusion of additional complexities when computationally modelling turbulence interaction noise, such as wind tunnel installation effects, anisotropic turbulence, and synthetic eddy methods.

Analytical studies

Most established analytical theories for the prediction of leading edge gust interaction noise are restricted to flat plates. However, attempts have been made to extend the theory to include real geometry effects. Goldstein and Atassi [85] described a second-order solution to the potential flow around an airfoil with finite thickness, camber, and AoA, by using thin airfoil theory. Atassi [86] then showed that Goldstein's solution could be separated into independent terms which separately account for the effects of thickness, AoA and camber, and later used this insight to study the effects of airfoil thickness [77, 87].

To avoid using complex analytical modelling approaches, Gershfeld [88] and Moreau *et al.* [67] both presented simple corrections to account for airfoil thickness. By developing a Greens function which considered the leading edge shape and foil thickness (using the earlier trailing edge analysis of Howe [89]), Gershfeld [88] showed that the radiated sound due to oncoming turbulence at high frequencies could be reduced by increasing the finite thickness of a flat plate. Moreau *et al.* [67] modified existing flat plate analytical theory with semi-empirical corrections, based on observations of thickness effects in experimental studies. The acoustic radiation term was modified to account for the position of the source on a more realistic airfoil surface. Rapid distortion theory was also used to account for the distortion of small eddies by the airfoil geometry. However, the chordwise distribution of the sources was unchanged.

Another method to correct solutions to account for the effects of real airfoil geometry was developed by Moriarty *et al.* [90]. The boundary-element method of Guidati [70] was used to obtain a geometrical correction factor that was then applied to Amiet's theory [30]. Using this combination of Amiet's and Guidati's theory, Moriarty *et al.* [90] obtained noise predictions that matched well with experimental measurements of the noise from wind turbines. Moriarty *et al.* [68] also developed a simplified version of this model, to obtain predictions more quickly and enable airfoil optimisation.

Glegg and Devenport [71] showed with a conformal mapping approach that the effect of increasing thickness is to reduce the noise at high frequencies. Santana *et al.* [69] used an unsteady panel code to show that the airfoil response is damped by the presence of thickness. However, this study did not consider the distortion of the disturbance by the surrounding meanflow. Lysak *et al.* [91] developed a method that uses step function gusts and conformal mapping to investigate the effects of airfoil thickness on the noise at high frequencies. By fitting trends to the obtained data, Lysak *et al.* produced an empirical gust response correction factor to account for real airfoil geometry effects. Most recently, Ayton and Peake [92] presented a semi-analytical method, based on rapid distortion theory, to predict the interaction noise of real airfoils in sheared flows.

Summary

In the previous work described above, there is clearly some agreement between the conclusions from each study as to the effects on noise due to airfoil thickness. All studies have found that the noise is reduced at high frequency due to increasing airfoil thickness. However, there are also some contradictions between the conclusions. Both computational works by Atassi *et al.* [77] and Lockard and Morris [79] found a forward skewing of the directivity pattern with increasing thickness. Noise measurements by Paterson and Amiet [63] and Moreau *et al.* [67] on NACA 0012 airfoils, and measurements by Olsen and Wagner [72] on a range of airfoil thicknesses, did not show this behavior. Additionally, Paterson and Amiet [63] suggested that flat plate theory is inaccurate for 12% thick airfoils at reduced frequencies above $K_t = 1$

(or $K = 8.3$ for 12% thick airfoils), whereas Atassi *et al.* [77] reported that thickness effects on noise become apparent for $K > 1$.

One reason why experimental measurements have not found an upstream skewing of the directivity pattern may be due to the difficulties associated with measuring acute upstream and downstream noise in a wind tunnel. The nozzle of the wind tunnel will prevent microphone placement at acute upstream angles, while the wind tunnel shear layer can affect measurements from microphones placed at acute downstream angles. Because of these factors, most experimental studies discussed here limited the range of observer angles at which noise was measured. For example, Hall *et al.* [73] presented noise spectra at the peak radiation angle of 61° from the downstream axis, Devenport *et al.* [62] measured the noise at 90°, and Moreau *et al.* [67] considered observer angles ranging between 0° and 105° from the downstream direction. Thus it may be the case that previous measurements have been unable to capture the upstream behavior predicted in CAA studies. Another potential reason for the difference between conclusions of the thickness effects on noise, may be that the computational and experimental studies used differing gust inputs. Most computational studies used harmonic transverse disturbances as opposed to the homogeneous turbulence generated for the experimental measurements. The use of harmonic transverse disturbances does not consider the contributions from the variety of swept gusts which are contained in a turbulent inflow, so this type of gust input may incite different leading edge noise behavior.

Table 1.4 summarises the discussed contributions towards understanding the effect of airfoil thickness on turbulence interaction noise.

Author	**Year**	**Study type**	**Noise type**	**Contribution**
Paterson & Amiet [63]	1976	Exp.	Turb.	Found that thickness reduces noise when comparing NACA 0012 and flat plate noise. Estimated the frequency at which flat plate theory breaks down ($K_t > 1$).
Olsen & Wagner [72]	1981	Exp.	Turb.	Found that noise reduction increases with both thickness and frequency.
Atassi *et al.* [77]	1990	Comp.	Harm.	Found that thickness can skew directivity pattern upstream at high frequency.
Lockard & Morris [79]	1998	Comp.	Harm.	Included viscous meanflow effects. Found an upward skewing of the directivity patten at high frequency due to thickness.
Guidati & Wagner [70]	1999	Analytic	Harm.	Used a boundary element method to study thickness effects. Found noise to be highly dependent on the mean flow-field.
Evers & Peake [76]	2002	Analytic	Harm. & Turb.	Showed reduced noise due to thickness at high f with cascade noise model. Found less sensitivity with turb. gusts than with harm. gusts.
Gershfeld [88]	2004	Analytic	Turb.	Showed that noise could be reduced through increasing finite thickness of a flat plate. Suggested a simple scaling parameter to account for the effects of thickness on the noise.
Oerlemans & Migliore [74, 75]	2004	Exp.	Turb.	Found that airfoils with more rounded leading edges produced less noise.
Moriarty *et al.* [90]	2004	Analytic	Turb.	Used boundary element method of Guidati [70] to obtain geometrical correction factor for effects of thickness, and combined this with Amiet's theory.

Moriarty *et al.* [68]	2005	Analytic	Turb.	Developed a simplified version of the model presented by Moriarty *et al.* [90].
Moreau *et al.* [67]	2005	Exp. & Analytic	Turb.	Used experimental results & rapid distortion theory to create an empirically altered analytical model to account for some real airfoil geometry effects.
Christophe *et al.* [83]	2007	Comp.	Turb.	Performed an LES simulation to predict the noise of a NACA 0012 airfoil in an anisotropic turbulent jet
Roger & Moreau [24]	2010	Exp.	Turb.	Compared results from several authors and suggested scaling parameters for thickness noise reduction.
Devenport *et al.* [62]	2010	Exp.	Turb.	Found reduction in noise at high frequencies due to thickness.
Glegg & Devenport [71]	2010	Analytic	Turb.	Used conformal mapping approach to show that thickness decreases noise at high frequencies.
Hall *et al.* [73]	2011	Exp.	Turb.	Varied geometry on front 20% of airfoil chord. Found maximum noise reduction at $K_t \approx 1$.
Deniau *et al.* [84]	2011	Comp.	Turb.	Performed compressible LES simulation of turbulence interaction noise, including wind tunnel installation effects.
Santana *et al.* [69]	2012	Analytic	Harm.	Used panel code to show airfoil response is damped by airfoil thickness.
Lysak *et al.* [91]	2013	Analytic	Harm.	Produced an empirical model to account for thickness effects.
Lau *et al.* [80, 81]	2013	Comp.	Harm.	Used Harmonic gusts to study effects of real airfoils with wave leading edges.
Haeri *et al.* [82]	2014	Comp.	Turb.	Extended work of Lau *et al.* to synthesise turbulence with synthetic eddy methods.

Table 1.4: Contributions towards understanding airfoil thickness effects on turbulence interaction noise.

1.6.3 Mechanisms

Thickness

It is desirable to understand the physical principles which cause the observed noise changes due to airfoil geometry, so that geometry effects on turbulence interaction noise can be explained. Chiang and Fleeter [93] found that increasing the airfoil thickness has the effect of reducing the amplitude of the leading edge surface pressure response. They also found that the location of the peak surface pressure response is moved downstream of the leading edge and is smoothed over a larger section of the airfoil chord as a result of airfoil thickness. Similar findings were reported in the analytical work of Glegg and Devenport [71]. However, previous literature has not addressed why the surface pressure response is altered by the presence of airfoil thickness.

Meanflow

Previous authors of computational studies have included the accurate modelling of a non-uniform meanflow in their investigations of airfoil geometry effects on leading edge noise. For example, Lockard and Morris [79] studied the effects on noise due to an airfoil with thickness, modelled in a non-uniform meanflow, and Evers and Peake [76] also included the modelling of a realistic non-uniform meanflow in their analytical model for the prediction of airfoil leading edge cascade noise. However, it has not previously been determined if the modelling of a non-uniform meanflow is a necessary step when investigating airfoil geometry effects on leading edge noise. Analytical models are typically useful for fast repeatable noise predictions, but it can be difficult for them to include the gust distortion that is caused by a non-uniform meanflow. If accurate predictions can be obtained by assuming a uniform meanflow, then the complex modelling of a non-uniform flow-field might be avoided.

1.7 Discussion of the Current Modelling Approach

This chapter has discussed the ways in which CROR noise, and BRWI noise in particular, can be modelled. The most successful studies of BRWI noise to date have used analytical methods to make far-field noise predictions, and some have coupled this with aerodynamic input data obtained from CFD simulations. However, the analytical approach for BRWI noise predictions assumes that the blades are unloaded flat plates. This thesis extensively tests the implications of assuming a flat plate geometry when modelling BRWI noise.

In this project, a CAA approach is used to test the effects of geometry on BRWI noise. Rather than study BRWI noise directly, the underlying mechanism of turbulence interaction noise (or leading edge noise) is modelled. This allows simulations to consider an isolated translating airfoil as opposed to a rotating cascade of airfoils, and therefore reduces the computational cost. Amiet, and Blandeau and Joseph [21,27], have discussed the use of translating airfoils to model the noise of rotors, and suggest that this simplification will not affect the conclusions of this work. Blandeau [14] also showed that an isolated airfoil can be considered as opposed to a cascade without loss of generality, because blade-to-blade correlation effects are not significant for most CROR configurations.

The CAA approach used here solves the LEEs, with a meanflow field provided as an input from a CFD simulation. This approach was chosen because it is computationally cheap in comparison to methods which solve the Navier-Stokes equations, and therefore allows a large number of cases to be considered. Because there is no viscosity to create turbulent wakes, vortical disturbances are injected into simulations. This method is discussed in more detail in Section 3.2. Although this CAA method is relatively cheap, some effort is also made to improve the efficiency of the method which is used to synthesise a turbulent inflow. This is discussed in Chapter 4.

The CAA method is used here to test the effects of airfoil geometry on turbulence interaction noise. Airfoil thickness, leading edge radius, angle-of-attack, and camber are investigated and their effects on the noise are shown. Additionally, the CAA method allows investigation into the physical mechanisms which cause the effects on turbulence interaction noise.

Chapter 2

CAA Analysis using Harmonic Gusts

This chapter uses CAA methods to systematically study the effects on turbulence interaction noise due to airfoil thickness t and leading edge radius R_{le}. The noise from real, symmetric, translating airfoils at zero angle-of-attack is considered. The noise is produced from interactions between the airfoils and sinusoidal transverse disturbances that vary only in the streamwise direction, and which are convected by the steady meanflow. This relatively simple CAA modelling approach was used as an initial investigation into the airfoil geometry effects on noise. In this chapter, the noise is referred to as leading edge noise, as opposed to turbulence interaction noise, because discrete frequency, constant amplitude, harmonic gust disturbances are used as a simplification of turbulence.

Predictions were performed of the noise due to airfoils with varying t and R_{le} interacting with single frequency harmonic gusts to highlight the effects on noise due to changes in both of these length-scale parameters. This study also assesses the validity of the flat plate assumption for modelling the leading edge noise of real airfoils. In addition, the effect of different assumptions used to compute the steady meanflow is assessed. Noise predictions were made using accurate predictions of the non-uniform meanflow around the airfoil and again when the meanflow was assumed to be uniform everywhere, in order to assess the importance of accurate representation of the non-uniform flow-field.

The flat plate analytical method and the CAA method are discussed in Sections 2.1 and 2.2 respectively. Results of the investigation into the effects of airfoil geometry on leading edge noise are presented in Section 2.3.

2.1 Analytical Method

The flat plate analytical noise model due to Amiet [30], modified to allow for 2D airfoils, was used for validation of the CAA method, and to assess the validity of using flat plate modelling for the prediction of real airfoil leading edge noise. The gust amplitude was assumed to be constant at all frequencies, and was therefore set equal to $0.01U_x$ in both the analytical and CAA methods. The formulation of the analytical model will now be described.

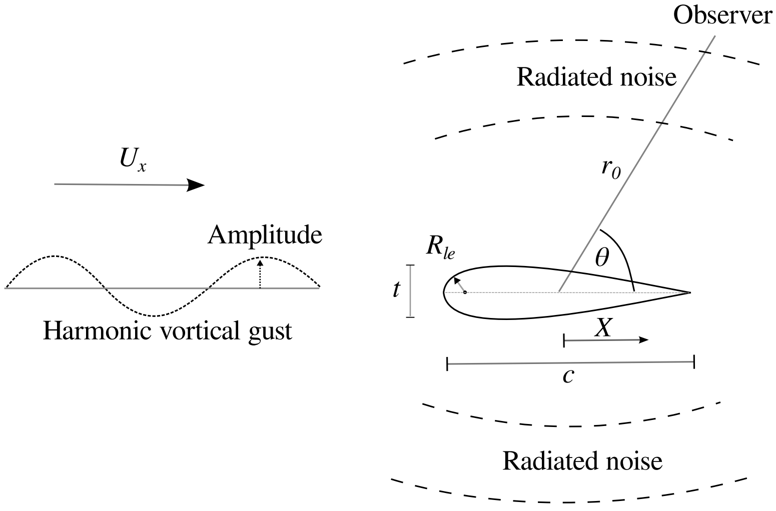

Figure 2.1: A schematic of a single frequency harmonic gust interacting with an airfoil at zero angle-of-attack, where t is the airfoil thickness, R_{le} is the leading edge radius, c is the airfoil chord, U_x is the freestream velocity, r_0 is the observer radius and θ is the observer angle from the downstream direction.

For a single frequency vortical gust with configuration as shown in Figure 2.1, with upwash velocity of the form $v_0 e^{-ik_x(X-U_X T)}$, the pressure jump Δp can be written as [30]

$$\Delta p(X,T) = 2\pi\rho_0 U_X v_0 g^{LE}(X,k_X,M_X)e^{ik_X U_X T}, \tag{2.1}$$

where U_X is the oncoming flow velocity in the direction of the blade chord, v_0 is the gust amplitude, g^{LE} is the non-dimensional transfer function between the upwash velocity and the pressure jump across the flat plate, k_x is the streamwise gust wavenumber, k_X is the chordwise gust wavenumber, M_X is the oncoming flow Mach number in the direction of the blade chord, and where T is time.

This unsteady jump can be written in the frequency domain as

$$\Delta\hat{p}(X,\omega) = 2\pi\rho_0 U_X v_0 g^{LE}(X,k_X,M_X), \tag{2.2}$$

where $\hat{p}$ denotes the pressure in the frequency domain.

By use of the Kirchoff-Helmholtz integral theorem, the radiated acoustic pressure due to the unsteady jump can be written as

$$p(x,y,\omega) = \frac{-1}{2\pi}\int_{-b}^{b}\Delta\hat{p}(X,\omega)\frac{\partial G}{\partial y}(x,y,X,\omega)dX, \tag{2.3}$$

where $G(x,y,X,\omega)$ is the two-dimensional time harmonic Green's function with mean flow effects included, given by Blandeau as [14]

$$G(x,y,X,\omega) = \frac{-i}{4\beta_X}H_0^{(2)}\left(\frac{k_0}{\beta_X^2}\sqrt{(x-X)^2+\beta_X^2 y^2}\right)e^{ik_0 M_X(x-X)/\beta_X^2}, \tag{2.4}$$

where $k_0 = \omega/c_0$, $\beta_X = \sqrt{1-M_X^2}$ and $H_0^{(2)}$ is a Hankel function of order 0 and of the second kind, x and y are the observer co-ordinates and X is the chordwise position on the flat plate as shown in Figure 2.1.

By applying the far-field assumption, the derivative of Equation 2.4 can be written as:

$$\frac{\partial G}{\partial y}(x, y, X, \omega) \approx \frac{iy}{4}\sqrt{\frac{2k_0}{\pi\sigma^3}}e^{i\frac{k_0}{\beta_X^2}[\sigma - Xx/\sigma - M_X(x-X)]+i\frac{3\pi}{4}}, \tag{2.5}$$

where $\sigma = \sqrt{x^2 + \beta_X^2 y^2}$.

This result and Equation 2.2 can now be substituted back into Equation 2.3 to give

$$p(x, y, \omega) = -2\pi\rho_0 U_X v_0 \frac{iy}{4}\sqrt{\frac{2k_0}{\pi\sigma^3}}\int_{-b}^{b} g^{LE}(X, k_X, M_X)e^{i\frac{k_0}{\beta_X^2}[\sigma - Xx/\sigma - M_X(x-X)]+i\frac{3\pi}{4}}dX. \tag{2.6}$$

By defining $A = \sqrt{1 - M_X^2 \sin^2\theta}$, and by changing to a 2D cylindrical co-ordinate system (r_0, θ) as shown Figure 2.1, Equation 2.6 can be written as

$$\begin{aligned} p(r_0, \theta, \omega) = -\frac{i\pi\rho_0 U_X v_0 r_0 \sin\theta}{2}\sqrt{\frac{2k_0}{\pi\sigma^3}}\int_{-b}^{b} & g^{LE}(X, k_X, M_X) \\ & \times \exp\left(\frac{ik_0}{\beta_x^2}\left(\frac{\cos\theta}{A} - M_X\right)(X+b) + \frac{i3\pi}{4}\right)dX, \end{aligned} \tag{2.7}$$

where X has been altered to $X + b$ to match the system shown in Figure 2.1.

Equation 2.7 can now be simplified to give the root-mean-square pressure p_{rms} as

$$p_{rms}(r_0, \theta, \omega) = \rho_0 U_X v_0 \sin\theta b\sqrt{\frac{\pi k_0}{2r_0 A^3}}\;|L^{LE}|, \tag{2.8a}$$

where $$L^{LE} = \frac{1}{b}\int_{-b}^{b} g^{LE}(X, k_X, M_X)\exp\left(\frac{ik_0}{\beta_x^2}\left(\frac{\cos\theta}{A} - M_X\right)(X+b) + \frac{i3\pi}{4}\right)dX \tag{2.8b}$$

is the unsteady loading term.

Analytical solutions for the chordwise loading integral g^{LE} exist and are given by Blandeau [14]. Differing solutions have been derived depending on the value of the acoustic reduced frequency $\mu_a = \frac{\omega b}{c_0 \beta_X^2}$. If $\mu_a < \pi/4$ then the low frequency response is used, and so Equation 2.8b becomes

$$L_{low}^{LE}(\theta, K_X, \kappa) = \frac{S(\mu_h)}{\beta_X} e^{i\mu_h f(M_X)} \left\{ J_0\left(\mu_a \frac{\cos\theta}{A(\theta, M_X)}\right) - iJ_1\left(\mu_a \frac{\cos\theta}{A(\theta, M_X)}\right) \right\}, \tag{2.9}$$

where $f(Mx) = (1-\beta_x)\ln M_X + \beta_X \ln(1+\beta_X)$, J_0 and J_1 are Bessel functions of the first kind and S is the Sears function, which is expressed as a function of the chord-based hydrodynamic reduced frequency $\mu_h = \mu_a/M_X$.

If $\mu_a > \pi/4$, the high frequency response function is used, and Equation 2.8b becomes

$$L_{high}^{LE}(\theta, K_X, \kappa) = L_1(\theta, K_X, \kappa) + L_2(\theta, K_X, \kappa), \tag{2.10}$$

where functions L_1 and L_2 are the leading and trailing edge scattering and back-scattering of sound. They are given by

$$L_1(\theta, K_X, \kappa) = \frac{\sqrt{2}}{\pi \beta_X \sqrt{\mu_h (1+M_X)\Theta_1}} E^*(2\Theta_1) e^{i\Theta_2}, \tag{2.11a}$$

$$\begin{aligned} L_2(\theta, K_X, \kappa) = {} & \frac{e^{i\Theta_2}}{\pi \Theta_1 \beta_X \sqrt{2\pi\mu_h(1+M_X)}} \Bigg[i(1-e^{-i2\Theta_1}) + (1-i) \\ & \times \left[E^*(4\mu_a\beta_x^2) - \sqrt{\frac{2}{1+\frac{\cos(\theta)}{A(\theta,M_X)}}} e^{-i2\Theta_1} E^*(2\Theta_3) \right] \Bigg], \end{aligned} \tag{2.11b}$$

where E^* is the conjugate of the Fresnel integral as defined by Amiet [36]. Θ_1, Θ_2, and Θ_3 have been introduced for brevity. They are defined as

$$\Theta_1 = \mu_a \left(1 - \frac{\cos\theta}{A(\theta, M_X)} \right) \tag{2.12a}$$

$$\Theta_2 = \beta_X^2 \mu_h + \mu_a \left(M_X - \frac{\cos\theta}{A(\theta, M_X)} \right) - \frac{\pi}{4} \tag{2.12b}$$

$$\Theta_3 = \mu_a \left(1 + \frac{\cos\theta}{A(\theta, M_X)} \right). \tag{2.12c}$$

Equations 2.9 to 2.12c can be used to solve Equation 2.8a for varying angles to examine the pressure directivity at any given frequency.

2.2 Computational Method

The computational method uses a high-order CAA code to solve the LEEs, known as SotonCAA. It was developed at the University of Southampton and has been used in previous aeroacoustic studies such as the study by Zhang *et al.* [94]. A sixth-order compact spatial discretisation scheme was used [38] with tenth-order filtering and a fourth-order low-dispersion and low-dissipation Runge-Kutta (LDDRK) 4-6 explicit temporal scheme [95]. Unsteady gusts were superimposed onto a steady meanflow solution, which convects the vortical gust towards the airfoil.

The linearised Euler equations are so called because they separate a linearly fluctuating term into a mean value and a perturbation term. The flow can then be solved as a series of perturbations around a steady mean value. This makes the LEEs ideal for modelling sound propagation. However, the effects of the sound on the meanflow (which are very small) are neglected.

The general approach of the computational method was to compute (or assume) a meanflow solution using a second-order CFD solver, onto which gust perturbations were then overlaid using SotonCAA. The resulting pressure field was then inputted into a time-domain FW-H solver to obtain the far-field noise caused by interaction between the gust and the airfoil. This approach allowed the relatively cheap LEEs to be used while still considering a realistic flow problem in an accurate manner.

All simulations discussed in this thesis were made using the Iridis4 High Performance Computing Facility at the University of Southampton. SotonCAA is a parallel solver, which allowed mutiple processors to be used for each simulation. Typically, 48 processors were used for each case. However, the exact processor usage varied throughout the project due to varying availabilities of the computational facility.

The simulations used a constant global timestep value to give a typical Courant-FriedrichsLewy (CFL) number of about 0.5. However, this number varied due to the unsteady nature of the simulations. Each simulation was run for sufficient time to develop the gust interaction process, and to then record one period of the data to allow far-field noise predictions.

2.2.1 LEE Boundary Conditions

In aeroacoustic simulations the correct choice of boundary conditions is critical. In addition to slip-wall conditions which are necessary to define the body of interest, buffer (or non-reflective) conditions must also be used at the edges of the simulation domain in order to prevent any spurious sound reflections back into the domain due to flow interactions with the domain edges. The purpose of a buffer region is to damp any flow perturbations to the steady mean flow value, so that there are no reflections back into the domain. In this study, an explicit damping function was used at the end of each timestep [96], i.e:

$$U^{n+1} = \overline{U^{n+1}} - \sigma(\overline{U^{n+1}} - U_{target}) \tag{2.13}$$

where $\overline{U^{n+1}}$ is the solution vector after each time step, U_{target} is the desired target value and σ is

$$\sigma(x_b) = \sigma_{max} \left| 1 - \frac{x_b - L_b}{L_b} \right|^{\beta} \tag{2.14}$$

where L_b is the width of the buffer zone, x_b is the distance from the domain boundary and σ_{max} and β are coefficients which set the shape of the damping function. In this study, $\sigma_{max} = 1$ and $\beta = 3$, and U_{target} was set as described in Section 2.2.2. The values of σ and β were chosen based on the parameter study of Richards *et al.* [96], who compared several different methods for obtaining a non-reflective boundary condition and found this configuration of explicit buffer region to be the most effective. This damping function was applied to all domain boundaries of the simulation.

The buffer zone velocity U_{target} value would ordinarily be set to 0. However, in the current work this was set equal to an unsteady value at the inflow in order to define the forced gust. This was done in order to prevent interactions between buffer zones and a separate gust boundary condition, and is similar to the method used by Kim *et al.* [97,98]. Therefore, the buffer zones provided the required gust forcing in addition to preventing acoustic reflections from the domain edges. Similarly to Kim *et al.* [97] the gust-enforcement of the buffer zones was ramped down towards the outflow of the simulation domain in order to prevent interactions between the forced gusts and outgoing convected vortical waves.

A schematic of a typical simulation domain is shown in Figure 2.2.

2.2.2 Gust Perturbation Definition

Transverse vortical gusts with velocity component normal to the freestream direction were defined in this study to be of the form of a summation of discrete frequency

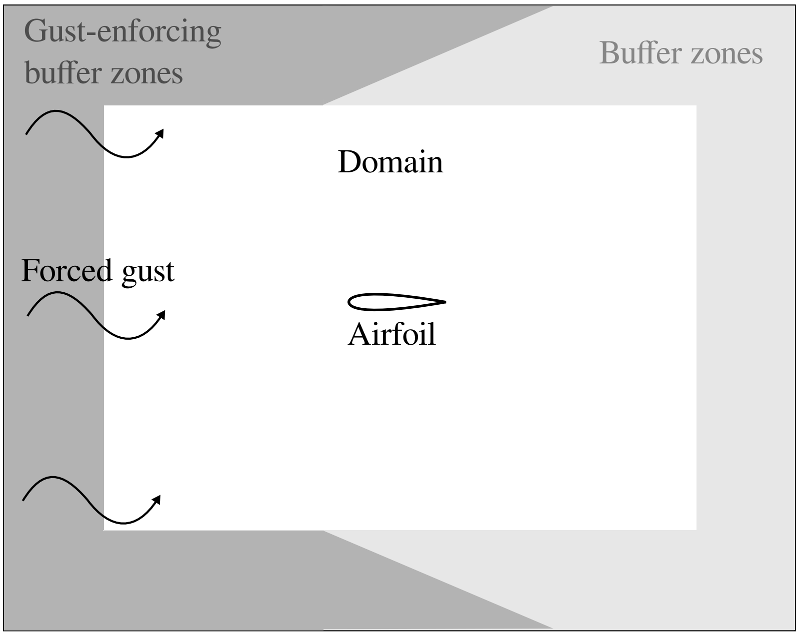

Figure 2.2: A schematic of a typical simulation domain.

gusts, and can expressed as

$$v(\boldsymbol{x},T)=\sum_{l=1}^{L} v_0 \cos\Big(k_{x,l}(x-U_xT)\Big), \tag{2.15}$$

where $v(\boldsymbol{x},T)$ is the instantaneous gust velocity, $k_{x,l}$ is the streamwise gust wavenumber of the $l^{\text{ th}}$ frequency, x is the streamwise location, T is time, v_0 is the maximum transverse gust amplitude (set to $v_0 = 0.01U_x$, which is within the amplitude limit found by Golubev *et al.* [99, 100] and Lockard and Morris [101] for linear interactions), and L is the total number of gust frequencies. Gusts at multiple discrete frequencies were defined in individual simulations, such that the vertical gust contained information at several discrete frequencies simultaneously. Sufficient numbers of frequency were chosen to resolve the spectral shape of the leading edge noise. Each forced frequency was chosen to be a harmonic of a given fundamental frequency, such that the simulation was periodic about the largest forced wavelength. Noise predictions at each discrete frequency were then recovered in post-processing via Fourier transformation.

2.2.3 Far-Field Sound Computation and Post-Processing

Far-field acoustic predictions were made using a time-domain FW-H solver which is a separate module of the SotonCAA package. It solves Formulation 1A by Farassat [44,102], which allows far-field noise predictions if the flow conditions are known on an integral surface which is on or near the body of interest. This integral surface often encloses the body, but this is not a requirement for Formulation 1A to be valid. In this study, on-body surfaces were used to prevent the forced gust from interfering with sound predictions, which can be problematic if off-body surfaces are used. Therefore, the CAA method neglects the acoustic refraction effects due to the non-uniform meanflow. However, this effect is not expected to have a significant effect on the noise in the conditions studied here. The strongest meanflow gradients are upstream of the airfoil, and therefore the sound radiated in the upstream direction ($210° > \theta > 150°$) will be the most affected by this approximation.

Values of the conserved variables were recorded on the FW-H integral surface such that the highest frequency waves were temporally resolved by 25 points per acoustic wavelength. This value was found to provide converged results. The signal recorded on the surface of the airfoil was periodic, because the forced vortical waves were periodic. Therefore, significant computational savings were made by recording only one period of the acoustic disturbances.

Frequency spectra were obtained via post-processing routines written in the commerical software MATLAB. These performed a Fourier transformation of the time-varying signal at each observer position. To reduce any errors associated with failing to capture a perfect period of the disturbances, a window function was applied to the temporal data.

2.2.4 Mesh Generation

C-shape grids were used near to the airfoil surface. Because of the differing grid requirements between viscous flow solutions and the inviscid LEE propagation calculations, different computational grids were needed for the meanflow calculation and the gust interaction stages of the CAA method. Viscous computations were performed to obtain the steady meanflow solution where an accurate representation of the boundary layer was provided by using Y^+ values of below two. For the inviscid LEE simulations the resolution was required to resolve the forced gust. Therefore the LEE computational grid resolution was chosen to resolve the smallest gust wavelengths by at least 12 points per wavelength. Computational grids extended to at least 7 chord lengths from the airfoil in all directions to prevent acoustic interference with the domain edges. To allow vortical gusts to be overlaid onto a viscous meanflow solution, the viscous flow-field was interpolated onto the inviscid grid.

For the inviscid acoustic grids used in SotonCAA to model the gust interaction process, an ideal grid would have a uniform density everywhere. However, this cannot be done with a C-shape grid because the cell size will grow radially from the airfoil. Therefore, the acoustic grids used a C-shape topology close to the airfoil surface, and a rectangular topology further away from the airfoil. An example of an inviscid acoustic grid topology for a NACA 0012-63 airfoil is shown in Figure 2.3. Far from the airfoil, the resolution requirement of 12 points per vortical wavelength was enforced. In the region surrounding the airfoil, the grid density was higher due to the use of the C-shape mesh. Therefore, the leading edge region of each airfoil was well resolved by the computational grid. Examples of the mesh in the leading edge region of a NACA0002 and a NACA0012-63 airfoil are shown in Figure 2.4.

Because the current project involved the use of a large number of computational grids to represent the different airfoil geometries, an in-house tool was used to assess the quality of the different meshes. This tool applied a high-order filtering scheme to each grid in order to highlight areas that could be improved. The tool highlighted areas of high skewness and discontinuities in the grid spacing or connector geometry. This tool allowed each grid to be individually optimised, and reduced the potential for mistakes in the grid-generation process. The largest values of skewness were usually identified to be in the leading edge region of the airfoil, as this is the region of highest curvature on the grid. Elsewhere, the skewness was typically significantly lower. Values of maximum skewness, and some values of average skewness, are given in Appendix C for different grids.

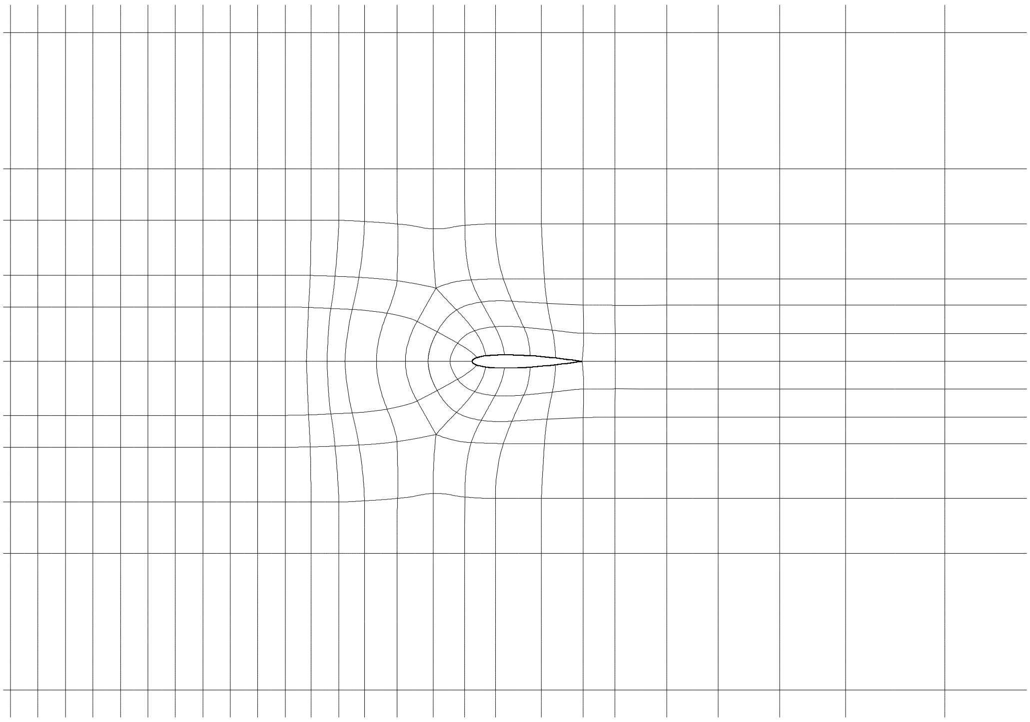

Figure 2.3: Showing an example of the grid topology for a NACA 0012-63 airfoil.

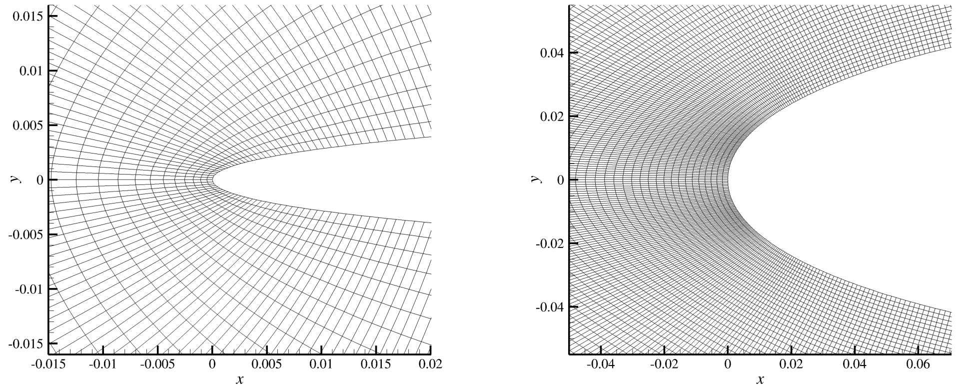

Figure 2.4: Showing the grid surrounding the leading edge of a NACA0002 (left) and a NACA0012-63 (right) airfoil.

2.2.5 Meanflow Simulations

Solutions for the non-uniform meanflow surrounding the airfoil were performed using the commercial solver FLUENT. As is discussed in Section 2.3.2, solutions for both inviscid and viscous meanflows were made. The domains for the meanflow simulations were sufficiently large that a far-field pressure boundary condition was used at the edges of the domain. A slip wall, and non-slip wall condition was used on the airfoil surface for the inviscid and viscous simulations respectively. For the inviscid meanflow simulations, the computational grid that was used to solve the meanflows was the same as that used to solve the LEE. For viscous meanflow simulations, a viscous grid was used and the meanflow solution was then interpolated onto the invsicid acoustic grid using interpolation options in the commercial software Tecplot. All solutions of the meanflow enforced the Kutta condition such that the stagnation point was located at the trailing edge. No additional Kutta condition was enforced in the LEE simulations, because the effect on the acoustic results was found to be small. This is discussed in Section 2.3.1.

2.2.6 Airfoil Geometry Definition

For most airfoil families, such as the NACA 4-series airfoils, the leading edge radius R_{le} and the thickness t are related. For example, the NACA 4-series airfoils define $R_{le} \propto t^2$. If the thickness of a NACA 4-series airfoil is modified, therefore, there will be a corresponding change to R_{le}. Any effects on the leading edge noise will therefore be due to a combination of these two length-scale changes. In the current work, the effects on noise of R_{le} and t are investigated independently for the first time by using the NACA modified 4-series airfoil family [103], which allow the separate specification of t and R_{le}. Leading edge radius R_{le} is related to thickness by

$$R_{le} = 0.5\left[0.2969\frac{t}{0.2}\left(\frac{I}{6}\right)\right]^2, \tag{2.16}$$

where I is a non-dimensional parameter that controls the shape of the leading edge, as seen in Figure 2.5. $I = 0$ defines an airfoil with $R_{le} = 0$, while $I = 6$ represents a standard NACA 4-series profile. Through variations in I, the effects of leading edge radius changes with constant t can be studied.

The effects on leading edge noise were studied due to gust interactions with airfoils whose maximum thickness varied between 6% (or $t = 0.06c$) and 24%, and whose I parameters varied between $I = 0$ and $I = 10$. An additional NACA 0002 case was also included for validation of the CAA method. This was the closest approximation to a flat plate that was used. Figure 2.5 shows the geometries of the airfoils investigated. The naming convention follows the standard NACA 4-series method with an additional two digits which represent the parameter I and the chordwise position of maximum thickness (in tenths of chord) respectively. In this work the chordwise position of maximum thickness position was fixed at $0.3c$ and the airfoil chord was fixed at $c = 1$ m.

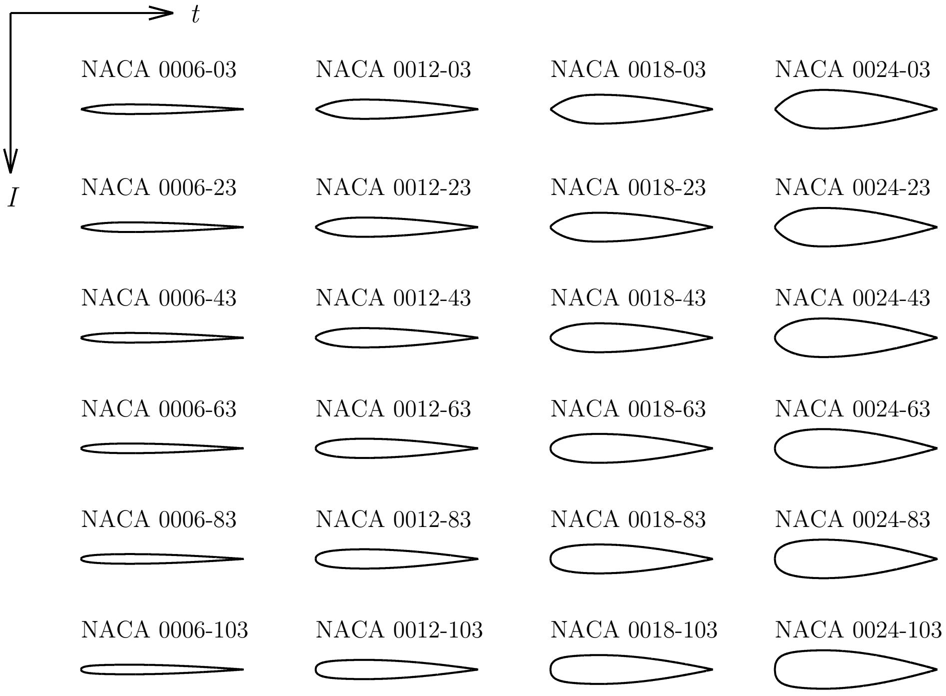

Figure 2.5: The various airfoil geometries used in the study. Both thickness and leading edge radius were varied to allow independent study of their effects on leading edge noise.

2.3 Results

2.3.1 Validation

The CAA method was validated by comparing 2D analytical flat plate predictions at $M = 0.2$ with noise predictions from the CAA method due to a thin NACA 0002 airfoil ($I = 6, t = 0.02c$) in a uniform meanflow. The NACA 0002 airfoil is the closest approximation to a flat plate that was tested. An exact flat plate was not investigated with the CAA method since spatial discretisation errors in finite difference codes make it difficult to use genuine flat plate geometry. This occurs because a wall condition cannot be properly applied to the infinitely thin leading edge surface, and therefore the singular point at the leading edge is simultaneously treated as both a wall point and a point in the flow-field. A uniform meanflow was used in the CAA prediction for better comparison with the analytical solution, which also assumes a uniform meanflow.

The leading edge far-field noise at $r_0 = 100$ m was predicted at reduced frequencies of between $K = 0.25$ and $K = 12.5$. Figure 2.6 compares the noise predictions from analytical flat plate theory with predictions from a NACA 0002 airfoil in the CAA method, where the NACA 0002 airfoil has been modelled by assuming a uniform and a viscous non-uniform meanflow. The $\mathrm{CAA}_{\text{non-uniform}}$ spectra and directivity shown in Figure 2.6 represent the CAA noise predictions in which viscous non-uniform meanflow effects around the NACA 0002 airfoil are included, and are discussed in Section 2.3.2.

Figure 2.6 shows agreement between the analytical and the $\mathrm{CAA}_{\text{uniform}}$ noise predictions of better than 1 dB at all tested gust frequencies and observer angles. The largest difference is seen in the directivity predictions at upstream observer angles, which can be attributed to the curvature of the NACA 0002 airfoil in the CAA method compared with a flat plate. Small oscillations in CAA spectral predictions can be seen. These are attributed to the assumption of discrete frequency forcing as opposed to a continuous spectrum, and to the fixed grid density, which causes each gust frequency to have a different temporal and spatial resolution in the simulation.

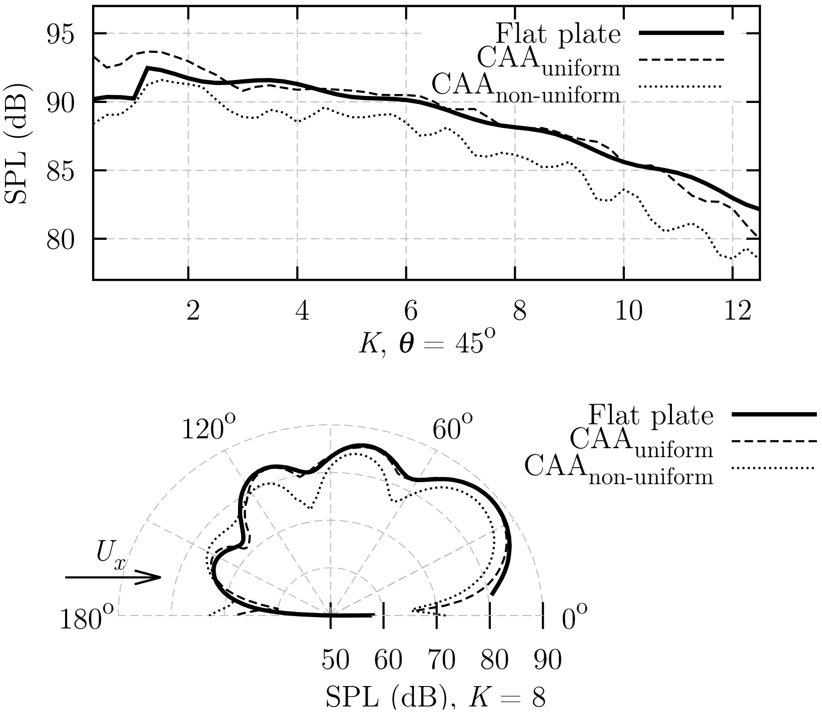

Figure 2.6: Spectral (upper) and directivity (lower) comparison of noise predictions from the CAA method using a NACA 0002 airfoil, and the analytical flat plate method. The spectral comparison is made at $\theta = 45°$ and the directivity comparison is made at $K = 8$. CAA predictions using both a uniform and non-uniform flow are shown.

Figure 2.7 compares the time-averaged p_{rms} response (normalised by $\rho_0 U_x^2$) on the surface of the NACA 0002 airfoil with the predicted response given by Amiet's theory. This prediction includes the response at all the tested reduced frequencies. A close agreement is seen between the numerical and analytical predictions. Small differences are seen at the leading edge, where the NACA 0002 prediction gives a lower response than the analytical prediction. This is attributed to the real geometry of the NACA 0002 airfoil in comparison to the flat plate. Additionally, a spike in response is seen at the trailing edge in the NACA 0002 prediction. This is caused by numerical discontinuities at the trailing edge associated with non-eforcement of the Kutta condition. However, the strongest source of leading edge noise is at the leading edge of an airfoil, as seen by the strong p_{rms} values at $X/c = 0$. The values at the trailing edge are significantly smaller than the values at the leading edge, suggesting that the Kutta condition will only have a small effect on the noise predictions.

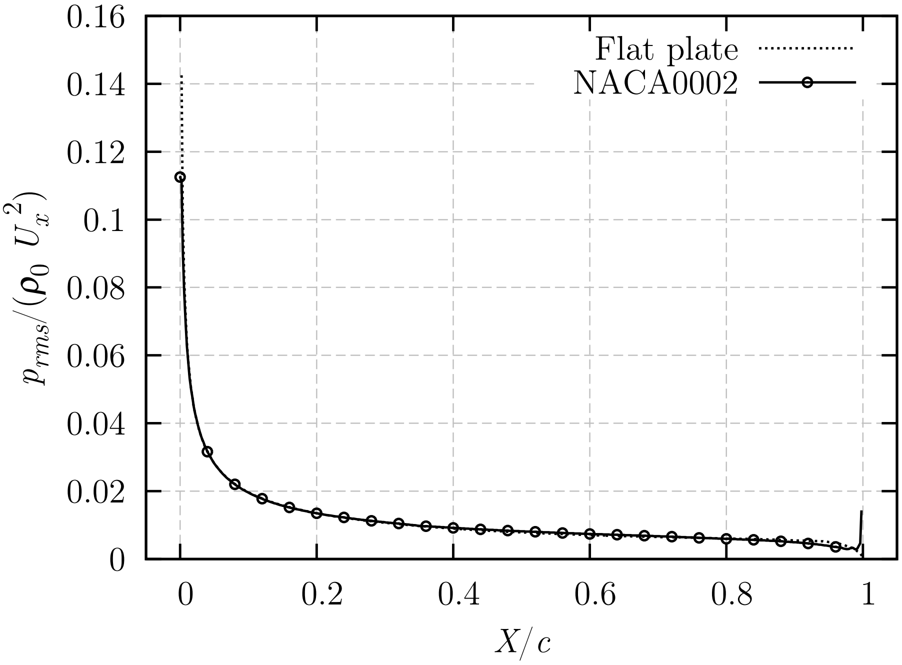

Figure 2.7: Showing chordwise p_{rms} variation on the surface of a NACA 0002 airfoil.

To ensure that the disturbance arriving at the airfoil leading edge was not changed by its passage through the domain, a monitor point was placed in the flow-field at a location of one chord above the leading edge ($x = 0$ m, $y = 1$ m in cartesian coordinates). The velocity could not be measured at the leading edge because at this location the gust is modified by the non-uniform meanflow and by interactions with the airfoil surface. The time-dependent transverse velocity at this monitor point was collected and was post-processed with the same fast-Fourier transformation method that was used to recover the noise at each discrete frequency. The frequency dependent transverse velocity spectra is shown in Figure 2.8.

Figure 2.8 shows that the computational method, and the post-processing routines, recover the analytical velocity amplitude value of $v = 0.002$ with good accuracy at all the frequencies used in this study. This suggests that the spatial and temporal resolution of the simulation is sufficient to propagate the disturbances towards

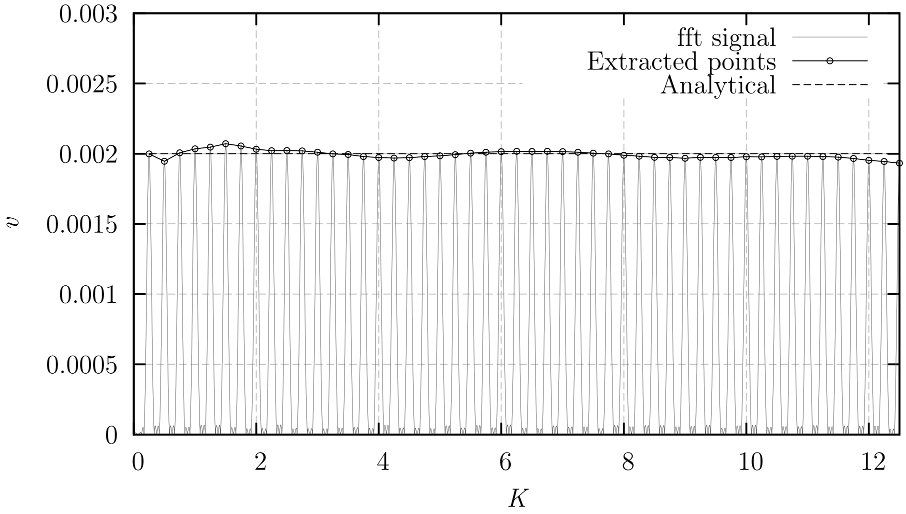

Figure 2.8: Gust velocity spectra at the airfoil leading edge.

the airfoil and to then record the unsteady fluctuations for noise predictions. The maximum error appears to occur at the highest frequencies, and corresponds to a 3% error in the amplitude at these frequencies. The cause of this error may be related to slight gust distortions due to non-uniform meanflow effects (this study was conducted when using an inviscid non-uniform meanflow), or may be showing dissipation caused by the spatial, temporal, and filtering schemes. However, propagation of the gust with an amplitude accuracy within 3% was considered sufficient for the current study.

2.3.2 Meanflow Modelling Assumptions

We now investigate whether the modelling of the non-uniform meanflow is necessary for accurate noise prediction, or if accurate noise predictions can be obtained by making the assumption of uniform meanflow. This comparison also elucidates the noise generation mechanism, which is discussed in more detail in Section 2.3.5. Figure 2.6 compares the noise predictions made with the CAA method for a NACA 0002 airfoil, by using both the viscous non-uniform meanflow solution and by assuming a meanflow that is uniform everywhere.

The non-uniform meanflow case predicts a reduced noise amplitude by as much as 3 dB at high frequency compared to the predictions made with a uniform meanflow and also to flat plate noise predictions, at all frequencies and at most observer angles. The noise difference increases slightly with increasing frequency. Therefore, even with a thin NACA 0002 airfoil, the effects of a non-uniform meanflow are important to leading edge noise predictions. Methods which do not account for the non-uniform meanflow are expected to over-predict the noise at high frequency. The effects of thickness on leading edge noise are discussed in further detail in Section 2.3.3.

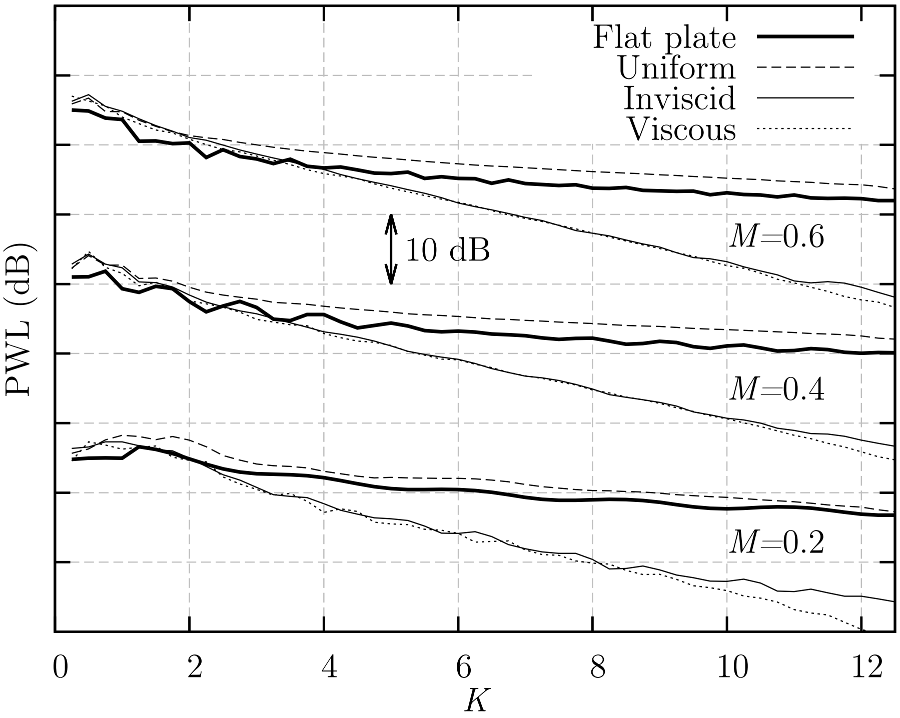

Figure 2.9: PWL due to harmonic sinusoidal gusts at varying reduced frequency interacting with a NACA 0012-63 airfoil. Predictions are made at $M = 0.2$, $M = 0.4$, and $M = 0.6$ by the analytical flat plate model and by the CAA method using differing meanflow assumptions.

Figure 2.9 shows the relative sound power level (PWL) predictions made using the analytical flat plate method, compared with predictions from the CAA method using a NACA 0012-63 airfoil at $M = 0.2$, $M = 0.4$, and $M = 0.6$. Here, PWL is defined as the power per unit span for a 2D airfoil [19]. At each Mach number, noise predictions were made by the CAA method assuming a viscous non-uniform meanflow, an inviscid non-uniform meanflow, and a uniform meanflow, so that the effects on noise due to different meanflow assumptions could be investigated. The uniform meanflow and the inviscid non-uniform meanflow computed for $M = 0.2$ are shown in Figure 2.10.

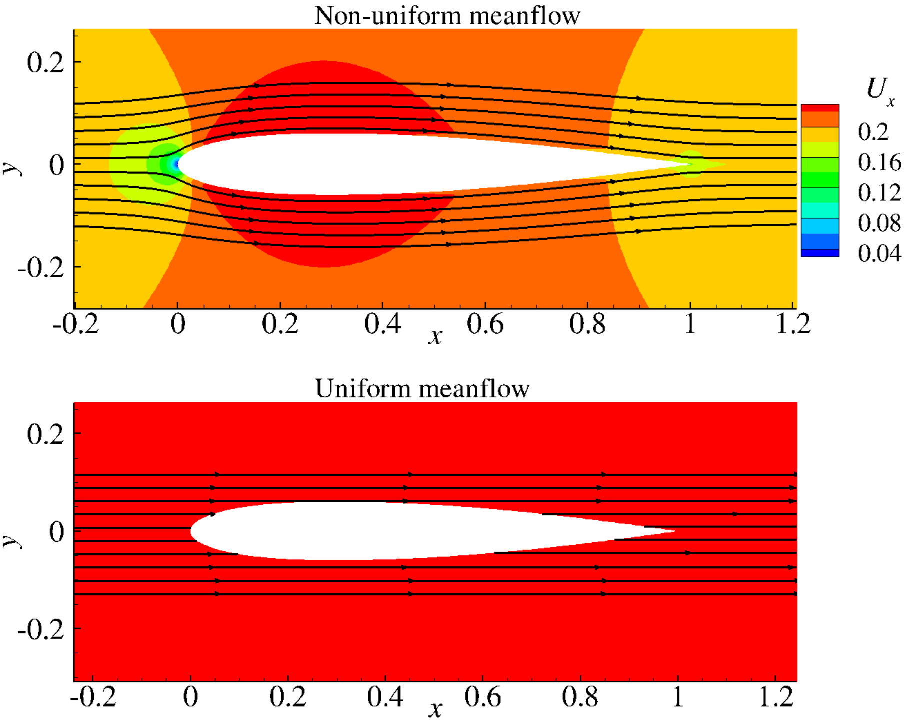

Figure 2.10: Comparison of an inviscid non-uniform and uniform meanflow result for a NACA 0012-63 airfoil at $M = 0.2$. Streamtraces outline flow direction and contours show U_x velocity.

Figure 2.9 shows that at all Mach numbers there is a significant difference between the CAA noise predictions that are made by assuming a uniform meanflow, and those made by including non-uniform meanflow effects. Predictions that include the effects of non-uniform meanflow show a reduction in noise due to the thickness of the NACA 0012-63 airfoil, whereas close agreement was obtained for the NACA 0002 airfoil in Figure 2.6. This reduction increases with increasing frequency and Mach number, which is in agreement with previous literature [72, 77]. At $K = 12$ and $M = 0.6$

the CAA predictions are approximately 18 dB lower than the predictions made with analytical flat plate theory. However, predictions that assume a uniform meanflow show an increase in noise in most cases. Therefore the non-uniform meanflow plays an important role in the leading edge noise generation mechanism of airfoils with real geometry.

Predictions made using a non-uniform meanflow show a reduction in noise above a threshold reduced frequency. At $M = 0.2$ this threshold reduced frequency is at about $K = 1$, but at $M = 0.6$ the threshold increases to about $K = 4$. Therefore the threshold reduced frequency at which leading edge noise becomes sensitive to airfoil geometry appears to have a dependence on Mach number.

Small differences of less than 1 dB are seen in the majority of the noise spectrum predicted by the CAA method between using a viscous and inviscid non-uniform meanflow solution. Assuming an inviscid flow-field causes the CAA method to over-predict the noise by up to 4 dB at high frequency and low Mach number. In other parts of the spectrum the difference between the viscous and inviscid predictions is negligible. Therefore, for predictions of leading edge noise due to symmetric airfoils interacting with harmonic gusts, an inviscid flow-field can be assumed in most cases without significant loss of accuracy.

The error incurred by assuming a uniform meanflow with regards to leading edge noise prediction of real airfoils has not been previously investigated. Additionally, the small loss in prediction accuracy of up to 1.5 dB caused by the assumption of an inviscid flow-field has not been previously reported. The remainder of this chapter sets $M = 0.2$ and assumes an inviscid non-uniform meanflow. Reasons for the inaccuracy of predictions made when assuming a uniform meanflow solution are discussed in Section 2.3.5.

2.3.3 Effects of Thickness

The sensitivity of leading edge noise to varying airfoil thickness is investigated in this section. Figure 2.11 compares the contours of sound pressure level (SPL) with varying observer angle θ and gust reduced frequency K, between the analytical flat plate noise predictions and predictions from the CAA method using a NACA 0024-03 airfoil. Two iso-lines of constant SPL are also shown in Figure 2.11 to assist comparison. A NACA 0024-03 airfoil has been chosen for the CAA prediction because it has a large thickness t and zero leading edge radius ($R_{le} = 0$), and therefore exhibits thickness effects on noise while minimizing any leading edge radius effects.

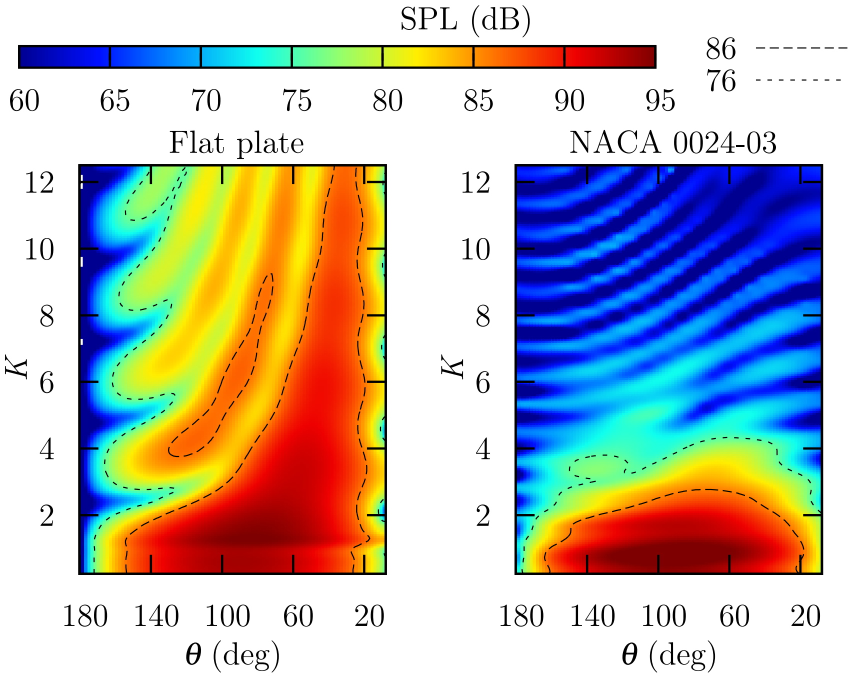

Figure 2.11: Comparison between the contours of SPL from analytical flat plate predictions and the CAA method using a NACA 0024-03 airfoil, at varying observer angle and gust frequency.

Figure 2.11 shows that the noise predictions from the analytical and CAA methods give similar predictions at low frequency. However, at frequencies above $K = 1$ the CAA predictions differ from the analytical predictions due to the thickness of the NACA 0024-03 airfoil. For frequencies above $K = 1$ the effect of thickness is to decrease the noise compared to flat plate noise predictions, such that the NACA 0024-03 noise predictions are approximately 15 dB quieter at $K = 12$. Additionally, contours of the analytical noise prediction show a strong directivity lobe at $\theta = 45°$ for $K > 2$, while the NACA 0024-03 predictions exhibit less sensitivity to observer angle. The amplitude of the analytical flat plate noise prediction oscillates with varying frequency at forward observer angles ($\theta > 140°$). The CAA noise prediction also shows oscillations in noise amplitude with varying reduced frequency above $K = 4$, but these oscillations are present over a wider range of angles compared with the analytical noise prediction.

Figure 2.12 compares the predicted noise spectra from the analytical flat plate solution and the CAA method using a NACA 0012-03 airfoil, at two observer angles. The noise predictions from the CAA method at the downstream observer angle ($\theta = 45°$) are lower than the analytical predictions. The difference between the two methods increases with increasing reduced frequency above $K = 1$. This effect of thickness on the noise predictions agrees with the findings of previous authors such as Paterson and Amiet [63], who report a smaller effect than predicted here. Paterson and Amiet reported a 5 dB reduction in noise at $\theta = 90°$ at $K_t = 1$ (or $K = 8.3$ for a 12% thick airfoil) due to an airfoil with 12% thickness, but Figure 2.12 shows a difference of about 8 dB. The increased sensitivity of leading edge noise to thickness, in comparison to Paterson and Amiet's work, may be due to the assumption of harmonic vortical gusts instead of turbulent interactions, as was reported by Evers and Peake [76] in their analytical study of airfoil geometry effects on cascade noise. Figure 2.12 shows that for observers at $\theta = 45°$, the effect of thickness on noise is significant at $K > 1$, which agrees with the conclusions of Atassi *et al.* [77], but is lower than Paterson and Amiet [63] who conclude that flat plate theory breaks down at thickness-based reduced frequencies of $K_t = t/\lambda > 1$ (or above about $K = 8.3$ for a 12% thick airfoil).

Figure 2.12 shows that at the upstream observer angle ($\theta = 150°$) the thickness effects do not reduce the predicted noise in the CAA method. Here, the effect of airfoil thickness on noise is to suppress the amplitude of the oscillations that occur in the spectrum compared to flat plate predictions. This effect is significant at $K > 2$ and does not vary with increasing frequency.

Figure 2.13 compares the directivity predictions at $K = 8$ from the CAA method using airfoils with varying thickness, with those obtained from flat plate theory. Figure 2.13 shows that the directivity pattern remains similar as thickness is varied, but

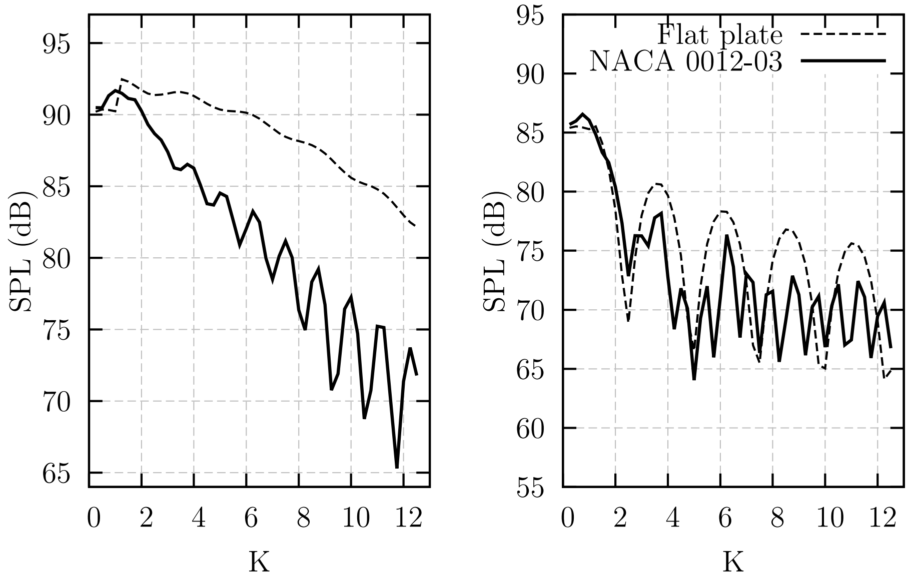

Figure 2.12: Comparison of thickness effects on the noise for a NACA 0012-03 airfoil at downstream observer angle $\theta = 45°$ (left), and upstream observer angle $\theta = 150°$ (right).

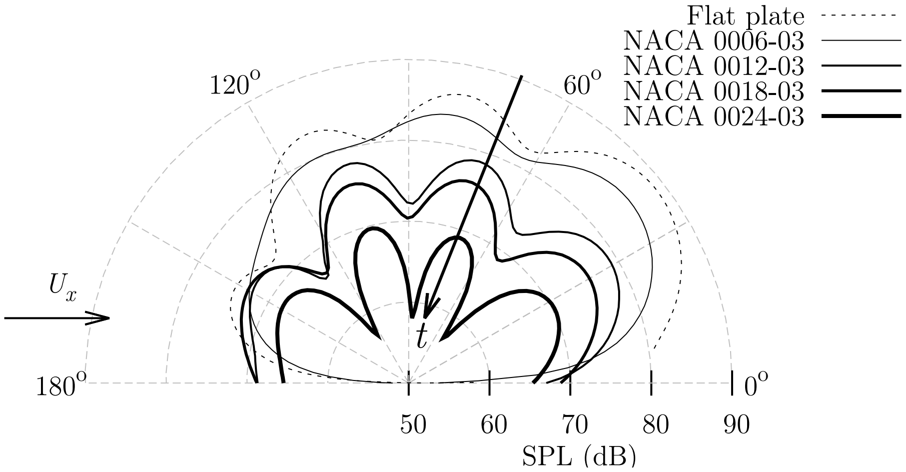

Figure 2.13: The effect on noise directivity predictions due to increasing airfoil thickness, with $R_{le} = 0$, at $K = 8$.

the predicted noise level reduces with increasing airfoil thickness at most observer angles. This finding agrees with the conclusions of several previous authors, including Olsen and Wagner [72]. However, at acute upstream observer angles (above

$\theta = 130°$) the noise amplitude is not reduced as a result of increasing thickness, as was also seen in Figure 2.12. Lockard and Morris [79] and Atassi *et al.* [77] both reported similar behaviour to that shown in Figure 2.13, with the exception that both studies reported slight increases in upstream noise. This increase is not seen in the current work.

Figure 2.14 shows the sensitivity of the sound power P prediction to airfoil thickness at constant reduced frequencies of $K = 4$ and $K = 8$, for airfoils with $I = 0$ so that any effects on P due to leading edge radius can be neglected. Solid lines are drawn as straight lines of best fit between sound power predictions and airfoil thickness. Figure 2.14 shows that the sound power at constant reduced frequency appears to decrease almost linearly with increasing airfoil thickness. The sensitivity of sound power to thickness reported here may be consistent with the experimental findings of Olsen and Wager [72], who measured a "linear" decrease in noise due to thickness compared with the noise generated by a 3% thick airfoil. However it is not clear if Olsen and Wagner refer to a linear change in SPL, or to a linear change in the acoustic pressure response.

2.3.4 Effects of Leading Edge Radius

The effect of leading edge radius on leading edge noise is now investigated. Figure 2.15 shows the predicted leading edge noise spectra and directivity pattern due to a family of 12% thick airfoils with varying leading edge radii corresponding to $I = 0$, $I = 6$, and $I = 10$. Figure 2.15 shows that the predicted noise for downstream observers is reduced by increasing the leading edge radius, and that the amount of noise reduction increases with increasing reduced frequency. At upstream observer positions there is an increase in noise due to an increase in leading edge radius, but this trend is less clear than the trend for downstream observers since noise predictions for the NACA 0012-63 airfoil are greater than for the NACA 0012-10 airfoil. In general, the effect of increasing leading edge radius is to cause a reduction in noise for downstream observers, and to cause a slight increase in noise for upstream observers. Noise predictions become sensitive to leading edge radius at reduced frequencies above about $K = 4$, which is higher than the frequency of

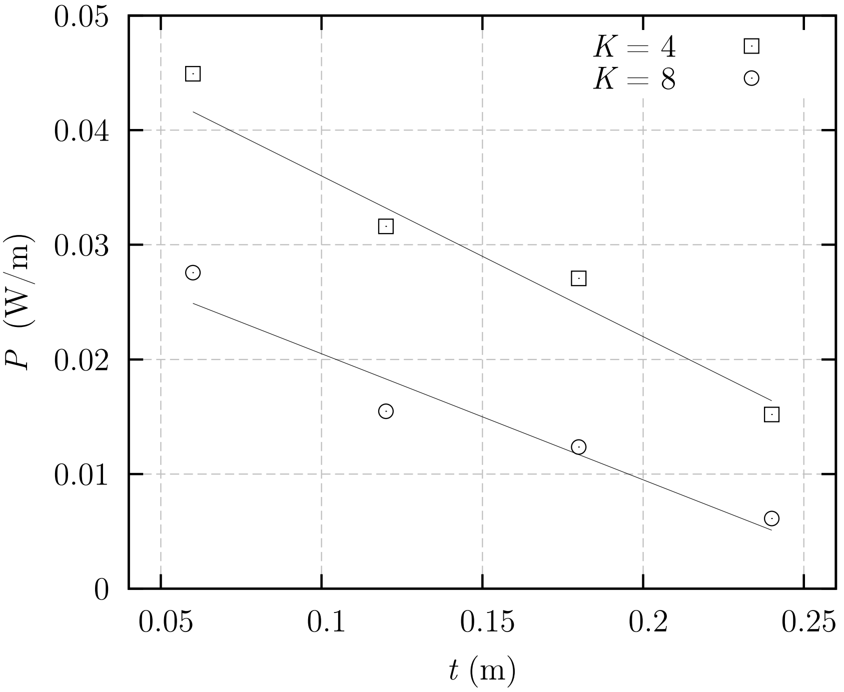

Figure 2.14: The behaviour of sound power P with airfoil thickness at reduced frequencies of $K = 4$ and $K = 8$. Solid lines are drawn as lines of best fit.

about $K = 1$ at which the noise appears to become affected by airfoil thickness in $M = 0.2$ flows.

We now investigate the relative sensitivity of the effects on noise due to thickness and leading edge radius. Figure 2.16 shows the PWL spectra for airfoils with 6% (or $t = 0.06c$) and 12% thickness, each with $I = 6$ and $I = 10$. At reduced frequencies above about $K = 1$, the noise predictions are significantly different between airfoils with differing thicknesses, with thicker airfoils generating less noise than thinner ones. Above reduced frequencies of about $K = 4$, the noise predictions for airfoils with equal thickness, but different leading edge radius, are reduced by an increase in the leading edge radius. Leading edge noise is therefore affected by airfoil thickness at lower reduced frequencies than it is affected by leading edge radius. Furthermore, the noise reduction due to the change from 6% to 12% thickness in Figure 2.16 is about 8 dB at $K = 12$, whereas the reduction in noise due to the change from $I = 6$ to $I = 10$ is about 4 dB at $K = 12$. Therefore leading edge noise appears to be

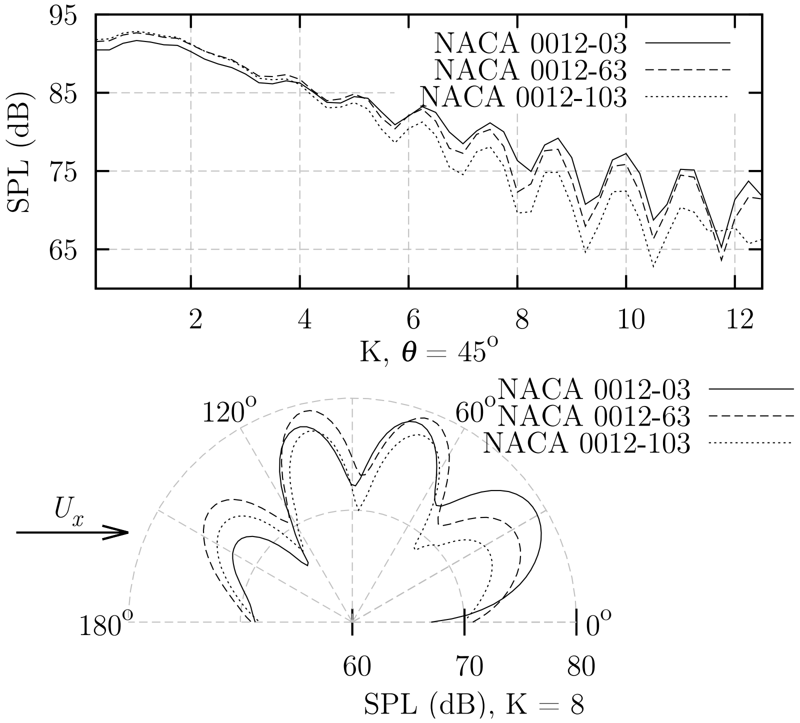

Figure 2.15: Spectral (upper) and directivity (lower) effects of the leading edge radius on noise from 12% thick airfoils. The spectral comparison is made at $\theta = 45°$, and the directivity comparison is made at $K = 8$.

more sensitive to the effects of airfoil thickness than to the effects of leading edge radius.

Figure 2.17 shows the behaviour of the predicted sound power P at a reduced frequency of $K = 8$ with varying $\sqrt{R_{le}/c}$. Each combination of airfoil thickness t and shape parameter I represents a unique value of R_{le}. Each data point in Figure 2.17 therefore represents one of the 24 airfoils shown in Figure 2.5. Figure 2.17 shows that for airfoils with constant thickness, there appears to be a linear relationship between the reduction in P and increasing $\sqrt{R_{le}/c}$ for $\sqrt{R_{le}/c} \leq 0.2$ for this data. Some data points deviate from this apparent linear trend, particularly for airfoils with 6% thickness, but these are likely to be errors resulting from small changes in the computational grids needed to examine each separate airfoil in turn. At sufficiently high values of leading edge radius ($\sqrt{R_{le}/c} > 0.2$) the apparent linear relationship between P and $\sqrt{R_{le}/c}$ breaks down. More extensive simulations are needed to fully

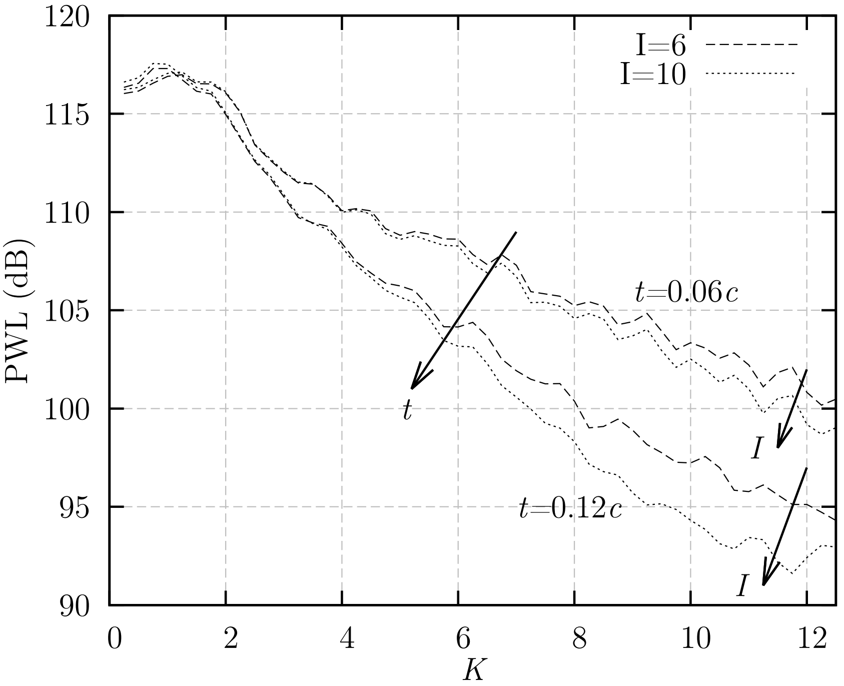

Figure 2.16: Comparison of the PWL behaviour with chord-based reduced frequency, for airfoils with varying thickness and leading edge radius.

identify this limit. Above the limit of $\sqrt{R_{le}/c} = 0.2$, the sound power is increased for 18% and 24% thick airfoils with increasing values of $\sqrt{R_{le}/c}$. However, in most applications of leading edge noise modelling such as turbo-machinery, the thickness is typically below 12% and therefore the leading edge radius of airfoil geometries is below the limit of $\sqrt{R_{le}/c} = 0.2$. Therefore, for most practical applications, an increase in the leading edge radius of an airfoil is expected to reduce leading edge noise.

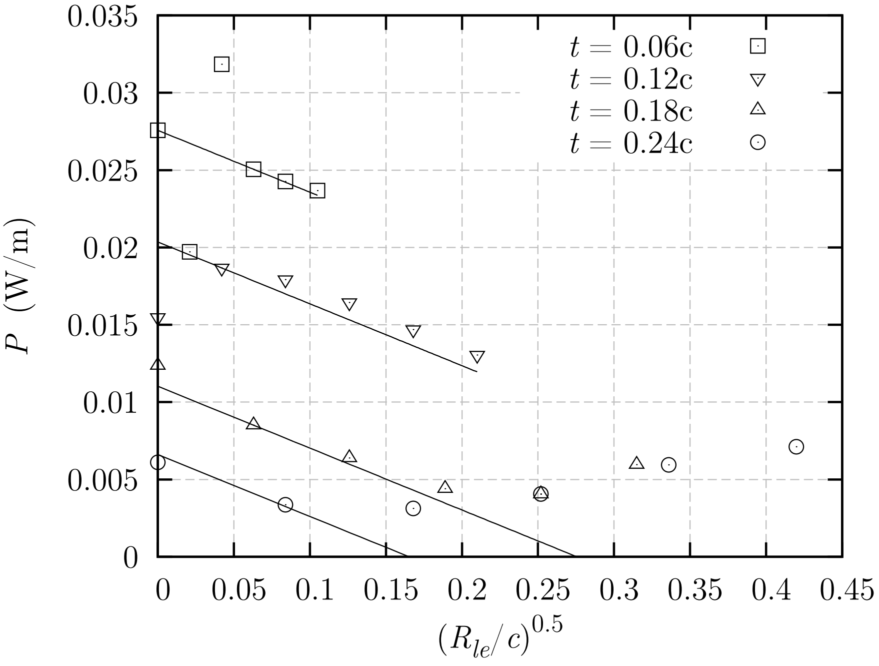

Figure 2.17: The behaviour of sound power P with varying leading edge radius at a reduced frequency of $K = 8$. Solid lines indicate linear lines of best fit.

2.3.5 Mechanism

This section investigates the mechanism underlying noise reductions due to increases in airfoil thickness and leading edge radius. Figure 2.18 shows the root-mean-square pressure p_{rms} along the surface of the front 20% of the airfoil chord, due to gust interactions at a reduced frequency of $K = 8$ with 2%, 6%, and 12% thick airfoils. Here, p_{rms} values have all been normalized on the peak p_{rms} value of the NACA 0002 prediction. Figure 2.18 shows that as airfoil thickness is increased, the leading edge surface p_{rms} response is reduced, and also that the peak value of p_{rms} is moved downstream. This reduction in surface pressure response is the cause of the reduced far-field sound predictions in the CAA model, and agrees with the conclusions of Chiang and Fleeter [93] who used an analytical method to study the effects of thickness on the surface pressure response of an oscillating airfoil. However, the previous literature is not clear why the surface pressure response is reduced for airfoils with real thickness compared to flat plate predictions. The CAA method used here allows this to be investigated by visualising the unsteady flow-field surrounding the airfoil.

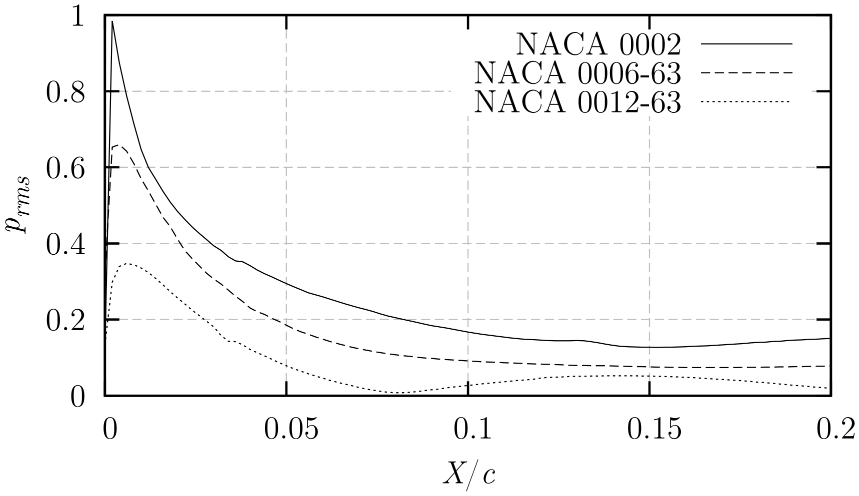

Figure 2.18: Normalized airfoil surface p_{rms} response due to a vortical gust at $K = 8$, for airfoils with $t = 0.02c$, $t = 0.06c$ and $t = 0.12c$.

Figure 2.19 shows a visualization of the instantaneous transverse velocity perturbations v for a high frequency vortical gust with $K = 8$, interacting with 2%, 6% and

12% thick airfoils. In this section v is non-dimensionalized by the speed of sound c_0. Figure 2.19 shows that the gust wavefront is distorted by the real airfoil, and that this distortion increases with airfoil thickness. Distortion of the gust wavefront is caused by the velocity gradients present in the leading edge stagnation region, and is stronger for airfoils with larger thickness because thick airfoils generate a larger stagnation region. Figure 2.19 also shows that v is increased as the flow passes around the airfoil leading edge curvature. This acceleration of the flow is caused by the induced circulation around the airfoil due to the gust. However, there is a smaller increase in v around the leading edge when the gust wavefront has been distorted. Therefore, thick airfoils which cause a larger distortion of the gust wavefront will interact with reduced v values at the leading edge, in comparison to thin airfoils.

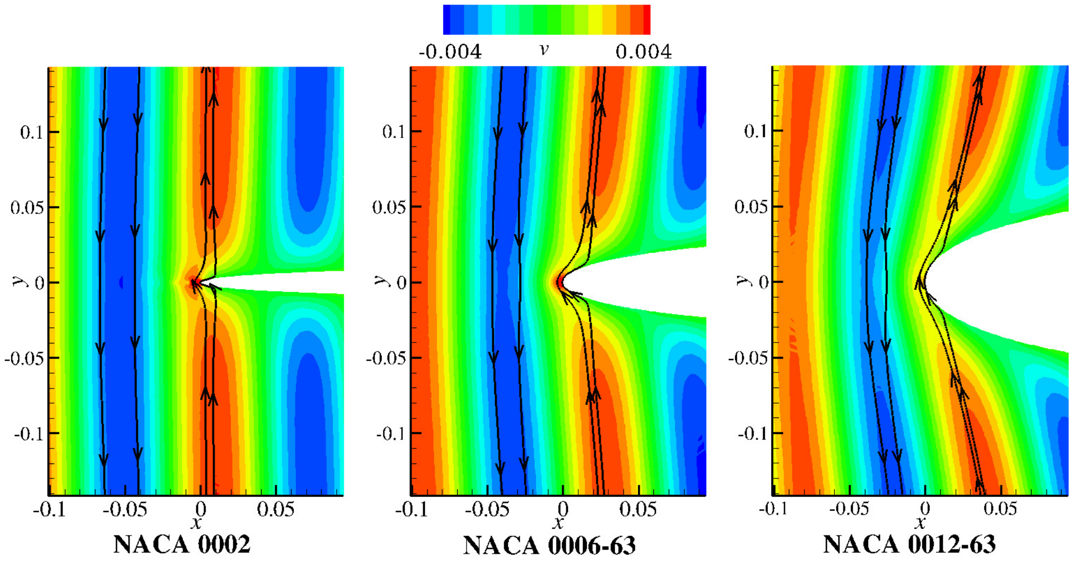

Figure 2.19: Contours of instantaneous transverse velocity perturbations v for a gust at $K = 8$ interacting with 2%, 6% and 12% thick airfoils. The contours are overlaid with lines to show the shape and direction of each gust wavefront.

The acceleration of the gust around the leading edge corresponds to an unsteady loading on the airfoil surface. This unsteady loading causes a pressure response which radiates as noise. Therefore, the reduction in the gust amplitude and the reduced acceleration around the leading edge curvature, is the main mechanism by which the leading edge noise of thick airfoils is reduced at high gust frequencies.

The reduction in transverse perturbation velocity for thick airfoils is shown more clearly in Figure 2.20, which shows contours of time-averaged transverse velocity perturbations v_{rms} over one gust cycle for three airfoil thicknesses. The corresponding p_{rms} contours are also shown in Figure 2.20, in order to demonstrate the link between v_{rmS} and p_{rms} in the gust interaction mechanism.

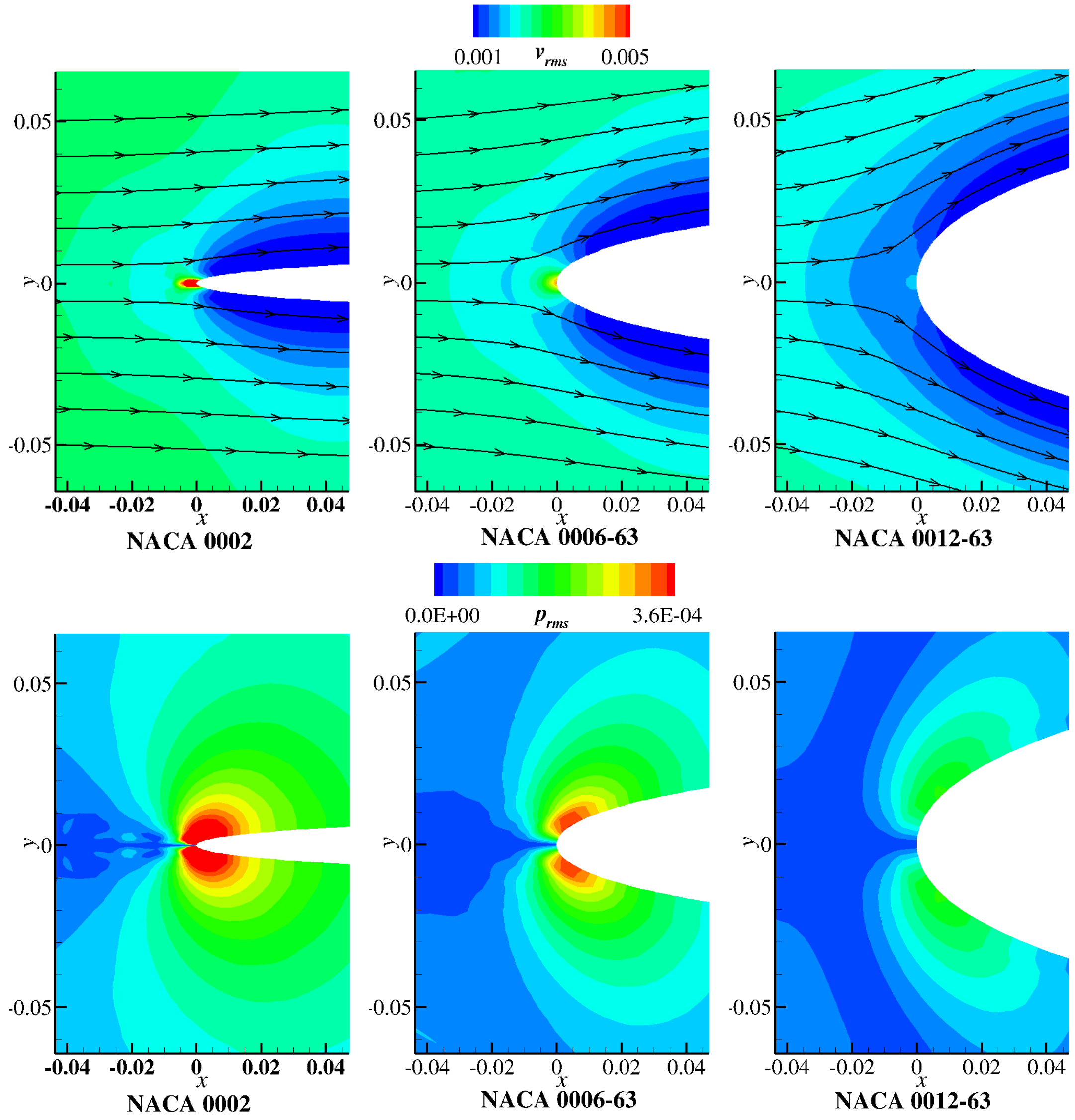

Figure 2.20: Contours of v_{rms} (top) and p_{rms} (bottom) for a gust at $K = 8$ interacting with 2%, 6% and 12% thick airfoils. The v_{rms} contours are overlaid with streamlines of the non-uniform meanflow around each airfoil.

Figure 2.21 shows contours of instantaneous acceleration around the three airfoil leading edges. These values are computed at the same time-step and from the same simulations displayed in Figure 2.19. Contours of du/dt, dv/dt, and dU/dt are shown, where $dU/dt = \sqrt{(du/dt)^2 + (dv/dt)^2}$. It can be seen from Figure 2.21 that streamwise acceleration is increased due to gust interactions with the airfoil, and that this acceleration is strongest for the 2% thick airfoil. The effect of thickness on dv/dt is not as clear in Figure 2.21. However, a region of high acceleration is seen at the leading edge of the 2% thick airfoil, which is not present on the thicker geometries. When the streamwise and transverse accelerations are combined into a single scalar value, dU/dt, it is clear that the gust is accelerated by a greater amount in the presence of a thin airfoil in comparison to a thick one. This agrees with the previous discussion in this section.

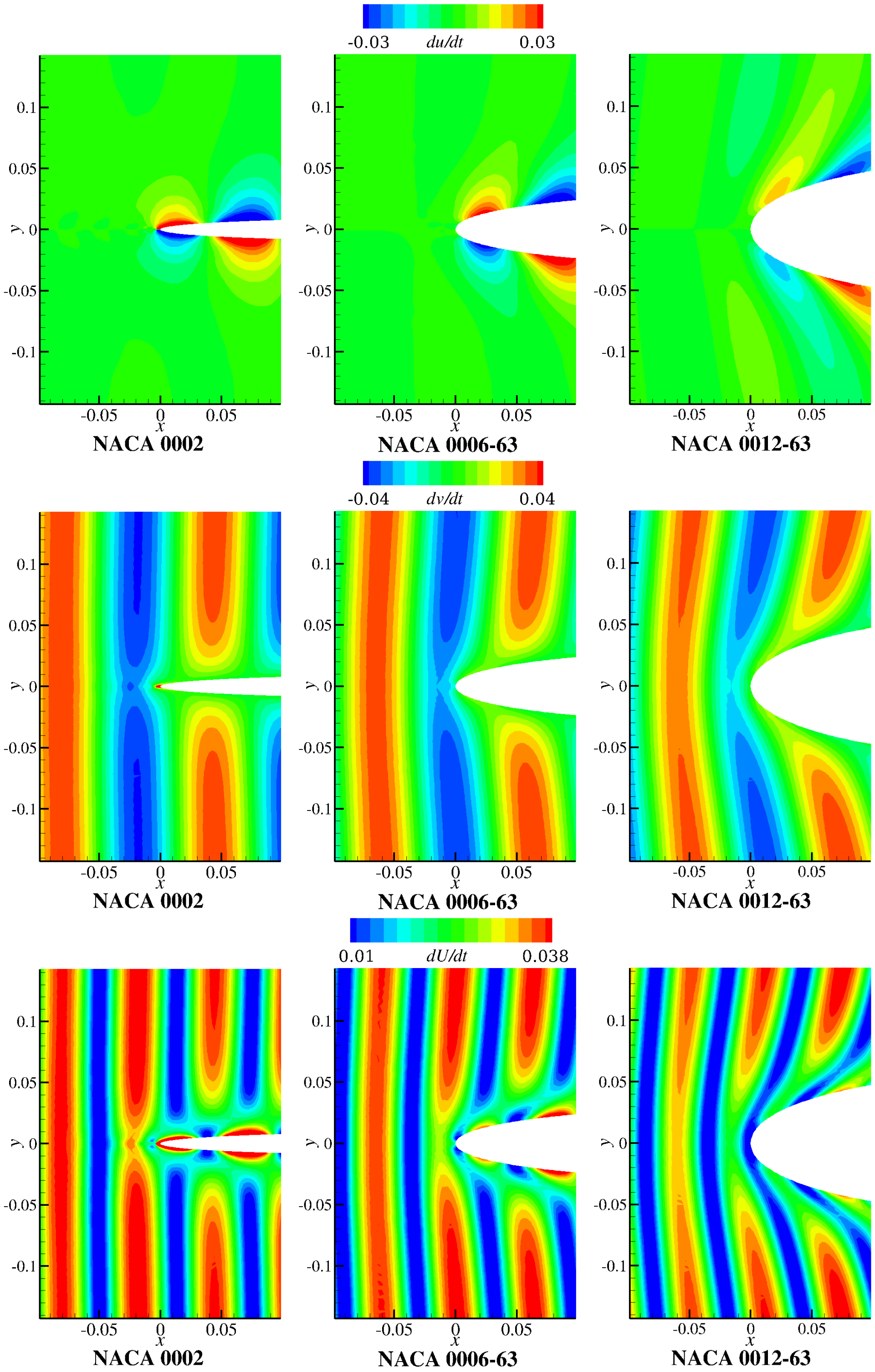

Figure 2.21: Contours of du/dt (top), dv/dt (middle), and dU/dt for a gust at $K = 8$ interacting with 2%, 6% and 12% thick airfoils.

Figure 2.22 shows contours of v for a low frequency vortical gust with $K = 1$, interacting with 2%, 6%, and 12% thick airfoils. Figure 2.22 shows that at low frequencies the airfoil thickness does not affect v. This is because the gust wavelength is large in comparison to the size of the stagnation region, so the gust wavefront is not significantly distorted by the velocity gradients.

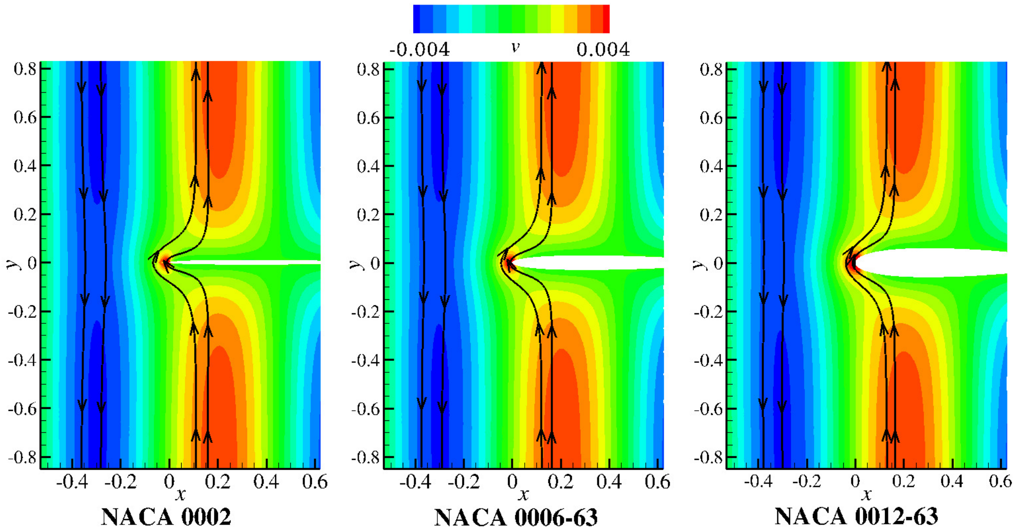

Figure 2.22: Contours of instantaneous transverse velocity perturbations v for a gust at $K = 1$ interacting with 2%, 6% and 12% thick airfoils. Lines are overlaid to show the shape and direction of each gust wavefront.

In Figure 2.23 contours of v_{rms} are shown for a NACA 0012-63 airfoil interacting with a vortical gust at $K = 8$, when a uniform and a non-uniform meanflow is assumed in the CAA method. Figure 2.23 shows that when the meanflow is assumed to be uniform, v_{rms} values at the leading edge are greater in comparison to those modelled with a non-uniform meanflow. There is no stagnation region in a uniform meanflow, so the transverse velocity reduction mechanism discussed above is not included when a uniform meanflow is assumed. This explains the inaccurate noise predictions obtained when modelling leading edge noise of real airfoils interacting with vortical gusts using a uniform meanflow.

The conclusion that the noise is affected by the leading edge stagnation region for real airfoils, implies that separating the effects on noise due to leading edge radius and to thickness is difficult. Both airfoil thickness and leading edge radius can influence

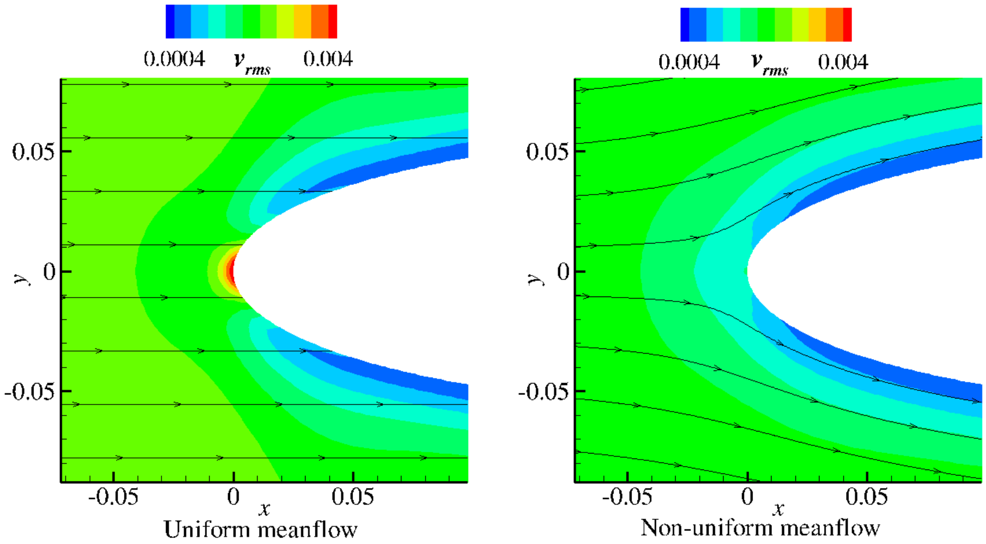

Figure 2.23: Contours of v_{rms} for a gust with $K = 8$ interacting with a NACA 0012-63 airfoil, modelled using a uniform and non-uniform meanflow. Streamlines are plotted to indicate the path of the steady meanflow field.

the size and shape of the stagnation region because they both modify the global shape of the airfoil. Furthermore, although Figures 2.19 to 2.23 indicate that the noise reduction mechanism for thick airfoils appears to be concentrated around the leading edge, the resulting reduction in surface p_{rms} for thick airfoils occurs along the entire airfoil chord. Therefore, it is the whole airfoil shape which affects the noise reduction mechanism, and the whole airfoil shape which experiences a reduced noise response. Representing a real airfoil by a single length-scale parameter, such as airfoil thickness, would ignore important aspects of the gust interaction process and would be likely to produce an incorrect noise prediction.

Distortion of the gust wavefront appears to be a dominant factor in the leading edge gust interaction mechanism. This suggests that the original shape of the gust, before it is deformed, may also have an influence on the noise. This chapter is limited to modelling harmonic gusts which do not vary in the transverse or spanwise directions. Therefore, a more realistic turbulent inflow that contains additional disturbances in the streamwise and spanwise directions may be deformed differently by the leading edge stagnation region. The effects on predictions due to including a more complex inflow disturbance are addressed in Chapters 3 and 4.

2.4 Summary

A CAA method has been applied to the modelling of leading edge noise due to harmonic vortical gusts interacting with various symmetric airfoil geometries at zero AoA. The effects of thickness and leading edge radius on the noise have been investigated, and the validity of flat plate analytical models has been assessed. Because the vortical disturbances have been modelled with zero transverse wavenumber, the analysis holds only for the interaction of an airfoil with parallel supercritical gusts. The key findings of this chapter are:

- The effect of increasing airfoil thickness is to reduce the leading edge noise in comparison to flat plate predictions, for reduced frequencies above about $K = 1$ at $M = 0.2$. The noise is reduced in the downstream observer direction more than it is reduced in the upstream observer direction. The noise reduction effect becomes stronger with increasing frequency and with increasing thickness.

- The threshold reduced frequency at which leading edge noise becomes sensitive to airfoil geometry appears to have some dependence on Mach number. At $M = 0.2$ the threshold is at about $K = 1$ whereas at $M = 0.6$ the threshold is at a higher reduced frequency of about $K = 4$.

- The effect of increasing the leading edge radius is to reduce the noise at downstream observers and to increase the noise at upstream observers, in comparison to analytical flat plate predictions. Leading edge noise becomes sensitive to leading edge radius changes for reduced frequencies above $K = 4$. However, leading edge noise is less sensitive to leading edge radius than it is to airfoil thickness.

- Increasing the airfoil thickness t causes a roughly linear decrease in the sound power due to leading edge noise at high frequencies. Additionally, increasing the square root of the leading edge radius up to $\sqrt{R_{le}/c} = 0.2$ also causes an approximately linear decrease in the sound power. The limit of $\sqrt{R_{le}/c} = 0.2$ is sufficiently high to contain most airfoil geometries which experience significant leading edge noise.

- The effects of airfoil geometry on leading edge noise are noticeable even for 2% thick airfoils, such that analytical flat plate predictions will over-predict the noise from a NACA 0002 airfoil by approximately 3 dB at high frequencies in $M = 0.2$ flow. For a NACA 0012-63 airfoil this over-prediction can be up to 18 dB, at $K = 12$ and $M = 0.6$. The accuracy of flat plate analytical predictions of leading edge noise can be expected to decrease with increasing airfoil thickness, gust frequency and Mach number.
- The dominant mechanism that causes the discussed effects on noise, is related to the leading edge stagnation region. Vortical gusts are distorted by the velocity gradients in the stagnation region such that the wavefront of the gust across the leading edge is smoothed and the gust amplitude is reduced. Because the dominant noise reduction mechanism is associated with the meanflow, it is not valid to make an assumption of uniform meanflow when modelling the leading edge noise of airfoils with real geometry. However, an inviscid meanflow can be assumed in most cases without loss of prediction accuracy.
- The effects on noise due to airfoil thickness and leading edge radius are linked, because both length-scales affect the overall airfoil shape which in turn affects the shape and size of the leading edge stagnation region. Rather than represent a real airfoil by a single length-scale parameter, such as airfoil thickness, the overall shape of the airfoil should be considered when modelling leading edge noise.

Although this chapter is considered a preliminary study, and does not consider turbulent interactions, some conclusions can be drawn with regards to the accuracy of using a flat plate models when predicting CROR BRWI noise. It appears that flat plate methods will over-predict the noise at high reduced frequencies, even for thin airfoils. Therefore, it is likely that BRWI predictions made with flat plate theory will be too loud at high frequencies.

A limitation of the work described in this chapter is that it only considers sinusoidal transverse gusts at zero AoA. Extension of the CAA method to enable the modelling of leading edge noise via synthesis of 2D turbulence is the subject of Chapter 3. The limitation of zero AoA is addressed in Chapter 5.

Chapter 3

CAA Analysis using Synthesised Turbulence

Chapter 2 studied the interactions between an airfoil and harmonic gusts at zero AoA. The work described in this chapter extends the CAA modelling approach to consider a synthesised 2D turbulent vortical field, which contains streamwise and transverse disturbances. This type of synthesised turbulence is referred to as a two-component forcing approach in this work, because the disturbance spatially varies with the streamwise and transverse wavenumber components, k_x and k_y, respectively. The two-component forcing approach is used in order to increase the realism of the noise simulations and to gain a better understanding of the limitations of harmonic gust modelling when studying turbulence interaction noise. In this chapter, airfoil geometries and flow conditions are chosen which are more representative of CROR blades than those used in Chapter 2.

The primary difference introduced by using a synthesised two-component forcing approach, as opposed to using harmonic gusts, is the inclusion of streamwise disturbances. Analytical models, such as Amiet's flat plate theory, do not consider the effect of streamwise vortical disturbances because a flat plate at zero AoA has no physical presence in this plane. However, when a real airfoil geometry is considered, the addition of streamwise disturbances may have an effect on the noise.

The choice of turbulence synthesis method is discussed in Section 3.1. The revised computational method, and the results of the study, are presented in Sections 3.2 and 3.5 respectively.

3.1 Synthesising a Turbulent Inflow

The most accurate method to model a turbulent inflow for the study of airfoil turbulence interaction noise would be to fully simulate a time varying disturbance using a DNS or LES method. For example, to model the BRWI noise experienced in CROR engines, a DNS simulation of the wake produced by a front rotor blade could be performed. However, this method is usually too computationally expensive to be practical, although it should be noted that studies of turbulence interaction noise have been made by Christophe *et al.* [83] and Deniau *et al.* [84] using LES methods.

To reduce the computational expense, this study focuses on synthesising an appropriate turbulent inflow using a stochastic method. While stochastic methods do not provide exact solutions of the Navier-Stokes equations, they can simulate the key features of turbulence, such as length- and time-scales, and energy distributions, at reduced computational cost.

There are three main approaches which have been used by previous authors to synthesise turbulence. These approaches consist of the summation of a series of discrete Fourier modes, the digital filtering of white noise, or the superposition of vortical eddies. The relative merits and limitations of these approaches will now be discussed.

3.1.1 Fourier Mode Summation

The generation of synthetic turbulence via the incoherent summation of a finite number of Fourier modes was first introduced by Kraichnan [104]. This method expresses the velocity field as a summation of harmonic, discrete frequency disturbances, and generates a 2D or 3D velocity field that is divergence-free, homogeneous, statistically stationary, and isotropic. The amplitude of the disturbances is chosen to follow an energy spectrum which Kraichnan prescribed as either a Gaussian spectrum (centred at a given wavenumber) or a single wavenumber component via the use of a Dirac delta function.

Kraichnan's method was later modified by other authors to create the family of stochastic noise generation and radiation (SNGR) methods. Bechara *et al.* [105] adapted Kraichnan's method to use the von Kármán turbulent energy spectrum when setting the amplitude of each frequency disturbance. They also proposed to obtain time decorrelated simulations by performing a number of independent realisations of the turbulent field. Bailly and Juvé [106] extended the method to include convection effects and time dependence via a change of reference frame. Billson *et al.* [107] incorporated time correlation and anisotropy in the turbulent velocity field.

Turbulence synthesis via Fourier mode summation has been used in a number of applications by previous authors. Bailly and Juvé [106], and Billson *et al.* [107] applied this type of turbulence synthesis to the study of jet noise. Reboul and Polacsek [108] used a similar method to model the propagation of broadband noise through, and radiated from, a turbofan bypass duct. Clair *et al.* [109] also synthesised turbulence with only transverse disturbances when studying the effect of leading edge serrations on airfoil turbulence interaction noise.

Turbulence synthesis methods based on Fourier mode summation are generally less complicated to implement than digital filter methods when generating simple flow fields such as homogeneous, isotropic turbulence. For the present study, they also have the advantage of being conceptually similar to the harmonic gust method that was introduced in Chapter 2. However, Fourier mode methods have difficulties representing more complex features of turbulence such as inhomogeneity, and are regarded as being computationally expensive in comparison to digital filter methods if a large number of modes and random numbers is required.

3.1.2 Filtering White Noise

The synthesis of turbulence via the digital filtering of white noise was proposed by Klein *et al.* [110], who showed that the method could accurately reproduce turbulence statistics, including autocorrelation functions. However, the method of Klein *et al.* [110] was only used to consider a Gaussian energy distribution, and did not produce an input that was divergence-free. Divergence-free turbulence is often required for CAA simulations to prevent the turbulence from interfering with the acoustic responses.

Careta *et al.* [111] presented a digital filter method to provide a divergence free input by expressing the velocity field in terms of the streamfunction. Ewert and Edmunds [112] also described what is known as the random particle mesh (RPM) method, which builds upon the work of Careta *et al.* [111] and Klein *et al.* [110] in order to provide a low-cost stochastic approach to allow CAA modelling of airfoil slat noise. The RPM method has been successfully used, particularly by Ewert *et al.* to study situations such as airfoil slat noise and airfoil trailing edge noise [113–115]. Dieste [116] developed a digital filtering model which considered more realistic energy spectra such as the Liepmann or von Kármán spectra, and applied this to the modelling of broadband fan/OGV interaction noise.

3.1.3 Superposition of Eddies

Jarrin *et al.* [117,118] proposed an inflow boundary condition known as the synthetic eddy method (SEM), which is based on the idea that turbulence can be represented as a superposition of eddies of varying size and strength. The SEM generates a superposition of vortical eddies that match prescribed time and length-scales. The characteristics of the eddies are calculated from statistical quantities, often obtained with a RANS solution. The SEM was used by Jarrin *et al.* as part of hybrid RANS-LES simulations to study channel and duct flows [119].

Some extensions to the SEM have been proposed by other authors. Pamiès *et al.* [120] found improvements over the original SEM by providing better definitions for the shape and characteristics of the eddies. Poletto *et al.* [121] proposed an extension to the SEM in order to provide a divergence-free turbulence inflow. The motivation of Poletto *et al.* was to reduce the development length of the synthesised turbulence. However, divergence-free turbulence is also useful in aeroacoustic applications to prevent the injected disturbances from interfering with other acoustic sources in the simulation. Haeri *et al.* [82] recently used a modified synthetic eddy method in an Euler simulation to generate a 3D turbulent inflow in order to study the effects of wavy leading edges on airfoils.

The primary advantage of digital filter methods and SEM when compared with Fourier based methods is that they can more easily represent complex turbulent flows. Inhomogeneous, anisotropic, and non-stationary flows can be considered without significant modifications to the methods being used. Additionally, continuous frequency spectra can be modelled by digital filter methods and SEM, whereas only discrete frequencies can be considered when using Fourier based methods.

3.2 Computational Method

The CAA method described in Chapter 2 was extended to synthesise a turbulent input. The turbulence synthesis method was adapted to use a finite summation of discrete Fourier modes, in a method similar to that used by Bechara *et al.* [105]. Time-decorrelation was obtained by the use of an ensemble average of pressure field results over multiple realisations of a single case. Other authors, such as Reboul and Polacsek [108], have used similar methods for CAA applications. This relatively simple turbulence synthesis method was chosen instead of a digital filter method because only a simple representation of turbulence was required in the study, and because it is conceptually similar to the harmonic gust study performed in Chapter 2. If future studies require a more complex broadband input, then a different turbulence synthesis method could be adopted.

The implementation of the turbulence synthesis method will now be described. Two-component vortical disturbances, $\boldsymbol{u}_{2C} = (u, v, w = 0)$, containing disturbances that are normal to the freestream and in the freestream direction, were defined to be of the form of a summation of discrete frequency gusts, and can be expressed as

$$\boldsymbol{u}_{2C}(\boldsymbol{x},T) = \sum_{l=1}^{L} \sum_{m=-M}^{M} W_{2C}(\boldsymbol{k}_{l,m}) \cos\Big(\boldsymbol{k}_{l,m} \cdot (\boldsymbol{x} - \boldsymbol{U}T) + \sigma_{l,m}\Big)\boldsymbol{\zeta}(\boldsymbol{k}_{l,m}) \tag{3.1}$$

where l and m are the summation modes which vary between limits L and M respectively, $\boldsymbol{k}_{l,m}$ and $\boldsymbol{\zeta}$ are the wave vector and direction of each combination of l and m modes, $\sigma_{l,m}$ is a randomly generated phase term that varies between 0 and 2π, and $W_{2C}(\boldsymbol{k}_{l,m})$ is the turbulence velocity spectrum. Each mode is assigned a randomly generated σ value that is unique to each realisation. To ensure a divergence free flow, $\boldsymbol{\zeta}$ was defined such that $\boldsymbol{k}_{l,m} \cdot \boldsymbol{\zeta}(\boldsymbol{k}_{l,m}) = 0$. This process is explained in Appendix A. When sufficient realisations are used, Equation 3.1 provides a divergence-free, homogeneous, isotropic input which contains multiple disturbance modes whose amplitudes follow a specified turbulence spectrum. Here, the Liepmann spectrum is chosen, and is defined as

$$W_{2C}(k_x, k_y, k_z = 0) = \sqrt{\frac{\Delta k_y}{4\pi k^2} \frac{8}{\pi} \overline{w^2} \Lambda \frac{(\Lambda k)^4}{(1 + \Lambda^2 k^2)^3}} \tag{3.2}$$

where $\overline{w^2}$ is the mean-squared turbulent velocity fluctuation, Λ is the turbulence integral lengthscale, Δk_y is the size of the step between k_y values, and $k = \sqrt{k_x^2 + k_y^2}$. Equation 3.2 uses $k_z = 0$, in order to consider only gusts with zero spanwise wavenumber. The behaviour of W_{2C} is shown in Figure 3.1. In this example, $\overline{w^2} = 7.67$ m^2.s^{-2}, and $\Lambda = 0.07$ m. Additional description and derivation of Equation 3.2 is given in Appendix B.

One key feature that is shown in Figure 3.1 is that the width of $W_{2C}(k_x, k_y)$ with k_y changes between low and high k_x values. At $k_x = 0.5\pi$ the majority of the energy is contained between $k_y = \pm 50$, whereas at $k_x = 25\pi$ the energy is distributed between $k_y = \pm 150$. This feature of the spectrum has implications for the discretisation of the computational turbulence synthesis method, which is discussed in Section 3.2.1.

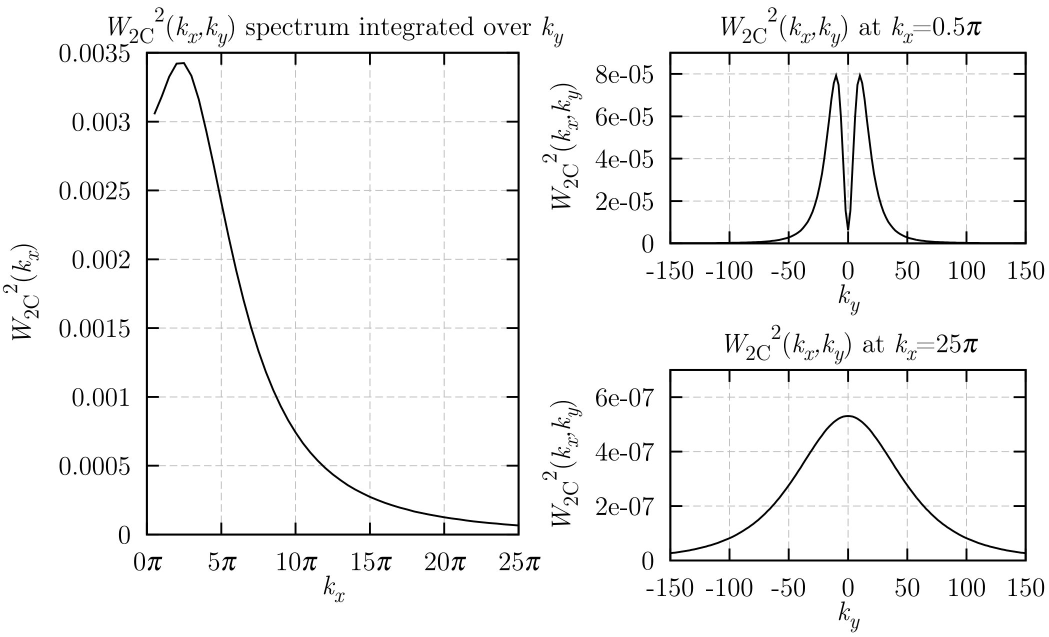

Figure 3.1: Showing the Liepmann spectrum defined by $W_{2C}(k_x, k_y)$ with varying k_x and k_y. Left shows the spectrum with varying k_x after integration over k_y. Right shows the spectrum with varying k_y at $k_x = 0.5\pi$ and 25π.

3.2.1 Discretising the Energy Spectrum

Because the computational method uses a discrete number of frequency modes when synthesising the vortical turbulent input, the continuous spectrum shown in Figure 3.1 must be appropriately discretised. Therefore, the summation limits L and M must be chosen such that the highest k_x and k_y values, k_x^{lim} and k_y^{lim}, can still be resolved by the computational grid.

Firstly, the frequency limits k_x^{lim} and k_y^{lim} must be decided. The value of k_x^{lim} represents the upper limit of streamwise frequencies in the simulation and is chosen to be the same value as was used in Chapter 2, $k_x^{lim} = 25\pi$ m^{-1}, such that the maximum chord-based reduced frequency $K = c/\lambda = 12.5$. The airfoil chord remains as $c = 1$ m in this study. To resolve the spectral shape, 100 equally spaced discrete values of k_x were used between the limits of 0 and k_x^{lim}.

The choice of k_y^{lim} value is not as straightforward as the choice of k_x^{lim}. Disturbances with differing k_y values represent swept gusts whose wavefront is not normal to the freestream direction. A turbulent flow contains disturbances at all k_y values, and so an ideal turbulence synthesis method would include all k_y wavenumbers between $k_y = \pm\infty$. However, in the CAA method used here, the frequency content of the synthesised disturbance is limited by the computational grid density. Therefore, the range of transverse gust frequencies must be truncated to $\pm k_y^{lim}$. The larger the value of k_y^{lim}, the more energy will be contained in the turbulent flow and the greater the realism of the simulation. However, large values of k_y^{lim} also require greater computational expense. Therefore, a compromise must be made.

In order to choose an appropriate value of k_y^{lim} the spectrum given in Equation 3.2 was integrated over different k_y ranges to give $W_{2C}(k_x)$, so that the convergence of the spectrum could be observed. This is shown in Figure 3.2.

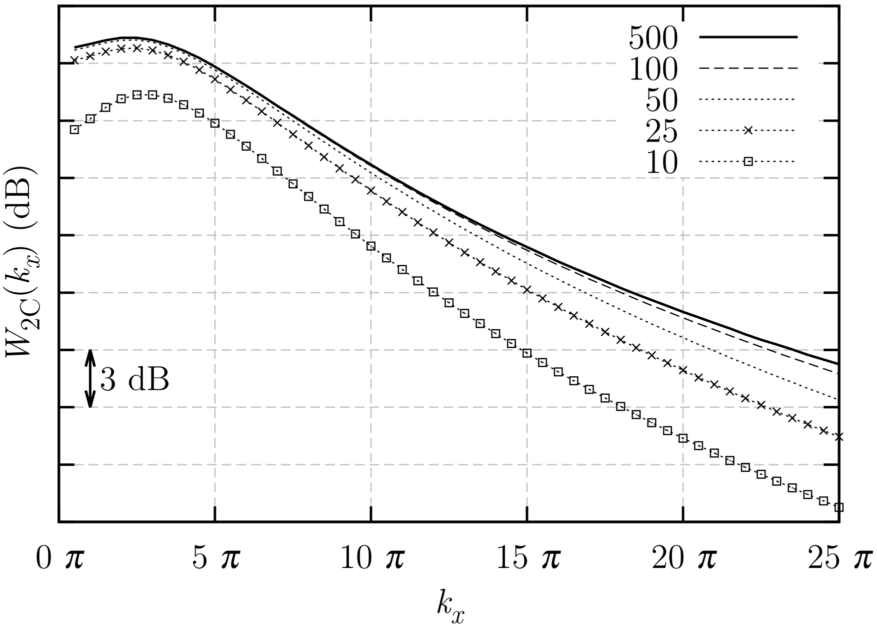

Figure 3.2: Convergence of $W_{2C}(k_x)$ at various reduced frequencies with increasing k_y^{lim} values. $W_{2C}(k_x, k_y)$ was integrated using k_y^{lim} = 10, 25, 50, 100, and 500 m^{-1}.

Figure 3.2 shows that the total energy contained in the spectrum increases as the k_y^{lim} range is increased. It is clear that the curve converges with large values of k_y^{lim} such that above $k_y^{lim} = 100$ m^{-1} there is relatively little energy added to the spectrum. When using $k_y^{lim} = 100$ m^{-1}, the convergence is very close at low k_x values, but a small amount of the turbulent energy is missed at $k_x = 25\pi$ m^{-1}. This agrees with Figure 3.1, which shows that at $k_x = 25\pi$ there is still some turbulent energy in the region outside the $k_y^{lim} = \pm 100$ m^{-1} range. At $k_x = 25\pi$ m^{-1} approximately 90% of the total energy is captured. This value increases for $k_x < 25\pi$. For the remainder of this study, The value of $k_y^{lim} = 100$ m^{-1} was chosen as a compromise to provide sufficiently cheap simulation costs while representing as much of the energy in the turbulence spectrum as possible.

Finally, the distribution of the discrete frequencies in the k_y direction must be chosen. Because the width of the spectrum in the k_y direction changes with increasing k_x, a discrete number of frequencies must be chosen that can accurately represent the spectrum shape at both low and high k_x frequencies. To achieve this, a fixed distribution of k_y was chosen that placed a greater density of modes around $k_y = 0$ than at high k_y values. This ensured that the narrow peak shown in Figure 3.1 for the $k_x = 0.5\pi$ m^{-1} case was adequately resolved. A total of 47 discrete frequencies were used in the k_y direction. The discretisation of Equation 3.2 is shown in Figure 3.3. This distribution is in contrast with Kraichnan [104], who used a stochastic distribution, but is more similar to Bailly and Juvé [106], and Bechara *et al.* [105] who used fixed-uniform and fixed-logarithmic distributions respectively.

An example of the turbulent vortical flow-field generated by the CAA method is shown in Figure 3.4 for one realisation, alongside the resulting pressure response from a NACA 0002 airfoil. For this example, $M = 0.5$, $\Lambda = 0.07$ m and $\sqrt{\overline{w^2}} = 0.04U_x$ ms^{-1}.

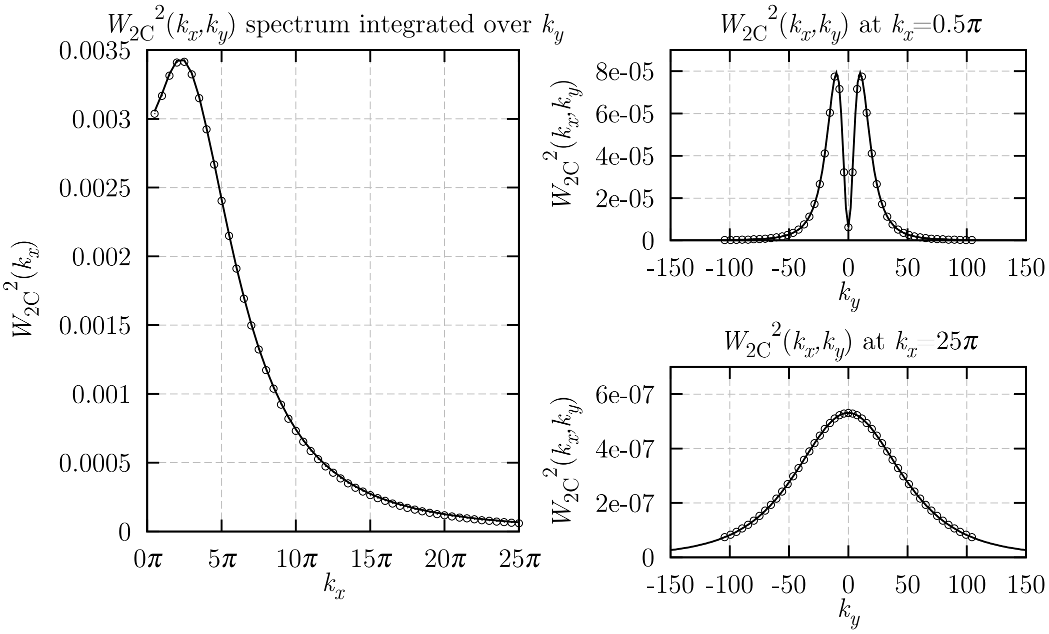

Figure 3.3: Showing the discretised $W_{2C}(k_x, k_y)$ spectrum with varying k_x and k_y.

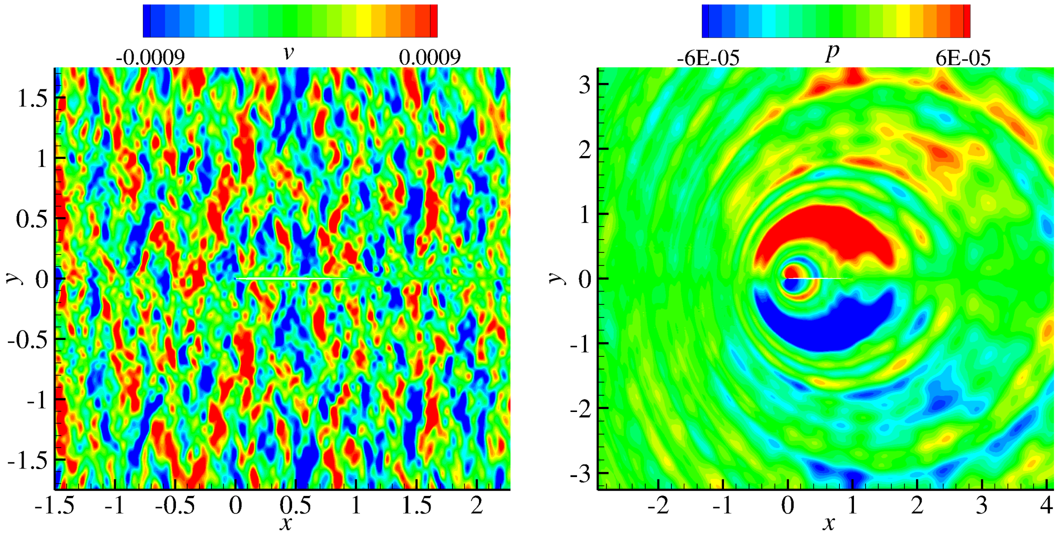

Figure 3.4: Example of the flow-field perturbations of transverse velocity v (left) and pressure p, during one realisation of the CAA method at $M = 0.5$. Quantities are non-dimensional.

3.3 Analytical Method

In order to validate the new CAA method with turbulence synthesis and to allow comparisons of the noise from real airfoils with the noise from a flat plate, Amiet's [30] flat plate analytical method was re-derived to include a turbulence spectrum as opposed to the constant amplitude gusts that were used in Chapter 2. The derivation of the analytical method is now outlined. This re-derivation is similarly described by Amiet [30] and also by Blandeau [14]. Symbols have the same meanings as in Section 2.1.

As was done in Chapter 2, the homogeneous and isotropic turbulent velocity field is assumed to have a frozen pattern as it passes the leading edge of the flat plate. The upwash turbulent velocity can be expressed as

$$v(X,T) = \frac{1}{2\pi}\int\limits_{-\infty}^{\infty} \hat{v}(k_X)e^{-ik_X(X-U_XT)}dk_X, \tag{3.3}$$

where $\hat{v}(k_X)$ is the gust upwash velocity in the frequency domain, defined as

$$\hat{v}(k_X) = \int\limits_{-\infty}^{\infty} v(X,T)e^{ik_XX}dX. \tag{3.4}$$

For a single frequency vortical gust with upwash velocity of the form $v_0e^{-ik_X(X-U_XT)}$, the pressure jump Δp can be written in the time domain as

$$\Delta p(X,T) = 2\pi\rho_0U_Xv_0g^{LE}(X,k_X,M_X)e^{ik_XU_XT}. \tag{3.5}$$

When multiple gusts are considered in a turbulent inflow, Equations 3.3 and 3.5 can be combined to give

$$\Delta p(X,T) = \rho_0U_X\int\limits_{-\infty}^{\infty} \hat{v}(k_X)g^{LE}(X,k_X,M_X)e^{ik_XU_XT}dk_X, \tag{3.6}$$

which can also be written in the frequency domain as

$$\Delta\hat{p}(X,\omega) = 2\pi\rho_0\hat{v}(K_X)g^{LE}(X,k_X,M_X). \tag{3.7}$$

where $K_X = \omega/U_X$. The Kirchoff-Helmholtz integral theorem can be used to give the radiated acoustic pressure due to the unsteady jump as

$$p(x,y,T) = \frac{-1}{2\pi}\int\limits_{-\infty}^{\infty}\int\limits_{-b}^{b}\Delta\hat{p}(X,\omega)\frac{\partial G}{\partial y}(x,y,X,\omega)e^{i\omega T}dXd\omega. \tag{3.8}$$

where $G(x,y,X,\omega)$ is the two-dimensional time harmonic Green's function. As was shown in Section 2.1, $\frac{\partial G}{\partial y}$ is given by

$$\frac{\partial G}{\partial y}(x,y,X,\omega) \approx \frac{iy}{4}\sqrt{\frac{2k_0}{\pi\sigma^3}}e^{i\frac{k_0}{\beta_X^2}[\sigma - Xx/\sigma - M_X(x-X)]+i\frac{3\pi}{4}}, \tag{3.9}$$

where $\sigma = \sqrt{x^2+\beta_X^2y^2}$.

Because turbulence is a random quantity, it is necessary to work with statistical quantities such as the power spectral density (PSD). The PSD of the acoustic pressure is defined by

$$S_{pp}(x,y,\omega) = \int\limits_{-\infty}^{\infty}\langle p^*(x,y,T)p(x,y,T+\tau)\rangle e^{-i\omega T}, \tag{3.10}$$

where the brackets $\langle\ \rangle$ represent the ensemble average. Substituting Equation 3.8 into Equation 3.10 gives

$$S_{pp}(x,y,\omega) = \frac{1}{2\pi}\iint\limits_{-\infty}^{\infty}\iint\limits_{-b}^{b} S_{QQ}(X_1,X_2,\omega_1,\omega_2)e^{i(\omega_1-\omega_2)t}\delta(\omega_1-\omega_2)$$
$$\times \frac{\partial G^*}{\partial y}(x,y,X_1,\omega_1)\frac{\partial G}{\partial y}(x,y,X_2,\omega_2)dX_1dX_2d\omega_1d\omega_2, \quad (3.11)$$

where $S_{QQ}(X_1,X_2,\omega_1,\omega_2)$ is the cross-spectrum of the unsteady pressure jump between points X_1 and X_2 on the chord of the flat plate at frequencies ω_1 and ω_2. S_{QQ} is written as

$$S_{QQ}(X_1,X_2,\omega_1,\omega_2) = (2\pi\rho_0)^2U_X$$
$$\times g^{LE*}(X_1,k_{X1},M)g^{LE}(X_2,k_{X2},M)\langle\hat{v}^*(K_{X1})\hat{v}(K_{X2})\rangle. \quad (3.12)$$

By assuming homogeneous turbulence, recognising the statistical orthoganality of the wavevectors, and by using Equation 3.4, the turbulence cross-spectrum can be written as

$$\langle\hat{v}^*(K_{X1})\hat{v}(K_{X2})\rangle = 2\pi\delta(k_{X1}-k_{X2})\Phi_{vv}(k_{X2}), \quad (3.13)$$

where $\Phi_{vv}(k_X)$ is the one-dimensional turbulence upwash velocity spectrum. To obtain this, the two-dimensional Liepmann spectrum (given in Ref. [122]) can be integrated with respect to k_y. However, in order to provide a better comparison with the computational method, the integration is not performed between $\pm\infty$. Instead the truncated range is chosen so that

$$\Phi_{vv}(k_x) = \frac{3\overline{w^2}\Lambda^2}{4\pi}\int\limits_{-k_y^{lim}}^{k_y^{lim}} \frac{\Lambda^2(k_x^2+k_y^2)}{\left(1+\Lambda^2(k_x^2+k_y^2)\right)^{2.5}}dk_y. \quad (3.14)$$

The final expression for the PSD of the acoustic pressure radiated to the far-field is obtained by combining Equations 3.9, 3.11, 3.12, and 3.13, and is given by

$$S_{pp}(r_0, \theta, \omega) = \frac{\pi k_0 U_X (\rho_0 b \sin\theta)^2}{2 r_0 A(\theta, M)^3} \Phi_{vv}(K_X) |L^{LE}(\theta, k_X)|^2 \qquad (3.15)$$

where $|L^{LE}(\theta, k_X)|$ is given by Equation 2.8b.

3.4 Airfoil Geometry Definition

As was done in the harmonic gust study discussed in Chapter 2, a range of airfoils was defined for use with the CAA method. Because the computational method is more expensive when synthesising turbulence in comparison to using single frequency harmonic gusts, a smaller number of airfoils was used. NACA 4-series airfoils were chosen with thicknesses which vary between 2% and 12% of the airfoil chord. This smaller range of airfoil thicknesses was chosen to more closely represent the airfoil profiles which are used in CROR engine designs. Only variations in airfoil thickness are explored in this chapter, because leading edge noise was shown in Chapter 2 to be most sensitive to thickness for symmetric airfoils at zero AoA. The airfoils that were used are shown in Figure 3.5. Some additional details on the simulations in this chapter are given in Appendix C.

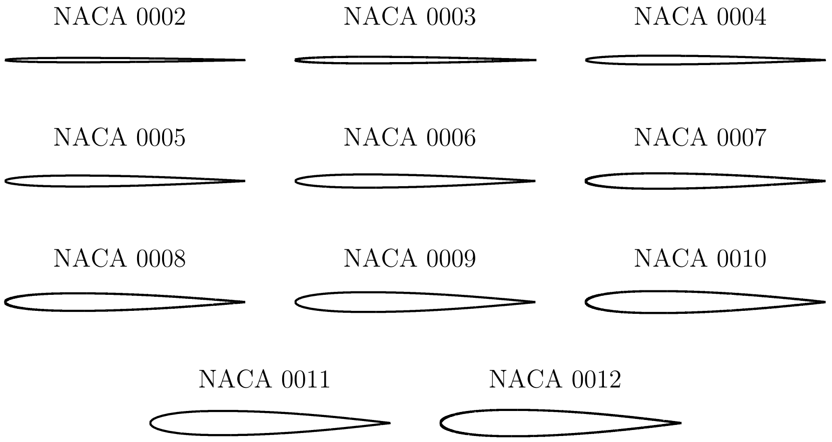

Figure 3.5: The various airfoils used in the study. The maximum thickness of NACA 4-series airfoils was varied between 2% and 12%.

3.5 Results

3.5.1 Comparison of the CAA Method with Analytical Theory

In order to validate the CAA method when synthesising turbulence, noise predictions for a thin NACA 0002 airfoil encountering upstream turbulence were compared with predictions made using Amiet's analytical flat plate theory. The turbulent inflow was defined to have $\sqrt{\overline{w^2}} = 0.04U_x$ and $\Lambda = 0.07$ m, which are comparable turbulence parameters to those used by Amiet [30]. These parameters are used in the majority of studies performed in this chapter. The validation was made at $M = 0.5$.

Before a comparison could be made, it was necessary to decide one final aspect of the computational method. The turbulence synthesis method used in this study does not provide a time-decorrelated solution. The disturbance will be periodic about the lowest k_x disturbance frequency. Therefore, a number of separate realisations of each simulation must be made, where each realisation uses a different set of random numbers σ to set the phase of the modes. Each realisation then produces a far-field pressure value $p_j(r_0, \theta, K)$, and the final incoherent result is found by an ensemble average across all separate realisations. The averaged result is found from

$$p(r_0, \theta, K) = \sqrt{\frac{1}{N_r} \sum_{j=1}^{N_r} |p_j(r_0, \theta, K)|^2} \tag{3.16}$$

where N_r is the total number of realisations, and j is the realisation number. As the number of separate realisations increases, the statistical error due to the random phases in each gust mode is reduced. Therefore, an effective number of required simulation realisations must be chosen to provide an acceptable error level without excessive computational cost. In order to decide on an appropriate value of N_r, noise predictions were made for the validation case using the analytical method and also using the computational method with increasing values of N_r. Then, the convergence of the computational result was investigated. The statistical error between the analytical and computational methods was calculated and plotted against increasing realisation number. The error $\epsilon(K)$ was calculated as

$$\epsilon(K) = \frac{P_{caa}(K) - P_{an}(K)}{P_{an}(K)} \times 100 \tag{3.17}$$

where $P_{caa}(K)$ and $P_{an}(K)$ are the 2D sound power per unit span [14] for the computational and analytical approaches respectively. Figure 3.6 shows the variation of the error ϵ with increasing realisations. Previous authors using similar methods, such as Reboul and Polaksec [108], have found the error to reduce equally at all frequencies. This was also found in the current work, and so Figure 3.6 shows the averaged error over all tested frequencies.

Figure 3.6 shows that the error between the analytical and computational approaches for the validation case reduces with increasing N_r. For $N < 20$, the error reduces proportionally to $\propto 1/\sqrt{N_r}$ which agrees with Reboul and Polaksec [108]. Above this value, increases in N_r do not provide further significant error loss, and the error remains at approximately 11%. This suggests that above $N_r = 20$, the error in the computational simulations is dominated by factors that are not related to the statistical turbulence generation process. The possible sources of error in the CAA

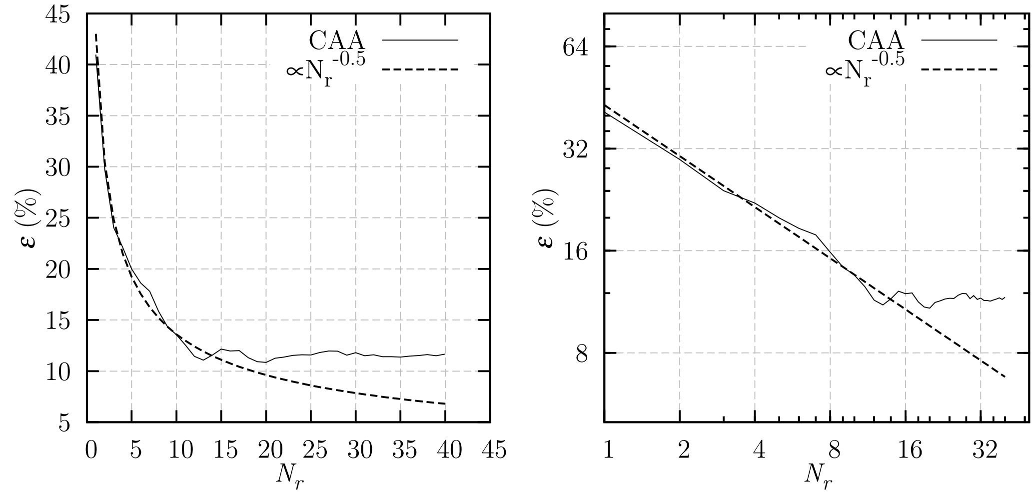

Figure 3.6: Stochastic error between analytical and computational methods for increasing realisation number N_r, shown on linear (left) and logarithmic (right) axes. The error ϵ has been averaged across all tested frequencies.

method were discussed in Chapter 2. For future simulations, a value of $N_r = 20$ was chosen to provide results with sufficient accuracy while minimising unnecessary computational expense. This is a higher value than used by Reboul and Polaksec [108] or by Clair *et al.* [109], who each used $N_r = 10$.

Following the suitable choice of N_r, the CAA method was validated by comparing CAA noise predictions with Amiet's analytical flat plate theory for the validation case discussed in this section. Figure 3.7 shows the comparison at various frequencies and observer angles.

Figure 3.7 shows agreement between the CAA and flat plate methods of better than 2 dB at all tested frequencies and observer angles. The slight reduction in accuracy in comparison to the CAA method used in Chapter 2 is caused by the stochastic nature of the turbulence modelling process. This stochastic "random phase" approach is the cause of the increased oscillations with increasing frequency that are shown in Figure 3.7 in comparison to the results shown in Figure 2.6. However, the oscillations are considered sufficiently small because the shape of the noise spectra, and the shape of the directivity, are both captured well by the CAA

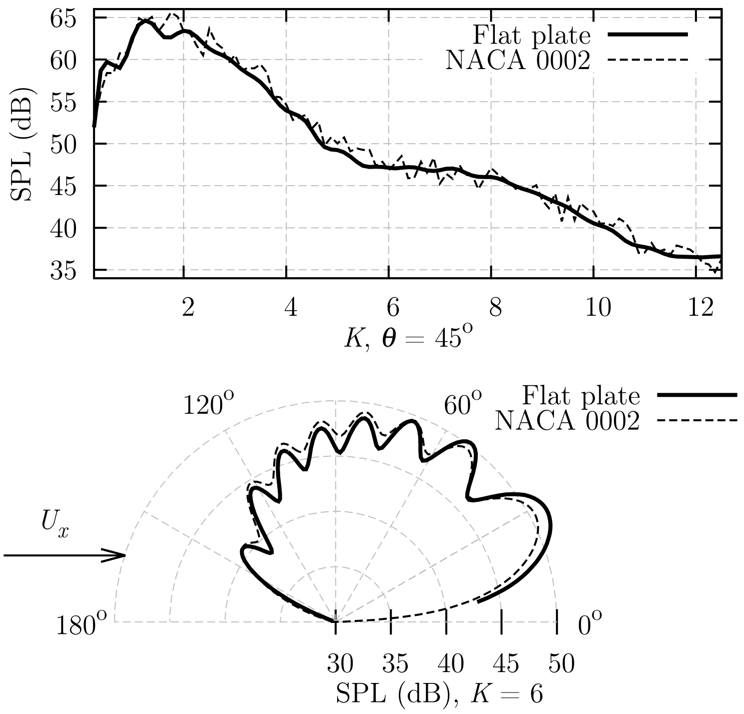

Figure 3.7: Spectral (upper) and directivity (lower) comparison of CAA and analytical flat plate methods for validation. Spectral comparison is made at $\theta = 45°$ and directivity comparison is made at $K = 12$. CAA predictions are made using a NACA 0002 airfoil with a uniform steady meanflow to minimise the effects of airfoil geometry.

method. As was seen in Figure 2.6, the small disagreements that are seen between the CAA and analytical noise predictions are at upstream angles. This is thought to be a result of the real geometry of the NACA 0002 airfoil used in the CAA method, as opposed to the infinitely thin flat plate used in the analytical formulation.

Figure 3.8 shows the turbulence velocity spectra, $W_{2D}(k_x)\boldsymbol{\zeta}(k_x)$ recorded by a monitor point placed in the flow-field at cartesian co-ordinates $x = 0$ m, $y = 1$ m, as was done in Chapter 2. Using the method described in this section, the time-varying signal was recorded in 20 independent realisations of the flowfield, and an ensemble average was taken to obtain the presented spectra. Here, both the streamwise and transverse velocity disturbance spectra are shown since the turbulence is two-dimensional. The values of $\zeta_x(k_x)$ and $\zeta_y(k_x)$, for the streamwise and transverse velocity disturbances respectively, are discussed in Appendix A. The spectra are compared with the analytical expressions for the velocity spectra.

A good agreement is seen between the computational and analytical expressions for the velocity spectra. The oscillations in the computational spectra indicate stochastic errors, which would be reduced with additional simulation realisations. The error between the computational and analytical W_{2D} spectra is within 25% across all tested reduced frequencies (which corresponds to being within 2 dB), with an average error of 7.7%. The agreement between the computational and analytical spectra demonstrates that the computational method can accurately synthesise and propagate the turbulence towards the airfoil.

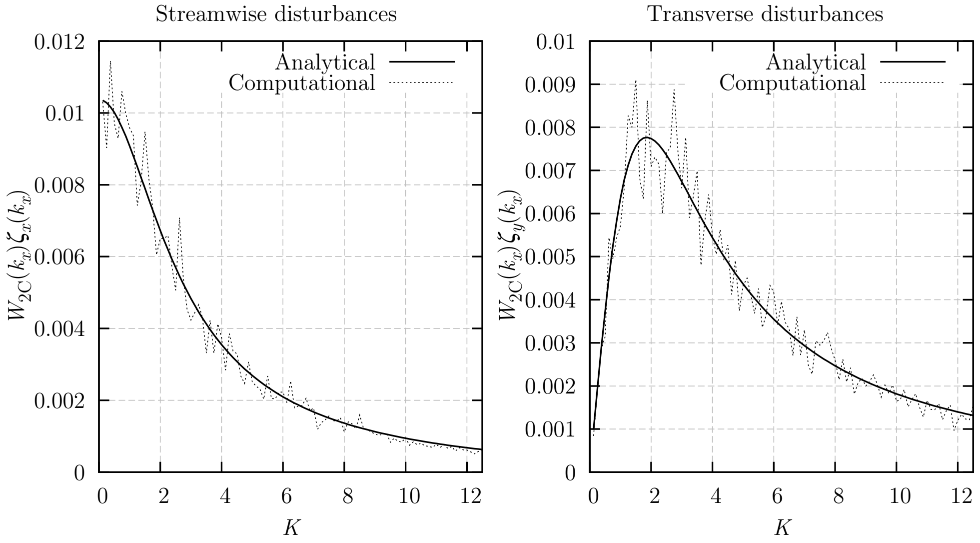

Figure 3.8: Showing the turbulence velocity spectra at the airfoil leading edge.

The agreement shown in Figures 3.7 and 3.8 was sufficient to validate the CAA method with turbulence synthesis, and permit further testing.

3.5.2 Comparison of CAA Method with Experiment

As a further validation of the CAA method, the effects on noise due to airfoil geometry were compared with previously measured effects by Paterson and Amiet [123].

In their experiment, Paterson and Amiet interacted a NACA 0012 airfoil with homogeneous grid-generated turbulence at $M = 0.175$, and measured an approximate 5 dB reduction (compared to flat plate theory) in the noise at $\theta = 90°$ and at $K_t = t/\lambda = 1$ (or where $K = c/\lambda = 8.3$ for a 12% thick airfoil). The grid-generated turbulence was characterised by $\Lambda = 0.13c$ and $\sqrt{\overline{w^2}} = 0.04U_x$.

The CAA method was used to predict the noise with the configuration used by Paterson and Amiet, and the results were compared with flat plate theory and with the experimental measurements. Figure 3.9 shows this comparison. Because the CAA method was two-dimensional and the experiment was three-dimensional, the results in Figure 3.9 have been expressed as noise per metre span, and the CAA and experimental results have not been directly compared. Additionally, the CAA predictions do not consider any effects of spanwise correlation.

Figure 3.9 shows a good agreement in spectral shape between the CAA predictions and the measurements at all frequencies. The gradient of the CAA spectra is steeper than the measurements because the CAA method is two-dimensional. Additionally, there may be differences in operating conditions. For example, it it not clear what the freestream density was during the experiment, so a value of $\rho = 1.22$ kg.m^{-3} was assumed in the computational method. Although these factors cause differences between the CAA and experimental approaches, Figure 3.9 is still useful for comparing the effects of the 12% thick airfoil on the noise.

The effects of the NACA 0012 airfoil shape that were measured by Paterson and Amiet are reproduced well by the CAA method. The NACA 0012 predictions start to differ from the flat plate data for $K = 5$ and above, because the spectral hump that is present in the analytical prediction around $K = 7$ appears to be suppressed by the presence of the real airfoil thickness. At $K = 8.3$ (or $K_t = 1$), the difference caused by the NACA 0012 airfoil thickness is 5-6 dB.

It initially seems that the CAA prediction agrees with Paterson and Amiet's [123] conclusion that $K_t = 1$ (or $K = 8.3$ for a NACA 0012 airfoil) can be considered as a measure of when flat plate theory breaks down, because a 5 dB difference can be seen between CAA and flat plate predictions at this frequency in Figure 3.9. However, Figure 3.9 does not consider the airfoil geometry effects at all observer angles. Figure

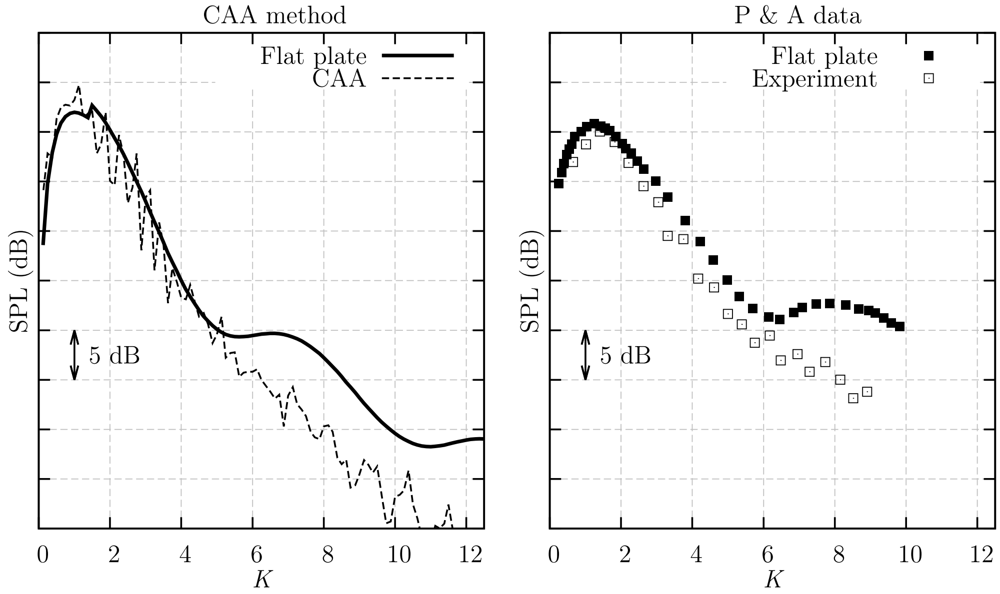

Figure 3.9: Comparison at $\theta = 90°$ between analytical flat plate predictions, CAA predictions, and experimental measurements from Paterson and Amiet [123], for a NACA 0012 airfoil at M=0.175 encountering upstream turbulence.

3.10 compares the PWL spectra (which does account for all observers) predicted by the CAA and analytical methods for the same configuration. A comparison with experimental data is not made because additional observer data was not provided by Paterson and Amiet. Figure 3.10 shows that when all observer angles are accounted for, the threshold frequency for airfoil geometry effects is between $K = 1$ and $K = 2$, which agrees with the findings in Chapter 2.

The successful validation of the CAA noise predictions against both experimental measurement and analytical modelling gave good confidence of the CAA method.

3.5.3 Effects of Thickness

Following the successful validation of the CAA method when synthesising turbulence, the effects of airfoil thickness on the noise were re-examined. Airfoil thicknesses ranging from 2% to 12% were examined at a Mach number of $M = 0.5$ in turbulence with $\Lambda = 0.07$ m and $\sqrt{\overline{w^2}} = 0.04U_x$. This Mach number is a represen-

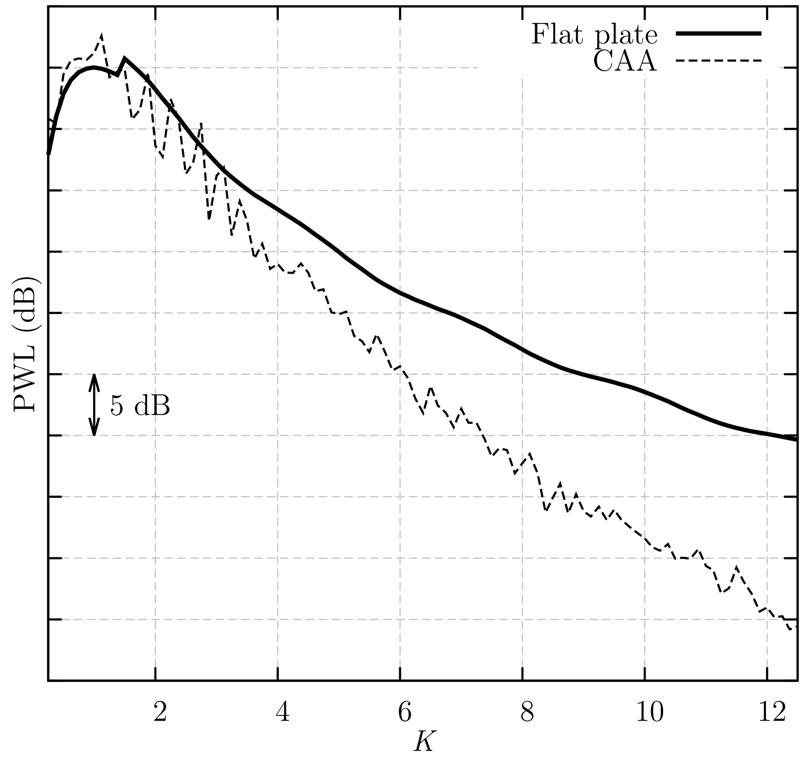

Figure 3.10: Comparison of PWL between analytical flat plate and CAA predictions for Paterson and Amiet's [123] experimental configuration.

tative flow speed for CROR blade sections during the take-off and landing phases of flight.

Figure 3.11 shows contours of SPL predictions from flat plate theory and from the CAA method when forcing two-component turbulence (containing both streamwise and transverse disturbances), using airfoils with 4%, 8% and 12% thickness. For each airfoil, the variation of SPL with both θ and K is shown so that the full effect of airfoil geometry on the noise can be seen. Figure 3.11 shows that SPL predictions for thick airfoils progressively become smaller in comparison to flat plate theory, and that this reduction increases with increasing thickness. It also shows that as the airfoil thickness is increased, SPL predictions become less sensitive to observer angle θ. Flat plate predictions are higher in level at $\theta = 20°$ compared with $\theta = 180°$, whereas there is little difference between SPL results at these two angles for the

NACA 0012 airfoil. Figure 3.11 also shows that oscillations which are seen in the analytical solution due to non-compactnes effects, become more smoothed as the airfoil thickness is increased. These oscillations are still present for the NACA 0004 airfoil but are no longer observable for the NACA 0012 airfoil.

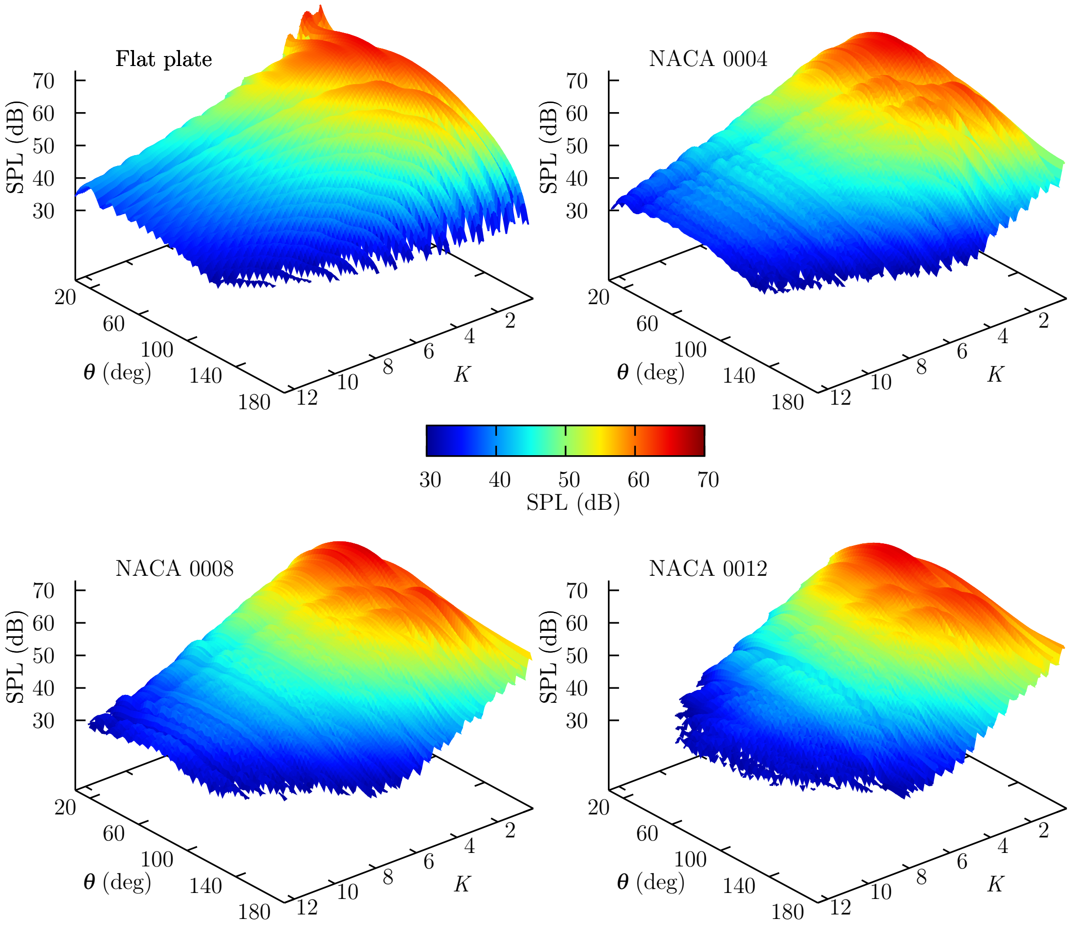
Flat plate

NACA 0004

NACA 0008

NACA 0012

Figure 3.11: Contours of SPL with varying observer angle θ and reduced frequency K for the analytical flat plate method, compared with CAA predictions using a 4%, 8%, and 12% airfoil.

In order to better visualise the noise reduction that is caused by airfoil geometry, contours of ΔSPL are plotted in Figure 3.12 for the 4%, 8% and 12% airfoils from Figure 3.11. ΔSPL was calculated as the difference in noise between each airfoil and the analytical flat plate prediction, so that $\Delta\text{SPL}(\theta, K) = \text{SPL}_{caa}(\theta, K) - \text{SPL}_{an}(\theta, K)$. The scale of the contours shown in Figure 3.12 is limited to only show areas where a reduction in noise was observed in comparison to the analytical prediction. Figure 3.12 shows that at downstream observer angles ($\theta < 90°$) there is a reduction in the noise at most frequencies, whereas upstream observer angles only experience a noise reduction at higher values of reduced frequency. Additionally, the reduction is greater in the downstream direction than in the upstream direction, as was observed in Chapter 2.

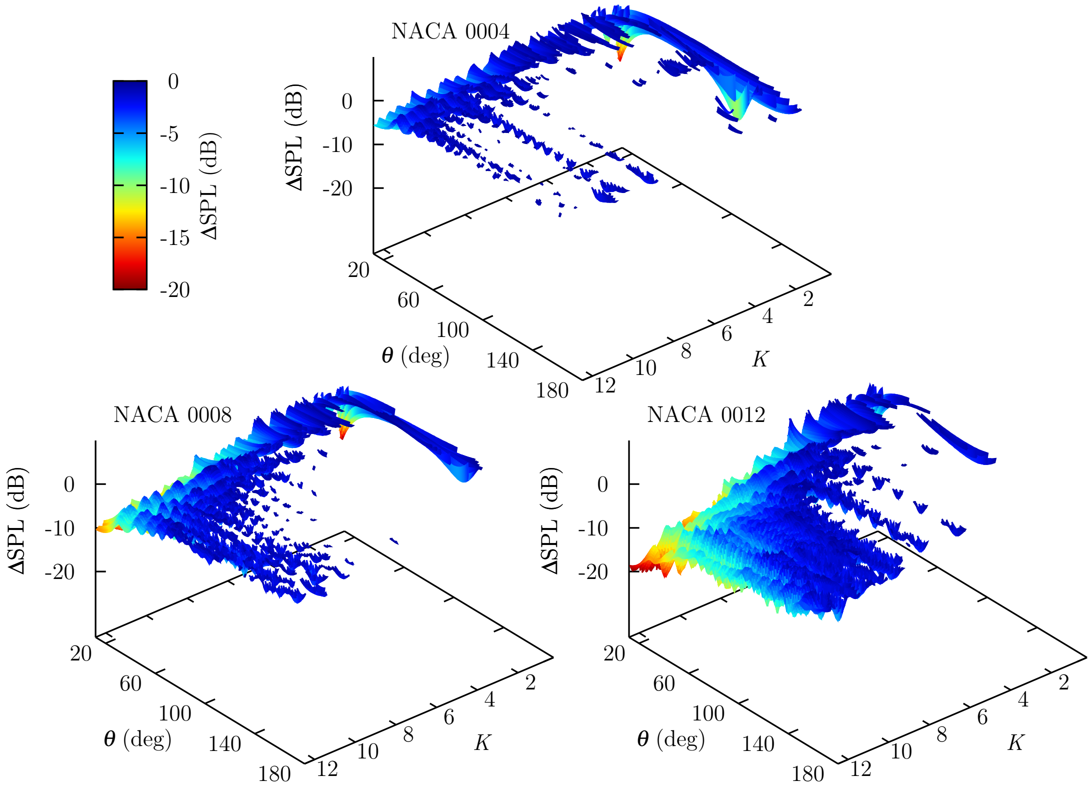

Figure 3.12: ΔSPL with varying observer angle θ and reduced frequency K against the baseline flat plate prediction, for a 4%, 8% and 12% thick airfoil.

Figure 3.13 compares PWL spectra and SPL directivity plots of airfoils with 4%, 8% and 12% thickness, in order to better quantify the effects on turbulence interaction noise due to airfoil geometry. The PWL spectra in Figure 3.13 shows that the reduced frequency above which the noise becomes sensitive to airfoil geometry is at about $K = 4$. The noise prediction for the NACA 0012 airfoil at $K = 12$ is about 8 dB lower than the flat plate noise prediction. Figure 3.13 also shows that the general shape of the directivity pattern appears to be unchanged by the presence of airfoil thickness, as was found in Chapter 2.

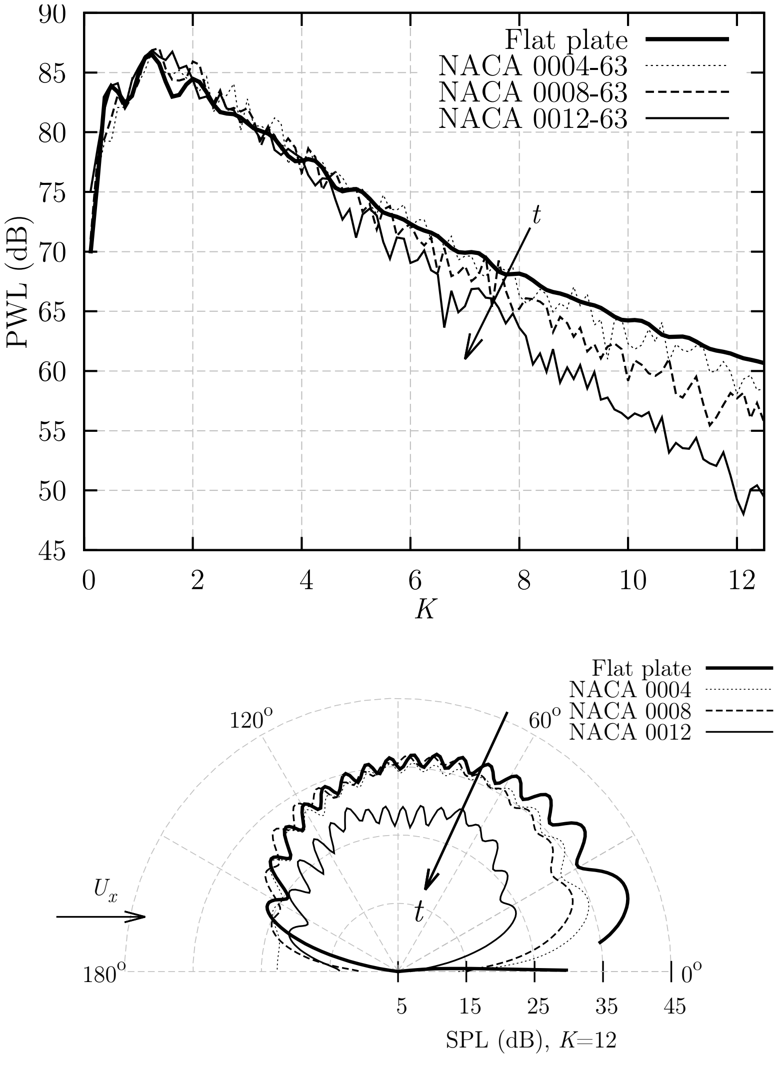

Figure 3.13: CAA PWL (upper) and directivity (lower) predictions for a 4%, 8%, and 12% airfoil compared with flat plate theory.

To study the trend of turbulence interaction noise more completely with varying thickness, the variation of PWL with increasing airfoil thickness t, is shown in Figure 3.14 at two reduced frequencies. Solid lines have also been drawn to indicate potential linear trends. Figure 3.14 shows that at constant reduced frequency, the PWL reduces with increasing thickness, and that a good fit of the data can be obtained with a linear regression. The CAA predictions vary around the trend line by up to 2 dB, which is a cumulative error caused by changes in computational grid, stochastic error in the turbulence synthesis, and numerical errors in the CAA approach. However, the data is considered to be sufficiently accurate to show the linear trend. This result agrees with the conclusions of several previous such as Olsen and Wagner [72], and Roger and Moreau [24]. However, it does not agree with Figure 3.13, which suggests a linear relationship between thickness and P, rather than PWL. This difference may be due to the small number of thickness data points used in Chapter 2.

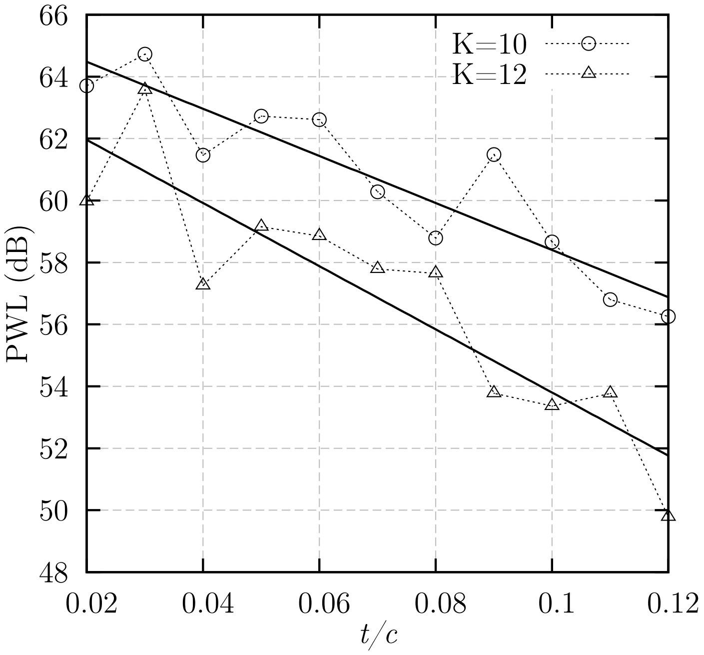

Figure 3.14: Sound power level (PWL) variation for airfoils with various thicknesses at $K = 10$ and $K = 12$. Solid lines are drawn as lines of best fit.

Figure 3.15 shows the ΔPWL in comparison to flat plate theory, caused by airfoil thicknesses ranging between 2 and 12%. This is plotted against the thickness-based reduced frequency $K_t = t/\lambda$. In addition to the CAA predictions, the correction factor that was used by Gershfeld [88] is plotted. This correction factor was used to account for the effects of thickness on turbulence interaction noise, and is given as

$$\begin{aligned}\Delta\mathrm{PWL} &= 10\log10\Big(\exp\big(-\frac{\omega t}{2U_x}\big)\Big), && (3.18)\\ &= 10\log10\big(\exp(-\pi K_t)\big). && (3.19)\end{aligned}$$

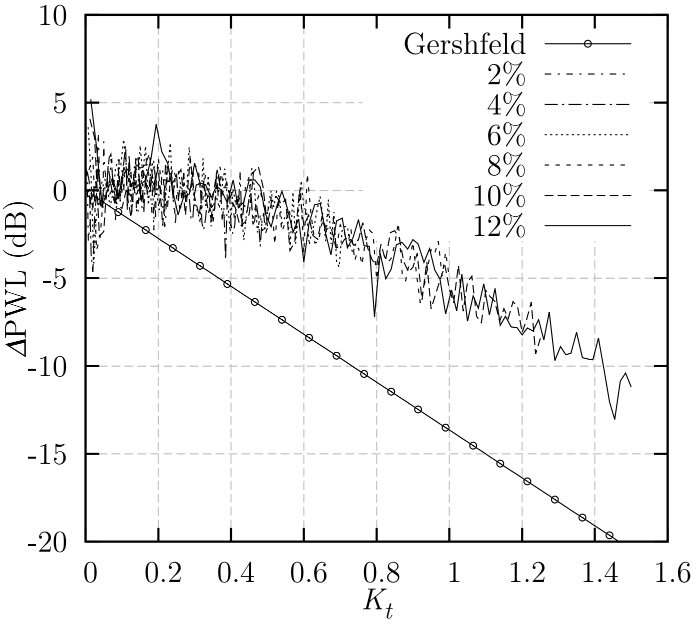

Figure 3.15: ΔPWL variation for airfoils with thicknesses ranging between 2 and 12 %, plotted against K_t. Data is also compared with the thickness correction factor used by Gershfeld [88].

Figure 3.15 shows that K_t is a good collapsing parameter for ΔPWL. The contributions from the various airfoil thicknesses appear to collapse onto a single trend when plotted in this way, suggesting that K_t is the dominant lengthscale that controls the reduction of the noise for airfoils with thickness. For $K_t > 0.6$, the gradient of the collapsed data is linear, and appears to be very similar to the gradient predicted by Gershfeld's correction factor. However, for $K_t < 0.6$ the gradient of $\Delta\mathrm{PWL}/K_t$ is not linear, and does not follow the trend predicted by Gershfeld. Although the gradient of the CAA prediction and Gershfeld's correction factor are similar, the correction factor predicts a larger reduction in the noise than is seen with the CAA predictions.

It is likely that Gershfelds's correction factor predicts a larger reduction than the CAA method because it assumes the effects of thickness are present for all values of K_t above 0. In the current work, it has been shown that thickness effects on the noise become significant above a threshold value of reduced frequency K, and that this threshold value has some dependence on Mach number (see Figures 2.9 and 3.13 for example). If the test was repeated at a reduced Mach number, the agreement with Gershfeld's correction factor may be improved because the threshold reduced frequency for thickness effects would be at a lower value of K.

3.5.4 Mechanism

To determine whether the mechanism that causes the reduced noise for thick airfoils is similar to the findings in Chapter 2, contours of the root-mean-square velocity perturbations around the airfoil leading edge are plotted for a 2%, 6% and 12% thick airfoil in Figure 3.16. Because the CAA method uses gusts with both transverse and streamwise velocity perturbations, Figure 3.16 shows contours of U_{rms} where $U_{rms} = \sqrt{u_{rms}^2 + v_{rms}^2}$. An ensemble average was taken of the flow-field from multiple realisations in order to provide the root-mean-square values shown.

Figure 3.16 shows that the U_{rms} values reach a peak value at the leading edge of the NACA 0002 airfoil, but that this peak is weaker for the thicker NACA 0006 and NACA 0012 airfoils. This finding is consistent with Figure 2.20 and also with the discussion given in Section 2.3.5, and therefore suggests that the mechanism for sound reduction is not changed when gusts with varying k_y wavenumber are included in the simulation.

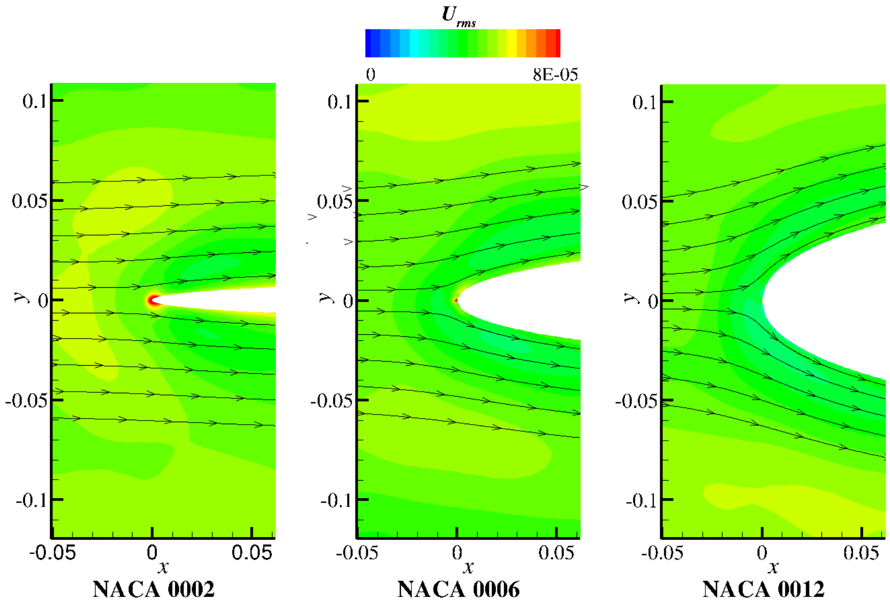

Figure 3.16: Contours of U_{rms} for gusts with $K = 8$ and various k_y wavenumber components interacting with 2%, 6%, and 12% thick airfoils. The contours are overlaid with streamlines of the non-uniform meanflow around each airfoil.

3.5.5 Effects of Turbulence Length-Scale

It was desired to investigate whether the turbulence interaction noise sensitivity to airfoil geometry was affected by the properties of the oncoming turbulence. Therefore, a NACA 0012 airfoil was interacted with turbulent flows at $M = 0.5$ with varying integral length-scales Λ. Figure 3.18 compares the CAA predictions with analytical predictions, for varying Λ values. The range of $0.04c < \Lambda < 0.30c$ was chosen to cover length-scales that were both significantly smaller and significantly larger than the airfoil thickness of $t = 0.12c$. An example of the turbulent flow-field perturbation vectors upstream of the airfoil is shown in Figure 3.17, during one realisation for $\Lambda = 0.04$ m and $\Lambda = 0.20$ m.

Figure 3.18 compares PWL predictions from the analytical and CAA methods for $\Lambda = 0.04$ m, $\Lambda = 0.07$ m, $\Lambda = 0.20$ m, and $\Lambda = 0.30$ m (corresponding to $\Lambda/t = 0.333$, $\Lambda/t = 0.583$, $\Lambda/t = 1.666$, and $\Lambda/t = 2.5$ respectively). As the turbulence length-scale Λ is increased, the amplitude of predictions is increased at low frequency

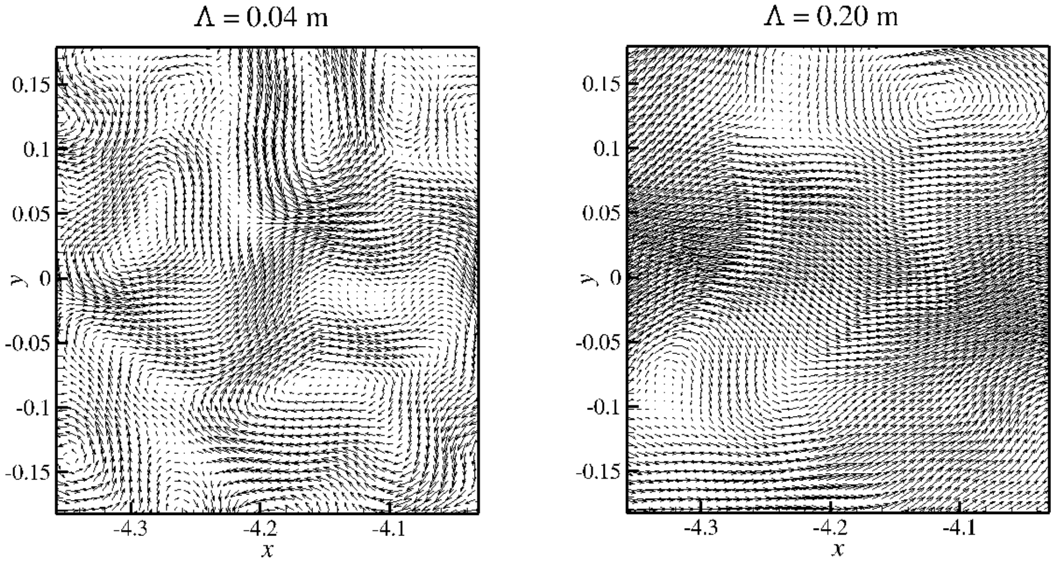

Figure 3.17: An example of the turbulent perturbation vectors upstream of the airfoil, during one realisation for $\Lambda = 0.04$ m and $\Lambda = 0.20$ m.

and is reduced at high frequency. This corresponds to the turbulent energy being contained within larger structures at lower frequency for large values of Λ. However, the noise prediction error incurred by assuming a flat plate geometry, does not appear to be affected by changes in Λ. For all Λ values, the noise reduction due to airfoil thickness appears to be about 10 dB at $K = 12$. Additionally, the threshold frequency at which the reduction begins to occur is also not affected. Reductions consistently appear at frequencies above $K = 4$. (This frequency is higher than the threshold frequency observer throughout Chapter 2 because the Mach number is also higher.) Therefore, it appears that airfoil geometry effects on turbulence interaction noise are not sensitive to the turbulence length-scale of the oncoming disturbance. The ΔPWL difference between the flat plate prediction and the NACA 0012 prediction is shown in Figure 3.19 for the four different values of Λ. Figure 3.19 shows that the ΔPWL curves for each value of Λ are very similar, and thus confirms that the noise reduction at a given value of K is independent of Λ.

The finding that the effect of airfoil thickness on the noise is independent of Λ contrasts with the conclusion of Roger and Moreau [24], who compared the experimental

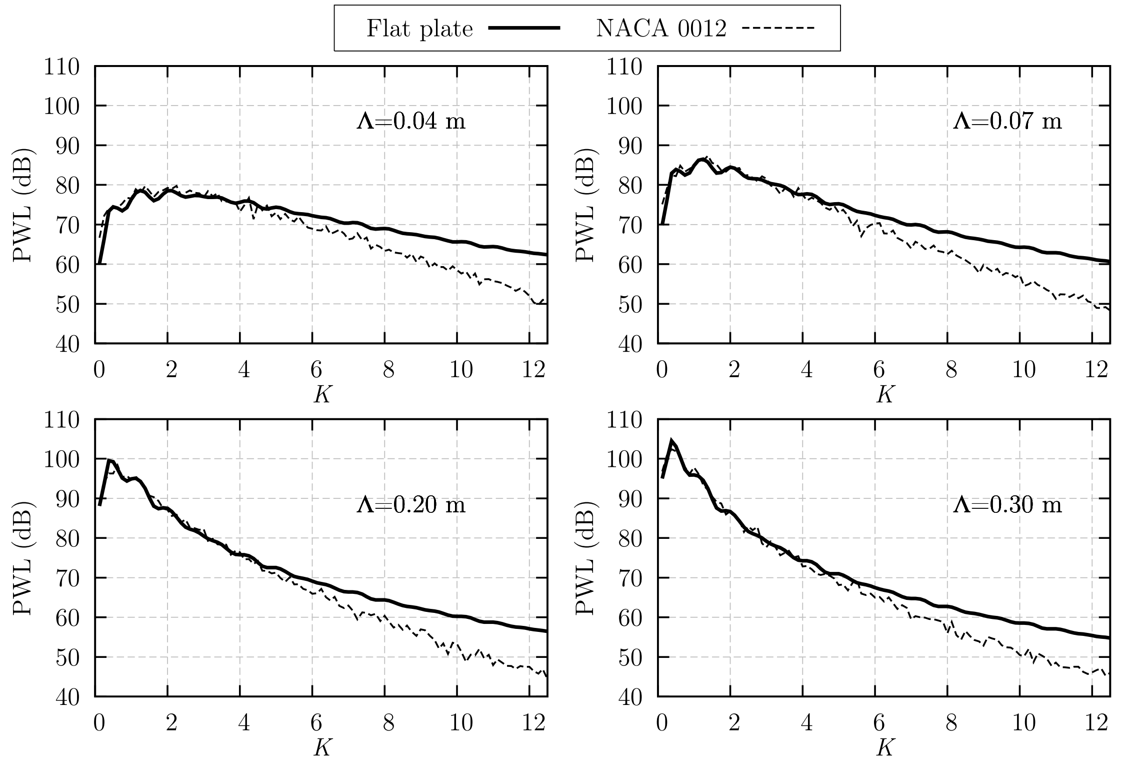

Figure 3.18: Comparison of PWL predictions from the analytical flat plate method and the CAA method using a NACA 0012 airfoil for different turbulence length-scale Λ values.

results of several authors and found that the noise reduction was proportional to both the thickness-based reduced frequency K_t and to the ratio t/Λ. The current work has found that the noise reduction scales with K_t, but does not scale with t/Λ.

The result of the current study is partially justified if it is considered in the context of this thesis. Because the simulation is assumed to be linear by the LEEs, the turbulence interaction noise scales linearly with the gust amplitude or turbulence intensity. Therefore, any effect on the noise due to the airfoil geometry is expected to be independent of the gust amplitude. Whether the turbulence intensity is $\sqrt{\overline{w^2}} = 0.01U_x$, $\sqrt{\overline{w^2}} = 0.04U_x$, or any other value, the noise reduction in Decibels will remain constant. Here, the effect of changing Λ is to simply alter the amplitude of each forced mode, and thus the noise reduction effect would be expected to remain

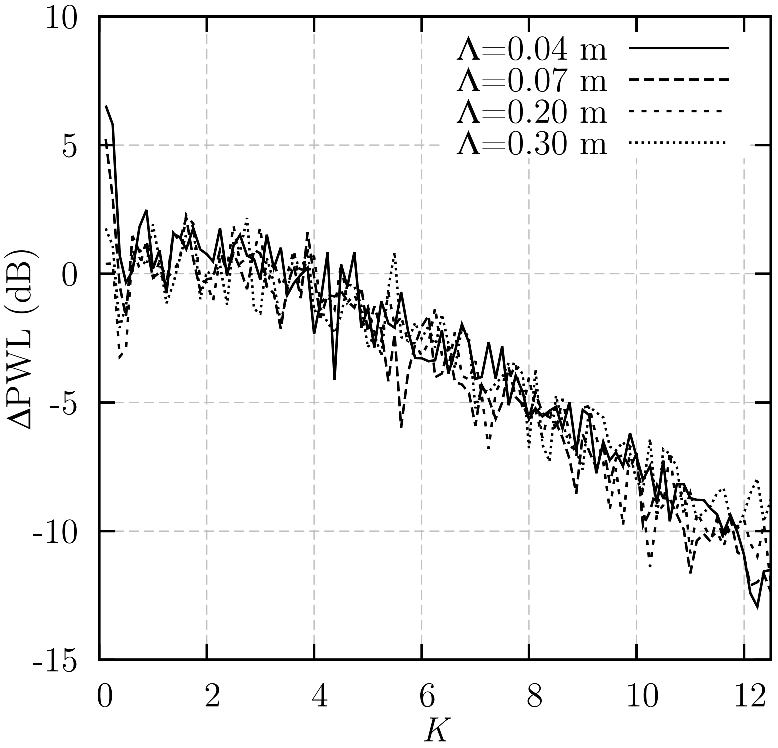

Figure 3.19: Comparison of ΔPWL between analytical flat plate method and the CAA method using a NACA 0012 airfoil for different turbulence length-scale Λ values.

constant with changes in Λ.

While this discussion justifies the current result, it does not explain the discrepancy with the findings of Roger and Moreau [24]. A possible cause is that the two studies consider different situations. The current study was performed at $M = 0.5$, with a single airfoil geometry, and with Λ as the only varying parameter. Roger and Moreau compared results from different experimental studies by different authors, and therefore considered different Mach numbers, (all lower than $M = 0.5$), different airfoil geometries and slightly altered freestream conditions. Additionally, Roger and Moreau make the assumption of flow similarity. This assumption is not obeyed in the current study because the shape of the spectra in Figure 3.18 is altered by the changes in Λ. Another source of the discrepancy may be a fundamental difference between the computational method and the experimental studies considered by

Roger and Moreau [24]. When Λ is varied in the computational method, the mode amplitudes are altered, but the number of modes and their spectral discretisation is unchanged. This contrasts with experimental studies, which will record different frequency content if Λ is changed.

While the turbulence interaction noise reduction at a given value of K is independent of Λ, it should be noted that the overall SPL (OASPL) noise reduction *will* be affected. When Λ is increased, there is greater energy contained at lower frequencies, which are not affected by the airfoil geometry. Therefore, as Λ is increased the OASPL sound reduction due to airfoil thickness can be expected to decrease.

3.6 Summary

The CAA method that was introduced in Chapter 2 has been extended to increase the realism of turbulence interaction noise modelling. This was achieved by modifying the CAA method to synthesise a two-component isotropic, homogeneous turbulence (with disturbances in the streamwise and transverse component directions) as opposed to forcing transverse harmonic disturbances. Using the CAA method with turbulence synthesis, the effects of airfoil thickness on turbulence interaction noise have been re-examined at conditions which are more representative of the operational conditions of CROR blade sections. The key findings of this chapter are:

- Airfoil thickness causes a reduction in turbulence interaction noise predictions at high reduced frequency. A larger reduction is seen at downstream observer angles compared with upstream observer angles. The presence of airfoil thickness was shown to suppress the amplitude oscillations which are seen in flat plate models due to non-compactness effects. Therefore, the effects of airfoil geometry on the noise, when modelled by the two-component CAA approach, are very similar to the effects that were reported in Chapter 2.

- There is a reduction in PWL with thickness at constant reduced frequency, which can be fitted well with a linear regression. Furthermore, the dominant length-scale associated with noise reduction appears to be the thickness-based reduced frequency K_t. For $K_t > 0.6$, there is a linear reduction in PWL with increasing K_t. The $K_t = 0.6$ threshold is likely to be affected by Mach number.

- The sensitivity of turbulence interaction noise to airfoil geometry does not appear to be affected by the integral length-scale of the turbulence. If the turbulence length-scale is changed, then the shape of both the analytical and CAA noise predictions are altered accordingly, but the amount of noise reduction caused by the real shape of a NACA 0012 airfoil is not affected.

- Symmetric airfoils with comparable thickness and flow conditions to CROR blades near the rotor tip ($t = 0.04c$, $M = 0.5$) have been tested with the CAA method. Relatively little noise reduction is seen in PWL levels in these conditions. However, For blade sections nearer the CROR hub, where t is larger and M is smaller, a greater effect on noise would be expected due to the airfoil geometry. Furthermore, the current tests were performed at zero AoA, which is a simplification of real CROR blade geometries and conditions.

Chapter 4

Single Velocity-Component Modelling of Turbulence Interaction Noise

In Chapter 3 it was shown that the behaviour of turbulence interaction noise from 2D airfoils with varying thickness geometry, as modelled by a CAA method using 2D turbulence synthesis (with streamwise and transverse disturbances), was similar to the behaviour seen in Chapter 2 which used harmonic transverse gusts. This suggests that transverse flow disturbances are more important to the noise generation than streamwise disturbances, because the addition of the streamwise disturbances does not affect the noise.

The analytical study of Amiet [30] showed that the turbulence interaction noise is primarily due to the turbulence disturbances in the transverse direction, when the noise is measured in the mid-span plan of a flat plate with semi-span d considerably larger than the turbulence lengthscale Λ. Streamwise disturbances were not included in Amiet's analysis because a flat plate has no physical extent to interact with streamwise disturbances.

Amiet showed that for a flat plate the spanwise turbulence disturbances are unimportant if the span is sufficiently large, while the results of Chapter 3 suggest that the streamwise turbulence components are also unimportant for real symmetric airfoils. Combining these conclusions suggests that accurate noise predictions can be made by representing turbulence as only transverse disturbances when considering symmetric real airfoils at zero AoA.

This chapter examines the error associated with using only transverse disturbances when modeling the turbulence interaction noise of 2D and 3D airfoils with finite thickness. The noise predictions from one-component (using transverse disturbances), two-component (including transverse and streamwise disturbances), and three-component (using transverse, streamwise, and spanwise disturbances) turbulence synthesis approaches will be used. This will assess the relative importance of transverse, streamwise, and spanwise disturbances for predicting the turbulence interaction noise of symmetric airfoils.

The representation of turbulence with only transverse disturbances which spatially vary only in the streamwise direction, is referred to here as Single Velocity-Component Modelling. If accurate noise predictions can be obtained for real airfoil geometries using a single velocity-component modelling approach, this will lead to significant computational savings.

The first test case considered in this chapter studies the noise of a single airfoil geometry by making predictions using the three different turbulence synthesis approaches. This is presented in Section 4.3. In order to study three-component synthesised turbulence, a 3D simulation must be used, which is computationally expensive. However, the one- and two-component turbulence forcing approaches require only a 2D simulation. Therefore, additional tests in Section 4.4 are made with different airfoil geometries, by using only the one- and two-component approaches in order to reduce the computational cost.

4.1 Case Description

Due to the expense of 3D simulations, a parameter study of different airfoil configurations was not practical. Therefore, one airfoil was used for the single velocity-component modelling comparison. A NACA 0012 airfoil geometry was interacted at $M = 0.5$ with synthesised turbulence that had $\Lambda = 0.07$ m and $\sqrt{\overline{w^2}} = 0.04U_x$. The NACA 0012 geometry was chosen so that airfoil geometry effects were well represented, while a $M = 0.5$ flow was chosen to provide a high gust convection speed which reduces the total computational time. In the 3D simulation the airfoil was assumed to have an infinite span via the use of periodic boundary conditions. Noise predictions were made per metre span to ensure consistency between the one-, two- and three-component simulations. The co-ordinate system that was used in the 3D CAA method is shown in Figure 4.1, which also shows an example of the turbulent vortical flow surrounding the airfoil.

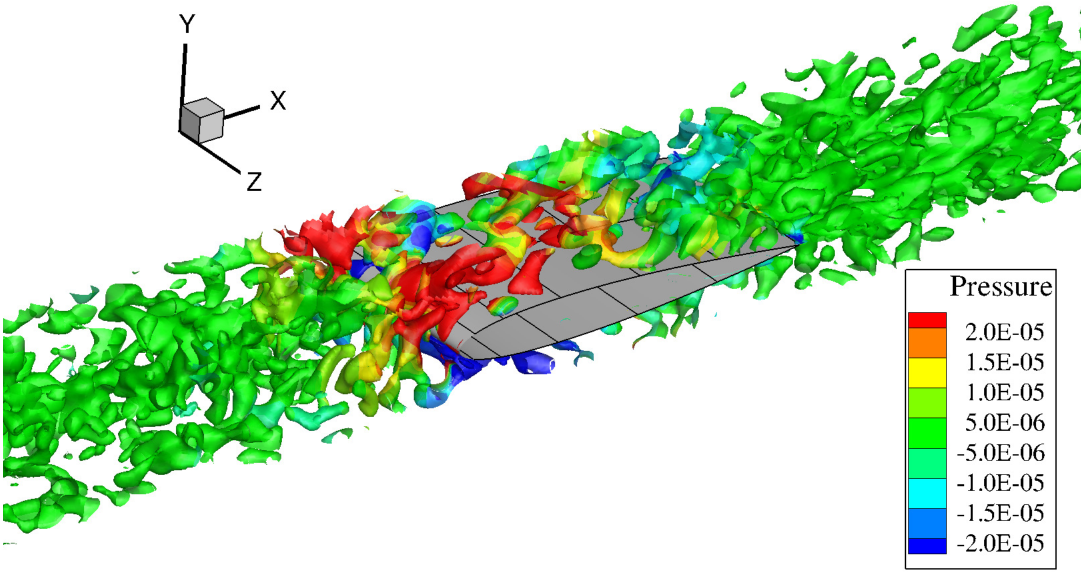

Figure 4.1: Iso-contours of vorticity near the airfoil surface coloured by pressure perturbations. Quantities are non-dimensional.

4.2 Computational Method

The CAA method used to force three-component synthesised turbulence was an extension of the methods used in Chapters 2 and 3. Three-component vortical gusts, with disturbances in the transverse, streamwise, and spanwise directions, were defined as

$$\boldsymbol{u}_{3C}(\boldsymbol{x},T)=\sum_{l=1}^{L}\sum_{m=-M}^{M}\sum_{n=-N}^{N}W_{3C}(\boldsymbol{k}_{l,m,n})\cos\Big(\boldsymbol{k}_{l,m,n}\cdot(\boldsymbol{x}-\boldsymbol{U}T)+\sigma_{l,m,n}\Big)\boldsymbol{\zeta}(\boldsymbol{k}_{l,m,n}) \tag{4.1}$$

where l, m, n are the summation modes in the streamwise, transverse and spanwise direction respectively, $\boldsymbol{k}_{l,m,n}$ and $\boldsymbol{\zeta}$ are the wave vector and direction of each combination of l, m, and n modes, and $W_{3C}(\boldsymbol{k}_{l,m,n})$ is set to follow the 3D Liepmann spectrum [23] as

$$W_{3C}(\boldsymbol{k})=\sqrt{\frac{\Delta k_y \Delta k_z}{4\pi k^2}\frac{8}{\pi}\overline{w^2}\Lambda\frac{(\Lambda k)^4}{(1+\Lambda^2k^2)^3}} \tag{4.2}$$

where $k=\sqrt{k_x^2+k_y^2+k_z^2}$. To ensure a divergence-free flow, $\boldsymbol{\zeta}$ was defined such that $\boldsymbol{k}_{l,m,n}\cdot\boldsymbol{\zeta}(\boldsymbol{k}_{l,m,n})=0$, as explained in Appendix A. Additional description and derivation of Equation 4.2 is given in Appendix B. $W_{3D}(\boldsymbol{k})$ was discretised in a similar manner to Chapter 3. This is described in more detail in Section 4.2.2.

4.2.1 Computational Efficiency

The largest obstacle when conducting a 3D CAA turbulence interaction simulation is the associated computational cost. 3D computational grids can be more than 100 times as expensive to solve in comparison to 2D computational grids because of the larger cell count and the larger number of governing equations that must be solved. Additionally, the extra summation in Equation 4.1 means that the three-component turbulence synthesis approach is significantly more expensive than the two-component approach. Therefore, only one simulation was considered with the 3D CAA method. Several techniques were also employed to reduce the expected computational time. These will now be discussed.

- ***Reduced cell count***. One of the most effective ways to reduce the computational expense is to reduce the number of cells in the simulation. However, this also reduces the highest resolvable frequency. Therefore, in conjunction with the reduction in cell count, the highest resolved frequencies in the transverse and streamwise directions were reduced. This is discussed further in Section 4.2.2.

- ***Spanwise periodicity***. Periodic boundary conditions were applied on the two spanwise faces of the simulation in order to simulate an infinite span airfoil. This reduced the computational expense by avoiding the complex geometry at the wing tips, and also made the 3D simulation more comparable to the 2D simulations. This simplification required the three-component synthesised turbulence to also be periodic in the spanwise direction. Therefore, the largest possible spanwise wavelength was set to be equal to the width of the domain.

- ***Reduced downstream resolution***. The wavelength of the vortical waves was smaller than the wavelength of the acoustic waves. This allowed the resolution of the grid to be reduced downstream of the airfoil. In this region, the vortical gusts do not need to be fully resolved since they have already interacted with the airfoil surface. Instead, the resolution requirement downstream of the airfoil was set to resolve only the acoustic waves, which allowed for a reduction in the total cell count. The final cell count of the 3D computational grid was approximately 26 million cells.

- ***Improved load balancing***. The simulations discussed in this project have used multi-processor simulations. A larger number of processors was required for the 3D simulation in order to obtain solutions in a reasonable time. The CAA method typically balances the load across multiple processors by ensuring that each processor is assigned a similar number of cells. However, when the three-component turbulence synthesis was activated, this balancing technique became less effective.

  The load balancing was made less effective because the synthesis of a three-component turbulent gust is computationally expensive. A summation is required over all l, m, and n modes to obtain the velocity at each timestep and grid point. Therefore, the computational cells in the buffer regions were under a higher computational load than cells elsewhere in the simulation, because they perform the turbulence synthesis. This reduced the computational efficiency of the overall simulation. To overcome this, the load balancing was improved by assigning fewer additional cells to processors that had been allocated buffer zone regions. The improved load balance was also coupled with an optimisation routine that re-ordered the parallel grid distribution in order to reduce the overall number of communications at each timestep. These techniques improved the computational efficiency by approximately 35%.

4.2.2 Discretising the Energy Spectrum

The energy spectrum $W_{3C}(\boldsymbol{k})$ was discretised similarly to the method used in Chapter 3. The L, M, and N summation limits were chosen such that the highest k_x, k_y, and k_z wavenumbers were equal to k_x^{lim}, k_y^{lim}, and k_z^{lim} respectively. The value of k_x^{lim} was chosen to be 16π m^{-1}, corresponding to a reduced frequency of $K = 8$. The value of k_y^{lim} was chosen to be 75 m^{-1}. The distribution of k_y was chosen with a greater density around $k_y = 0$ than at higher values in order to resolve the shape of $W_{3C}(\boldsymbol{k})$. Both k_x^{lim} and k_y^{lim} values were smaller here than those used in Chapter 3 in order to reduce the required grid resolution for the three-component turbulence synthesis.

The value of k_z^{lim} was chosen to be 85 m^{-1}. The disturbances were required to be periodic about the spanwise width of the simulation. Therefore a spanwise simulation width of 0.5 m was chosen, and all k_z values in the range -85 m$^{-1} < k_z < 85$ m^{-1} were chosen to be harmonics of the fundamental 0.5 m wavelength. The distribution of k_y and k_z wavenumbers in the discretised spectrum is shown in Figure 4.2 for $k_x = 0.5\pi$ m^{-1} and $k_x = 16\pi$ m^{-1}. The non-discretised spectrum is also shown for comparison.

Figure 4.2 shows that the Liepmann spectrum was not resolved completely in either the k_y direction or the k_z direction at high values of k_x. As a result, when the spectrum was integrated over the discretised range of 19 k_y and 13 k_z values, approximately 70% of the total energy was captured. In Chapter 3 approximately 90% of the energy of the 2D Liepmann spectrum was captured. However, the lack of spanwise resolution was considered acceptable due to additional considerations

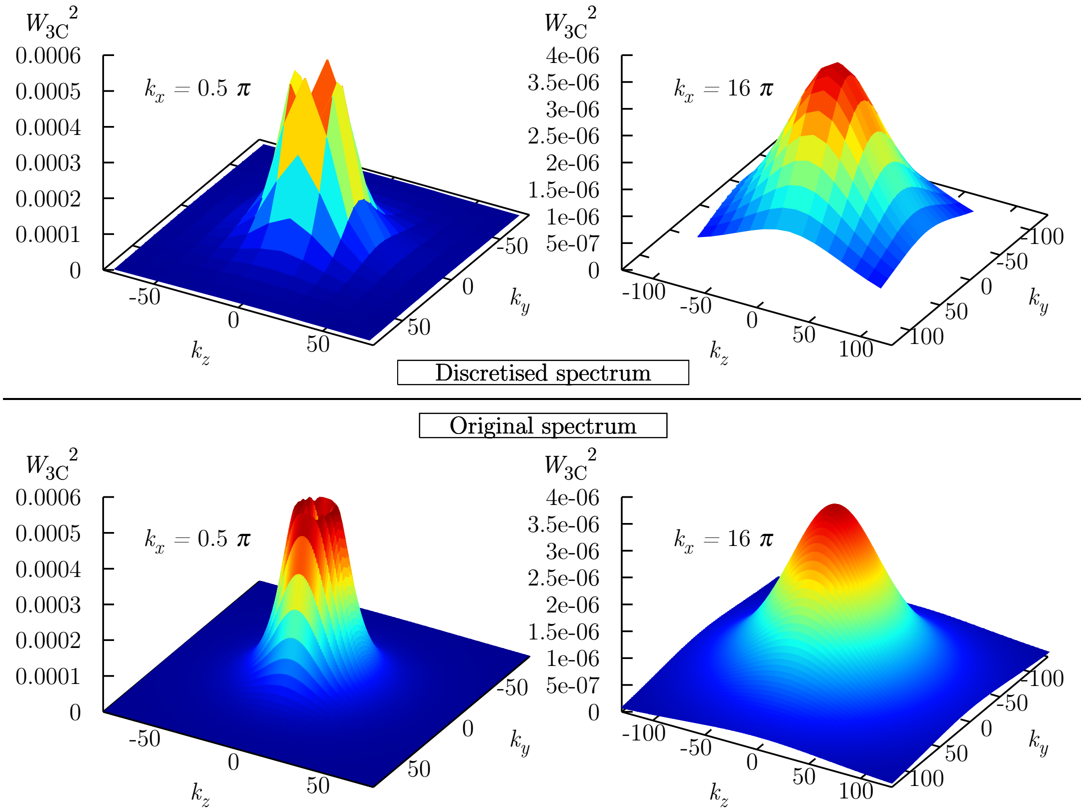

Figure 4.2: The discretised 3D Liepmann spectrum at low and high values of k_x. $M = 0.5$, $\Lambda = 0.07$ m, $\sqrt{\overline{w^2}} = 0.04U_x$.

which will now be discussed. it may be accurate to use only transverse disturbances when modelling the turbulence interaction noise of real symmetric airfoils in addition to flat plates.

4.2.3 Spanwise Wavenumber Contributions

Amiet's analysis of flat plate interaction noise [30] showed that only gusts with $k_z = 0$ would contribute to the sound if the airfoil span is considerably larger than the turbulence length-scale and the observer is in the mid-span plane. Amiet gave the far-field PSD of a flat plate with finite span interacting with oncoming turbulence as

$$S_{pp}(\boldsymbol{x},\omega) = \left(\frac{\omega y \rho_0 b}{c_0 \sigma^2}\right)^2 U\pi d \int\limits_{-\infty}^{\infty} \left[\frac{\sin^2(d(k_z + \omega\sigma z/c_0))}{(k_z + \omega\sigma z/c_0)^2 \pi d}\right] |L^{LE}(x, K_x, k_z)|^2 \Phi_{vv}(K_x, k_z) dk_z, \tag{4.3}$$

where d is the semi-span of the flat plate. This expression can be simplified by recognising that

$$\lim_{d\to\infty} \left[\frac{\sin^2(d\xi)}{\xi^2 \pi d}\right] \to \delta(\xi) \tag{4.4}$$

where $\xi = k_z + \omega\sigma z/c_0$. Therefore, if the observer is in the mid-span plane ($z = 0$), only gusts with $k_z = 0$ will contribute to the sound.

Amiet's analysis was limited to a flat plate. However, if the analysis is also applicable to generic airfoil profiles, then the lack of k_z resolution in the discretised 3D Liepmann spectrum will not affect the noise predictions. In fact, one aim of the current work is to show that the noise is unaffected by the presence of additional gusts with $k_z \neq 0$.

Figure 4.3 shows the discretised $W_{3C}(\boldsymbol{k})$ spectrum with varying k_z, with $k_x = 16\pi$ m^{-1}, $k_y = 0$, and where plots of Equation 4.4 have also been included to indicate how much of the spectrum is expected to contribute to the noise. Equation 4.4 has been plotted for airfoil spans of 0.1 m, 1 m, and 10 m, and has been scaled to the maximum value of $W_{3C}(\boldsymbol{k})$.

In Figure 4.3, the range of k_z values which contribute to the sound is reduced with increasing d. The current 3D case assumes an infinite span airfoil, which is the limit of Equation 4.4 where only gusts with $k_z = 0$ will contribute to the sound. However, in order to reduce computational costs, the spectral resolution in the k_z direction is considerably larger than the width of Equation 4.4, even for large values of d. Therefore, if an integration of the spectrum over k_z is made by using Δk_z, as is written in Equation 4.2, the resulting noise will be over-predicted. This issue could be overcome by increasing the spanwise spectral resolution, but the computational

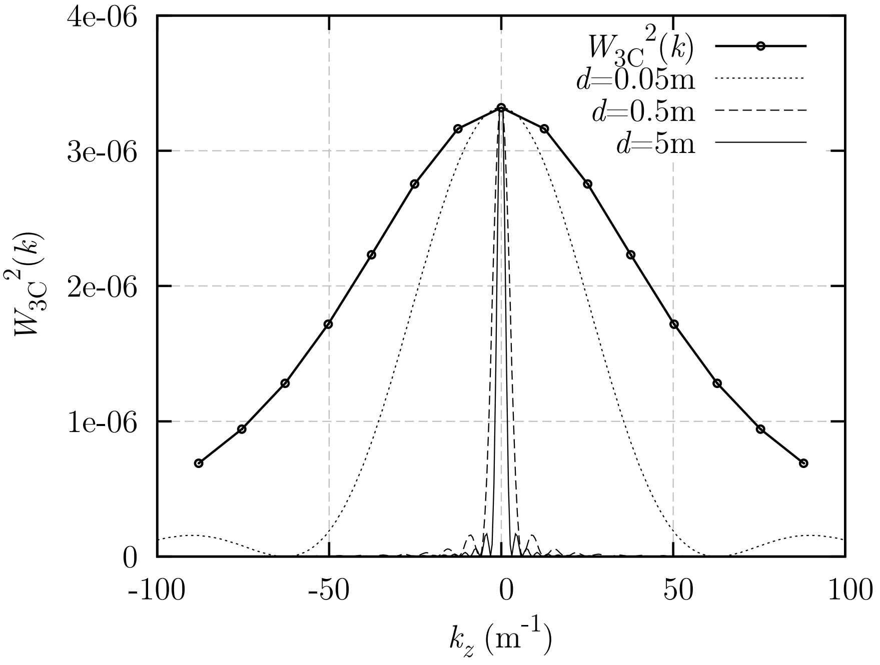

Figure 4.3: Showing the discretised $W_{3C}(\boldsymbol{k})$ spectrum at $k_x = 16\pi$, $k_y = 0$ with varying k_z values, compared with plots of Equation 4.4 to indicate which k_z values are expected to contribute to the noise. Equation 4.4 has been plotted for $d = 0.05$ m, 0.5 m and 5 m, and has been scaled to the maximum value of $W_{3C}(\boldsymbol{k})$.

.

cost would be too high. Instead, the method of Clair *et al.* [109] was used, whereby Δk_z was set to $\Delta k_z = 2\pi/L_{span}$ in order to account for the differences between the 3D non-compact and the 2D compact $W_{3C}(\boldsymbol{k})$ formulations. Here, $L_{span} = 1$ m to provide the noise per unit span. Clair *et al.* used this method to predict the turbulence interaction noise from a 3D airfoil by only including gusts with $k_z = 0$. Therefore, this method is only appropriate if gusts with $k_z \neq 0$ do not contribute to the noise.

An example of the acoustic pressure perturbations from one realisation of the 3D simulation is shown in Figure 4.4.

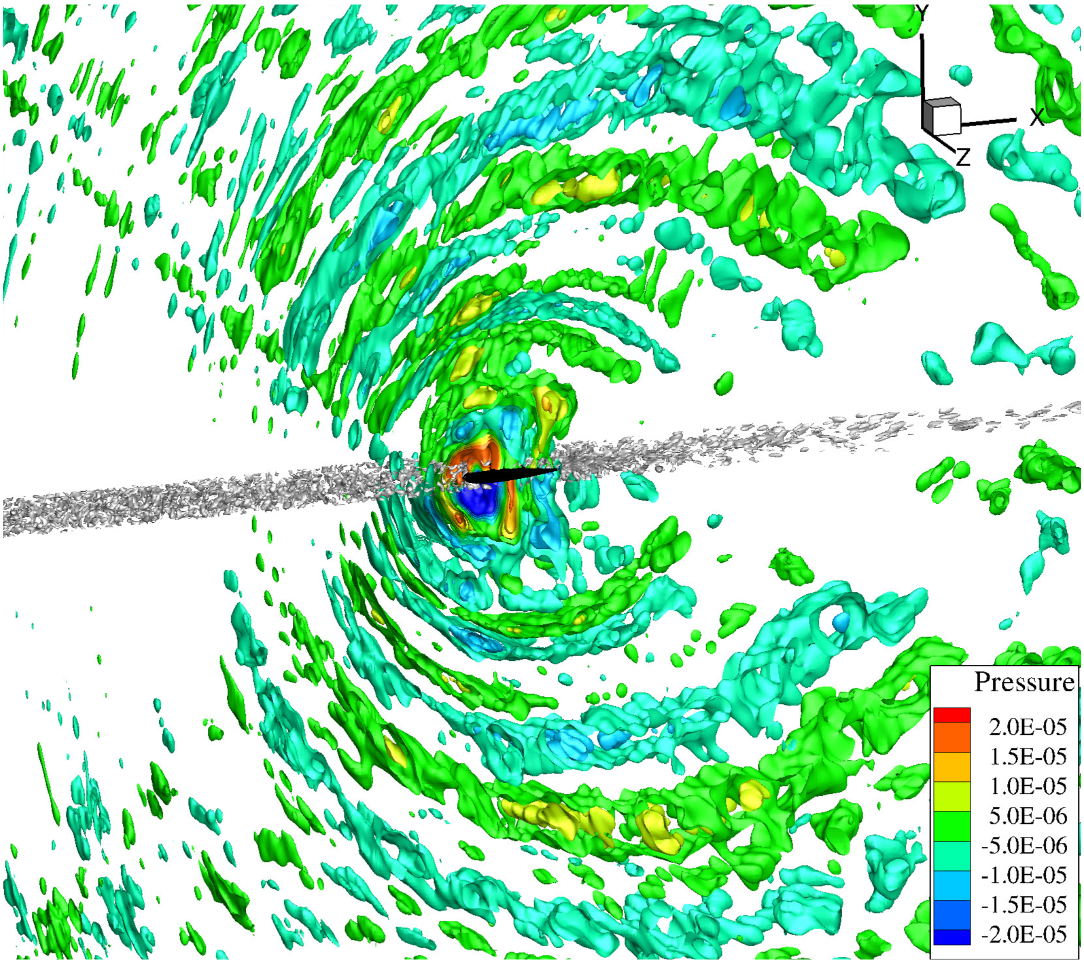

Figure 4.4: Example of the flow-field pressure perturbations. Grey iso-contours show the vorticity magnitude in the plane of the airfoil, and coloured iso-contours show the instantaneous non-dimensional pressure. Quantities are non-dimensional.

4.2.4 Description of Single Velocity-Component Approaches

This chapter aims to show that only gusts with $k_z = 0$ will contribute to the noise from real airfoils. Therefore, we expect the three-component turbulence interaction noise to be similar to the one- and two-component interaction noise if the turbulence spectrum sets $k_z = 0$. This section gives a summary of the one-, two-, and three-component turbulence synthesis approaches before the noise comparisons are made.

Three-component Turbulence Forcing

The three-component turbulence forcing approach requires a 3D simulation, because vortical disturbances are forced in the streamwise, transverse and spanwise directions. The disturbances spatially vary with three wavenumber components, k_x, k_y, and k_z, which requires a large number of Fourier mode summations and consequently makes the three-component approach computationally expensive. The three-component turbulence synthesis approach contains more turbulent energy than the two-component approach due to the inclusion of spanwise disturbances. The disturbances are forced according to Equation 4.1, and the amplitude of the disturbances is set according to Equation 4.2 but with Δk_z set equal to $2\pi/L_{span}$. This approach produces disturbances that are periodic about the largest forced wavelength, so an ensemble average must be made for noise predictions.

Two-component Turbulence Forcing

Only a 2D simulation is required for the two-component approach, which forces disturbances in the streamwise and transverse directions. The disturbances spatially vary with the two wavenumber components k_x and k_y. The disturbances are forced according to Equation 3.1, with amplitudes following Equation 3.2 which assumes that $k_z = 0$. The two-component approach contains less turbulent energy than the three-component approach because it neglects the spanwise disturbances, but contains more energy than the one-component approach because of the additional streamwise disturbances. This approach produces disturbances that are periodic about the largest forced wavelength, so an ensemble average must be made for noise predictions.

One-component Turbulence Forcing

In the one-component turbulence forcing approach, disturbances are forced only in the transverse direction, and spatial variation is dependent on only one wavenumber component, k_x. This approach is also referred to in this project as a single velocity-component modelling approach. This approach is significantly cheaper than the two- and three-component approaches because only one realisation is needed for noise predictions due to the orthoganality of the wavefronts of the forced disturbance. The one-component approach contains less turbulent energy than the two- and three-component approaches because it only contains disturbances in the transverse direction.

The one-component turbulence forcing approach is based on the CAA method with harmonic gust forcing that was described in Chapter 2. However, some modification is required in order to synthesise 1D turbulence. The approach described in Chapter 2 forced gusts with a constant amplitude set to $v_0 = 0.01U_x$, whereas here the amplitudes should be set to follow a turbulence spectrum. Therefore, the v_0 term in Equation 2.15 was replaced with the 1D Liepmann velocity spectrum $W_{1D}(k_x, k_z = 0)$.

The 1D Liepmann spectrum was obtained by integrating Equation 3.2 between the limits of $k_y = \pm\infty$ to give

$$W_{1C}(k_x, k_z = 0) = \sqrt{\frac{3\overline{w^2}\Lambda^2}{4\pi}\frac{\Lambda^2 k_x^2}{(1 + \Lambda^2 k_x^2)^{2.5}}}. \tag{4.5}$$

Additional description and derivation of Equation 4.5 is given in Appendix B. For this single velocity-component modelling study, Equations 4.5 and 3.2 were discretised similarly to Equation 4.2. For both the one- and two-component approaches $k_x^{lim} = 16\pi$ m^{-1}. For the two-component approach, k_y^{lim} was set to be 75 m^{-1}. Therefore, a small difference in the total turbulent energy existed between the one-component turbulence approach and both the two- and three-component approaches. The W_{1C} spectrum assumed an integration of W_{2C} between $k_y = \pm\infty$, whereas the others used $k_y^{lim} = 75$ m^{-1}. The same 2D computational mesh was used for the two- and one-component turbulence cases, and consisted of approximately $400,000$ cells.

An example of the one-, two-, and three-component instantaneous turbulent vorticities is shown in Figure 4.5.

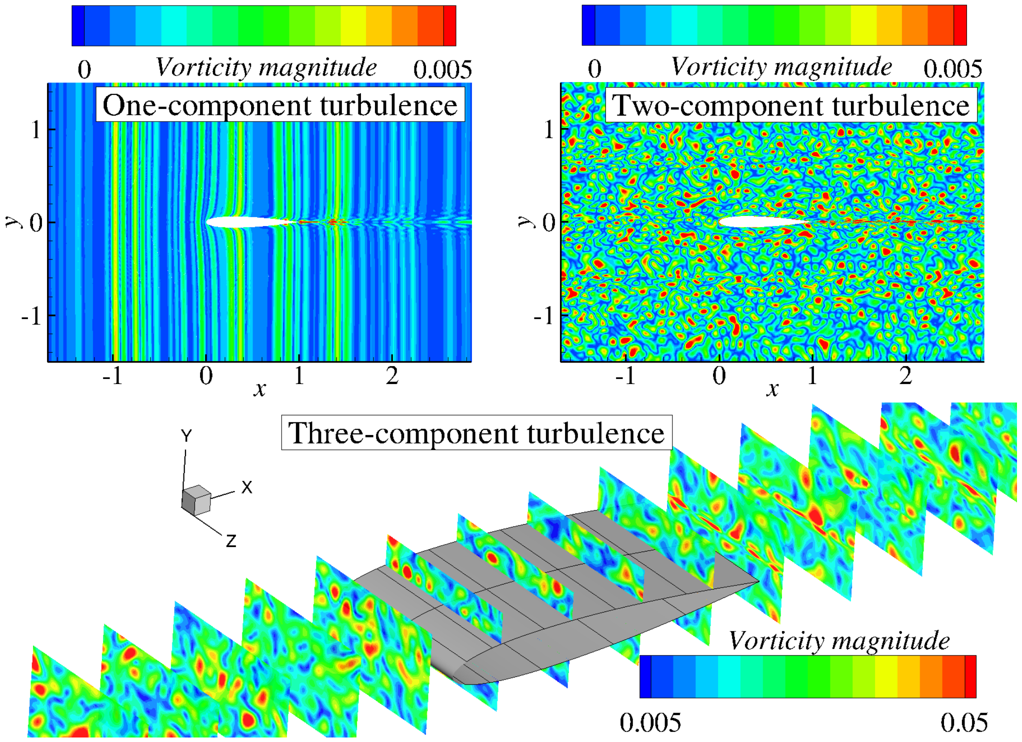

Figure 4.5: Example flow-field vorticity for the one-, two-, and three-component turbulence synthesis approaches. The two- and three-component examples show one realisation of the turbulent field. Quantities are non-dimensional.

4.3 Results

4.3.1 Comparison of Noise Predictions

The far-field noise was predicted by the CAA method, using one-, two-, and three-component turbulent interactions with a NACA 0012 airfoil. A comparison of the SPL spectra predictions from each approach, and from Amiet's flat plate theory, is shown in Figure 4.6.

Figure 4.6 shows that very similar noise predictions are given by the one-, two-, and three-component turbulence synthesis approaches at both of the observer angles studied. The difference in noise between predictions from the three approaches is usually less than 1 dB. Additional comparisons are given in Figure 4.7, which shows

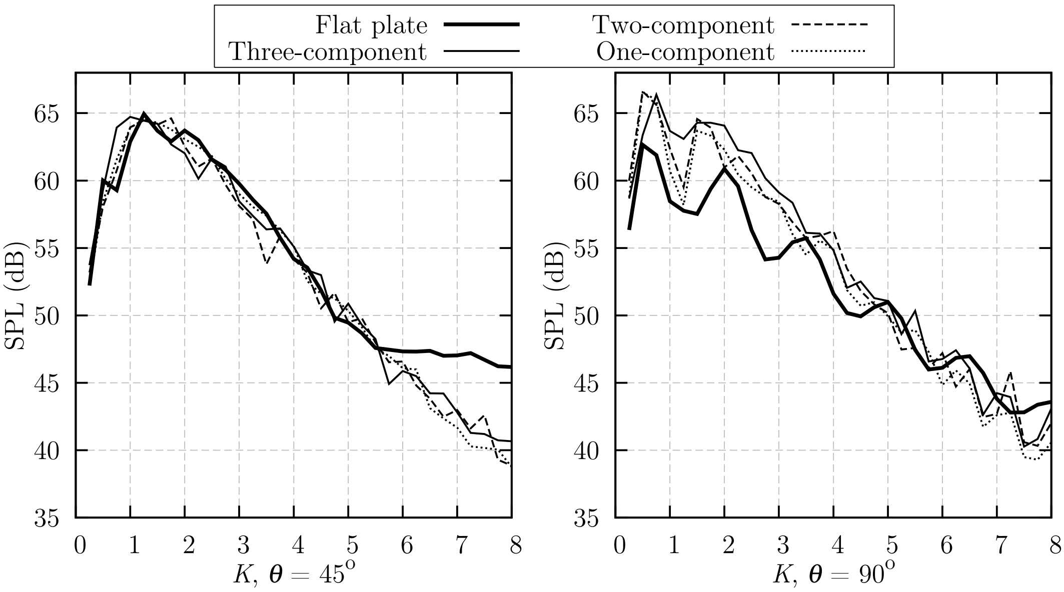

Figure 4.6: SPL Predictions at observer positions of $\theta = 45^{\circ}$ (left) and $\theta = 90^{\circ}$ (right) due to a NACA 0012 airfoil interacting with one-, two-, and three-component turbulence, compared with Amiet's analytical theory.

a comparison of the PWL noise, and Figure 4.8 which compares the SPL directivity from each turbulence synthesis approach. Close agreement is seen between the three approaches for PWL predictions and for SPL directivity predictions. Therefore, Figures 4.7 and 4.8 both show that similar predictions can be obtained by using a single velocity-component modelling approach as opposed to synthesising 3D turbulence. Small differences in SPL predictions are seen between the three approaches at acute upstream values of θ, where the one-component approach predicts a lower amplitude, but these may be due to stochastic errors from the turbulence synthesis process.

Figures 4.6, 4.7, and 4.8 demonstrate that a reduced modelling approach can provide accurate noise predictions for real symmetric airfoils at zero AoA. This implies that turbulence interaction noise is not sensitive to the presence of streamwise and spanwise disturbances, which can be neglected without significant loss of accuracy.

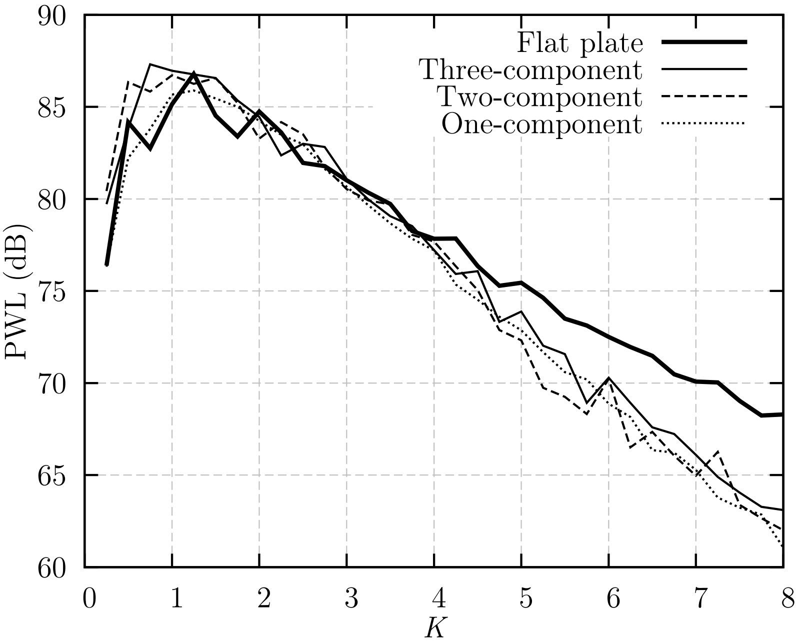

Figure 4.7: PWL predictions due to a NACA 0012 airfoil interacting with one-, two-, and three-component turbulence in $M = 0.5$ flow, compared with Amiet's analytical theory.

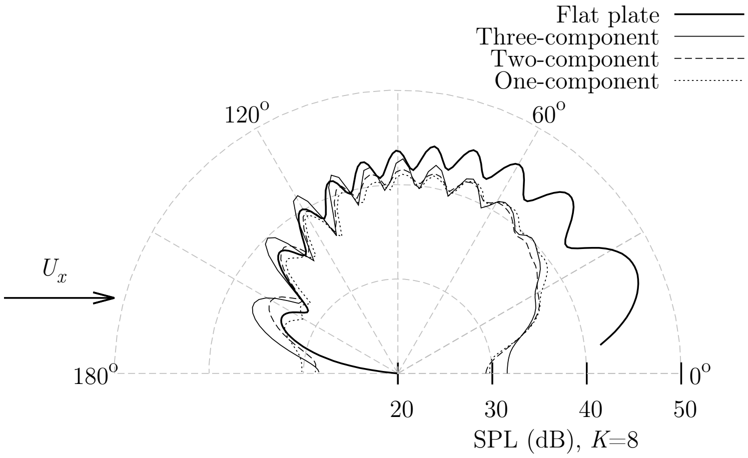

Figure 4.8: SPL directivity predictions at $K = 8$ due to a NACA 0012 airfoil interacting with one-, two-, and three-component turbulence in $M = 0.5$ flow, compared with Amiet's analytical theory.

4.3.2 Comparison of the Computational Cost

This chapter has demonstrated that accurate turbulence interaction noise predictions can be made for real airfoils by using a single velocity-component modelling approach. This is beneficial because it allows significants saving in computational cost. Table 4.1 compares the computational expense needed for the one-, two-, and three-component turbulence synthesis approaches. The three cases were each run in SotonCAA using the Iridis4 High Performance Computing Facility at the University of Southampton.

A single parameter was desired to compare the total expense of the three simulations. Therefore, in Table 4.1, the total expense is calculated as *total expense* = *time for 1 realisation* × *no realisations* × *number of cores.*

Approach	**No. cells**	**No. cores**	**Time for one realisation (s)**	**No. realisations**	**Total expense (s)**
One-component	$400,116$	16	3716	1	$59,456$
Two-component	$400,116$	16	4053	20	$1,296,000$
Three-component	$27,907,192$	192	$77,725$	20	$298,464,000$

Table 4.1: Comparison of computational expense of the one-, two-, and three-component turbulence synthesis approaches.

A large difference in computational expense is seen between the three approaches. The three-component approach is most expensive due to the significantly larger computational grid that is required. The one-component approach makes cost savings by having a smaller computational grid, and by requiring only one realisation because the disturbance wavefronts are orthogonal to one-another. The result is that the one-component approach is approximately $5,000$ times cheaper to compute than the three-component approach.

The difference in computational expense between one- and three-component simulations may be less extreme if an alternative turbulence synthesis method were used. However, testing the computational expense of alternative turbulence synthesis methods is beyond the scope of the current study. Additionally, a smaller number of realisations could be used in the two-, and three-component approaches in order to reduce their computational time. Clair *et al.* [109], for example, used 10 realisations. However, 20 realisations were used in this study for consistency with Chapter 3.

4.4 Detailed Comparison Between One- and Two-Component Approaches

In order to thoroughly study the ability of the single velocity-component modelling approach to predict the turbulence interaction noise of real airfoils, further tests were made with varying airfoil geometry. These tests only compared predictions from the one- and two-component turbulence synthesis approaches in order to reduce the computational cost.

For this study, the noise due to a NACA 0006, NACA 0008, NACA 0010, and a NACA 0012 airfoil interacting with turbulence with $\Lambda = 0.07$ m, and $\sqrt{\overline{w^2}} = 0.04U_x$ at $M = 0.5$ was predicted. For the tests described in this section, the Liepmann turbulence spectrum was discretised using the parameters discussed in Chapter 3. This was done to give a better frequency resolution than was permitted by the single airfoil case comparison in Section 4.3.

Figure 4.9 shows the PWL spectra predictions from the one- and two-component approaches for different airfoil thicknesses. A close match is seen between the noise from the two forcing approaches for all airfoils up to $K = 8$. This agrees with the results from the single case study in Section 4.3. However, for the thick airfoils at $K > 8$, the one-component forcing approach appears to under-predict the noise by up to 2 dB. This under-prediction becomes larger with increasing reduced frequency. This result suggests that while the transverse disturbances are usually dominant for turbulence interaction noise, the additional energy contained in the streamwise disturbances begins to have an effect in cases where there is both high frequency content ($K > 8$) and a thick airfoil ($t > 0.08c$).

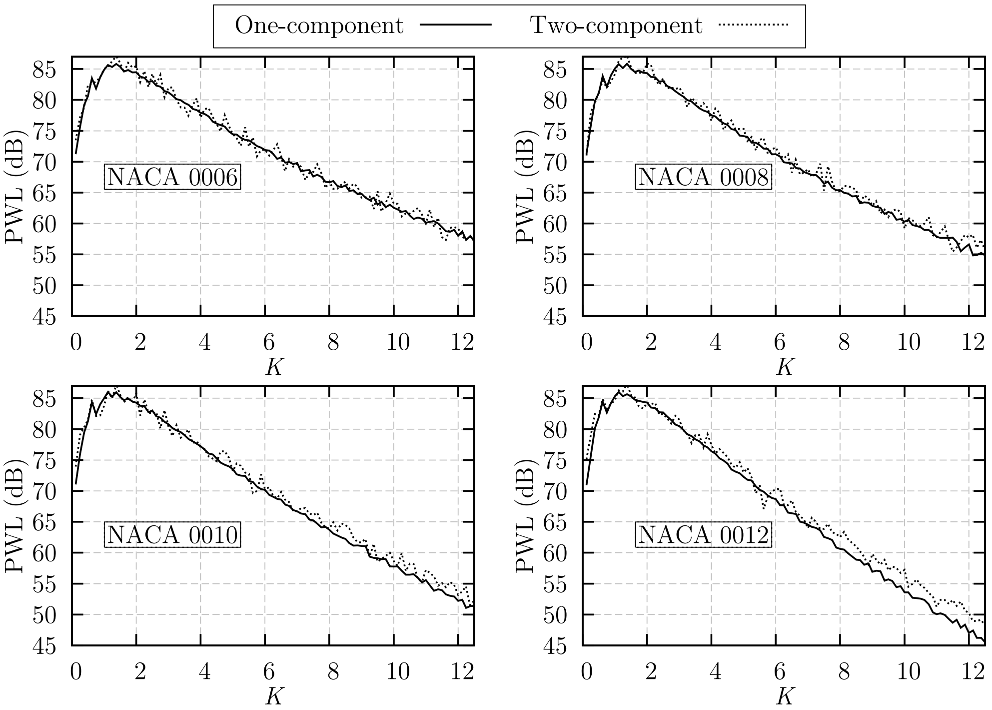

Figure 4.9: Comparison of PWL noise predictions for airfoils with 6%, 8%, 10%, and 12% thickness interacting with one- and two-component turbulence at $M = 0.5$.

Figure 4.10 shows SPL directivity predictions from the different airfoils and gust forcing approaches at $K = 12$. This value of K was chosen to be in the high reduced frequency region where the one- and two-component noise predictions differ. Figure 4.10 shows that the directivity agreement between the two approaches is close for all airfoils, except at acute upstream angles for the NACA 0010 and NACA 0012 cases where $\theta > 150°$. In this region, it appears that the one-component approach does not accurately predict the amplitude of the directivity lobe. This under-prediction is the cause of the PWL under-prediction seen in Figure 4.9. The lobe is likely to be caused by the interaction of the streamwise disturbances with the frontal area of the thick airfoils. The one-component approach does not include streamwise disturbances, and therefore would not include this noise source.

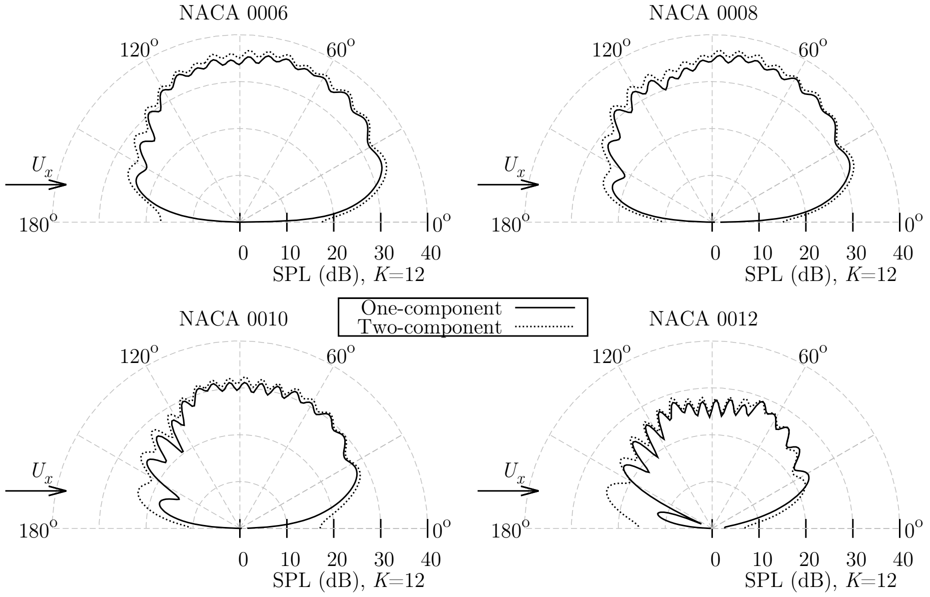

Figure 4.10: Comparison of SPL directivity predictions for airfoils with 6%, 8%, 10%, and 12% thickness interacting with one- and two-component turbulence at $M = 0.5$.

4.5 Summary

The CAA method has been extended to model three-component, homogeneous, and isotropic turbulence interacting with a three-dimensional airfoil with constant and infinite span. Turbulence interaction noise has been predicted using the new three-component turbulence for one airfoil geometry, and for additional airfoils using the previously described two- and one-component turbulence forcing approaches. This has been done to test the relative importance of transverse, streamwise, and spanwise gust disturbances on the noise.

It has been shown that the transverse disturbances are dominant in the noise generation process, and that the streamwise and spanwise disturbances have only a small effect. This means that in many situations a one-component turbulence forcing approach can be used without loss of accuracy in order to save computational expense. A similar hypothesis was first suggested by Amiet [30] for modelling flat plate turbulence interaction noise, but the result has been reproduced here for airfoils with real geometry.

Spanwise disturbances can be ignored if the airfoil has a constant span that is significantly larger than the turbulence integral length-scale. Streamwise disturbances can be ignored below a high frequency limit if the airfoil is sufficiently thin. This study has shown good agreement when neglecting streamwise disturbances for frequencies in the range $K < 8$ and for airfoil thicknesses below 10% of the chord. ($t = 0.1c$). If the one-component turbulence forcing approach is used outside these constraints, a 2 dB under-prediction in noise has been observed by this study. Is is beneficial to use the single velocity-component modelling approach where possible, because it is computationally cheaper than the two- or three-component approaches.

This analysis is currently limited to the modelling of symmetric airfoils with constant span at zero AoA. An investigation of the validity of single velocity-component modelling for non-symmetric airfoils at non-zero AoA is detailed in Chapter 5.

Chapter 5

Modelling Angle-of-Attack and Camber

Thus far, this work has modelled the turbulence interaction noise of symmetric airfoils at zero angle-of-attack (AoA). The effects of airfoil camber and AoA have been previously neglected because authors such as as Staubs [61], Devenport *et al.* [62], Paterson and Amiet [63], and Moreau *et al.* [67] have shown the effects to be small for airfoils interacting with isotropic homogeneous turbulence. Devenport *et al.* [62] report a change in noise of less than 1 dB for a NACA 0012 airfoil varying between $\alpha = 0°$ and 12°. Moreau *et al.* [67] report no noticeable difference in the noise measured between geometrical AoA's of $\alpha = 0°$ and 15° for a NACA 0012 airfoil. However, Devenport *et al.* [62] note that the airfoil response function is affected by AoA, but the effects are counterbalanced by an isotropic turbulence spectrum such that the noise appears insensitive to AoA.

In Chapter 4 it was shown that the turbulence interaction noise of symmetric airfoils at zero AoA can be accurately modelled by representing turbulence with only transverse disturbances. This single velocity-component modelling approach allows computational savings in comparison to modelling more complex turbulence. Therefore, it is useful to investigate whether single velocity-componental modelling is also applicable to airfoils with non-zero values of camber and AoA.

In order to assess the accuracy of single velocity-component modelling when including AoA or camber, the two parameters are studied independently in this chapter. Because the three-component turbulence synthesis that was introduced in Chapter 4 is computationally expensive, this chapter is limited to considering the one- and two-component approaches. It is assumed that the spanwise disturbances are unimportant in this study (as was found in Chapter 4), because there are no variations in airfoil geometry in the spanwise direction.

5.1 Effects of Angle-of-Attack on the Noise

This section investigates the effects on turbulence interaction noise predictions when non-zero AoA values are introduced. A NACA 0006 airfoil and a NACA 0012 were interacted with both one- and two-component turbulence with $\Lambda = 0.07$ m and $\sqrt{\overline{w^2}} = 0.04U_x$, in $M = 0.3$ flow. Airfoil AoA values of $\alpha = 0^\circ, 2^\circ, 4^\circ$, and 6° were used. The values of M and α were limited in order to avoid simulation stability issues that are associated with transonic meanflow speeds. The local Mach number in the vicinity of the airfoil leading edge was found to approach unity if larger values of M or α were used.

The airfoils that were used in this study are shown in Figure 5.1, and a schematic of the configuration is shown in Figure 5.2. The airfoil leading edge was used as the centre of rotation. This was chosen so that the dominant noise generating region (the leading edge) would not move vertically between the different airfoil configurations.

5.1.1 Modelling the meanflow

As was done previously in this thesis, the meanflow around the airfoil was computed using an inviscid CFD solver. The meanflow solutions for a NACA 0006 airfoil at $\alpha = 2^\circ, 4^\circ$, and 6° are shown in Figure 5.3.

The assumption of an inviscid meanflow may not be valid when considering airfoils at large AoA, because the suction-side boundary layer will become large and will

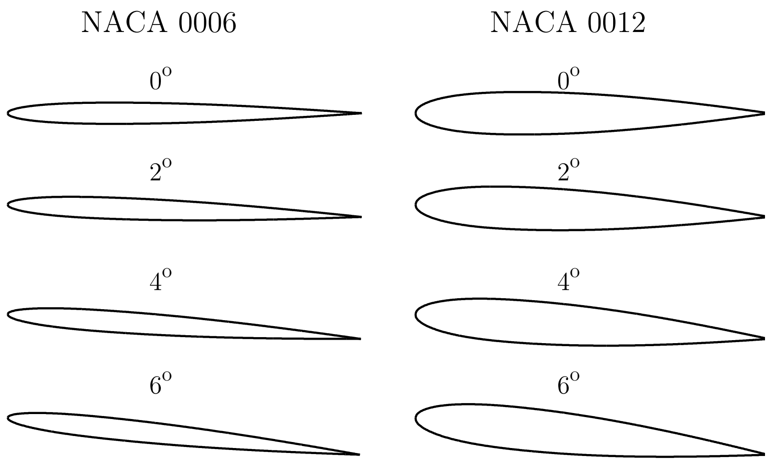

Figure 5.1: The various airfoil AoA values used in the study.

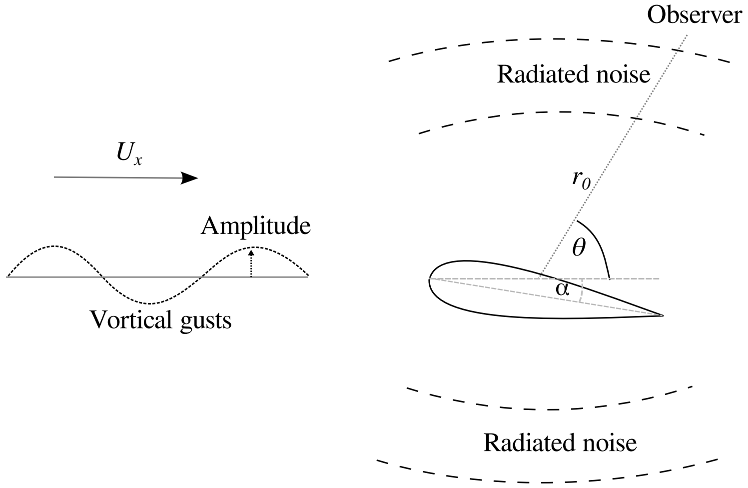

Figure 5.2: A schematic of the AoA configuration. The centre of rotation was set at the airfoil leading edge.

potentially separate from the airfoil surface. This would then affect the propagation of both the noise and the vortical disturbances. This situation would contain regions of highly sheared flow, and would not be modelled well by the LEEs if it was included because highly sheared meanflow solutions can generate instabilities

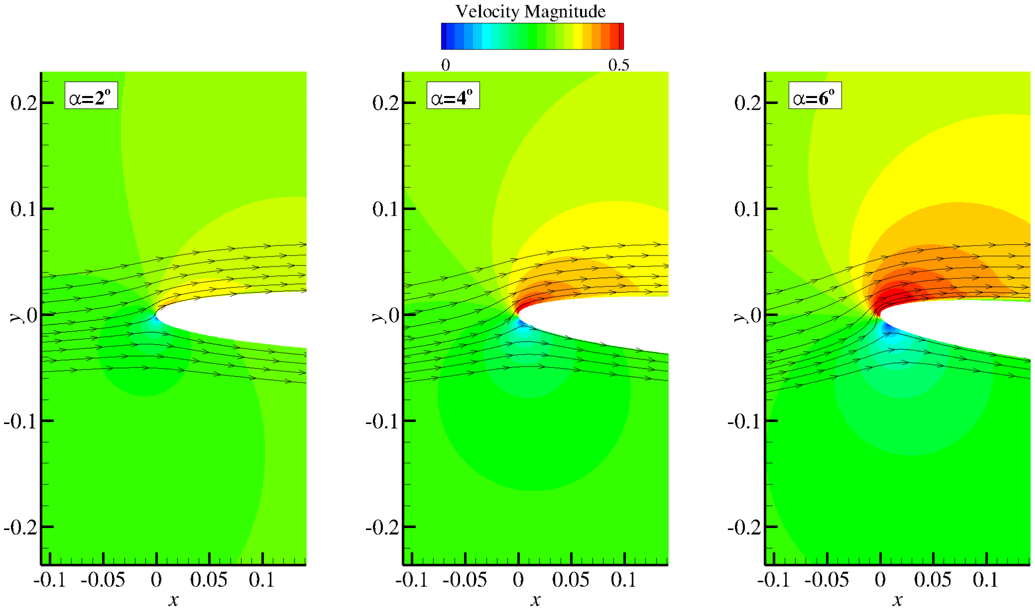

Figure 5.3: Comparison of mean flow-fields for a NACA 0006 airfoil in $M = 0.3$ flow at $\alpha = 2°$, $\alpha = 4°$, and $\alpha = 6°$.

in LEE simulations.

Methods do exist to provide stable LEE computations in sheared flows (see Refs. [124–127]), such that it may be possible to use the LEEs for airfoils at high AoA. However, the presence of the sheared flow region would also deform the vortical disturbances that are being propagated. This deformation of the frozen turbulent disturbances would create noise that would interfere with simulation results.

In order to avoid problems with the deformation of turbulent disturbances, and with numerical stability, the boundary layer effects were neglected by using an inviscid meanflow solution. Future work to investigate the effects of viscosity on turbulence interaction noise when airfoils are at large AoA would be useful, but this is beyond the scope of the current study.

5.1.2 Turbulent Interaction Noise Predictions

Figure 5.4 compares noise predictions from the CAA method for a NACA 0006 airfoil at $\alpha = 0°$ and for $\alpha = 4°$. These predictions have been made with both the one- and two-component turbulence forcing approaches, and are also compared with predictions from analytical theory. The comparison is made at observer angles of $\theta = 45°$ and $\theta = 315°$.

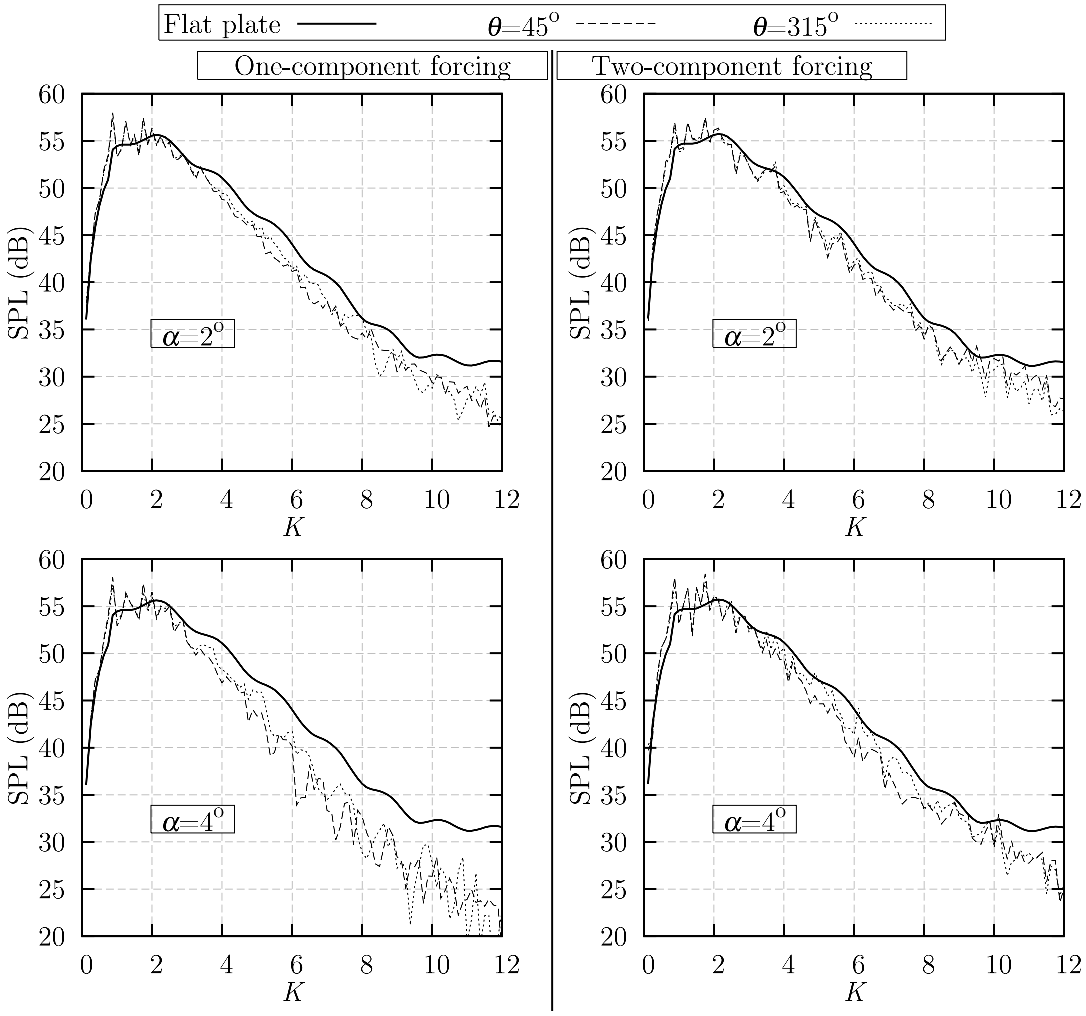

Figure 5.4: Comparison of SPL predictions made at $\alpha = 2°$ and $4°$ using the one- and two-component turbulence synthesis methods, for NACA 0006 airfoil in $M = 0.3$ flow.

Figure 5.4 shows that when two-component turbulence forcing is used, there is little effect on the noise due to the change from $\alpha = 2°$ to $\alpha = 4°$. Additionally, there is also negligible difference between predictions from the suction side ($0° < \theta < 180°$) and from the pressure side ($180° < \theta < 360°$). This suggests that the noise is not sensitive to AoA, which is in agreement with previous literature.

The predictions made with the one-component turbulence synthesis approach show different behaviour to the two-component predictions. In this case, a drop in SPL is seen between the $\alpha = 2°$ and $\alpha = 4°$ cases at high frequencies. This does not agree with previous literature and is not thought to be an accurate representation of turbulence interaction noise behaviour with AoA. Figure 5.4, therefore, suggests that it is not valid to simplify the turbulence to a one-component disturbance when airfoils are considered at AoA.

Figure 5.5 plots the NACA 0006 PWL predictions from the one- and two-component turbulence synthesis approaches for cases with varying AoA. The reduction in noise at high frequencies that is predicted by the one-component approach is clearly shown in this Figure. It appears that the one-component approach will under-predict the noise for AoA values above $\alpha = 2°$, and for reduced frequency values above about $K = 4$. In order to accurately predict the noise outside this range, a two-component disturbance should be used, comprising of both streamwise and spanwise disturbances.

The comparison was also made for NACA 0012 airfoils, and the PWL predictions are shown in Figure 5.6. The one-component approach also gives inaccurate predictions of the noise from a NACA 0012 airfoil at AoA. The noise is under-predicted at $K = 12$ by approximately 10 dB in comparison to the two-component approach, for both the NACA 0006 and NACA 0012 airfoils. Therefore, the effects of AoA and the accuracy of the single velocity-component modelling approach, appear to be independent of airfoil thickness.

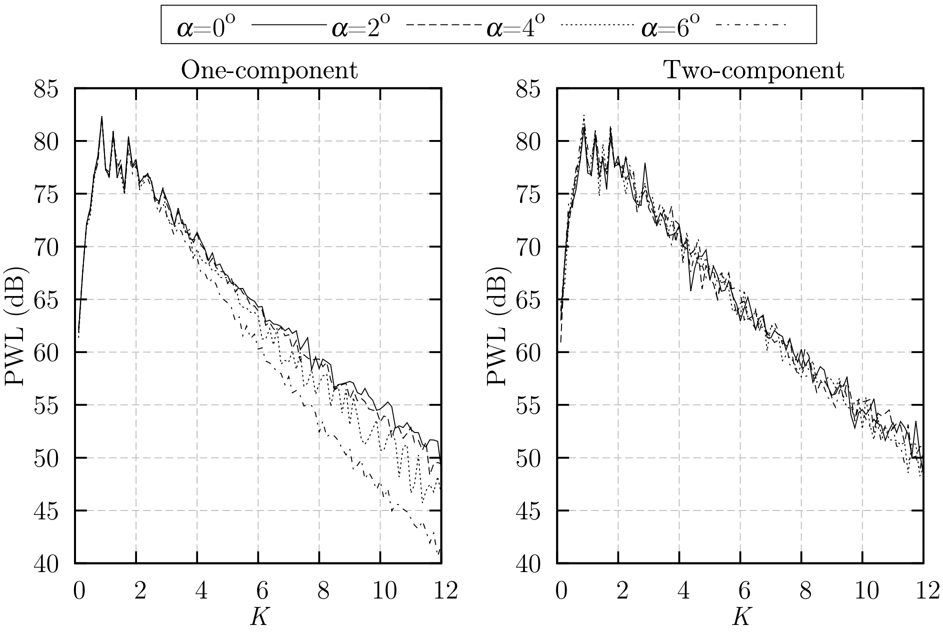

Figure 5.5: Comparison of PWL predictions for a NACA 0006 airfoil with varying α, made by the one- and two-component turbulence forcing approaches.

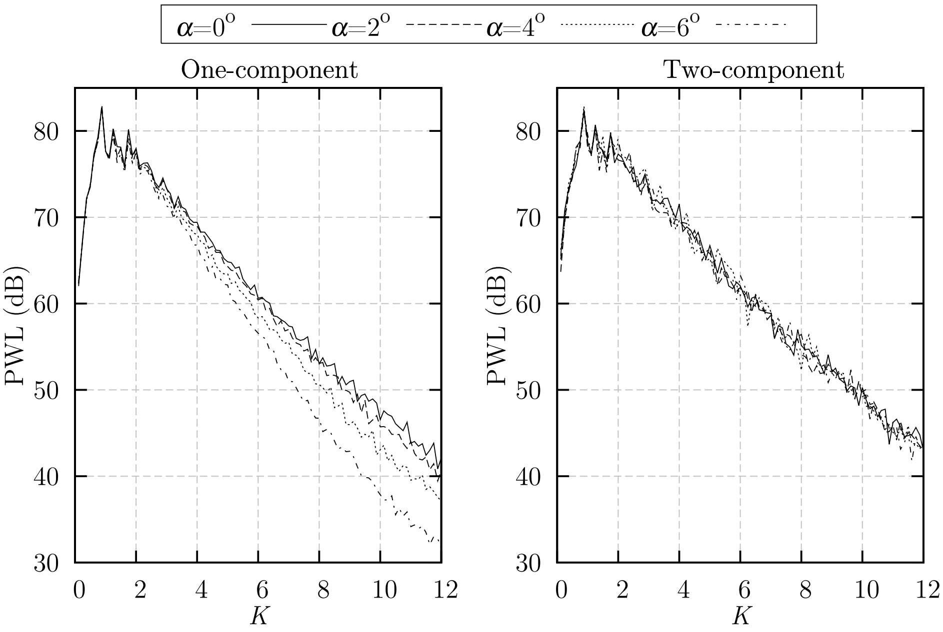

Figure 5.6: Comparison of PWL predictions for a NACA 0012 airfoil with varying α, made by the one- and two-component turbulence forcing approaches.

5.1.3 Mechanism

As an initial investigation to find the reason why the single velocity-component modelling approach does not support airfoils at AoA, the flow-field p_{rms} and U_{rms} were plotted in the region around the leading edge of a NACA 0006 airfoil for $\alpha = 0°$ and $\alpha = 6°$, for both the one- and two-component turbulence synthesis approaches. This was done at a reduced frequency of $K = 8$. Figure 5.7 shows the p_{rms} flow-field, and Figure 5.8 shows the U_{rms} flow-field.

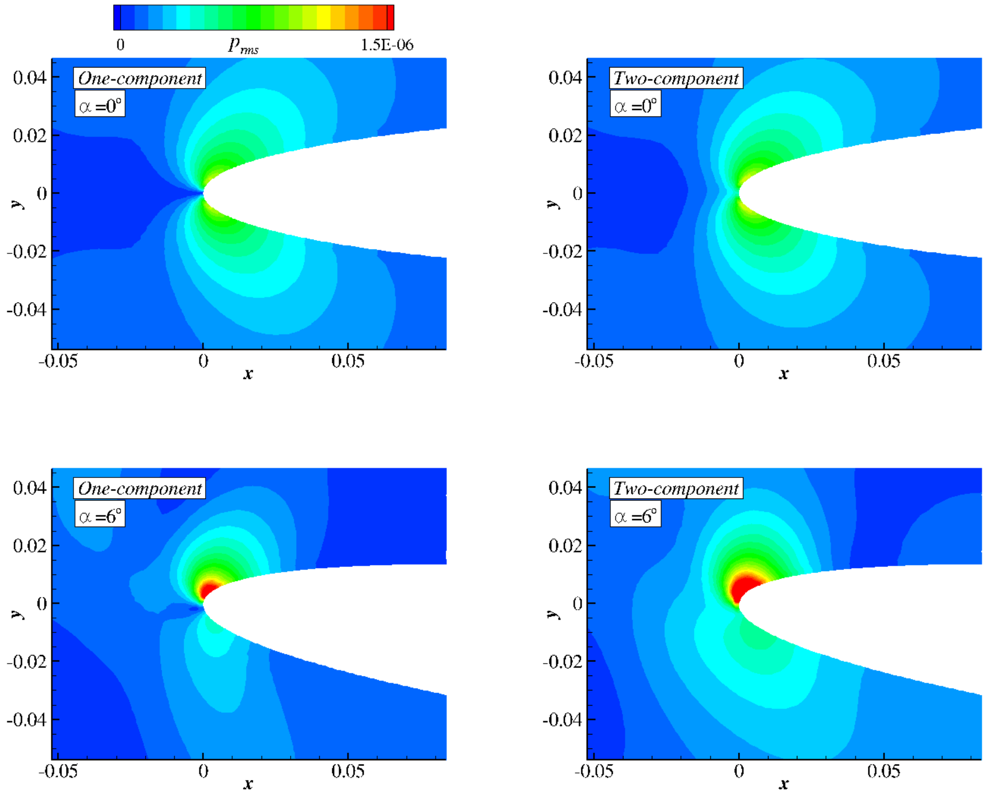

Figure 5.7: Contours of the non-dimensional p_{rms} at the leading edge of a NACA 0006 airfoil, for the one- and two-component forcing approaches at $K = 8$ and for $\alpha = 0°$ and $\alpha = 6°$.

Figure 5.7 shows that for $\alpha = 0°$, there is little difference between the flow-field pressure response seen from the one- or two-component approaches. However, at $\alpha = 6°$, the two-component response is significantly larger than the one-component response. Additionally, the position of peak response has moved to the suction side of the airfoil, and the position of least response has moved to the approximate location of the stagnation region.

The behaviour of the flow-field U_{rms} response is similar to the p_{rms} behaviour. At $\alpha = 6°$ the U_{rms} values predicted by the two-component approach are stronger than those from the one-component approach. This suggests that it is the change in U_{rms} that causes changes in the p_{rms} response, as was previously found in Chapter 2.

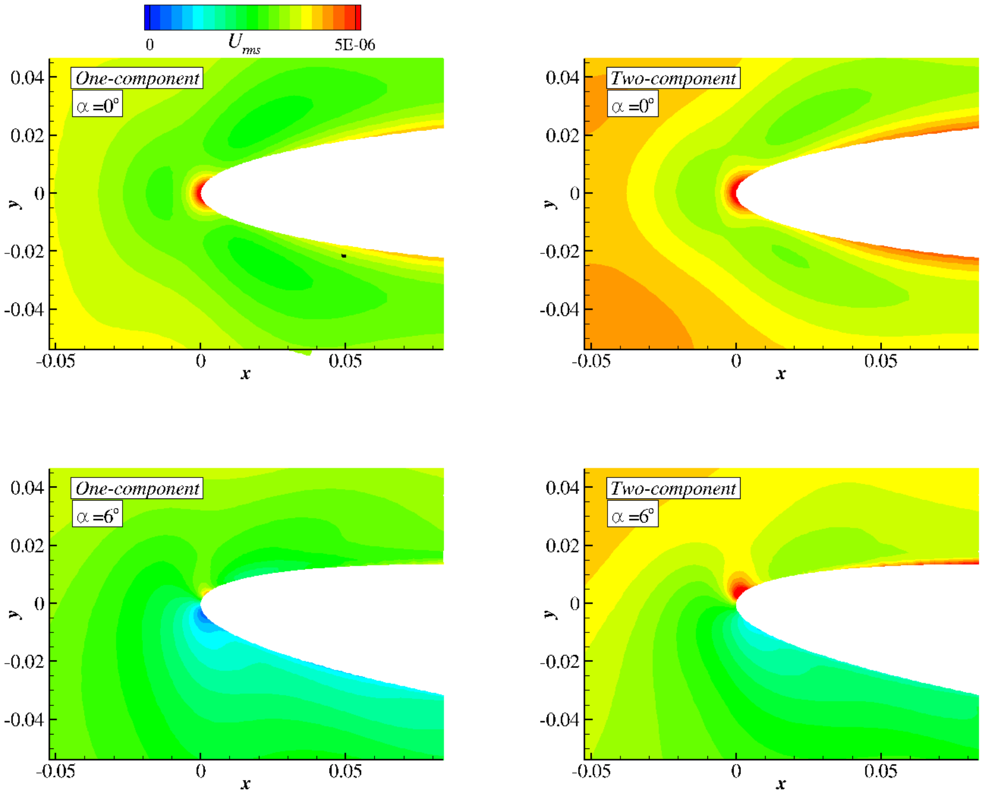

Figure 5.8: Contours of non-dimensional U_{rms} at the leading edge of a NACA 0006 airfoil, for the one- and two-component turbulence synthesis approaches at $K = 8$ and for $\alpha = 0°$ and $\alpha = 6°$.

In order to better understand the noise interaction process for airfoils at AoA, the AoA study was repeated by using a modified CAA turbulence synthesis method. The turbulence synthesis was altered to use only a single k_y wavenumber in 47 separate simulations, so that the noise from the turbulence interaction was decomposed into separate contributions from each k_y mode. This method is more expensive than the original turbulence synthesis method, because it requires a separate simulation for each of the 47 k_y wavenumbers that were present in the simulation. However, this new approach has the advantage of allowing the independent noise contribution from each k_y wavenumber to be investigated.

The contribution to PWL from each combination of k_x and k_y wavenumber is shown in Figure 5.9.

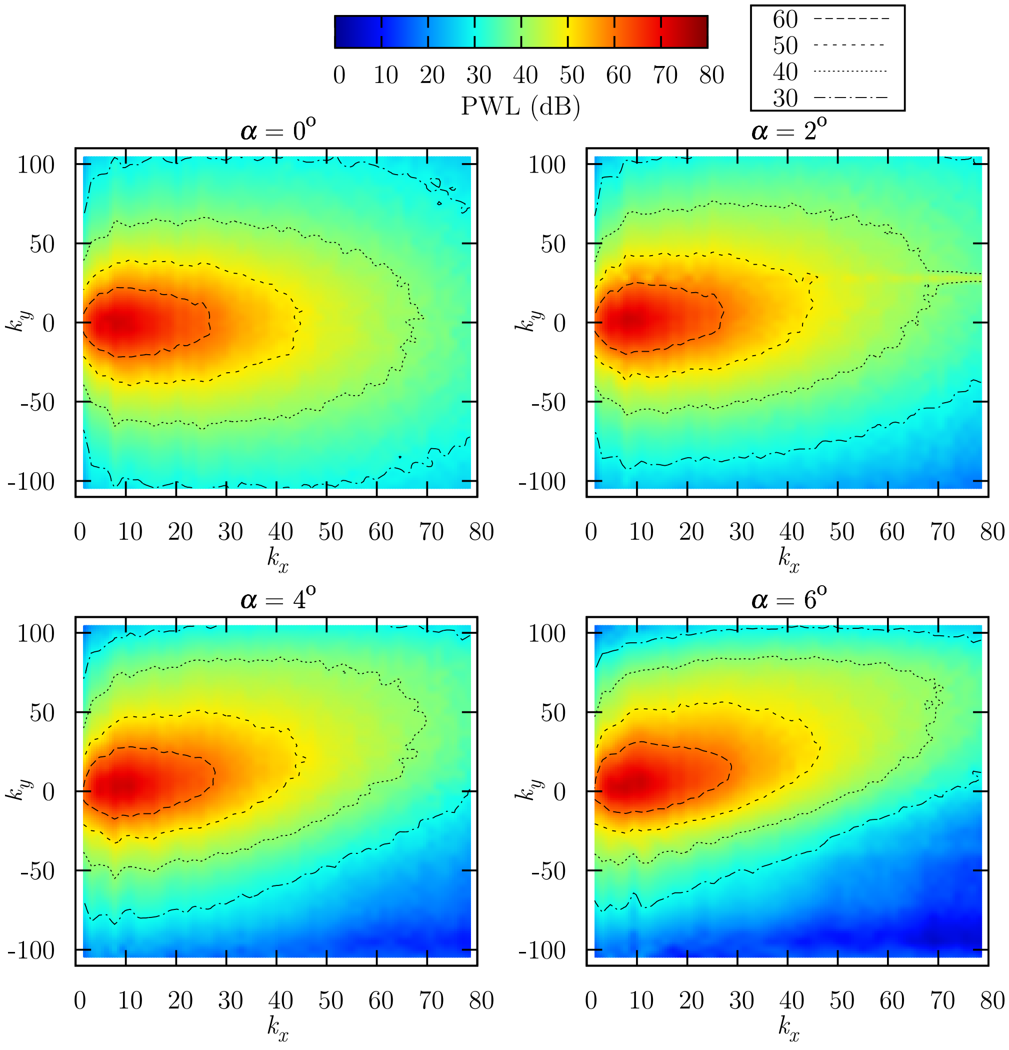

Figure 5.9: Contours of PWL with varying k_x and k_y wavenumbers, for a NACA 0006 airfoil at $\alpha = 0°$, $2°$, $4°$, and $6°$.

Figure 5.9 shows that the peak response occurs at low k_x values and around $k_y = 0$, which follows the shape of the turbulence spectrum that was plotted earlier in Figure 3.1. At $\alpha = 0°$, the peak response is found at $k_y = 0$ for all values of k_x. However, as α increases, the peak PWL value is found at non-zero values of k_y. This effect appears to increase with increasing k_x. For example, at $k_x = 50$ m^{-1} in the $\alpha = 6°$ case, the peak value is found at approximately $k_y = 25$ m^{-1}. Therefore, it seems that the effect of AoA is to shift the range of k_y wavenumbers at which a significant noise response occurs.

To allow some quantitative analysis, Figure 5.10 shows the P and PWL k_y spectrum response at a single reduced frequency of $K = 8$ (or $k_x = 50.26$ m^{-1}) with varying α. Again, the peak response is seen to shift towards positive k_y values with increasing α. Although the response is shifted sideways, the amplitude of the peak response does not change significantly.

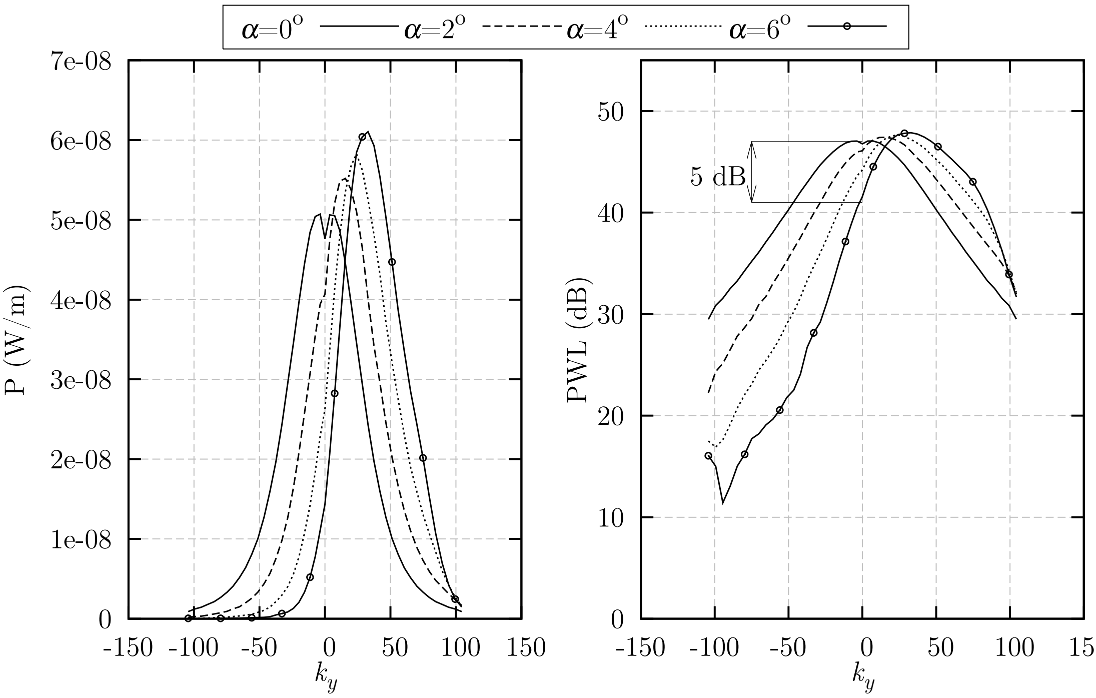

Figure 5.10: Sound power and PWL due to different k_y wavenumbers at $K = 8$, for a NACA 0006 airfoil at $\alpha = 0°$ to $6°$.

The one-component turbulence synthesis approach limits itself to considering gusts with $k_y = 0$. When $\alpha = 0°$, the peak response is found at $k_y = 0$. However, in a case with non-zero AoA, the peak response is shifted in the k_y spectrum such that a simulation at $k_y = 0$ will not capture the peak response, and will therefore predict a lower sound. Figure 5.10 shows that the difference in PWL at $k_y = 0$, caused by the shift in peak response, is about 5 dB at $\alpha = 6°$. This 5 dB under-prediction of the peak level explains the 5 dB under-prediction that is seen by the one-component approach at $K = 8$ in the PWL spectra in Figure 5.5.

As a result of the shift of the response in the k_y spectrum, it is not valid to use a single velocity-component modelling approach for significant values of α for predictions at high reduced frequency. As shown in Figure 5.5, the results from the one-component turbulence synthesis approach are valid for $\alpha \leq 2°$ and $K \leq 4$. A two-component turbulence synthesis approach should be used for situations that fall outside these constraints. A single velocity-component modelling approach that assumes $k_y \neq 0$ may allow the accurate modelling of airfoils with AoA. However, attempts to predict the k_y position of the peak PWL value have thus far been unsuccessful.

5.2 Study of the Mechanism using Harmonic Gusts

Section 5.1.3 has shown that the spectrum of airfoil response for turbulence interaction noise is shifted in k_y by the presence of a non-zero airfoil AoA. This section aims to develop a more complete understanding of this process by investigating why the airfoil response spectrum is shifted in this way. In this section, harmonic gusts with constant amplitude are used in order to remove any effects that the turbulence spectrum might have on the results shown in Section 5.1.3. The amplitude of the harmonic gusts in this section was set to $v_0 = 0.01U_x$, and the study considered a NACA 0006 airfoil.

The P and PWL response at all combinations of k_x and k_y frequency was examined again with varying AoA. However, in this repeated test, harmonic gusts with constant amplitude were used instead of gusts which follow a turbulence spectrum. This is a test of the airfoil leading edge noise response to various angles of skewed gust at each k_x frequency. Figure 5.11 shows contours of PWL at various k_x and k_y frequencies, for α values ranging between $\alpha = 0°$ and $6°$.

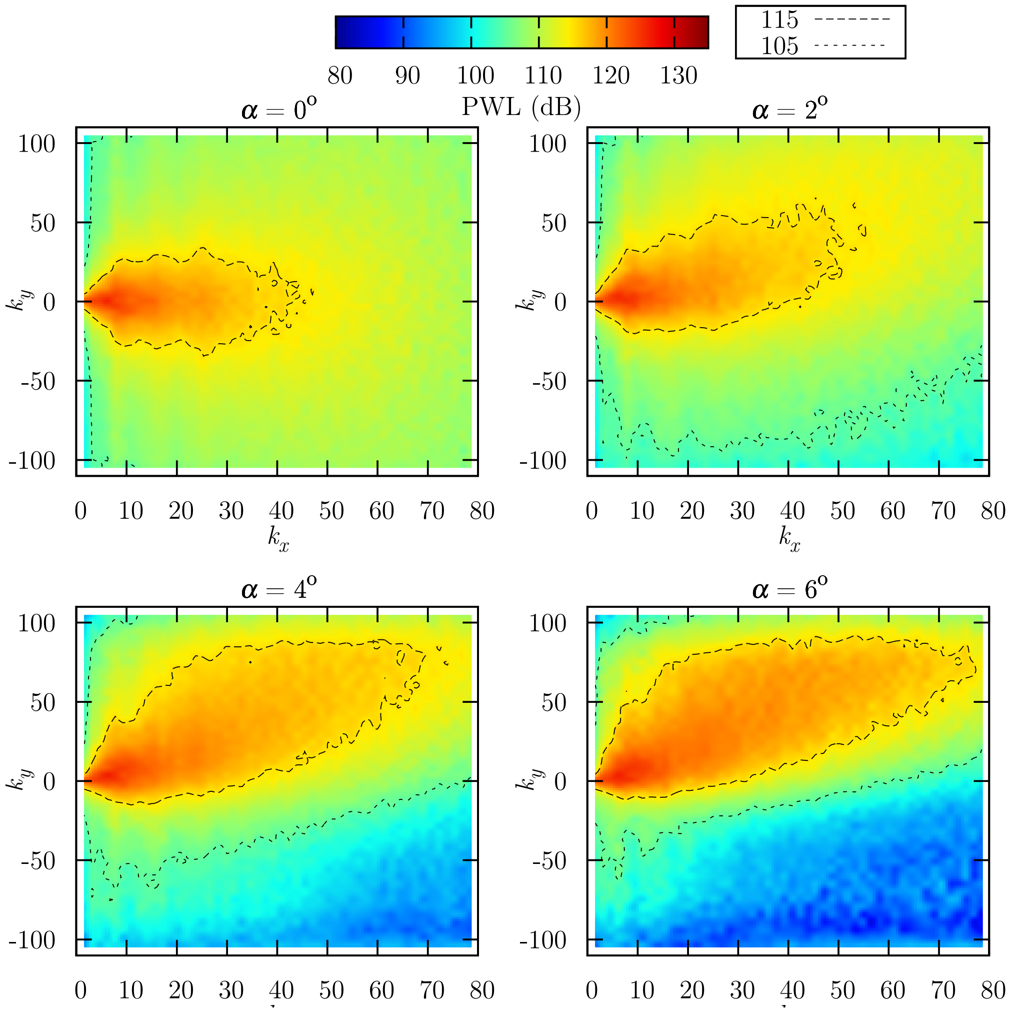

Figure 5.11: Contours of PWL with varying k_x and k_y wavenumbers, for a NACA 0006 airfoil interacting with harmonic gusts with $v_0 = 0.01U_x$ at $\alpha = 0°$, $2°$, $4°$, and $6°$.

Similar PWL behaviour with increasing α is seen in Figure 5.11 in comparison to the behaviour that was seen in Figure 5.9. As α is increased, the location of the peak PWL response for a given k_x value is shifted away from $k_y = 0$. However, in Figure 5.11, which shows the response to harmonic gusts, the position of peak response is shifted by a greater amount than in Figure 5.9, which shows the response to turbulent disturbances. For $\alpha = 6°$ and at $k_x = 50$, the peak response is found at about $k_y = 25$ m^{-1} when turbulent disturbances are used, whereas the peak response is found at about $k_y = 75$ m^{-1} for cases using harmonic gusts.

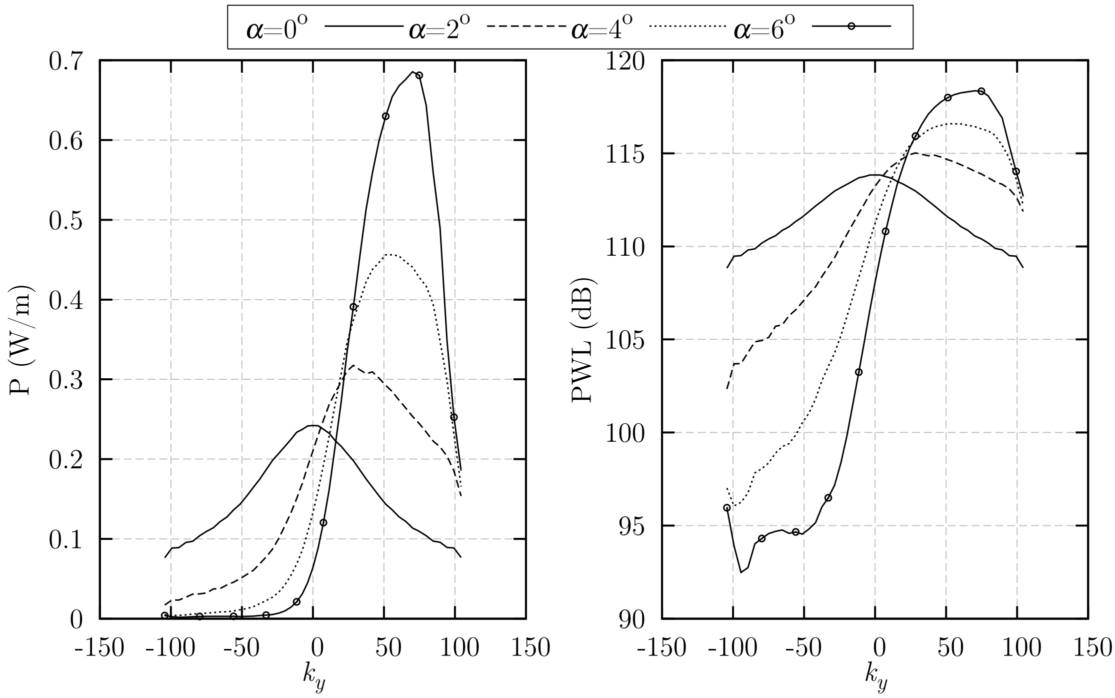

Figure 5.12: Sound power and PWL due to different k_y wavenumbers at $K = 8$, for a NACA 0006 airfoil interacting with harmonic gusts at $\alpha = 0°$ to $6°$.

Figure 5.12 shows the P and PWL response at a constant reduced frequency of $K = 8$ (or $k_x = 50.25$ m^{-1}), for different values of α. The k_y shift of the peak response clearly increases with increasing α. Additionally, the peak amplitude appears to be affected by AoA. It is increased with increasing α, such that the peak PWL amplitude for $\alpha = 6°$ is approximately 5 dB higher than the peak amplitude for $\alpha = 0°$. This behaviour was not seen in Figure 5.10 when the AoA test was performed using turbulent gusts, where the peak amplitude was not sensitive to AoA. This is because the results in Figure 5.10 show a combination of the effects of the airfoil response and of the effects of the turbulence spectrum. When the peak response is shifted away from $k_y = 0$, it is moved away from the location of peak energy in the turbulence spectrum (which was plotted earlier in Figure 3.1) to a region where there is less turbulent energy. Therefore the increased peak gust response is counterbalanced by the reduction in turbulent energy at non-zero k_y wavenumbers.

This finding has a significant implication. This work, and previous literature, has showed that turbulence interaction noise appears to be insensitive to AoA. This study suggests that this is not strictly correct. The airfoil response is affected by AoA, such that gusts with non-zero k_y wavenumbers cause an increased noise response in comparison to the noise made at zero AoA. However, gusts with non-zero k_y wavenumbers are less energetic than those with $k_y = 0$, and so the increased airfoil response is counterbalanced by the reduced turbulent energy. This averaged effect gives the appearance that turbulence interaction noise is insensitive to AoA. The insensitivity of the noise to AoA is partially a function of the shape of the turbulence spectrum. In situations with different turbulent content, for example with non-isotropic turbulence, the turbulence interaction noise might exhibit a higher sensitivity to AoA. This discussion agrees with the conclusions given by Devenport *et al.* [62], who studied the behaviour of the gust response function with varying AoA by using a panel method.

5.2.1 Examination of the Flow-Field

The final method used to examine the mechanism behind AoA effects on the noise was to visually examine the flow-field. Cases were chosen from the individual simulations at $K = 8$ (or $k_x = 50.26$ m^{-1}) that were run on the NACA 0006 airfoil at $\alpha = 6°$. Cases with $k_y = -35$, $k_y = 0$, and $k_y = 75$ m^{-1} were chosen, in order to represent the flow-field caused by a negatively swept gust (negative k_y), a positively swept gust (positive k_y), and a transverse gust ($k_y = 0$). Additionally, $k_y = 75$ m^{-1} is the wavenumber at which the maximum gust response is seen in this configuration.

Figures 5.13 and 5.14 show contours of the flow-field velocity disturbance magnitude U, and p_{rms}, respectively around the leading edge of the airfoil. All three cases in Figure 5.13 show that the gust wavefront is distorted by the presence of the meanflow, which accelerates over the suction-side of the airfoil. The distortion causes the $k_y = 0$ case to appear to be a negatively swept gust, despite this gust being exactly transverse to the airfoil when it was created at the inflow boundary. The distortion of the gust is most severe (i.e. the wavefront is the least smooth) for the $k_y = 75$ m^{-1} case, and least severe (i.e. the wavefront is smooth) for the $k_y = -35$ m^{-1} case.

Examination of the p_{rms} contours in Figure 5.14 confirms that the $k_y = 75$ m^{-1} case produces the highest p_{rms} response. Although the strength of the response is affected by k_y, the position of the maximum response appears to be the same for all three cases.

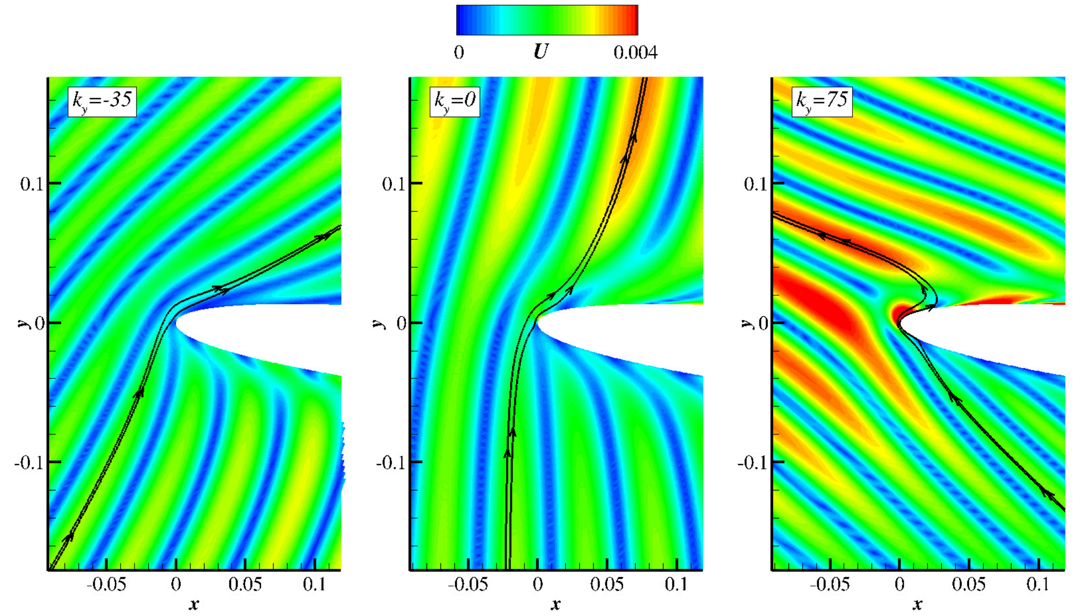

Figure 5.13: Contours of disturbance velocity magnitude U, caused by gusts with $K = 8$ and $k_y = -35$, 0, and 75 m^{-1}, interacting with a NACA 0006 airfoil at $\alpha = 6°$. Lines are also drawn to indicate the shape of the gust wavefront.

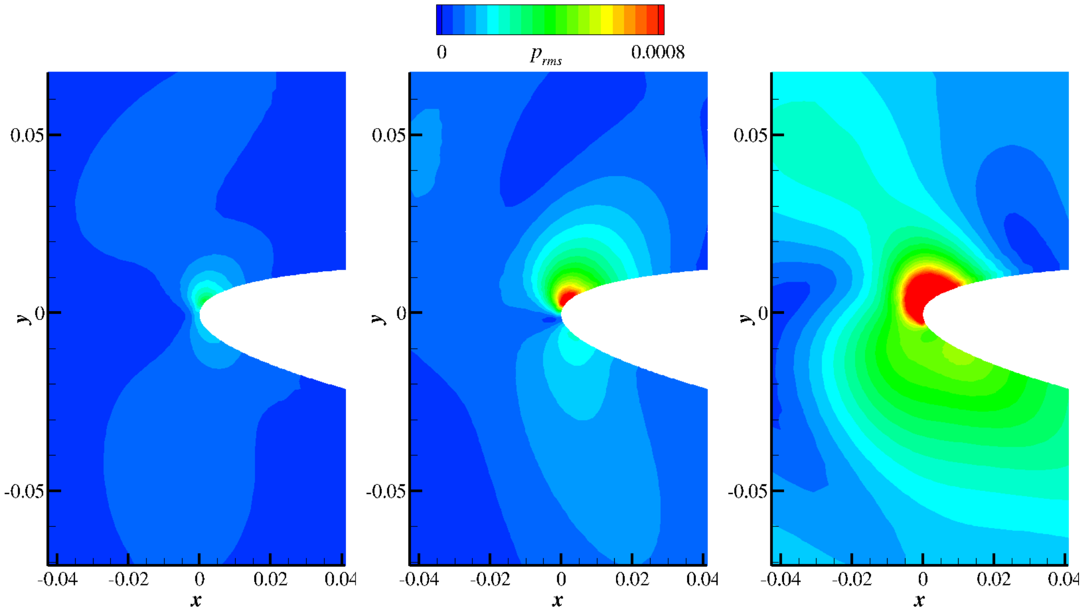

Figure 5.14: Contours of p_{rms}, caused by gusts with $K = 8$ and $k_y = -35$, 0, and 75 m^{-1}, interacting with a NACA 0006 airfoil at $\alpha = 6°$.

Figures 5.13 and 5.14 show that there is a link between the amount of gust wavefront distortion and the pressure response of the airfoil, where a larger amount of distortion will result in greater noise. This finding is consistent with the conclusions of Chapter 2. In Chapter 2, it was found that smoother wavefronts, caused by the meanflow gradients of thick airfoils, will generate less noise in comparison to non-smooth gust wavefront interaction with thin airfoils (see Figure 2.19). Therefore, the effects of AoA on the airfoil noise response are caused by distortion of the gust wavefronts due to the asymmetry of the meanflow. For positive α (as used here) the effect is to severely distort the wavefronts of positively swept gusts, which increases the noise. Negatively swept gusts are also distorted, but in this case the wavefront remains smooth and the noise response is small. The result is that a positive α will shift the peak airfoil noise response from $k_y = 0$ towards positive values of k_y.

In Chapter 2, the distortion of vortical gusts was found to be caused by velocity gradients in the leading edge stagnation region. Here, the distortion is also affected by the asymmetry of the meanflow, which suggests that multiple aerodynamic flow features can contribute to the changes in noise caused by airfoil geometry.

5.3 Effects of Camber on the Noise

This section investigates the effects on turbulence interaction noise predictions when non-zero airfoil cambers are introduced. NACA 4-digit airfoils were used, with camber values ranging from 1% to 5%, with a position of maximum camber set at 40% of the blade chord, and with a maximum thickness of 6%. These airfoils were tested at an AoA of $\alpha = 0°$ so that camber effects were tested independently of AoA effects. The airfoils that were used in this study are shown in Figure 5.15. Examples of the inviscid meanflow solutions that were obtained for the study are shown in Figure 5.16. As was done with the AoA tests, these airfoils were interacted with both one- and two-component turbulence with $\Lambda = 0.07$ m and $\sqrt{\overline{w^2}} = 0.04U_x$ in $M = 0.3$ flow.

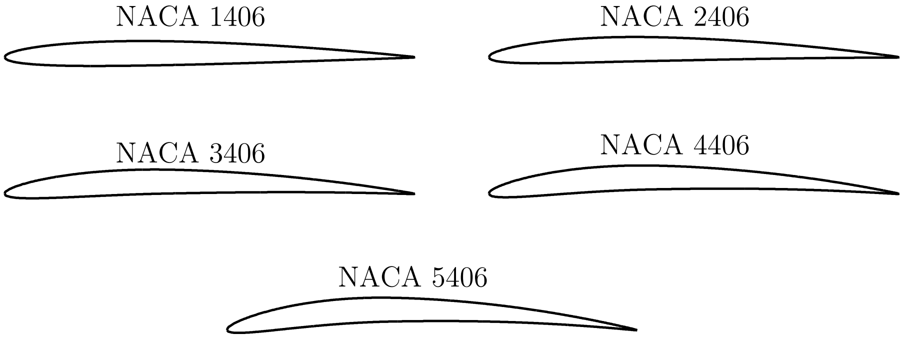

Figure 5.15: The various airfoils used in the camber study.

Figure 5.17 shows SPL predictions from the one- and two-component turbulence synthesis approaches for the NACA 1406 and NACA 5406 airfoils. A prediction is given at $\theta = 45°$ and at $\theta = 315°$ to investigate the differences in noise from the suction and pressure sides of the airfoil respectively. Noise predictions from the suction and pressure sides of the NACA 1406 airfoil are very similar. However, for the NACA 5406 airfoil the pressure side noise appears to be about 1 dB louder than the suction side at most frequencies. Therefore, large values of camber appear to affect the directivity of the noise. SPL levels for the two airfoils appear to be quite similar, which suggests that turbulence interaction noise is insensitive to camber, which is in agreement with previous literature. Additionally, SPL predictions from

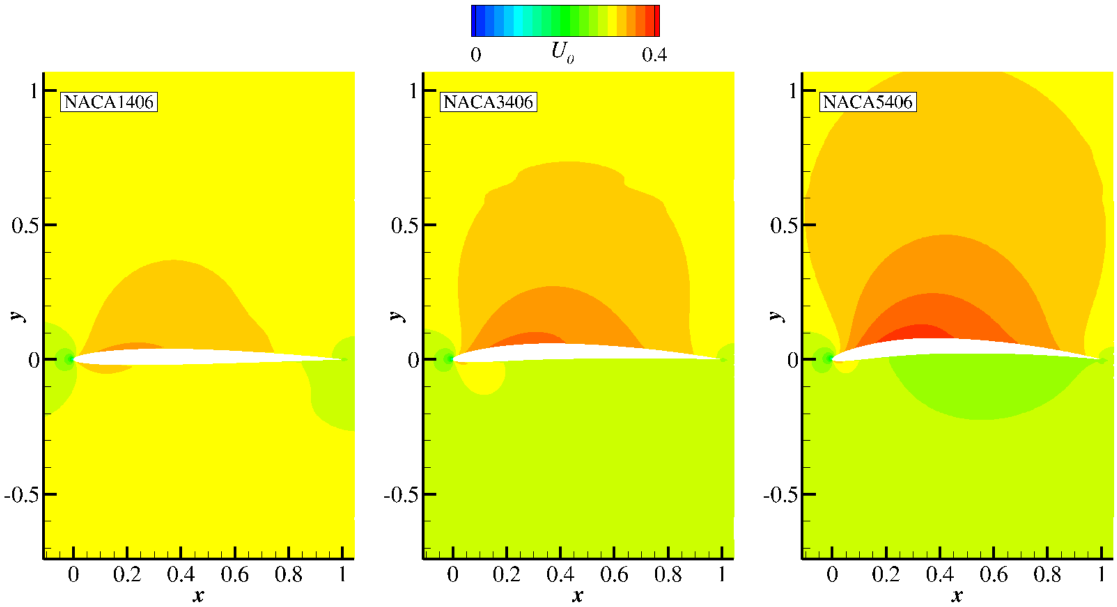

Figure 5.16: Example meanflow solutions for airfoils with 1%, 3%, and 5% camber. Contours of non-dimensional streamwise velocity are shown.

the one- and two-component synthesis approaches are similar for both airfoils, which suggests that the single velocity-componental modelling approach is applicable to airfoils with camber.

Figure 5.18 summarises the predictions from all observer angles by plotting PWL for airfoils with 1%, 3%, and 5% camber, as predicted by the one- and two-component turbulence synthesis approaches respectively. Both turbulence forcing approaches provide similar predictions, which again suggests that the single velocity-component modelling approach is suitable for cambered airfoils. PWL predictions do not appear to be significantly affected by the presence of camber.

The present study has fixed the position of maximum camber at 40% along the airfoil chord. If the maximum camber value was placed closer to the leading edge then it is likely that a greater effect would be seen on the noise. The single velocity-component modelling approach may also become less accurate in this case. Therefore, the conclusions of this section are restricted to airfoils with a position of maximum camber that is not close to the leading edge.

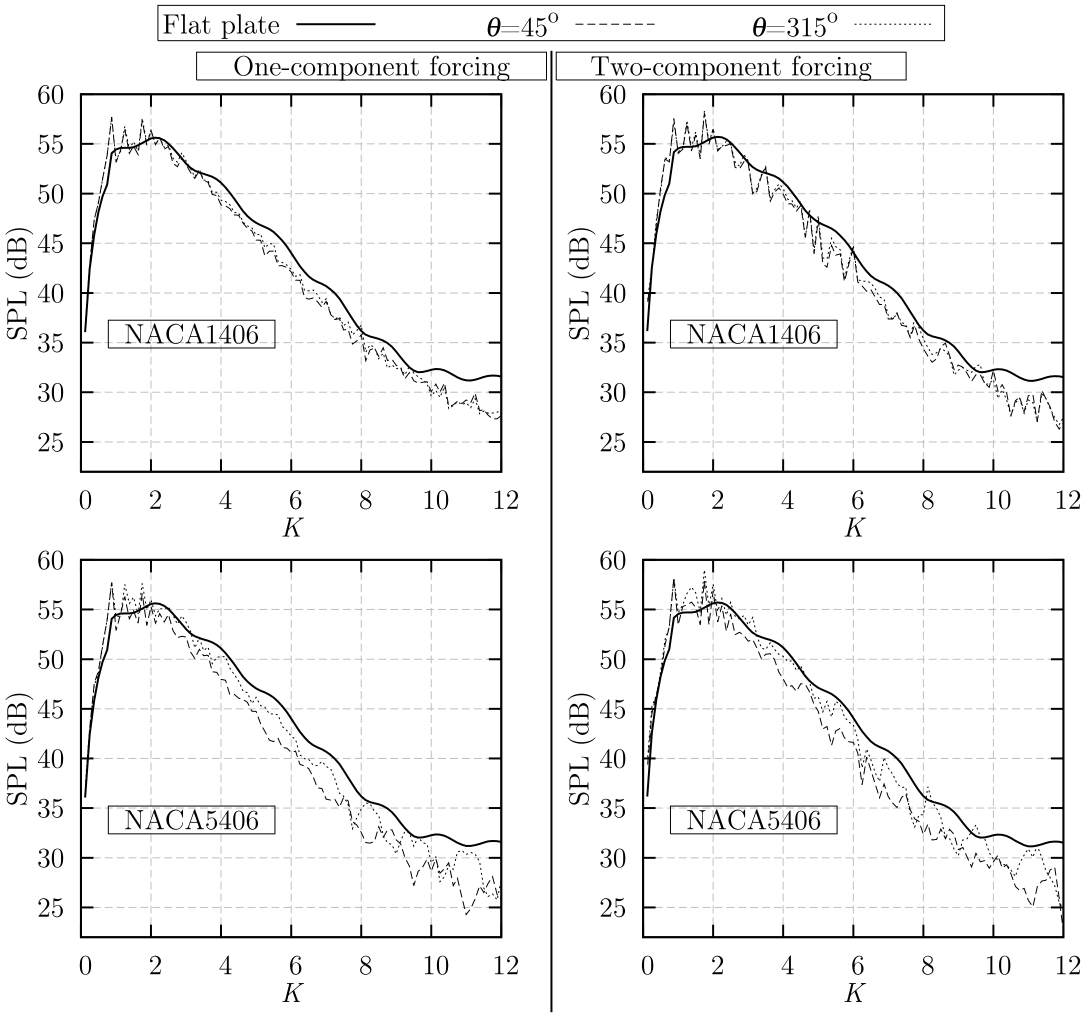

Figure 5.17: Comparison of SPL predictions made by the one- and two-component turbulence synthesis approaches for a NACA 1406 and a NACA 5406 airfoil in $M = 0.3$ flow.

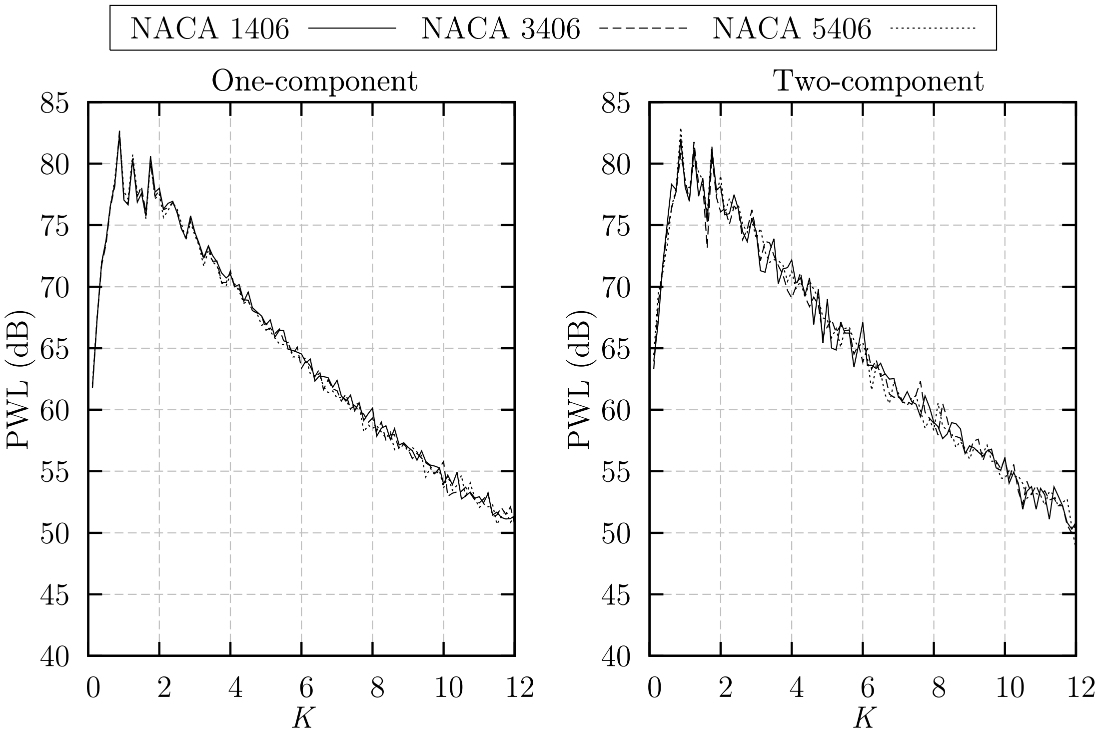

Figure 5.18: Comparison of PWL predictions made by the one- and two-component turbulence synthesis approaches for airfoils with 1%, 3%, and 5% camber in $M = 0.3$ flow.

In order to confirm the insensitivity of turbulence interaction noise to airfoil camber, additional simulations were made at $K = 8$, where a single k_y wavenumber component was forced in each individual simulation. This is the approach that was used to study the AoA effects in Section 5.1.3, and shows the relative contributions to the noise from the various k_y gust wavenumbers. The variation of P and PWL with k_y is shown in Figure 5.19, which shows that the effects of camber on the airfoil response appears to be small at all k_y values.

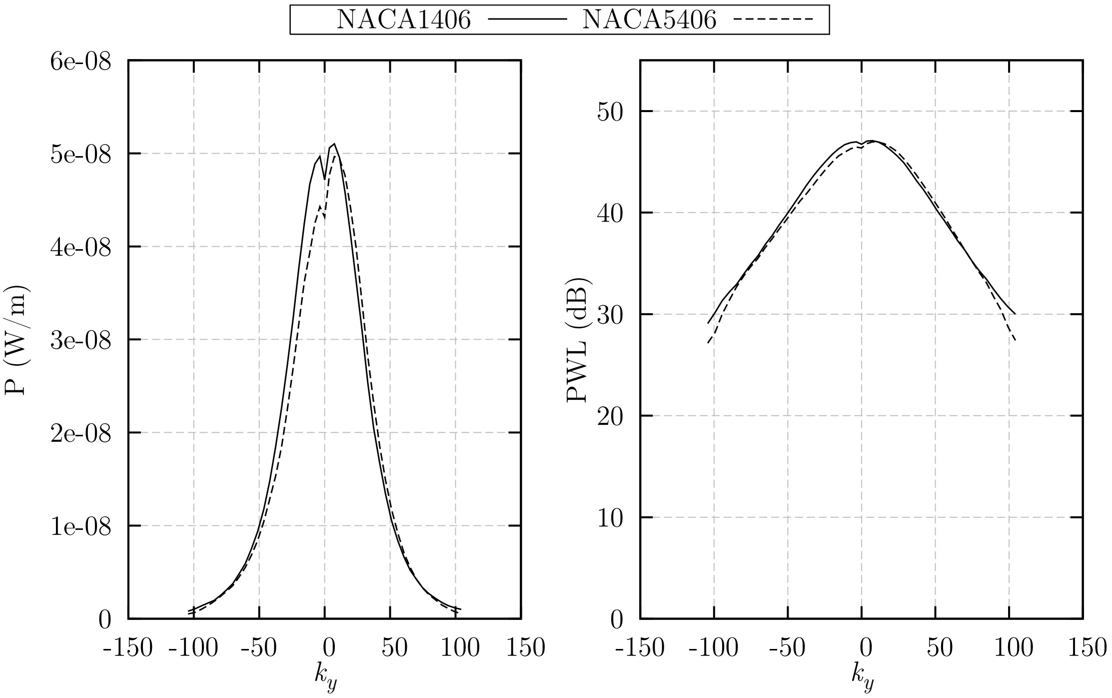

Figure 5.19: Variation of P and PWL with k_y wavenumber at $K = 8$, for a NACA 1406 and a NACA 5406 airfoil.

The reason that the single velocity-component modelling approach provides an accurate prediction for the noise of a cambered airfoil is related to the meanflow. Figure 5.16 shows that the flow is accelerated around the suction side of the airfoil as a result of the camber. However, in comparison to the acceleration caused by AoA (shown in Figure 5.3), the acceleration due to camber is at a greater distance from the airfoil leading edge, and has little effect on the position of the stagnation point, for example. Therefore, the gust distortion in the leading edge region will not be as severe as was seen for larger AoAs, and so the response can still be approximated by gusts which use $k_y = 0$.

Directivity predictions made with the two-component turbulence synthesis approach and with varying percentage of camber, are shown in Figure 5.20 at a reduced frequency of $K = 10$. Figure 5.20 shows that as the percentage of camber increases, the directivity appears to be rotated slightly in the anti-clockwise direction, such that upstream predictions on the suction side become stronger, and downstream predictions on the pressure side become stronger. However, this effect appears to be small, causing differences between the suction and pressure sides that are usually less than 2 dB for the largest value of camber that was tested. An exception to this is at acute upstream angles for the NACA 5406 airfoil, where there is a difference of about 8 dB between the directivity lobes on the suction and pressure sides of the airfoil.

The behaviour seen in this study agrees with the conclusions of Moreau *et al.* [67] and of Devenport *et al.* [62].

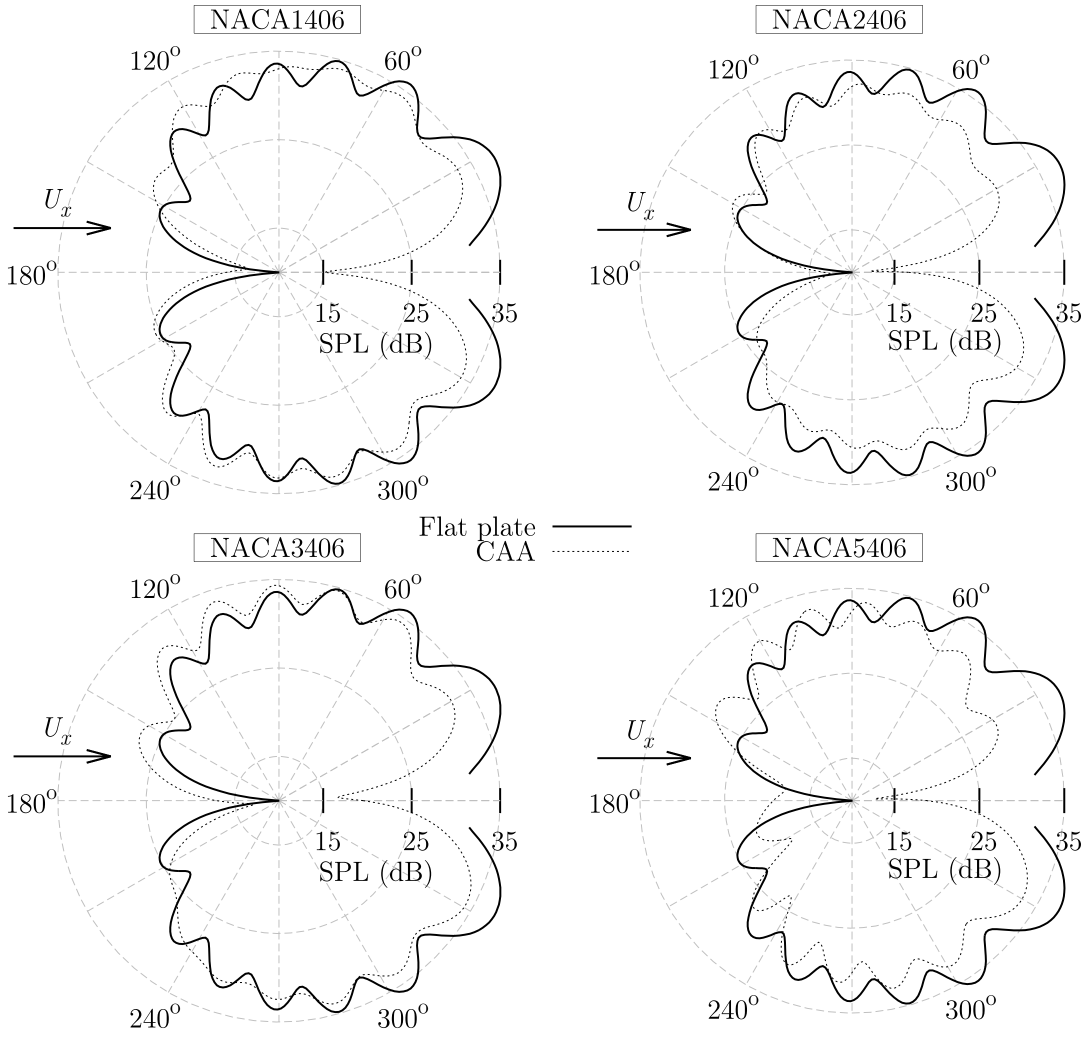

Figure 5.20: Directivity comparisons at $K = 10$ from the two-component turbulence synthesis approach, for airfoils with 1%, 2%, 3%, and 5% camber.

5.4 Summary

In this chapter, the single velocity-component modelling approach has been applied to cambered airfoils and to airfoils at non-zero AoA. The effects of AoA and camber have been investigated separately. It was shown in Chapter 4 that streamwise disturbances are relatively unimportant when modelling turbulence interaction noise for symmetric airfoils at zero AoA. This chapter has tested if this is also true for airfoils with non-zero camber and AoA. The key findings are:

- Isotropic turbulence interaction noise due to isotropic turbulence is not sensitive to AoA. When modelled with a two-component turbulence synthesis approach, the effects of varying AoA are nearly negligible at all frequencies and directivities.
- The effects of AoA on the noise are not predicted accurately by a single velocity-component modelling approach (which represents turbulence as only transverse disturbances). At non-zero AoA the gusts are distorted by the meanflow, such that the greatest contribution of noise is due to gusts whose k_y wavenumber is non-zero. Because the one-component approach inherently assumes that the highest response is from gusts with $k_y = 0$, it cannot be used in this case.
- Although turbulence interaction noise appears to be insensitive to AoA, the gust response of the airfoil is affected by AoA. The peak gust response is increased in comparison to the response for an airfoil at zero AoA, and the position of peak response is shifted from $k_y = 0$ to non-zero k_y wavenumbers. However, this increased airfoil response is counterbalanced by the turbulence spectrum, which contains less energy at non-zero k_y wavenumbers. Averaging the increased gust response and the decreased turbulent energy gives an overall negligible effect on the noise due to AoA. However, this result may be specific to isotropic turbulence. In the case of non-isotropic turbulence, the effects of AoA may become significant.
- Turbulence interaction noise is not sensitive to airfoil camber. Introducing a non-zero camber has a negligible effect on PWL. However, there is a small

effect in directivity. The position of directivity lobes appears to be rotated slightly in the clockwise direction. The strength of the downstream lobes on the pressure side of the airfoil is increased, while the strength of the lobes on the suction side of the airfoil is decreased.

- The effects of airfoil camber on the noise are predicted accurately by using a single velocity-component modelling approach. As was seen for AoA effects, the introduction of camber will cause asymmetry in the meanflow solution. However, the effects are concentrated away from the airfoil leading edge and do not affect the stagnation region, for example. The shift in k_y response that is seen for AoA is not seen for camber effects, and therefore the situation can be accurately modelled with turbulence that contains disturbances only in the transverse direction.
- This study has used airfoils with maximum camber at 40% along the chord. If the position of maximum camber was moved closer to the leading edge, then the effects on the noise may be increased, and the one-component turbulence synthesis approach may become less accurate.

Chapter 6

Analysis of a Realistic CROR Blade Profile

One aim of this thesis is to assess the accuracy of noise predictions from analytical flat plate models when they are used to consider CROR blade noise. This chapter builds upon the knowledge gained throughout the current project in order to predict the noise from a realistic CROR blade profile. This will allow the accuracy of flat plate analytical CROR noise predictions to be assessed.

6.1 Industrial Predictions of Turbulence Interaction Noise

This project has focused on the mechanism of turbulence interaction noise because it is a dominant noise mechanism in CROR engines, and because an improved understanding of this noise source is desirable. In a CROR engine, the wakes from front rotors can interact with the leading edge of the rear rotor blades, which causes broadband rotor-wake interaction (BRWI) noise. This interaction process is depicted in Figure 6.1.

Blandeau and Joseph [19, 20] and Blandeau *et al.* [31] have described an analytical

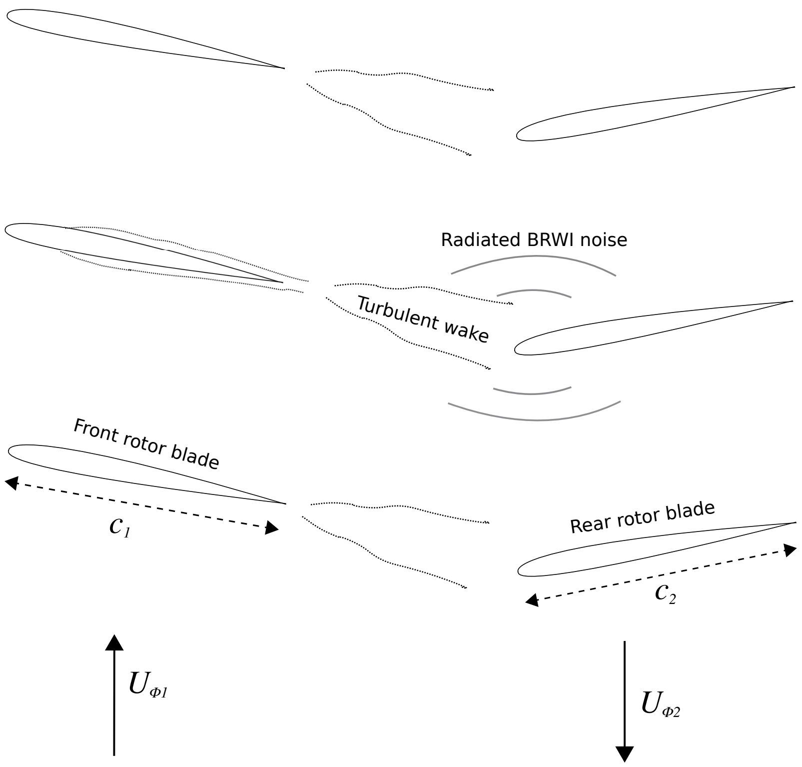

Figure 6.1: Schematic of the BRWI noise generation process.

model which can predict CROR BRWI noise by using the flat plate theory of Amiet [30]. This model has been further developed by the Airbus Noise Technology Centre (ANTC) at the University of Southampton, and is currently used by Airbus to assist with future CROR engine designs and to improve understanding of CROR broadband noise [9].

The analytical CROR noise code, titled “Broadband Noise of Open Rotor Blades” (BoB), is capable of predicting the dominant broadband noise sources of installed and uninstalled CROR engines. The uninstalled noise sources are:

- ***Broadband rotor-wake interaction (BRWI) noise***. The noise produced by a rotor wake interacting with the leading edge of a rear rotor blade.
- ***Broadband rotor trailing-edge (BRTE) noise***. The noise produced by interactions between a turbulent boundary layer and the trailing edge of a rotor blade.

Predictions of these noise sources can be made by using the geometrical configuration of the CROR engine (blade number, blade shape etc.) and aerodynamic parameters (turbulence intensity, wake width, boundary layer thickness etc.) as inputs. Aerodynamic parameters can be predicted using empirical models, or by using data from CFD simulations. More detail on the specification of inputs for BoB is given in Ref. [9]. Strip theory is used to account for 3D blade geometries, as originally suggested by Amiet [27].

Figures 6.2 and 6.3 show example predictions of the BRTE and BRWI noise from BoB for two thrust settings (here referred to as sideline and cut-back flight conditions), compared with experimental measurements that were made on the RIG145 model during the DREAM programme in 2008. These experimental measurements of CROR noise have previously been published by authors such as Parry *et al.* [128] and Ricouard *et al.* [129]. While BRTE noise is not the focus of this thesis, it is useful to compare with BRWI noise in Figures 6.2 and 6.3 in order to assess the relative importance of BRWI noise at various frequencies.

The noise predictions in Figures 6.2 and 6.3 have been made for a typical CROR geometry using the Airbus AI-PX7 blade. The CROR geometry considered the front rotor to have 11 blades and the rear rotor to have 9 blades. The flight speed of the engine was $M = 0.2$ in both cases. The noise predictions are given in both Hz and in terms of reduced frequency $K = c/\lambda$. The CROR blade geometry is 3D, therefore the chord and the local blade velocity are not constant along the blade span. The averaged chord and the averaged blade velocity along the blade span have been used to calculate K in Figures 6.2 and 6.3. This has been done to give an approximate value of K to indicate the frequencies at which airfoil geometry can be expected to have an effect on the BRWI noise.

The BRWI noise is predicted by BoB to be the dominant broadband noise source at low frequencies at both the cut-back and sideline conditions. The peak value of BRWI noise occurs at approximately 600 Hz. At sideline conditions the BRWI noise is also the dominant noise source at all frequencies, with BRTE noise predicted to be at least 5 dB lower than BRWI noise everywhere, whereas at cut-back conditions the BRTE noise becomes significant in comparison to BRWI noise for $f > 1$ kHz. The

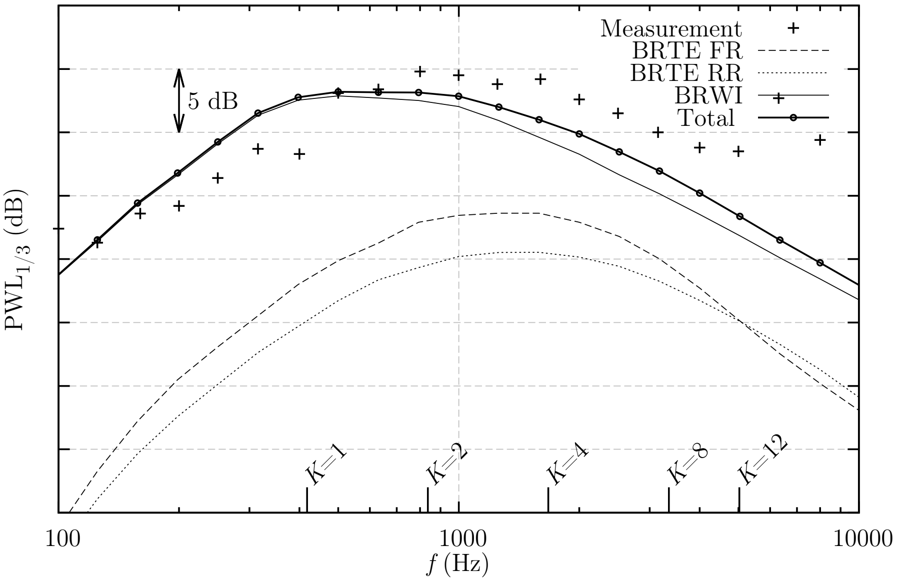

Figure 6.2: Example PWL$_{1/3}$ prediction of the BRTE and BRWI noise from BoB, for sideline thrust conditions.

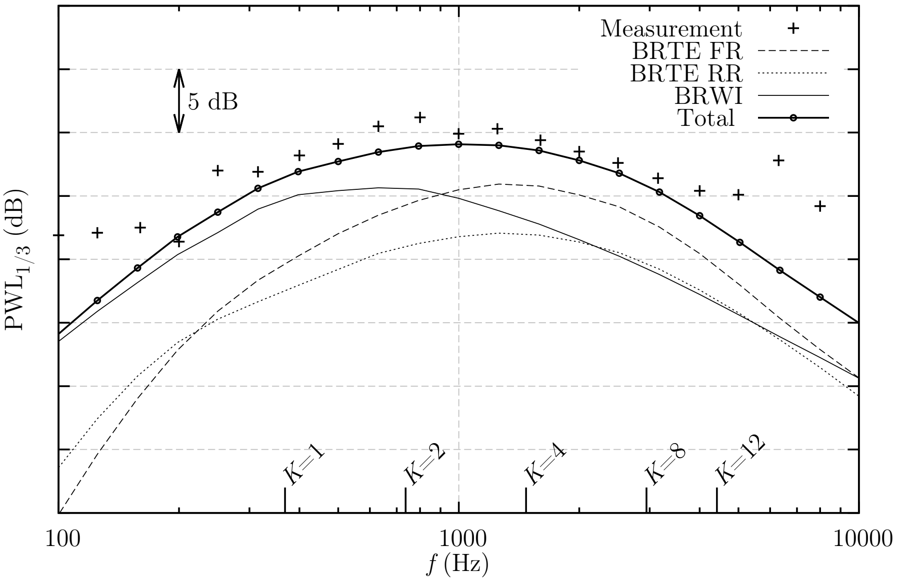

Figure 6.3: Example PWL$_{1/3}$ prediction of the BRTE and BRWI noise from BoB, for cut-back thrust conditions.

noise predictions from BoB agree with the experimental measurements of the noise in terms of spectral shape and amplitude, which gives confidence in the accuracy of the predictions.

The peak BRWI noise is predicted to be at around $f = 600$ Hz for both conditions, which corresponds to blade reduced frequencies of between $K = 1 - 2$. Previous tests in Chapters 2 to 5 have shown that the effects of blade geometry occur at high reduced frequencies. For blades at $M = 0.5$, the effects of blade geometry were seen in Figure 4.7 to be above about $K = 4$. Therefore, this preliminary analysis suggests that the airfoil geometry will mostly affect the BRWI noise spectra for frequencies above the peak noise frequency. Figure 6.3 shows that BRWI noise may not be the dominant noise source in the frequency region where airfoil geometry has an effect, because it is quieter than BRTE noise for $f > 1$ kHz. Consequently, this preliminary analysis suggests that the effects of airfoil geometry on CROR BRWI noise may not be significant to the overall broadband noise predictions.

The cases used to test the importance of airfoil geometry effects on BRWI noise will now be described.

6.2 Case Description

In order to study the effects of the real CROR blade geometry on the noise using the CAA method discussed in this project, the situation requires some simplification. By using the knowledge gained in previous chapters, assumptions can be made while maintaining reasonable confidence in the accuracy of the final conclusions. The simplifications were:

- Two 2D blade cross-sections were considered, as opposed to the whole 3D blade. This was done in order to reduce computational expense.
- Translating airfoils were considered, and the effects of rotation were neglected. Therefore, the CAA predictions were not directly comparable to predictions from the analytical CROR noise code. However, comparison was made with Amiet's theory [30] for translating flat plates in order to view the effects of

the airfoil geometry. This comparison indicates the accuracy or inaccuracy of flat plate theory for airfoils at the same conditions as the CROR blades, and therefore indicates the accuracy of the CROR noise prediction. In other words, the effects of rotation will affect the overall noise levels, but will not affect the relative changes to the noise caused by the airfoil geometry.

- An isolated airfoil prediction was made, as opposed to considering a cascade of airfoils. This is justified by the study made by Blandeau [14], who showed that blade-to-blade correlation effects can be neglected for most CROR configurations.
- The noise was predicted using isotropic, homogeneous turbulence. This is a simplification in comparison to the turbulent wakes from a real CROR engine. However, this approximation is also used in the BoB code.
- The airfoils were simulated at zero AoA. The reasons for this simplification are discussed below. However, it was shown in Chapter 5 that changing the AoA has a negligible effect on noise generated by airfoils interacting with isotropic turbulence. Therefore, this simplification does not have a significant effect on the results.
- A one-component transverse turbulence synthesis approach (i.e. the single velocity-component modelling approach) was used for the CAA study. This is justified by results in Chapters 4 and 5, which show that for airfoils at zero AoA, an accurate noise prediction can be obtained by considering a turbulent inflow that contains only transverse disturbances.
- An inviscid and steady meanflow solution was used in order to avoid any complications in LEE simulations caused by strongly sheared meanflow.

Two blade geometries and two thrust configurations were chosen to test the effects of CROR geometry on BRWI noise. A blade cross-section from near the blade hub (at 55% of the tip radius) and a cross-section from near the blade tip (at 90% of the tip radius) were used. These are referred to as the hub and tip cases respectively. The two blade geometries are shown in Figure 6.4, and the details of the four cases (two blade cross-sections, each at two thrust settings) are given in Table 6.1.

Figure 6.4: Showing the 2D cross-sections of the hub and tip airfoil profiles.

Case	**Mach no.**	**AoA**	$\sqrt{\overline{w^2}}$	Λ	**Max. thickness**	**Blade chord**
Hub, sideline	0.45	4.47°	$0.0221U_x$	0.0269 m	$0.065c$	0.52 m
Hub, cut-back	0.4	3.6°	$0.020U_x$	0.0252 m	$0.065c$	0.52 m
Tip, sideline	0.65	3.86°	$0.0161U_x$	0.045 m	$0.032c$	0.42 m
Tip, cut-back	0.6	3.5°	$0.010U_x$	0.0327 m	$0.032c$	0.42 m

Table 6.1: Simulation details of the hub and tip profiles at two thrust settings.

Table 6.1 shows that the blade Mach number is $M \geq 0.4$, and at a positive AoA of at least $\alpha = 3.5°$ in the chosen cases. However, these configurations cannot be modelled by the current CAA method. The reason for this is explained by Figure 6.5, which shows the calculated meanflow around the airfoils for the two blades in the sideline thrust configuration.

Figure 6.5 shows that the local flow speed becomes supersonic around the leading edge of the airfoil in both the hub and tip cases. The current CAA method is not capable of modelling supersonic flow, and therefore cannot consider this configuration. In order to model the configuration with the current CAA method, the AoA of each blade was modified to be $\alpha = 0°$. It was shown in Chapter 5 that turbulence interaction noise is not affected by AoA if the incoming turbulence is isotropic. Therefore, this simplification is not expected to significantly affect the conclusions of the study.

This simplification means that the effects of supersonic flow, and shockwaves, on the noise are not considered here. The effects of supersonic flow on aeroacoustic noise are not well known, but are beyond the scope of the current study. Future

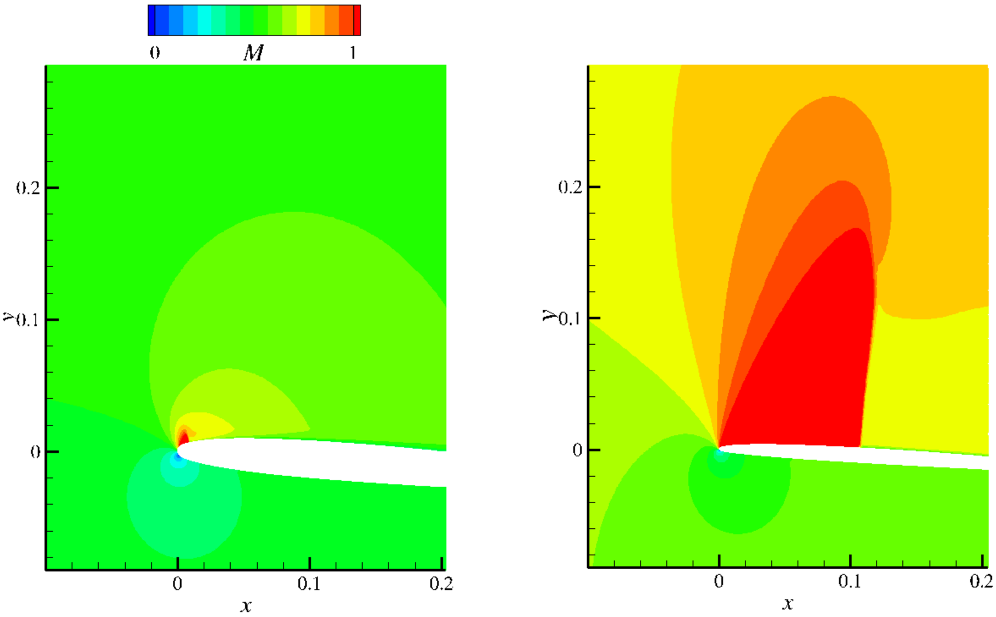

Figure 6.5: Showing the predicted meanflow Mach number of the hub and tip cases at sideline thrust conditions.

work is recommended to investigate the effects of locally supersonic flow on BRWI noise.

6.3 Results

PWL predictions were made for the hub and tip profiles at sideline and cut-back configurations, and were compared with the results from flat plate analytical theory. This comparison is given in Figure 6.6 for the sideline thrust configuration, and in Figure 6.7 for the cut-back configuration. Figures 6.6 and 6.7 compare PWL predictions for the hub and tip profiles and display the spectra with both frequency f and reduced frequency K. In Figures 6.6 and 6.7 the tip predictions have been increased by 10 dB in order to separate the hub and tip spectra.

Both the sideline and cut-back configurations show a similar effect on the noise due to the geometry of the CROR profiles. Noise predictions of the hub blade profile

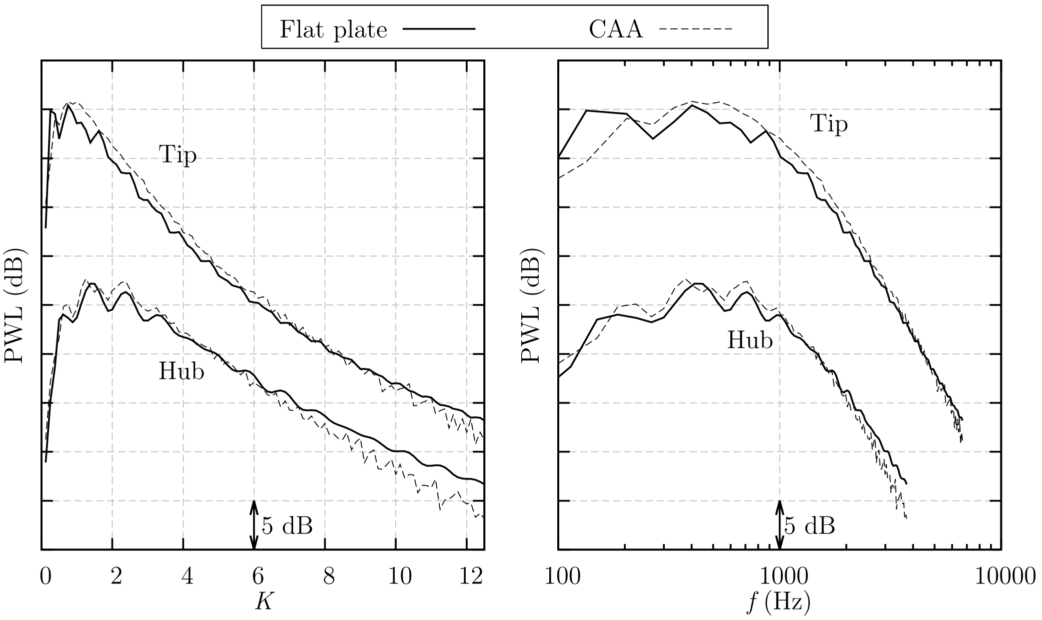

Figure 6.6: Comparison of PWL predictions from the hub and tip profiles with flat plate theory, for the sideline configuration. Results from the tip configuration are increased by 10 dB for clarity.

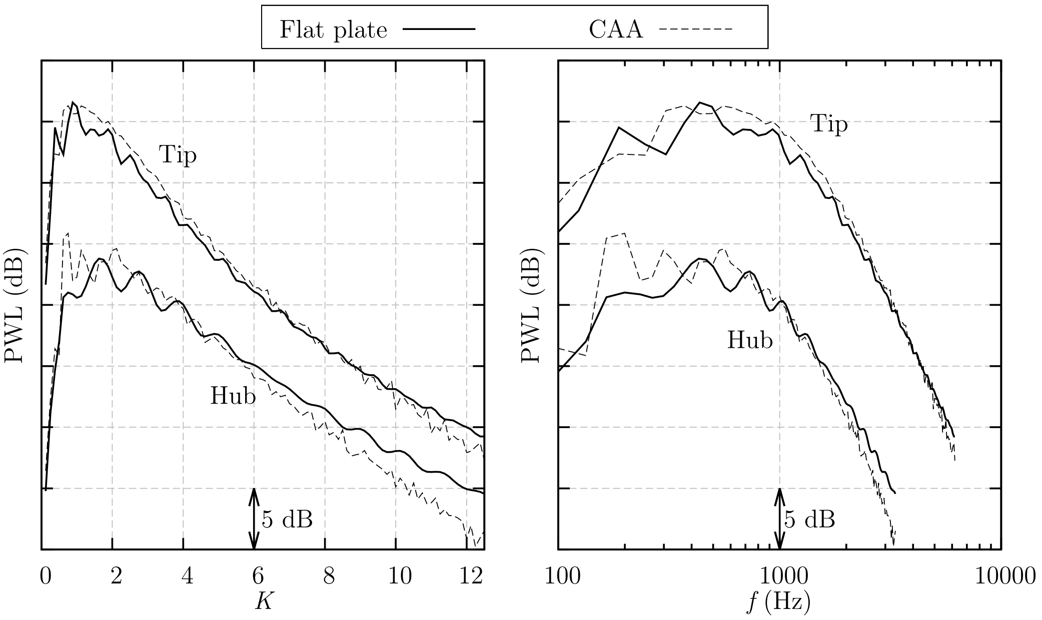

Figure 6.7: Comparison of PWL predictions from the hub and tip profiles with flat plate theory, for the cut-back configuration. Results from the tip configuration are increased by 10 dB for clarity.

show a good agreement for $K < 6$, or $f < 2$ kHz and $f < 1.5$ kHz for the sideline and cut-back configurations respectively. Above $K = 6$ the analytical method over-predicts the noise because it does not account for the blade geometry. At $K = 12$ the analytical method over-predicts the noise by about 3 dB and 4 dB in the sideline and cut-back configurations respectively. The peak BRWI noise level is between $K = 1 - 2$ and is therefore captured well by the analytical flat plate theory.

Noise predictions of the tip blade profile show a good agreement between CAA and flat plate theory for most frequencies. Noise reductions due to blade geometry appear above about $K > 10$, or $f > 4$ kHz. At $K = 12$ the over-prediction by analytic theory is approximately 2 dB.

Because the geometry of the tip profile is similar to a flat plate (i.e. it has around 3% thickness), the flat plate theory gives a closer prediction at high frequency than it does when predicting the noise from the hub profile. The tip profile is also generally louder than the hub profile because the speed of the rotor blade at the tip is higher. Therefore, the analytical theory gives good predictions of the dominant blade tip noise sources, but less accurate predictions of the quieter hub noise sources.

The effects of blade geometry on the CROR BRWI noise appear to be relatively small. The over-prediction given by flat plate theory is likely to be less than 4 dB, and is at sufficiently high frequencies that the peak BRWI noise levels are not affected. In the cut-back configuration, the over-prediction given by flat plate theory will occur in a spectral region where BRTE noise is higher than BRWI noise. Therefore, the total CROR broadband noise predictions will not be significantly affected by this over-prediction.

6.4 Summary

The noise at two cross-sections along the span of a CROR blade has been predicted with the CAA method and with analytical flat plate theory for two thrust settings. This has been done in order to assess the accuracy of analytical flat plate models in predicting the turbulence interaction noise from CROR engines. The key findings are:

- The effects of airfoil geometry on the noise occur at frequencies that are higher than the peak BRWI noise levels. In some cases, blade geometry will only affect the BRWI noise in spectral regions where other broadband noise sources are louder than BRWI noise. Therefore, any over-predictions given by flat plate theory will not have a significant impact on total CROR broadband noise predictions.

- Analytical and CAA noise predictions of the hub profile agree up to $K = 6$ or $f = 2$ kHz and $f = 1.5$ kHz in the sideline and cut-back configurations respectively, and $K = 10$ or $f = 4$ kHz in the configurations using the tip profile. At frequencies above these thresholds, the geometry of the blade will cause a noise reduction in comparison to the flat plate prediction. At $K = 12$, Flat plate theory will over-predict the noise by about 4 dB compared to the hub profile, and by 2 dB compared to the tip profile.

- CROR blades tend to be thick near the hub ($t = 0.06c$), and thinner near the tip ($t = 0.03c$). Therefore, analytical flat plate models will be less accurate for noise predictions near the hub than for predictions near the tip. However, the noise at the tip is generally louder than the noise at the hub, because the flow speed is higher. This indicates that flat plate theory will predict the loudest sources of BRWI noise with the best accuracy.

This study has made several assumptions in order to simplify the comparison. The most significant assumption is the use of zero AoA, which removes the presence of locally supersonic flow around the leading edge of the blades. Future work to investigate the effects of locally supersonic flow on the noise would provide interesting study.

Chapter 7

Conclusions and Future Work

7.1 Conclusions

CROR engines show potential in helping the aviation industry meet future environmental targets. However, CRORs generate significant tonal and broadband noise, which must be mitigated before they can enter service. BRWI noise is a dominant CROR broadband noise source, caused by interactions between turbulent wakes and the leading edge of airfoils, and is often predicted without accounting for the geometry of the airfoil. Instead, the airfoil is typically assumed to be an infinitely thin flat plate.

This research has used CAA methods to improve current understanding of the effects of airfoil geometry on turbulence interaction noise, which is the underlying mechanism of BRWI noise. A high-order CAA method has been used and extended to model the interaction of airfoils with synthetic turbulence. This method has been used to perform a thorough parametric study on the effects of airfoil thickness, leading edge radius, angle-of-attack, and camber on turbulence interaction noise. The study was concluded with a test of real CROR blade geometries and conditions, to directly evaluate the accuracy of industrial flat plate CROR noise predictions. The accuracy of flat plate modelling has been assessed in comparison to the CAA method throughout the project, to investigate the error incurred by ignoring the geometry of the airfoil when making noise predictions.

In addition to studying the effects of airfoil geometry on turbulence interaction noise, this project has aimed to improve the efficiency of CAA predictions of the noise. A single velocity-component modelling approach has been presented and assessed, which aims to reduce the computational expense of CAA simulations by representing the turbulence as a series of transverse disturbances.

The main conclusions of this research are now presented.

7.2 Effects of Airfoil Thickness on the Noise

- Increasing the thickness of an airfoil will cause a reduction in the turbulence interaction noise for high reduced frequencies $K = c/\lambda$.
- The noise is reduced by a significant amount due to the presence of airfoil thickness. A NACA 0012 airfoil will reduce PWL predictions at $K = 12$ by about 11 dB in comparison to flat plate theory, in $M = 0.5$ flow.
- The threshold reduced frequency, above which reductions in the noise are seen, appears to have some dependence on Mach number. In $M = 0.2$ flow noise reductions have been seen above about $K = 1$, whereas for $M = 0.5$ flow the reductions are seen above about $K = 4$.
- The noise, in terms of decibels, is reduced linearly with increasing thickness and reduced frequency (above the threshold reduced frequency). A good spectral collapsing parameter is therefore the thickness-based reduced frequency K_t.
- The reduction of noise due to airfoil thickness is sensitive to observer angle. The noise is increased by a greater amount in the downstream direction than in the upstream direction.
- The accuracy of analytical flat plate methods when predicting turbulence interaction noise can be expected to decrease with increasing airfoil thickness and frequency.

7.3 Effects of Airfoil Leading Edge Radius on the Noise

- Increasing the leading edge radius of an airfoil can also cause a reduction in the noise prediction. The noise appears to reduce proportionally to $\sqrt{R_{le}/c}$.
- Similarly to the effects of airfoil thickness, the noise is reduced by a greater amount in the downstream observer direction in comparison to the upstream direction.
- The noise is sensitive to leading edge radius above a higher threshold of K than for airfoil thickness. This is likely due to the smaller size of the leading edge radius in comparison to the airfoil thickness.
- The noise is less sensitive to leading edge radius than to airfoil thickness.

7.4 Mechanism of Noise Reductions due to Airfoil Geometry

- The effects on noise due to airfoil thickness and leading edge radius are linked, because both length-scales affect the overall airfoil shape and aerodynamic properties such as the shape and size of the stagnation region. It is thought that the effects of the thickness and leading edge radius length-scales are difficult to separate, and that any methods to account for realistic airfoil shape on the noise should consider the complete airfoil profile, as opposed to using a single length-scale such as thickness or leading edge radius.
- The primary mechanism that causes the reduction of noise for real airfoils is related to the leading edge stagnation region. Vortical gusts are distorted by the velocity gradients in the stagnation region such that the wavefront of the gust across the leading edge is smoothed and the gust amplitude is reduced.
- Because the dominant noise reduction mechanism is related to the stagnation region, it is essential to accurately represent the potential flow surrounding an

airfoil when modelling leading edge noise. However, the effects of viscosity on leading edge noise are minimal and can be ignored in most situations.

7.5 Effects of Angle-of-Attack and Camber on the Noise

- Isotropic turbulence interaction noise is not sensitive to the presence of angle-of-attack (AoA) or camber.

- The apparent insensitivity of the noise to camber may be changed if the position of maximum camber is moved closer to the leading edge region. In this study, the position of maximum camber was fixed at 40% of the airfoil chord, and therefore the conclusions are restricted to airfoils with positions of maximum camber that are not close to the leading edge.

- The presence of AoA does has an effect on the airfoil response function. The response is shifted in the k_y spectrum as AoA is increased, and the peak value of the response is increased with increasing AoA. However, when the increased gust response at non-zero k_y values is combined with the decreased turbulence energy at non-zero k_y values, the effects counterbalance each other and cause an overall insensitivity of the noise to AoA.

- The described effects on the gust response function are caused by gust distortions due to the asymmetric meanflow field around airfoils. For positive AoA, the velocity gradients severely distort positively skewed gusts, which increases the noise. For negatively swept gusts the wavefronts are smoothed, which reduces the noise.

- The insensitivity of the noise to AoA is partially a function of the turbulence spectrum. Therefore, for example, if a non-isotropic turbulence spectra was used, the noise may become sensitive to changes in AoA.

7.6 The Single Velocity-Component Modelling Approach

- Accurate turbulence interaction noise predictions can be made with simulations that represent the turbulence as a summation of only transverse disturbances, which is referred to here as a single velocity-component modelling approach. This approach is accurate because the noise is predominantly caused by the transverse disturbances, and the contributions from streamwise and spanwise disturbances are small.

- The single velocity-component modelling approach is valid for symmetric and non-symmetric airfoils, with constant spanwise cross-section, at zero angle-of-attack.

- At reduced frequencies above $K > 8$, for thick airfoils above $t = 0.08c$, the single velocity-component modelling approach has been found to under-predict the noise by as much as 2 dB for symmetric airfoils. In this region, it appears that the streamwise disturbances do have an effect on the noise.

- Airfoils at significant values of AoA (above $\alpha = 2°$) cannot be modelled using the single velocity-component modelling approach. This approach does not accurately represent the effects that non-zero AoA has on the airfoil gust response function.

- The single velocity-component modelling approach provides significant savings in computational expense. Solutions were found approximately 22 times faster than when using a 2D turbulence synthesis method, and $5,000$ times faster than when using a 3D turbulence synthesis method.

7.7 Effects of Airfoil Geometry on CROR Noise Predictions

- The effects of CROR blade geometry on the turbulence interaction noise are small at realistic CROR flow conditions. This is because the geometry of CROR blades near the rotor tip is thin.
- The geometry of CROR blades is likely to cause a reduction in noise of between 2 and 4 dB, in comparison to predictions made using flat plate theory. However, these reductions are at high frequencies (above $2-4$ kHz) that are typically above the peak noise level. Additionally, in this frequency region, BRWI noise is not always the dominant CROR broadband noise source. Therefore, the total CROR broadband noise can be accurately modelled using analytic flat plate theory in most circumstances.

7.8 Future Work

This section suggests possible topics of future work:

- ***Empirical correction of analytical models.*** The thorough parametric study of the noise in this project has shown relatively simple trends between the airfoil geometry (for example, airfoil thickness), and the resulting noise in comparison to flat plate predictions. Therefore, it may be possible to define a simple correction factor which can empirically account for the effects on noise due to airfoil geometry. Gershfeld [88], for example, has presented a similar correction, although it does not account for the apparent Mach number dependency of the effects on noise. This type of correction factor would permit more accurate industrial predictions of CROR noise, and would also permit the efficient optimisation of blade geometry with regards to noise.
- ***Complex turbulence synthesis***. The current work has synthesised turbulence via a summation of Fourier modes, which is a relatively simple method. An interesting study could compare the noise predictions, and the computa-

tional efficiency, of the Fourier summation method with more complex turbulence synthesis via digital filtering, for example.

- ***Improved CROR noise modelling***. In Chapter 6 the noise of a realistic CROR configuration was studied to assess the effects of blade geometry on the noise. However, this study considered only a translating airfoil in order to reduce computational expense. An improved method might be to combine computational simulations with analytical theories, such as the CROR broadband noise theory by Blandeau [20], so that the blade surface pressure response is obtained via a CAA approach and the noise radiation in a rotating system is derived analytically. This would provide a hybrid CROR broadband noise method which is able to accurately account for blade geometry.

- ***Turbulence distortion noise.*** The turbulence synthesis method used here assumes the turbulence to be divergence-free, isotropic, homogeneous and frozen. In complex turbo-machinery systems it is likely that the distortion of the turbulence will act as an additional source of noise. Prediction of this noise source has begun to be addressed by Ayton and Peake [92], for example. It may be beneficial to investigate this noise source computationally.

- ***Airfoil geometry effects on noise in the transonic flow regime.*** In the cruise regime, rotor tip speeds for CROR engines can reach transonic speeds. Due to the presence of supersonic flow, the current noise prediction method is unable to simulate the noise in this configuration. A future study could consider the interaction noise in the transonic flow regime and assess the importance of additional flow features, such as shockwaves.

- ***Effects of viscosity on airfoils at AoA.*** When studying the effects of AoA on the noise, this project has assumed an inviscid meanflow in order to simplify the modelling. However, this approach ignores any effects that may occur due to flow separation, for example. Future work to remove this simplification would be beneficial.

- ***Effects of non-isotropic turbulence.*** This project has assumed isotropic turbulence throughout. However, in Chapter 5 it was found that the effects of AoA on the noise are partially dependent on the shape of the turbulence spectrum. Therefore, it would be useful to investigate the effects of angle-of-attack on the noise when non-isotropic turbulence is used, for example.

Appendix A

Generating Divergence-Free Turbulence

The synthesised turbulence is required to be divergence-free in the current project in order to prevent the turbulence from generating pressure fluctuations and interfering with acoustic results. The method used to ensure divergence-free gust forcing is described here.

A.1 Divergence-free Two-Component Turbulence

When generating two-component synthesised turbulence in 2D simulations, the divergence-free condition (i.e. $\boldsymbol{u}_{2C} \cdot \boldsymbol{x} = 0$) is applied by setting $\boldsymbol{k}_{l,m} \cdot \boldsymbol{\zeta}(\boldsymbol{k}_{l,m})$ in Equation 3.1. The parameter $\boldsymbol{\zeta}$ is a unit vector which describes the direction of each gust mode. Therefore, an additional constraint is $|\boldsymbol{\zeta}| = \sqrt{\zeta_x^2 + \zeta_y^2} = 1$ so that the amplitude of the forced gusts is not affected. In two-dimensions, only one solution of $\boldsymbol{\zeta}$ exists to provide divergence-free turbulence. This is done for each combination of l and m modes by setting

$$\boldsymbol{\zeta} = \begin{pmatrix} \zeta_x \\ \zeta_y \end{pmatrix} = \begin{pmatrix} \pm\dfrac{k_y}{|\boldsymbol{k}|} \\ \mp\dfrac{k_x}{|\boldsymbol{k}|} \end{pmatrix}, \tag{A.1}$$

where $|\boldsymbol{k}| = \sqrt{k_x^2 + k_y^2}$.

A.2 Divergence-free Three-Component Turbulence

When generating three-component synthesised turbulence in 3D, multiple solutions of $\boldsymbol{\zeta}$ exist for each combination of l, m, and n modes, because there are three variables (ζ_x, ζ_y, and ζ_z) being used to satisfy the two conditions $\boldsymbol{k} \cdot \boldsymbol{\zeta}(\boldsymbol{k}) = 0$ and $|\boldsymbol{\zeta}| = 1$. In order to choose a solution, random number generation is used. Three random numbers are generated to define a random vector $\boldsymbol{A}$, as

$$\boldsymbol{A} = \begin{pmatrix} A_x \\ A_y \\ A_z \end{pmatrix}. \tag{A.2}$$

The cross-product is taken between $\boldsymbol{k}$ and the random vector, for each combination of l, m, and n mode, i.e.

$$\boldsymbol{B} = \boldsymbol{k} \times \boldsymbol{A} = \begin{pmatrix} k_y A_z - k_z A_y \\ -k_x A_z + k_z A_x \\ k_x A_y - k_y A_x \end{pmatrix}, \tag{A.3}$$

which gives a vector $\boldsymbol{B}$ that is perpendicular to both the randomly chosen vector $\boldsymbol{A}$ and the wavenumber vector $\boldsymbol{k}$. The final value of $\boldsymbol{\zeta}$ is found by dividing $\boldsymbol{B}$ by its magnitude, i.e.

$$\boldsymbol{\zeta} = \frac{\boldsymbol{B}}{|\boldsymbol{B}|}, \tag{A.4}$$

where $|\boldsymbol{B}| = \sqrt{B_x^2 + B_y^2 + B_z^2}$. This process provides the unit vector $\boldsymbol{\zeta}$, which satisfies both the requirements of $\boldsymbol{k} \cdot \boldsymbol{\zeta}(\boldsymbol{k}) = 0$ and $|\boldsymbol{\zeta}| = 1$, and therefore provides a divergence-free gust disturbance.

Appendix B

Description of Turbulence Spectra

The computational methods discussed in this thesis make use of different velocity spectra for the one-, two-, and three-component turbulence synthesis approaches. The formulation and relations between these spectra are described in this section.

The formulation of the Fourier summation turbulence synthesis method, in 3D, is written in Chapter 4 as

$$\boldsymbol{u}_{3C}(\boldsymbol{x},T)=\sum_{l=1}^{L}\sum_{m=-M}^{M}\sum_{n=-N}^{N}W_{3C}(\boldsymbol{k}_{l,m,n})\cos\Big(\boldsymbol{k}_{l,m,n}\cdot(\boldsymbol{x}-\boldsymbol{U}T)+\sigma_{l,m,n}\Big)\boldsymbol{\zeta}(\boldsymbol{k}_{l,m,n}) \tag{B.1}$$

where the amplitude of the disturbances is set by the velocity amplitude term $W_{3C}(\boldsymbol{k})$. W_{3C} is related to the turbulent energy wavenumber spectrum $E(k)$ by

$$W_{3C}(\boldsymbol{k}_{l,m,n})=\sqrt{E(k_{l,m,n})\Delta k_{l,m,n}} \tag{B.2}$$

where $k_{l,m,n}=\sqrt{k_{x,l}^2+k_{y,m}^2+k_{z,n}^2}$.

In this study the interest lies in separating the k_x, k_y, and k_z components, so it is useful to separate Δk into the individual wavenumber components. To do this, we first wite the relation between the turbulent kinetic energy and the velocity fluctuations in the x, y, and z directions as

$$TKE = \int\limits_{0}^{\infty} E(k)dk = \frac{1}{2}\iiint\limits_{-\infty}^{\infty} \big(\Phi_{uu}(\boldsymbol{k}) + \Phi_{vv}(\boldsymbol{k}) + \Phi_{ww}(\boldsymbol{k})\big) dk_x dk_y dk_z. \tag{B.3}$$

It is also known that for homogeneous and isotropic turbulence [130]

$$\frac{E(k)}{2\pi k^2} = \Phi_{uu}(\boldsymbol{k}) + \Phi_{vv}(\boldsymbol{k}) + \Phi_{ww}(\boldsymbol{k}). \tag{B.4}$$

Using equations B.3 and B.4, it can be shown for a single combination of l, m, and n modes that

$$\Delta k = \frac{\Delta k_x \Delta k_y \Delta k_z}{4\pi k^2}. \tag{B.5}$$

By combining Equation B.5 and Equation B.2, we can write

$$W_{3C}(k) = \sqrt{\frac{E(k)}{4\pi k^2}\Delta k_x \Delta k_y \Delta k_z}. \tag{B.6}$$

These equations can now be used to give expressions of the velocity amplitude spectrum for the one-, two-, and three-component turbulence synthesis approaches.

B.1 Three-component turbulence

The Liepmann energy wavenumber spectrum is given by Ref. [30] as

$$E(k) = \frac{8}{\pi}\overline{w^2}\Lambda\frac{(\Lambda k)^4}{(1+\Lambda^2 k^2)^3}, \tag{B.7}$$

which can be substituted into equation B.6 to obtain

$$W_{3C}(\boldsymbol{k}) = \sqrt{\frac{\Delta k_y \Delta k_z}{4\pi k^2} \frac{8}{\pi} \overline{w^2} \Lambda \frac{(\Lambda k)^4}{(1+\Lambda^2 k^2)^3}} \tag{B.8}$$

where the Δk_x has been ommitted because the intention here is to predict the noise at a set of specific individual wavenumbers, and not to recover a realistic value of the turbulent kinetic energy. Because the k_x modes that are used in this thesis are harmonics of the largest frequency, the value of Δk_x would be constant in each simulation. Therefore the effect of including this term would consist of scaling the amplitude of all results, and would have no effect on the shape of the predicted spectra. This term is also ommitted in the one-, and two-component turbulence synthesis methods.

Equation B.7 can be used in the three-component turbulence synthesis approach that is decribed in Chapter 4.

B.2 Two-component turbulence

The two-component turbulence amplitude spectrum is obtained similarly to the three-component approach. However, in this case the value of k_z is set to zero, and the Δk_z term, which represents the bandwidth of the spanwise modes, is set to an arbitrary unit value. An integration over all k_z values is not required because the two-component turbulence synthesis method includes the energy only from modes with $k_z = 0$. This method was shown by Amiet [30] to be valid for flat plates (and is shown in this thesis to also be valid for generic airfoil profiles) if the observer is in the mid-span plane and the span is large in comparison to the turbulence integral length-scale.

By considering the above discussion, Equations B.6 and B.7 can be combined to give the two-component velocity amplitude spectrum as

$$W_{2C}(k_x, k_y, k_z = 0) = \sqrt{\frac{\Delta k_y}{4\pi k^2}\frac{8}{\pi}\overline{w^2}\Lambda\frac{(\Lambda k)^4}{(1+\Lambda^2 k^2)^3}} \tag{B.9}$$

where $k = \sqrt{k_x^2 + k_y^2}$.

B.3 One-component turbulence

The one-component velocity amplitude spectrum is obtained similarly to the two-, and three-component spectra, but with some differences in order to represent the energy from all k_y modes and in order to only force velocity disturbances in the transverse direction.

The vertical velocity fluctuations are related to $E(k)$ by [130]

$$\Phi_{vv}(\boldsymbol{k}) = \frac{E(k)}{4\pi k^2}\left(1 - k_y^2/k^2\right). \tag{B.10}$$

By setting $k_z = 0$, as was done for the two-component approach, Equation B.10 can be rewritten as

$$\frac{E(k)}{4\pi k^2} = \frac{k^2}{k_x^2}\Phi_{vv}(\boldsymbol{k}). \tag{B.11}$$

where $k = \sqrt{k_x^2 + k_y^2}$. By substituting Equation B.11 into Equation B.6 and including the component of the unit vector in the transverse direction, the amplitude of the transverse velocity disturbance can be written as

$$W_{1C}(k_x, k_y, k_z = 0) = \xi_x(k_x)\sqrt{\Delta k_x \Delta k_y \frac{k^2}{k_x^2}\Phi_{vv}(\boldsymbol{k})}. \tag{B.12}$$

It was shown in Appendix A that $\xi_x = \mp k_x/\sqrt{k_x^2 + k_y^2}$ in order to provide 2D divergence-free turbulence. This can be substituted into Equation B.12 to give

$$W_{1C}(k_x, k_y, k_z = 0) = \sqrt{\Delta k_x \Delta k_y \Phi_{vv}(\boldsymbol{k})}. \tag{B.13}$$

The final step to obtain the one-component velocity amplitude spectrum is to perform an integration over all k_y modes so that the energy at all k_y values is represented by the amplitude of gusts with $k_y = 0$. This integration is done analytically, as opposed to the numerical integration that is implicitly used in the two-component turbublence synthesis approach. Therefore, the discretised integration in Equation B.13 is replaced by an analytical integration, i.e.

$$\lim_{\Delta k_{y,m} \to 0} \sum_{m=-\infty}^{\infty} \Delta k_{y,m} \Phi_{vv}(\boldsymbol{k}_{l,m,n}) = \int_{-\infty}^{\infty} \Phi_{vv}(\boldsymbol{k}) dk_y. \tag{B.14}$$

The vertical velocity amplitude Liepmann spectrum, after integration over all k_y wavenumbers, and with $k_z = 0$, is given by Ref. [30] as

$$\Phi_{vv}(k_x, k_z = 0) = \frac{3\overline{w^2}\Lambda^2}{4\pi} \frac{\Lambda^2 k_x^2}{(1 + \Lambda^2 k_x^2)^{2.5}}. \tag{B.15}$$

Equation B.15 can be substituted into Equation B.13 to give the one-component velocity amplitude spectrum as

$$W_{1C}(k_x, k_z = 0) = \sqrt{\frac{3\overline{w^2}\Lambda^2}{4\pi} \frac{\Lambda^2 k_x^2}{(1 + \Lambda^2 k_x^2)^{2.5}}}. \tag{B.16}$$

Appendix C

Additional Simulation Information

This appendix contains additional information on various grids and cases that were used throughout the project. This is not an exhaustive list of all the cases that were performed. Instead, this information is intended to give examples of parameters such as the maximum and average values of grid skewness, the total simulation time, the timestep, and number of grid points. Where simulation times are quoted, this usually refers to the time taken when using the two-component turbulence synthesis method, except in Table C.5 which refers to the one-component method that was used in Chapter 6.

Values of maximum skewness in the leading edge region are given as an indicator of grid quality. Due to the leading edge curvature, the skewness was highest in this region. Throughout the remainder of each grid the skewness was significantly lower, resulting in the low values of average skewness seen in Table C.1. Here, skewness refers to the equi-angular skew, which is calculated as

$$Skewness = \max\left[\frac{\theta_{max} - \theta_e}{180 - \theta_e}, \frac{\theta_e - \theta_{min}}{\theta_e}\right], \tag{C.1}$$

where θ_{min} and θ_{max} are respectively the largest and smallest angles in a cell, and $\theta_e = 90°$ is the ideal angle for the cell.

Airfoil	M	Δt **(non-dim)**	**No. Procs.**	**No. Cells**	**Max. leading edge skewness**	**Average skewness**
NACA0002	0.2	1×10^{-4}	48	$939,112$	5×10^{-1}	1.75×10^{-2}
NACA0012-63	0.2	2×10^{-4}	48	$878,380$	3.4×10^{-1}	1.56×10^{-2}
NACA0012-63	0.4	2×10^{-4}	48	$878,380$	3.4×10^{-1}	1.56×10^{-2}
NACA0012-63	0.6	2×10^{-4}	48	$878,380$	3.4×10^{-1}	1.56×10^{-2}
NACA0006-03	0.2	2×10^{-4}	48	$878,380$	8×10^{-1}	1.66×10^{-2}
NACA0006-23	0.2	2×10^{-4}	48	$878,380$	6.5×10^{-1}	1.65×10^{-2}
NACA0006-43	0.2	2×10^{-4}	48	$878,380$	5.5×10^{-1}	1.66×10^{-2}
NACA0006-63	0.2	2×10^{-4}	48	$878,380$	4.6×10^{-1}	1.66×10^{-2}
NACA0006-83	0.2	2×10^{-4}	48	$878,380$	4.5×10^{-1}	1.66×10^{-2}
NACA0006-103	0.2	2×10^{-4}	48	$878,380$	3.8×10^{-1}	1.66×10^{-2}
NACA0012-03	0.2	2×10^{-4}	48	$878,380$	6.7×10^{-1}	1.56×10^{-2}
NACA0012-23	0.2	2×10^{-4}	48	$878,380$	4.6×10^{-1}	1.56×10^{-2}
NACA0012-43	0.2	2×10^{-4}	48	$878,380$	3.8×10^{-1}	1.56×10^{-2}
NACA0012-63	0.2	2×10^{-4}	48	$878,380$	3.4×10^{-1}	1.56×10^{-2}
NACA0012-83	0.2	2×10^{-4}	48	$878,380$	2.5×10^{-1}	1.56×10^{-2}
NACA0012-103	0.2	2×10^{-4}	48	$878,380$	1.15×10^{-1}	1.56×10^{-2}
NACA0018-03	0.2	2×10^{-4}	48	$878,380$	5.6×10^{-1}	1.55×10^{-2}
NACA0018-23	0.2	2×10^{-4}	48	$878,380$	2.9×10^{-1}	1.55×10^{-2}
NACA0018-43	0.2	2×10^{-4}	48	$878,380$	1.71×10^{-1}	1.55×10^{-2}
NACA0018-63	0.2	2×10^{-4}	48	$878,380$	1.27×10^{-1}	1.55×10^{-2}
NACA0018-83	0.2	2×10^{-4}	48	$878,380$	1.45×10^{-1}	1.56×10^{-2}
NACA0018-103	0.2	2×10^{-4}	48	$878,380$	2.1×10^{-1}	1.56×10^{-2}
NACA0024-03	0.2	2×10^{-4}	48	$878,380$	4.7×10^{-1}	1.57×10^{-2}
NACA0024-23	0.2	2×10^{-4}	48	$878,380$	2.63×10^{-1}	1.57×10^{-2}
NACA0024-43	0.2	2×10^{-4}	48	$878,380$	1.61×10^{-1}	1.57×10^{-2}
NACA0024-63	0.2	2×10^{-4}	48	$878,380$	9.9×10^{-2}	1.56×10^{-2}
NACA0024-83	0.2	2×10^{-4}	48	$878,380$	1.33×10^{-1}	1.56×10^{-2}
NACA0024-103	0.2	2×10^{-4}	48	$878,380$	1.9×10^{-1}	1.56×10^{-2}

Table C.1: Additional simulation information for Chapter 2.

Airfoil	M	Δt **(non-dim)**	**No. Procs.**	**No. Cells**	**Max. leading edge skewness**	**Simulation time (s) (One realisation)**
NACA0002	0.5	1×10^{-4}	48	$966,540$	5.6×10^{-1}	$37,803$
NACA0003	0.5	1×10^{-4}	48	$966,540$	5.5×10^{-1}	$49,842$
NACA0004	0.5	2×10^{-4}	48	$966,540$	5.5×10^{-1}	$41,338$
NACA0005	0.5	2×10^{-4}	48	$966,540$	5.2×10^{-1}	$41,439$
NACA0006	0.5	2.5×10^{-4}	48	$966,540$	5×10^{-1}	$39,660$
NACA0007	0.5	2×10^{-4}	48	$966,540$	4.1×10^{-1}	$41,426$
NACA0008	0.5	2.5×10^{-4}	48	$966,540$	3.8×10^{-1}	$39,563$
NACA0009	0.5	2×10^{-4}	48	$966,540$	3.7×10^{-1}	$40,647$
NACA0010	0.5	2.5×10^{-4}	48	$966,540$	4×10^{-1}	$39,469$
NACA0011	0.5	2×10^{-4}	48	$966,540$	3.9×10^{-1}	$41,287$
NACA0012	0.5	2×10^{-4}	48	$966,540$	3.9×10^{-1}	$41,277$

Table C.2: Additional simulation information for Chapter 3.

Airfoil	M	Δt **(non-dim)**	**No. Procs.**	**No. Cells**	**Max. leading edge skewness**	**Simulation time (s) (One realisation)**
One-Component	0.5	5×10^{-4}	16	$450,116$	3.7×10^{-1}	$3,716$
Two-Component	0.5	5×10^{-4}	16	$450,116$	3.7×10^{-1}	$4,053$
Three-Component	0.5	5×10^{-4}	192	$27,907,192$	3.7×10^{-1}	$77,725$

Table C.3: Additional simulation information for the NACA0012 airfoil simulations in Chapter 4.

Airfoil	M	Δt **(non-dim)**	**No. Procs.**	**No. Cells**	**Max. leading edge skewness**	**Simulation time (s) (One realisation)**
NACA0006 $\alpha = 0°$	0.3	2.5×10^{-4}	48	$966,540$	5×10^{-1}	$29,320$
NACA0006 $\alpha = 2°$	0.3	2.5×10^{-4}	48	$966,540$	5×10^{-1}	$28,227$
NACA0006 $\alpha = 4°$	0.3	1×10^{-4}	48	$966,540$	5×10^{-1}	$49,965$
NACA0006 $\alpha = 6°$	0.3	2×10^{-4}	48	$966,540$	5.24×10^{-1}	$32,760$
NACA0012 $\alpha = 0°$	0.3	2.5×10^{-4}	48	$966,540$	3.9×10^{-1}	$30,118$
NACA0012 $\alpha = 2°$	0.3	2.5×10^{-4}	48	$966,540$	3.9×10^{-1}	$30,608$
NACA0012 $\alpha = 4°$	0.3	2.5×10^{-4}	48	$966,540$	3.9×10^{-1}	$28,676$
NACA0012 $\alpha = 6°$	0.3	2.5×10^{-4}	48	$966,540$	3.9×10^{-1}	$28,646$
NACA1406	0.3	2.5×10^{-4}	48	$966,540$	4.8×10^{-1}	$28,258$
NACA2406	0.3	2.5×10^{-4}	48	$966,540$	5×10^{-1}	$28,503$
NACA3406	0.3	2.5×10^{-4}	48	$966,540$	5.3×10^{-1}	$28,672$
NACA4406	0.3	2.5×10^{-4}	48	$966,540$	5.8×10^{-1}	$27,980$
NACA5406	0.3	2.5×10^{-4}	48	$966,540$	6.1×10^{-1}	$28,225$

Table C.4: Additional simulation information for simulations in Chapter 5.

Case	M	Δt **(non-dim)**	**No. Procs.**	**No. Cells**	**Max. leading edge skewness**	**Simulation time (s) (One realisation)**
Hub, sideline	0.45	1×10^{-4}	48	$966,540$	5.4×10^{-1}	$14,589$
Hub, cut-back	0.4	1×10^{-4}	48	$966,540$	5.4×10^{-1}	$15,848$
Tip, sideline	0.65	5×10^{-5}	48	$966,540$	5.3×10^{-1}	$16,543$
Tip, cut-back	0.6	5×10^{-5}	48	$966,540$	5.3×10^{-1}	$16,844$

Table C.5: Additional simulation information for simulations in Chapter 6.

Bibliography

[1] J. Leahy, "Airbus global market forecast 2010-2029," 2010.

[2] "Flightpath 2050 europe's vision for aviation: Report of the high level group research," European Commission, 2011.

[3] D. B. Hanson, "Noise of counter rotation propellers," *Journal of Aircraft*, vol. 22, pp. 609–617, 1985.

[4] W. Strack, G. Knip, A. L. Weisbrich, J. Godston, and E. Bradley, "Technology and benefits of aircraft counter rotation propellers," Tech. Rep. 82983, NASA, 1982.

[5] G. Electric, "GE and NASA to initiate wind-tunnel testing for open rotor jet engine systems.." Press Release "`http://www.geae.com/aboutgeae/presscenter/other/other_20081024.html`", 24 October 2008, Last accessed 14/08/2014.

[6] Airliners.net, "The antonov an-22 antei." "`http://www.airliners.net/aircraft-data/stats.main?id=36`", Last accessed, 27/09/2011.

[7] J. Gill, X. Zhang, P. Joseph, and T. Node-Langlois, "Effects of real airfoil geometry on leading edge gust interaction noise," in *19th AIAA/CEAS Aeroacoustics Conference, Berlin Germany*, no. 2013-2203, 2013.

[8] J. Gill, X. Zhang, P. Joseph, and T. Node-Langlois, "Reduced dimension modeling of leading edge turbulent interaction noise," in *20th AIAA/CEAS Aeroacoustics Conference, Atlanta Georgia*, no. 2014-2321, 2014.

[9] T. Node-Langlois, F. Wlassow, V. Languille, Y. Colin, B. Caruelle, J. Gill, X. Chen, X. Zhang, and A. Parry, "Prediction of contra-rotating open rotor broadband noise in isolated and installed configurations," in *20th AIAA/CEAS Aeroacoustics Conference, Atlanta Georgia*, no. 2014-2610, 2014.

[10] J. Gill, X. Zhang, and P. Joseph, "Symmetric airfoil geometry effects on leading edge noise," *Journal of the Acoustical Society of America*, vol. 134, no. 4, pp. 2669–2680, 2013.

[11] J. Gill, X. Zhang, and P. Joseph, "Single velocity-component modeling of leading edge turbulence interaction noise," *(Submitted to) Journal of the Acoustical Society of America*, 2014.

[12] B. Magliozzi, D. B. Hanson, and R. K. Amiet, "Propeller and propfan noise," Tech. Rep. 92-10599, NASA, Langley Research Center, 1991.

[13] P. R. Spalart, "Initial noise predictions for open rotors using first principles," in *16th AIAA/CEAS Aeroacoustics Conference, Stockholm Sweden*, no. 2010-3793, 2010.

[14] V. Blandeau, *Aerodynamic Broadband Noise from Contra-Rotating Open Rotors.* PhD thesis, ISVR, University of Southampton, 2011.

[15] J. Dittmar, "The effect of front-to-rear propeller spacing on the interaction noise of a model counterrotation propeller at cruise conditions," Tech. Rep. 100121, NASA, 1987.

[16] M. J. Lighthill, "On sound generated aerodynamically: General theory," *Proceedings of the Royal Society*, pp. 564–587, 1951.

[17] V. Blandeau, P. F. Joseph, and B. J. Tester, "Broadband noise prediction from rotor-wake interaction in contra-rotating propfans," in *15th AIAA/CEAS Aeroacoustics Conference, Miami Florida*, 2009.

[18] A. B. Parry, M. Kingan, and B. J. Tester, "Relative importance of open rotor tone and broadband noise sources," in *17th AIAA/CEAS Aeroacoustics Conference, Portland Oregon*, no. 2011-2763, 2011.

[19] V. Blandeau and P. F. Joseph, “Broadband noise due to rotor-wake/rotor interaction in contra-rotating open rotors,” *AIAA Journal*, vol. 48, pp. 2674–2686, 2010.

[20] V. Blandeau and P. F. Joseph, “Parameter study of the broadband noise predictions from uninstalled contra-rotating open rotors,” in *14th CEAS-ASC Workshop and 5th Scientific Workshop of X3-Noise*, 2011.

[21] V. Blandeau and P. F. Joseph, “Validity of amiet’s model for propeller trailing-edge noise,” *AIAA Journal*, vol. 49, pp. 1057–1066, 2011.

[22] M. Kingan, “Open rotor broadband interaction noise,” in *18th AIAA/CEAS Aeroacoustics Conference, Colorado Springs*, 2012.

[23] R. K. Amiet, “Noise due to turbulent flow past a trailing edge,” *Journal of Sound and Vibration*, vol. 47, pp. 387–393, 1976.

[24] M. Roger and S. Moreau, “Extensions and limitations of analytical airfoil broadband noise models,” *International Journal of Aeroacoustics*, vol. 9, pp. 273–305, 2010.

[25] R. Sandberg, N. Sandham, and P. Joseph, “Direct numerical simulations of trailing-edge noise generated by boundary-layer instabilities,” *Journal of Sound and Vibration*, vol. 304, pp. 677–690, 2007.

[26] J. F. Williams and D. L. Hawkings, “Sound generation by turbulence and surfaces in arbitrary motion,” *Royal Society of London*, vol. 264, pp. 321–341, 1969.

[27] R. K. Amiet, “Noise produced by turbulent flow into a propeller or helicopter rotor,” *AIAA Journal*, vol. 15, pp. 307–308, 1977.

[28] W. J. Sears, “Some aspects of non-stationary airfoil theory and its practical applications,” *Journal of Aerospace Sciences*, vol. 8, pp. 104–108, 1941.

[29] J. M. Graham, “Similarity rules for thin aerofoils in non-stationary subsonic flows,” *Journal of Fluid Mechanics*, vol. 43, no. 4, pp. 753–766, 1970.

[30] R. K. Amiet, “Acoustic radiation from an airfoil in a turbulent stream,” *Journal of Sound and Vibration*, vol. 41, no. 4, pp. 407–420, 1975.

[31] V. Blandeau, P. Joseph, M. Kingan, and A. Parry, “Broadband noise predictions from uninstalled contra-rotating open rotors,” *International Journal of Aeroacoustics*, vol. 12, no. 3, pp. 245–282, 2013.

[32] A. Carazo, M. Roger, and M. Omais, “Analytical prediction of wake-interaction noise in counter-rotation open rotors,” in *17th AIAA/CEAS Aeroacoustics Conference, Portland Oregon*, no. 2011-2758, 2011.

[33] M. Roger and A. Carazo, “Blade-geometry considerations in analytical gust-airfoil interaction noise models,” in *16th AIAA/CEAS Aeroacoustics Conference, Stockholm Sweden*, vol. 2010-3799, 2010.

[34] J. F. Williams and D. L. Hawkings, “Theory relating to the noise of rotating machinery,” *Journal of Sound and Vibration*, vol. 10, pp. 10–21, 1969.

[35] R. K. Amiet, “Compressibility effects in unsteady airfoil theory,” *AIAA Journal*, vol. 12, pp. 252–255, 1974.

[36] R. K. Amiet, “High frequency thin-airfoil theory for subsonic flow,” *AIAA Journal*, vol. 14, pp. 1076–1082, 1975.

[37] C. K. W. Tam, “Computational aeroacoustics: Issues and methods,” *AIAA Journal*, vol. 33, pp. 1788–1796, 1995.

[38] R. Hixon, “Prefactored small-stencil compact schemes,” *Journal of Computational Physics*, vol. 165, pp. 522–541, 2000.

[39] G. Ashcroft and X. Zhang, “Optimised prefactored compact schemes,” *Journal of Computational Physics*, vol. 190, no. 2, pp. 459–477, 2003.

[40] J. W. Kim, “Optimised boundary compact finite difference schemes for computational aeroacoustics,” *Journal of Computational Physics*, vol. 225, pp. 995–1019, 2007.

[41] J. W. Kim, “High-order compact filters with variable cut-off wavenumber and stable boundary treatment,” *Computers and Fluids*, vol. 39, pp. 1168–1182, 2010.

[42] T. Colonius and S. K. Lele, “Computational aeroacoustics: Progress on non-linear problems of sound generation.,” *Progress in Aerospace Sciences*, vol. 40, pp. 345–416, 2004.

[43] N. Curle, “The influence of solid bodies upon aerodynamic sound,” *Royal Society of London*, vol. 231, pp. 505–514, 1955.

[44] F. Farassat and G. P. Succi, “The prediction of helicopter rotor discrete frequency noise,” *Vertica*, vol. 7, no. 4, pp. 309–320, 1983.

[45] D. Angland and X. Zhang, “Installation effects of landing gears,” in *19th AIAA/CEAS Aeroacoustics Conference, Berlin Germany*, no. 2013-2138, 2013.

[46] S. Richards, X. Chen, X. Huang, and X. Zhang, “Computation of fan noise radiation through an engine exhaust geometry with flow,” *International Journal of Aeroacoustics*, vol. 6, no. 3, pp. 223–241, 2007.

[47] X. Zhang, “Aircraft noise and its nearfield propagation computations,” *Acta Mechanica Sinica*, vol. 28, no. 4, pp. 1–18, 2012.

[48] E. J. Hall and R. A. Delaney, “Investigation of advanced counterrotation blade configuration concepts for high speed turboprop systems,” Tech. Rep. NAS3-25270, NASA, 1991.

[49] E. R. Busch, M. Kebler, and E. Kramer, “Aeroacoustics of a high-fidelity CFD calculation of a counter-rotating open rotor in take-off conditions,” in *19th AIAA/CEAS Aeroacoustics Conference, Berlin Germany*, no. 2013-2202, 2013.

[50] A. Stuermer and J. Yin, “Low-speed aerodynamics and aeroacoustics of cror propulsion systems,” in *AIAA/CEAS Aeroacoustics Conference, Miami, Florida*, 2009.

[51] T. Gerhold, "Overview of the hybrid rans code TAU," *Notes on Numerical Fluid Mechanics and Multidisciplinary Design*, vol. 89, pp. 81–92, 2005.

[52] R. Schnell, J. Yin, S. Funke, and H. Siller, "Aerodynamic and basic acoustic optimisation of a contra-rotating open rotor with experimental verification," in *18th AIAA/CEAS Aeroacoustics Conference, Colorado Springs*, no. 2012-2127, 2012.

[53] R. A. D. Akkermans, A. Steurmer, and J. W. Delfs, "Assessment of front-rotor trailing-edge-blowing for the reduction of open rotor noise emissions," in *19th AIAA/CEAS Aeroacoustics Conference, Berlin Germany*, no. 2013-2200, 2013.

[54] P. R. Spalart, A. K. Travin, M. L. Shur, and M. K. Strelets, "Initial noise predictions for open rotors using first principles," in *16th AIAA/CEAS Aeroacoustics Conference, Stockholm , Sweden*, no. 2010-3793, 2010.

[55] T. Deconinck, P. Hoffer, and C. Hirsch, "Prediction of near- and far-field noise generated by contra-rotating open rotors," in *16th AIAA/CEAS Aeroacoustics Conference, Stockholm Sweden*, no. 2010-3794, 2010.

[56] T. Deconinck, A. Capron, V. Berbieux, and C. Hirsch, "Sensitivity study on computational parameters for the predictions of noise generated by counter-rotatings open rotors," in *17th AIAA/CEAS Aeroacoustics Conference, Portland Oregon*, no. 2011-2765, 2011.

[57] S. Guerin, A. Moreau, C. Menzel, and C. Weckmuller, "Open-rotor noise prediction with a RANS-informed analytical approach," in *18th AIAA/CEAS Aeroacoustics Conference, Colorado Springs*, no. 2012-2303, 2012.

[58] F. Falissard, R. boisard, and G. Delattre, "Aeroacoustic computation of a contra rotating open rotor model with test rig installation effects," in *18th AIAA/CEAS Aeroacoustics Conference, Colorado Springs*, no. 2012-2218, 2012.

[59] Y. Colin, B. Caruelle, and A. B. Parry, "Computational strategy for predicting cror noise at low-speed part iii: Investigation of noise radiation with the ffowcs

williams-hawkings analogy," in *18th AIAA/CEAS Aeroacoustics Conference, Colorado Springs*, no. 2012-2223, 2012.

[60] A. Sharma and H. Chen, "Prediction of tonal aerodynamic noise from open rotors," in *18th AIAA/CEAS Aeroacoustics Conference, Colorado Springs*, no. 2012-2265, 2012.

[61] J. K. Staubs, Real Airfoil Effects on Leading Edge Noise. PhD thesis, Virginia Polytechnic Institute and State University, 2008.

[62] W. J. Devenport, J. K. Staubs, and S. A. L. Glegg, "Sound radiation from real airfoils in turbulence," *Journal of Sound and Vibration*, vol. 329, pp. 3470–3483, 2010.

[63] R. W. Paterson and R. K. Amiet, "Acoustic radiation and surface pressure response of an airfoil due to incident turbulence," Tech. Rep. CR-2733, NASA, 1976.

[64] M. Myers and E. J. Kerschen, "Influence of incidence angle on sound generation by airfoils interacting with high frequency gusts," *Journal of Fluid Mechanics*, vol. 292, pp. 271–304, 1995.

[65] M. Myers and E. J. Kerschen, "Influence of camber on sound generation by airfoils interacting with high-frequency gusts," *Journal of Fluid Mechanics*, vol. 353, pp. 221–259, 1997.

[66] S. A. L. Glegg and W. J. Devenport, "Unsteady loading on an airfoil of arbitrary thickness," *Journal of Sound and Vibration*, vol. 319, pp. 1252–1270, 2009.

[67] S. Moreau, M. Roger, and V. Jurdic, "Effect of angle of attack and airfoil shape on turbulence interaction noise," in *11th AIAA/CEAS Aeroacoustics Conference, Monterey, California*, no. 2005-2973, 2005.

[68] P. J. Moriarty, G. Guidati, and P. Migliore, "Prediction of turbulent inflow and trailing-edge noise for wind turbines," in *11th AIAA/CEAS Aeroacoustics Conference, Monterey CA*, no. 2005-2881, 2005.

[69] L. Santana, C. Schram, and W. Desmet, “Panel method for turbulence-airfoil interaction noise prediction,” in *18th AIAA/CEAS Aeroacoustics Conference, Colorado Springs*, no. 2012-2073, 2012.

[70] G. Guidati and S. Wagner, “The influence of airfoil shape on gust-airfoil interaction noise in compressible flows,” *AIAA Journal*, no. 99-1843, pp. 279–286, 1999.

[71] S. A. L. Glegg and W. J. Devenport, “Panel methods for airfoils in turbulent flow,” *Journal of Sound and Vibration*, vol. 329, pp. 3709–3720, 2010.

[72] W. Olsen and J. Wagner, “Effect of thickness on airfoil surface noise,” *AIAA Journal*, vol. 20, no. 3, pp. 437–439, 1981.

[73] A. M. Hall, O. Atassi, and J. Gilson, “Effects of leading-edge thickness on high-speed airfoil-turbulence interaction noise,” in *17th AIAA/CEAS Aeroacoustics Conference, Portland, Oregon*, no. 2011-2861, 2011.

[74] S. Oerlemans and P. Migliore, “Aeroacoustic wind tunnel tests of wind turbine airfoils,” in *10th AIAA/CEAS Aeroacoustics Conference, Manchester United Kingdom*, no. AIAA 2004-3042, 2004.

[75] P. Migliore and S. Oerlemans, “Wind tunnel aeroacoustic tests of six airfoils for use on small wind turbines,” in *AIAA Wind Energy Symposium*, 2004.

[76] I. Evers and N. Peake, “On sound generation by the interaction between turbulence and a cascade of airfoils with non-uniform mean flow,” *Journal of Fluid Mechanics*, vol. 463, pp. 25–52, 2002.

[77] H. M. Atassi, S. Subramaniam, and J. R. Scott, “Acoustic radiation from lifting airfoils in compressible subsonic flow,” Tech. Rep. AIAA-90-3911, NASA, 1990.

[78] J. R. Scott and H. M. Atassi, “Numerical solutions of the linearized euler equations for unsteady vortical flows around lifting airfoils,” Tech. Rep. 102466, NASA, 1990.

[79] D. Lockard and P. Morris, “Radiated noise from airfoils in realistic mean flows,” *AIAA Journal*, vol. 36, no. 6, pp. 907–914, 1998.

[80] A. S. H. Lau and J.-W. Kim, "The effect of wavy leading edges on airfoil-gust interaction noise," in *19th AIAA/CEAS Aeroacoustics Conference, Berlin Germany*, no. 2013-2120, 2013.

[81] A. Lau, S. Haeri, and J. W. Kim, "The effect of wavy leading edges on aerofoil gust interaction noise," *Journal of Sound and Vibration*, vol. 332, pp. 6234–6253, 2013.

[82] S. Haeri, J. W. Kim, S. Narayanan, and P. Joseph, "3D calculations of aerofoil-turbulence interaction noise and the effect of wavy leading edges," in *20th AIAA/CEAS Aeroacoustics Conference, Atlanta Georgia*, no. 2014-2325, 2014.

[83] J. Christophe, J. Anthoine, P. Rambaud, C. Schram., F. Mathey, and S. Moreau, "Prediction of incoming turbulent noise using a combined numerical / semi-empirical method and experimental validation," in *13th AIAA/CEAS Aeroacoustics Conference, Rome*, no. 2007-3468, 2007.

[84] H. Deniau., G. Dufour, C. Polacsek, , and S. Moreau, "Affordable compressible les of airfoil-turbulence interaction in a free jet," in *17th AIAA/CEAS Aeroacoustics Conference, Portland OR*, no. 2011-2707, 2011.

[85] M. E. Goldstein and H. Atassi, "A complete second-order theory for the unsteady flow about an airfoil due to a periodic gust," *Journal of Fluid Mechanics*, vol. 74, pp. 741–765, 1976.

[86] H. M. Atassi, "The sears problem for a lifting airfoil revisited - new results," *Journals of Fluid Mechanics*, vol. 141, pp. 109–122, 1984.

[87] H. M. Atassi, M. Dusey, and C. M. Davis, "Acoustic radiation from a thin airfoil in nonuniform subsonic flows," *AIAA Journal*, vol. 31, p. 1993, 1993.

[88] J. Gershfeld, "Leading edge noise from thick foils in turbulent flow," *Journal of the Acoustical Society of America*, vol. 116, no. 3, pp. 1416–1426, 2004.

[89] M. Howe, *Acoustics of Fluid-Structure Interactions.* Cambridge University Press, 1998.

[90] P. J. Moriarty, G. Guidati, and P. G. Migliore, "Recent improvement of a semi-empirical aeroacoustic prediction code for wind turbines," in *10th AIAA/CEAS Aeroacoustics Conference, OR*, no. 2004-3041, 2004.

[91] P. Lysak, D. Capone, and M. Jonson, "Prediction of high frequency gust response with airfoil thickness effects," *Journal of Fluids and Structures*, vol. 39, pp. 258–274, 2013.

[92] L. Ayton and N. Peake, "An analytic approach to high-frequency gust-aerofoil interaction noise in steady shear flows.," in *20th AIAA/CEAS Aeroacoustics Conference, Atlanta Georgia*, no. 2014-2322, 2014.

[93] H. D. Chiang and S. Fleeter, "Prediction of oscillating thick cambered aerofoil aerodynamics by a locally analytic method," *International Journal of Numerical Methods in Fluids*, vol. 8, pp. 913–931, 1988.

[94] X. Zhang, X. X. Chen, and P. A. Nelson, "Computation of spinning modal radiation from an unflanged duct," *AIAA Journal*, vol. 42, no. 6, pp. 1795–1801, 2004.

[95] F. Hu, M. Y. Hussaini, and J. Manthey, "Low-dissipation and low-dispersion runge-kutta schemes for computational aeroacoustics," *Journal of Computational Physics*, vol. 124, no. 52, pp. 177–191, 1996.

[96] S. K. Richards, X. Zhang, X. X. Chen, and P. A. Nelson, "The evaluation of non-reflecting boundary conditions for duct-acoustic computation," *Journal of Sound and Vibration*, vol. 270, pp. 539–557, 2004.

[97] J. W. Kim, A. S. H. Lau, and N. D. Sandham, "CAA boundary conditions for airfoil noise due to high-frequency gusts," *Periodica Engineering*, vol. 6, no. 6, pp. 244–253, 2010.

[98] J. W. Kim, A. S. H. Lau, and N. D. Sandham, "Proposed boundary conditions for gust-airfoil interaction noise," *AIAA Journal*, vol. 48, pp. 2705–2709, 2010.

[99] V. V. Golubev, R. R. Mankbadi, and J. R. Scott., "Numerical inviscid analysis of nonlinear airfoil response to impinging high-intensity high-frequency gust,"

in *10th AIAA/CEAS Aeroacoustics Conference, Manchester United Kingdom*, no. 2004-3002, 2004.

[100] V. V. Golubev, R. R. Mankbadi, M. Visbal, J. R. Scott, and R. Hixon, "A parameteric study of nonlinear gust-airfoil interaction," in *12th AIAA/CEAS Aeroacoustics Conference, Cambridge Massachusetts*, no. 2006-2426, 2006.

[101] D. P. Lockard and P. J. Morris, "A parallel implementation of a computational aeroacoustic algorithm for airfoil noise," *Journal of Computational Acoustics*, vol. 5, no. 4, pp. 337–353, 1997.

[102] F. Farassat, "Derivation of formulations 1 and 1a of farassat," Tech. Rep. 2007-214853, NASA, 2007.

[103] C. Ladson, C. Brookes, A. Hill, and D. Sproles, "Computer program to obtain ordinates for naca airfoils," Tech. Rep. 4741, NASA, 1996.

[104] R. H. Kraichnan, "Diffusion by a random velocity field," *The Physics of Fluids*, vol. 13, no. 1, pp. 22–31, 1970.

[105] W. Bechara, C. Bailly, and P. Lafon, "Stochastic approach to noise modelling for free turbulent flows," *AIAA Journal*, vol. 32, no. 3, pp. 244–463, 1994.

[106] C. Bailly and D. Juve, "A stochastic approach to compute subsonic noise using linearized euler's equations," in *5th AIAA/CEAS Aeroacoustics Conference, Greater Seatle, Washington*, no. AIAA 99-1872, 1999.

[107] M. Billson, L.-E. Eriksson, and L. Davidson, "Jet noise modeling using synthetic anisotropic turbulence," in *10th AIAA/CEAS Aeroacoustics Conference, Manchester United Kingdom*, no. 2004-3028, 2004.

[108] G. Reboul and C. Polacsek, "Toward numerical simulation of fan broadband noise aft radiation from aeroengines," *AIAA Journal*, vol. 48, no. 9, pp. 2038–2048, 2010.

[109] V. Clair, C. Polacsek, T. L. Garrec, G. Reboul, M. Gruber, and P. Joseph, "Experimental and numerical investigation of turbulence-airfoil noise reduction using leading edge serrations," in *18th AIAA/CEAS Aeroacoustics Conference, Colorado Springs*, no. AIAA 2012-2189, 2012.

[110] M. Klein, A. Sadiki, and J. Janicka, "A digital filter based generation of inflow data for spatially developing direct numerical or large eddy simulations," *Journal of Computational Physics*, vol. 186, pp. 652–665, 2003.

[111] A. Careta, F. Sagues, and J. Sancho, "Stochastic generation of homogeneous isotropic turbulence with well-defined spectra," *Physical Review E*, vol. 48, no. 3, pp. 2279–2287, 1993.

[112] R. Ewert and R. Emunds, "CAA slat noise studies applying stochastic sound sources based on solenoidal digital filters," in *11th AIAA/CEAS Aeroacoustics Conference, Monterey California*, no. 2005-2862, 2005.

[113] R. Ewert, "Rpm - the fast random particle-mesh method to realise unsteady turbulent sound sources and velocity ffield for caa applications," in *13th AIAA/CEAS Aeroacoustics Conference, Rome*, no. 2007-3506, 2007.

[114] R. Ewert, J. Dierke, N. Neifeld, C. Appel, M. Siefert, and O. Kornow, "Caa broadband noise prediction for aeroacoustic design," *Procedia Engineering*, vol. 6, pp. 254–263, 2010.

[115] R. Ewert, J. Dierke, A. Neifeld, and S. M. A. Moghadam, "Linear and nonlinear perturbation equations with relaxation source terms for forced eddy simulation of aeroacoustic sound generation," in *20th AIAA/CEAS Aeroacoustics Conference, Atlanta GA*, no. 2014-3053, 2014.

[116] M. Dieste, *Random-Vortex-Particle Methods Applied to Broadband Fan Interaction Noise*. PhD thesis, Institute of Sound and Vibrational Research, University of Southampton, 2011.

[117] N. Jarrin, S. Benhamadouche, D. Laurence, and R. Prosser, "A synthetic-eddy-method for generating inflow conditions for large-eddy simulations," *International Jornal of Heat and Fluid Flow*, vol. 27, pp. 585–593, 2006.

[118] N. Jarrin, *Synthetic Inflow Boundary Conditions for the Numerical Simulation of Turbulence*. PhD thesis, School of Mechanical, Aerospace and Civil Engineering, University of Manchester, 2008.

[119] N. Jarrin, R. Prosser, J.-C. Uribe, S. Benhamadouche, and D. Laurence, "Reconstruction of turbulent fluctuations for hybrid rans/les simulations using a synthetic-eddy method," *International Journal of Heat and Fluid Flow*, vol. 30, pp. 435–442, 2009.

[120] M. Pamiès, P. Weiss, E. Garnier, S. Deck, and P. Sagaut, "Generation of synthetic turbulent inflow data for large eddy simulation of spatially evolving wall-bounded flows," *Physics of Fluids*, vol. 21, no. 045103, pp. 1–15, 2009.

[121] R. Poletto, T. Craft, and A. Revell, "A new divergence free synthetic eddy method for the reproduction of inlet flow conditions for les," *Flow, Turbulence, and Combustion*, vol. 91, pp. 519–539, 2013.

[122] C. Cheong, P. Joseph, and S. Lee, "High frequency formulation for the acoustic power spectrum due to cascade-turbulence interaction," *Journal of the Acoustical Society of America*, vol. 119, no. 1, pp. 108–122, 2006.

[123] R. W. Paterson and R. K. Amiet, "Noise and surface pressure response of an airfoil to incident turbulence," *J. Aircraft*, vol. 14, no. 8, pp. 729–736, 1977.

[124] X. Zhang and X. Chen, "Linearised divergence equations for sound propagation," in *17th AIAA/CEAS Aeroacoustics Conference, Portland Oregon*, no. 2011-2930, 2011.

[125] J. Manera, B. Schiltz, R. Leneveu, S. Caro, J. Jacqmot, and S. Rienstra, "Kelvin-helmholtz instabilities occurring at a nacelle exhaust," in *14th AIAA/CEAS Aeroacoustics Conference, Vancouver, British Columbia Canada*, no. 2008-2883, 2008.

[126] R. Ewert and W. Schroder, "Acoustic perturbation equations based on flow decomposition via source filtering," *Journal of Computational Physics*, vol. 188, pp. 365–398, 2003.

[127] X. Zhang, X. Chen, and J. Gill, "Gradient term filtering for stable sound propagation with linearized euler equations," in *20th AIAA/CEAS Aeroacoustics Conference, Atlanta Georgia*, no. 2014-3306, 2014.

[128] A. B. Parry, K. M. Britchford, M. J. Kingan, and P. Sureshkumar, "Aeroacoustic tests of isolated open rotors at high speed," in *18th AIAA/CEAS Aeroacoustics Conference, Colorado Springs*, no. 2012-2220, 2012.

[129] J. Ricouard, E. Julliard, M. Omais, V. Regnier, A. Parry, and S. Baralon, "Installation effects on contra-rotating open rotor noise," in *16th AIAA/CEAS Aeroacoustics Conference, Stockholm Sweden*, no. 2010-3795, 2010.

[130] S. B. Pope, *Turbulent Flows.* Cambridge University Press, 1st ed., 2000.